Cosmological consequences of theories of modified gravity

Jurgen Mifsud

The University Of Sheffield.

A thesis submitted for the degree of
Doctor of Philosophy

School of Mathematics and Statistics
Faculty of Science
The University of Sheffield

Supervised by Professor Carsten van de Bruck

July 2018

Declaration

I hereby declare that except where specific reference is made to the work of others, the contents of this thesis are original and have not been submitted in whole or in part for the consideration for any other degree or qualification in this or any other university. This thesis has been composed by myself and contains nothing which is the outcome of work done in collaboration with others, except as specified in the following acknowledgements.

I confirm that all the work which has formed part of jointly–authored publications is my own work, including the entire text and figures. This includes the work of chapter 4 which is based on Ref. [1] and Ref. [2], the considered model of chapter 5 was presented in Ref. [3], while the analysis of chapter 6 is based on the work published in Ref. [4] that was motivated by our preceding analysis of Ref. [5].

Abstract

Our theoretical understanding of the dynamical evolution of the Universe has certainly improved during the recently established era of precision cosmology. However, the nature of the dark sector remains the greatest puzzle in cosmology. Although we re–establish that the concordance model of cosmology is in agreement with current cosmological observations, this simplistic model is unequivocally theoretically unappealing. Thence, we investigate a number of alternative cosmological models and illustrate their distinctive cosmological consequences.

For instance, we consider a scalar–tensor theory of gravitation, such that the minimally coupled scalar field is explicitly coupled to multiple fluid components. The assumed coupling functions are specified by the theoretically well–motivated conformal and disformal coupling functions. We perform a dynamical systems analysis, in which we establish the existence and stability conditions for every fixed point, and illustrate that disformally coupled systems have a dissimilar cosmological evolution with respect to the conformally coupled and uncoupled systems. We further show that a disformal coupling between the matter and radiation sectors is characterised by a varying fine–structure constant.

Moreover, a direct coupling between dark energy and dark matter is not theoretically forbidden and might be incorporated in extensions of the standard model of particle physics. We consider a coupled quintessence model, in which the dark energy scalar field only couples to dark matter via the conformal and disformal coupling functions, and is decoupled from the conventional baryonic matter sector. We scrutinise the distinctive features of this cosmological model, where we particularly show that when the dark sector constituents are disformally coupled, intermediate–scales and time–dependent damped oscillations appear in the matter growth rate function. We confront this coupled quintessence model with current cosmological data sets, and illustrate that Nature is consistent with a null coupling within the dark sector of the Universe.

Contents

List of figures

List of tables

For mum

Acknowledgments

First and foremost, I would like to thank my supervisor Professor Carsten van de Bruck for his inspiration, guidance, enthusiasm, and encouragement in pursuing an academic career in cosmology. For this I will always be grateful.

I would also like to thank my collaborators Professor José Pedro Mimoso, Dr. Jack Morrice, and particularly Dr. Nelson Nunes for their invaluable advice and fruitful discussions. They have each been fantastic to work with, and I am grateful for their helpful input.

Many thanks also go to all the CRAG group members, past and present, with whom I enjoyed having discussions on various subjects.

Finally, I am profoundly grateful for my family's continued and unfailing support, and for taking interest in my research studies. I really appreciate how all of you have stuck with me through thick and thin.

Space–time tells matter how to move; matter tells space–time how to curve.

John Archibald Wheeler

1 Introduction

The scientific understanding of the origin, dynamical evolution, current status, and ultimate fate of the Universe are all robustly addressed with cosmology. This exploration of the entire Universe along with all its contents evidently demands knowledge from every branch of physics, which makes the unique subject of cosmology one of the most prosperous and stimulating scientific disciplines. In spite of the astounding progress that has been made over the last few decades towards a better understanding of the cosmos, cosmologists are still pondering on a number of fundamental questions about the Universe.

One of the most intriguing aspects of cosmology lies within its ability to probe a vast range of scales. This is evident from the units that are often adopted by cosmologists, for instance the megaparsec (Mpc) and gigayear (Gyr) units are used instead of the metric units of metre (m) and second (s), respectively. Since cosmology also deals with microscopic scales, cosmologists have adopted the particle physics energy units of electron–volts (eV) instead of joules (J). The latter also shows the connection of cosmology with another well–established area of physics.

Although cosmology could be regarded as an attempt to draw enormous conclusions from a strikingly restricted number of cosmological observations, theoretical cosmology has always looked for a plausible explanation of the reported observation. Fortunately, observational cosmology has been recently making rapid progress, which consequently led to a better theoretical understanding of the Universe. Even before the current era of the so–called precision cosmology, observational advances have ruled out some elegant theoretical proposals, such as the steady–state theory in which the expanding Universe has no beginning and no end. Other ideas, such as the hot Big Bang theory, have survived solely because we have not yet found out what might be wrong with them. However, we are now at a crucial point where we can confront our theoretical speculations on how the cosmos works, with several ex-

periments that are able to probe various cosmic epochs. This would hopefully steer us towards that theoretical model which best describes the cosmological evolution of our Universe.

In this introductory chapter we will first introduce the well–established theory of General Relativity which governs the evolution of the Universe. Thus, in section 1.1 we present the theory of General Relativity and apply it to cosmology. In section 1.2 we first review the standard model of Big Bang cosmology, and further consider the framework of the concordance model of cosmology, in which we discuss its present–day status. We conclude this chapter in section 1.3.

1.1 General Relativity & cosmology

Albert Einstein reported the final form of his theory of General Relativity to the Prussian Academy of Sciences in November 1915 [6, p. 245]. This theory along with Quantum Field Theory are now widely considered as the keystones of modern physics. The theory of General Relativity is a geometric field–theory par excellence, which pioneered the use of differential geometry in physical theories, as Einstein himself remarked [6, p. 98] that *"nobody who really grasped it (General Relativity) can escape from its charm, because it signifies a real triumph of the general differential calculus as founded by Gauss, Riemann, Christoffel, Ricci, and Levi–Civita"*. Remarkably, the equations that Einstein presented in his paper [6, p. 245] titled *"Die Feldgleichungen der Gravitation"* (*The Field Equations of Gravitation*), remained completely unchanged. These equations are now better known as the Einstein field equations, which are still our best description of how space–time behaves on macroscopic scales.

Einstein's theory of General Relativity has been repeatedly tested and, till now, it has passed these tests with flying colours. We will first mention two classical tests of General Relativity, and then discuss a rigorous test of the theory which was only possible to conduct very recently. The first test, or rather confirmation, of General Relativity was its ability to predict the already discovered anomalous perihelion precession of Mercury. This was first pointed out by Urbain Jean Joseph Le Verrier [7] and was considered as a crisis of Newtonian dynamics. A number of unsuccessful solutions were proposed, including Le Verrier's hypothetical Vulcan planet that was postulated to reside in an orbit between the Sun and Mercury. This discrepancy between the observed rate of precession and that predicted by Newtonian theory was reported to be (45 ± 5) arc–seconds per century at the time when Einstein was formulating his theory. In 1915 Einstein [6, p. 116] calculated a perihelion advance of 43 arc–seconds per century, which clearly illustrated that the theory of General Relativity can fully explain this reported disagreement. More recent measurements were also found to be in an excellent agreement with the latter predicted value,

for instance the *MESSENGER* spacecraft reported [8] this to be (42.9799 ± 0.0009) arc–seconds per century.

The other classical test that we will mention is the famous prediction of the deflection of starlight by the Sun. Einstein calculated [6, p. 114] a deflection angle of ~ 1.75 arc–seconds with the aid of his theory of General Relativity, whereas a recent measurement of $(0.9998 \pm 0.0004) \times 1.75$ arc–seconds [9] was reported from very–long–baseline interferometry. This prediction was first confirmed [10] by Sir Arthur Stanley Eddington together with his collaborators after their observation of the total solar eclipse of May 29, 1919. These two classical tests are both mentioned in the paper [10] by Eddington and his collaborators in which they remark that *"it appears now to be established that Einstein's law of gravitation gives the true deviations from the Newtonian law both for the relatively slow–moving planet Mercury and for the fast–moving waves of light"*.

A more recent stringent test of General Relativity was conducted by multi–messenger gravitational–wave astronomy. Gravitational–waves are a prediction of all known relativistic theories of gravity, however the direct observation of gravitational–waves opened a new window that would enable us to validate the underlying gravitational theory that governs the dynamics of our Universe. The first direct detection of gravitational–waves was reported [11] in 2016 by the Laser Interferometer Gravitational–Wave Observatory (LIGO) scientific collaboration and Virgo collaboration, which originated from the merger of a pair of black holes. The same collaborations were able to detect other events [12–15], particularly the gravitational–wave event GW170817 [16], which was the first detection of gravitational–waves from the inspiral of a binary neutron star system. The latter event was further followed by observations of its electromagnetic counterpart GRB 170817A [17], consequently making multi–messenger gravitational–wave astronomy a reality. This GW170817 event led to a very tight constraint on the fractional speed difference between the speed of gravitational–waves (c_{GW}) and that of light (c), which was reported [18] to be $-3 \times 10^{-15} \leq \Delta c/c \leq 7 \times 10^{-16}$, where $\Delta c = c_{GW} - c$. This is a very strong confirmation of General Relativity which predicts that the speed of gravitational–waves is strictly equal to the speed of light in vacuum.

As we already mentioned, the theory of General Relativity treats gravity as a physical manifestation of geometry. This statement is attributed to the fact that General Relativity forms part of the so–called family of gravitational metric theories, which for instance includes the first metric theory of Gunnar Nordström's conformally–flat scalar gravitational theory [19]. At the heart of all metric theories of gravitation lies the well–known Einstein's equivalence principle. This principle of equivalence embraces the more elementary equivalence principle, better known as the weak equivalence principle, which in its simplest form states that two distinct bodies in a gravitational field fall with the same acceleration; thus, often referred to

as the universality of free–fall. Therefore, according to the weak equivalence principle, the trajectory of an uncharged test body is independent of its internal structure and composition, such that this test body has a negligible binding gravitational energy and evades the inhomogeneities of the gravitational field. A direct test of the weak equivalence principle is normally conducted by comparing the acceleration of two bodies of different composition in an external gravitational field, with which one checks for a violation of the principle by comparing the relative difference in their respective free–fall accelerations. For instance, this is currently being carried out by the *MICROSCOPE* [20] space mission which has tested the weak equivalence principle at a precision of $\sim 10^{-14}$, and is aiming for a further improvement in its sensitivity by another order of magnitude.

The Einstein equivalence principle further requires that the conditions of local position invariance and local Lorentz invariance are satisfied. The former imposes that the result of any local non–gravitational experiment is independent of where and when in the Universe it is performed, whereas the latter states that the outcome of an arbitrary local non–gravitational experiment is independent of the motion of the laboratory as long as it is free–falling. Local Lorentz invariance has been tested by several experiments, such as Michelson–Morley type experiments [21] and the more accurate Hughes–Drever type experiments [22–24]. On the other hand, the other required condition of local position invariance was mainly tested by gravitational redshift experiments, such as the one of Gravity Probe–A [25] which compared the frequency of a hydrogen–maser clock that was on the ground with the frequency of another clock that was flown on a rocket.

Finally, if Einstein's equivalence principle is valid, then gravitation is not interpreted as a force, but as a manifestation of geometry in curved space–time. This leads to the properties of a metric theory of gravitation in which: the geometry of space–time is specified by a metric, freely–falling test bodies follow the geodesics (a line of shortest path) of that metric, and that in a local freely–falling reference frame the non–gravitational laws of Nature take the same form as in special relativity. We should also remark that Einstein's equivalence principle is contained in the more restrictive strong equivalence principle, which further includes bodies with self–gravitational interactions and of experiments involving gravitational forces. Examples of gravitational theories that satisfy the strong equivalence principle are Einstein's theory of General Relativity and Nordström's theory, however the latter was abandoned as it does not predict deflection of light.

At this point, after we have motivated the theory of General Relativity from the physics point of view, we now introduce the mathematical framework which can embody this gravitational theory. As already mentioned, the trajectory of a freely–falling body which is only experiencing the force of gravity, can be described by a geodesic in a four–dimensional curved space–time. Space-time is therefore depicted

as a four–dimensional continuum, such that one requires four values to locate each event. For the case of General Relativity this will be modelled as a four–dimensional manifold, that is, a space consisting of neighbourhoods that are locally like $\mathbb{R}^4$ and that can be continuously glued together. Thus, it is imperative to briefly introduce some necessary elements of differential geometry along with the notation that will be used throughout this thesis, unless stated otherwise.

We recall that a tensor T of rank $(p,\, q)$ is a multilinear map from $(V_s)^p \times (V_s^*)^q$ to $\mathbb{R}$, such that

$$T = T^{\mu_1 \cdots \mu_p}{}_{\nu_1 \ldots \nu_q}\, \partial_{\mu_1} \otimes \ldots \otimes \partial_{\mu_p} \otimes \mathrm{d}x^{\nu_1} \otimes \ldots \otimes \mathrm{d}x^{\nu_q} \ , \tag{1.1}$$

where the basis of the vector space V_s and of the dual space V_s^* are respectively denoted by $\partial/\partial x^\mu \equiv \partial_\mu$ and $\mathrm{d}x^\nu$, and we use $\otimes$ for the tensor product. This tensor is said to be p–times contravariant and q–times covariant. In particular, we remark that a scalar is a tensor of rank $(0,\, 0)$, while a vector is a tensor of rank $(1,\, 0)$. Moreover, in a coordinate transformation, the components of a tensor transform as follows

$$T^{\mu'_1 \cdots \mu'_p}{}_{\nu'_1 \ldots \nu'_q} = \frac{\partial x^{\mu'_1}}{\partial x^{\alpha_1}} \cdots \frac{\partial x^{\mu'_p}}{\partial x^{\alpha_p}} \frac{\partial x^{\beta_1}}{\partial x^{\nu'_1}} \cdots \frac{\partial x^{\beta_q}}{\partial x^{\nu'_q}} T^{\alpha_1 \ldots \alpha_p}{}_{\beta_1 \ldots \beta_q} \ . \tag{1.2}$$

Some useful properties of tensor calculus are that one can add tensors of the same rank, compute the tensor product of two tensors, along with the contraction of the indices of a given tensor. A special characteristic of a symmetric tensor is that it satisfies $T^{\mu\nu} = T^{\nu\mu}$, and a tensor is said to be antisymmetric if $T^{\mu\nu} = -T^{\nu\mu}$.

An important tensor in curved space–time is the metric tensor, by which one can define the square of the distance between two neighbouring points. Thus, the metric tensor $g_{\mu\nu}$, with its inverse denoted by $g^{\mu\nu}$, should be a symmetric and non–degenerate tensor of rank $(0,\, 2)$, implying that it has ten components. We can now define the line–element between two events to be

$$\mathrm{d}s^2 = g_{\mu\nu}\, \mathrm{d}x^\mu\, \mathrm{d}x^\nu \ . \tag{1.3}$$

The metric tensor is also used to raise and lower the indices of a given tensor, for instance

$$Q^{\mu_1 \cdots \mu_p \mu}{}_{\nu_2 \ldots \nu_q} = Q^{\mu_1 \cdots \mu_p}{}_{\nu_1 \nu_2 \ldots \nu_q} g^{\nu_1 \mu} \ . \tag{1.4}$$

We will denote the determinant of the metric by $g = \det g_{\mu\nu}$, with its derivative given by $\partial_\alpha g = g\, g^{\mu\nu} \partial_\alpha g_{\mu\nu}$. We should also point out that the relationship of $g^{\mu\nu} g_{\mu\nu} = 4$, implies that $g^{\mu\nu} \partial_\alpha g_{\mu\nu} = -g_{\mu\nu} \partial_\alpha g^{\mu\nu}$. Finally, in this thesis we will be adopting the metric signature $(\ -\ +\ +\ +\ )$, and we will be setting the units such that the speed of light is unity, unless stated otherwise.

We now introduce the Christoffel connection with its associated coefficients known

as the Christoffel symbols, which will constantly appear when we describe the properties of curved space–time. We define a metric–compatible and torsion–free connection by the Christoffel symbols

$$\Gamma^{\sigma}_{\mu\nu} = \frac{1}{2} g^{\sigma\rho} \left(\partial_{\mu} g_{\nu\rho} + \partial_{\nu} g_{\rho\mu} - \partial_{\rho} g_{\mu\nu} \right) \ , \tag{1.5}$$

which transforms like a connection, and therefore is not a tensor. We remark that in four–dimensions we find forty Christoffel symbols, and by a torsion–free connection we mean that it is symmetric in its lower indices. From the above relationships, we find a useful property that $\Gamma^{\mu}_{\mu\alpha} = \partial_{\alpha}(\ln\sqrt{-g})$. The fundamental use of a connection is to take a covariant derivative ∇_{μ}, which for an arbitrary tensor this is given by

$$\begin{aligned} \nabla_{\alpha} T^{\mu_1 \cdots \mu_p}{}_{\nu_1 \ldots \nu_q} = & \partial_{\alpha} T^{\mu_1 \cdots \mu_p}{}_{\nu_1 \ldots \nu_q} + \Gamma^{\mu_1}_{\alpha\lambda_1} T^{\lambda_1 \mu_2 \cdots \mu_p}{}_{\nu_1 \ldots \nu_q} + \ldots + \Gamma^{\mu_p}_{\alpha\lambda_p} T^{\mu_1 \cdots \mu_{p-1} \lambda_p}{}_{\nu_1 \ldots \nu_q} \\ & - \Gamma^{\lambda_1}_{\alpha\nu_1} T^{\mu_1 \cdots \mu_p}{}_{\lambda_1 \nu_2 \ldots \nu_q} - \ldots - \Gamma^{\lambda_q}_{\alpha\nu_q} T^{\mu_1 \cdots \mu_p}{}_{\nu_1 \ldots \nu_{q-1} \lambda_q} \ . \end{aligned} \tag{1.6}$$

Consequently, this shows that the Christoffel connection is metric–compatible, since the covariant derivative of the metric vanishes $\nabla_{\alpha} g_{\mu\nu} = 0$. It also follows that for a scalar ϕ, we have that $\nabla_{\mu}\phi = \partial_{\mu}\phi$. Moreover, we define parallel transport of a tensor T, along the path $x^{\mu}(\lambda)$, with λ being the affine parameter, by the following condition

$$\frac{\mathrm{d}x^{\sigma}}{\mathrm{d}\lambda} \nabla_{\sigma} T^{\mu_1 \cdots \mu_p}{}_{\nu_1 \ldots \nu_q} = 0 \ , \tag{1.7}$$

which for the particular case of a tangent vector being parallel transported along a curve, also known as auto–parallel transport, gives the geodesic equation. We will be denoting the covariant derivative either with the symbol ∇_{μ} or with the subscript $;\mu$, such that $\nabla_{\mu} T^{\nu} \equiv T^{\nu}{}_{;\mu}$. Similarly, for the ordinary partial derivative we adopt the notation of $\partial_{\mu} T^{\nu} \equiv T^{\nu}{}_{,\mu}$.

We now introduce the Riemann curvature tensor $R^{\mu}{}_{\nu\alpha\beta}$, which provides a local description of the curvature of space–time at each point. This is defined by $(\nabla_{\alpha}\nabla_{\beta} - \nabla_{\beta}\nabla_{\alpha}) T^{\mu} = R^{\mu}{}_{\nu\alpha\beta} T^{\nu}$, where the Riemann tensor is explicitly given by

$$R^{\mu}{}_{\nu\alpha\beta} = \partial_{\alpha}\Gamma^{\mu}_{\nu\beta} - \partial_{\beta}\Gamma^{\mu}_{\nu\alpha} + \Gamma^{\mu}_{\sigma\alpha}\Gamma^{\sigma}_{\nu\beta} - \Gamma^{\mu}_{\sigma\beta}\Gamma^{\sigma}_{\nu\alpha} \ , \tag{1.8}$$

which satisfies the following conditions

$$R_{\sigma\nu\alpha\beta} = g_{\sigma\mu} R^{\mu}{}_{\nu\alpha\beta} \ , \quad R_{\alpha\mu\nu\sigma} = -R_{\mu\alpha\nu\sigma} = -R_{\alpha\mu\sigma\nu} \ , \quad R_{\alpha\mu\nu\sigma} = R_{\nu\sigma\alpha\mu} \ , \tag{1.9}$$

along with the identity

$$R_{\alpha\mu\nu\sigma} + R_{\alpha\nu\sigma\mu} + R_{\alpha\sigma\mu\nu} = 0 \, . \tag{1.10}$$

These properties of the Riemann tensor imply that it has twenty independent components in a four–dimensional curved space–time. The Riemann tensor is also characterised by a cyclic symmetry property of

$$R_{\alpha\mu\nu\sigma;\beta} + R_{\alpha\mu\sigma\beta;\nu} + R_{\alpha\mu\beta\nu;\sigma} = 0 \, , \tag{1.11}$$

which is better known as the Bianchi identity. From the Riemann tensor, we can construct the symmetric Ricci tensor defined by

$$R_{\mu\nu} = R^{\alpha}{}_{\mu\alpha\nu} = -R^{\alpha}{}_{\mu\nu\alpha} \, , \tag{1.12}$$

which has ten independent components. The trace of the Ricci tensor defines the Ricci scalar, such that $R = R_{\mu\nu} g^{\mu\nu}$. Moreover, the twice–contracted Bianchi identity leads us to

$$\nabla^{\mu} G_{\mu\nu} = 0 \, , \quad G_{\mu\nu} = R_{\mu\nu} - \frac{1}{2} R \, g_{\mu\nu} \, , \tag{1.13}$$

where the symmetric tensor $G_{\mu\nu}$ is known as the Einstein tensor.

We will now turn our attention to cosmology, where we will be utilising our acquired knowledge from the above tests of the gravitational theory, which were conducted on a scale of the order of the size of the Solar System, and extrapolate this to the whole Universe. The first time that the theory of General Relativity was applied to cosmology was in 1917 by Einstein himself [26], which undoubtedly started the ball rolling for modern cosmology. Einstein presented a cosmological solution which was inspired by Mach's philosophy, and led him to postulate a Universe that is static, spatially finite, and closed such that no boundary conditions are needed. In order to achieve his goal of a static Universe, Einstein introduced the additional Λ term, or cosmological constant, to his field equations. Indeed, he emphasised that the introduction of this term was not justified by the theory of General Relativity, however its inclusion was motivated by the quest for a static solution of his equations.

One can derive the Einstein field equations by varying the action of the gravitational theory with respect to the metric. The gravitational Lagrangian that was proposed by Einstein and Hilbert reduces to the scalar curvature R, from which one can deduce the vacuum field equations. The relevant action that we will be considering for the so–called concordance model of cosmology, is given by

$$\mathcal{S} = \frac{1}{2\kappa^2} \int (R - 2\Lambda) \sqrt{-g} \, \mathrm{d}^4 x + \int \mathcal{L}_{\mathrm{mat}} \sqrt{-g} \, \mathrm{d}^4 x \, , \tag{1.14}$$

where κ^2 is a coefficient that is determined by requiring that the theory reduces to Newtonian gravity in the weak–field limit, which imposes that $\kappa^2 = 8\pi G$, where G is Newton's gravitational constant. The matter fields are represented by the matter Lagrangian $\mathcal{L}_{\rm mat}$, and Λ is the already mentioned cosmological constant. We will refer to other choices of the action from the one presented in Eq. (1.14) as extensions of the standard case. After varying Eq. (1.14) with respect to $g_{\mu\nu}$, we get to the general form of Einstein's equations

$$G_{\mu\nu} + \Lambda\, g_{\mu\nu} = \kappa^2\, T_{\mu\nu}\ , \tag{1.15}$$

where we introduced a rank two symmetric energy–momentum tensor $T_{\mu\nu}$, defined by

$$T_{\mu\nu} = -\frac{2}{\sqrt{-g}}\frac{\delta\left(\mathcal{L}_{\rm mat}\sqrt{-g}\right)}{\delta\, g^{\mu\nu}}\ . \tag{1.16}$$

By using the above Einstein field equations along with the fact that the covariant derivatives of the Einstein tensor and the metric tensor vanish, we get to the energy–momentum conservation equation in curved space–time

$$\nabla_\mu\, T^{\mu\nu} = 0\ . \tag{1.17}$$

We remark that this conservation equation is satisfied by the total energy–momentum tensor, which is composed of all matter components that fill the Universe.

Finally, we now turn our attention to cosmological solutions in the theory of General Relativity. As already mentioned, Einstein first applied his theory of General Relativity to the entire Universe, where he derived a static and closed solution for his equations. A few months after Einstein published his solution, Willem de Sitter reported [27] that he had found a completely different cosmological model which was devoid of matter. Because of this absence of matter, Einstein was not comfortable with de Sitter's solution.

A path–breaking paper on a truly dynamic Universe appeared in 1922 by Alexander Alexandrovich Friedmann [28]. In his solution, Friedmann also recovered Einstein's and de Sitter's cosmological models. At first, Einstein thought that Friedmann's solution was not compatible with his field equations of General Relativity [29]. After Einstein realised his error, he acknowledged that mathematically Friedmann was correct, but he further remarked that Friedmann's dynamical solution was hardly of physical significance; a comment which was deleted in the published version [30]. In 1927, Einstein was again confronted with Friedmann's dynamic Universe, that was independently revisited by Georges Lemaître [31]. Lemaître was well aware of the observational status of cosmology at the time, which consequently led him to further incorporate the velocities of the galaxies measured by Vesto Melvin Slipher (published by Gustaf Strömberg [32]) along with their distance measurements deter-

mined by Edwin Powell Hubble [33]. Remarkably, Lemaître concluded that these observations were compatible with his postulate of an expanding Universe, and further determined, what is now called, the Hubble constant to be $\sim 625\,\mathrm{km\,s^{-1}Mpc^{-1}}$. This was later refined to $\sim 500\,\mathrm{km\,s^{-1}Mpc^{-1}}$ by Hubble [34], where he also reported a linear relationship between the galaxy's recession velocities and their respective distances; a discovery that became known as Hubble's law.

Regardless of the theoretical studies of Friedmann and Lemaître along with the observational evidence on the expansion of the Universe, it turned out that Einstein still considered his own idea of a static Universe. Indeed, during the Solvay meeting in 1927, Einstein told Lemaître that *"from a physical point of view this looked to him abominable"* [30]. However, in 1930 Eddington showed [35] that Einstein's immutable cosmos is unstable. This triggered Einstein's acceptance of the expanding Universe model, which consequently led him to sideline his original solution. As Einstein highlighted in his 1931 publication [36], Hubble's observational evidence was of secondary importance to him, however it is somewhat puzzling that Einstein did not realise that his original model was unstable after he became aware of Friedmann's solution. At this point, Einstein adopted Friedmann's oscillating solution of a positively curved Universe with vanishing cosmological constant. This Friedmann–Einstein model led to the proposal of a flat matter–only cosmological model by Einstein and de Sitter [37]. The Einstein–de Sitter Universe was popular until the early 1990s when cosmological data was not agreeing with this model. Indeed, as we will discuss in section 1.2, current cosmological observations are in an excellent agreement with the Λ–cold–dark–matter (ΛCDM) model, often referred to as the concordance model of cosmology.

1.2 The emergence of the concordance model

We will now discuss the construction of the so–called concordance model of cosmology, which is based on the theory of General Relativity that governs the overall behaviour of the Universe, together with an extension of the hot Big Bang model. As we have seen in section 1.1, the general theory of relativity is currently well–established in the sense that no obvious excursion from this gravitational theory has ever been observed. Thus, we will first focus on the hot Big Bang model and discuss its extended concordance model of cosmology, which we will show that the latter is in an excellent agreement with current cosmological observations.

The idea that the Universe was once very hot and dense, and has expanded and cooled to its present state was first coined by Lemaître when he postulated that the *"whole Universe would be produced by the disintegration of this primeval atom"* [38]. The formulation of the Big Bang model was developed in the 1940s by George Gamow [39–43] along with his collaborators Ralph Asher Alpher, Hans Bethe, and

Robert Herman [44–52]. Their ground–breaking proposal that the abundances of the elements could be explained via the cosmic history of the Universe, consequently led them to the prediction of the presence of a relic background radiation with a temperature of order a few Kelvin. Thus, the formation of light nuclei during primordial nucleosynthesis, the existence of the cosmic background radiation, along with the expansion of the Universe lie at the heart of the standard model of Big Bang cosmology.

As we already discussed, the first piece of evidence for the Big Bang model was shown by Hubble when he clearly illustrated this expansion of the Universe with his discovery of a linear relationship between the recessional velocity of the observed galaxies and their distance. This Hubble diagram has constantly been revisited by several experiments, each using its own distinct method. These experiments led to a better determination of the current expansion rate of the Universe, better known as the Hubble constant. In chapter 3 we will discuss current measurements of the Hubble constant, particularly focusing on some current unresolved discrepancies between some of the most recent direct and indirect measurements of the present expansion rate of the Universe. Remarkably, in the current era of precision cosmology, these measurements of the Hubble constant are now at the basis of most of the cosmological tests that check for consistency with the concordance model of cosmology.

However, by itself, the Hubble expansion did not provide sufficient evidence for the acceptance of the Big Bang model. The definitive evidence for the hot Big Bang model was brought by the discovery of the $3.3 \pm 1.0\,\mathrm{K}$ cosmic microwave background (CMB) radiation by Arno Allan Penzias and Robert Woodrow Wilson [53, 54] in 1965. Their serendipitous detection was immediately interpreted by Robert Henry Dicke and his collaborators [55] to be the relic blackbody radiation that was theoretically proposed nearly two decades earlier. This observation singled out the Big Bang model as the prime candidate to describe our Universe, which has now superseded other alternatives, such as the steady–state model that was proposed in 1948 by Hermann Bondi, Thomas Gold, and Fred Hoyle [56, 57]. Particularly, the CMB radiation spectrum was later shown to be in an excellent agreement with a blackbody spectrum by the Far Infrared Absolute Spectrophotometer [58, 59] instrument on the COBE satellite. Such an observation was very challenging to be explained with the other alternative models, which consequently paved the way for the acceptance of this model as the standard model of cosmology. We will further discuss the CMB radiation along with the implications of tiny departures from the blackbody profile, commonly known as spectral distortions, in chapter 2. Finally, we should mention that a number of experiments were able to measure the temperature of the CMB radiation at earlier epochs [60–62], and these were found to be in a remarkable agreement with the expected scaling of the temperature in an expanding Universe.

Last, but certainly not least, the theoretical Big Bang nucleosynthesis prediction

of the abundances of light elements are found to be in an excellent agreement with the actual measurements. Big Bang nucleosynthesis describes the production of helium–4, deuterium, helium–3, and lithium–7, along with other negligible traces of heavier nuclei, during the first few minutes of the Universe. This cosmic epoch was characterised by relatively high densities and temperatures with respect to the current state of the Universe, which consequently allowed for a series of nuclear reactions to take place. For the formation of heavy elements, it is crucial that deuterium is synthesised before the reaction chain can continue; commonly referred to as the deuterium bottleneck. Since various nuclear processes can take place during the evolution of the Universe which could modify the primordial abundances of light nuclei, the comparison between the observed and predicted abundances is not trivial. However, the few key parameters that describe the process of primordial nucleosynthesis are now very–well determined. For instance, the neutron lifetime has been measured in nuclear physics laboratories [63], the number of light neutrino species has also been very–well determined from Z boson electron–positron collider experiments [64], and the number density of baryons per photon was accurately probed by cosmological observations [65]. Evidently, Big Bang nucleosynthesis is an invaluable tool which enables us to not only test the Big Bang model, but also to probe nuclear physics and general astrophysics.

The above observational pillars strongly suggest that the Big Bang standard model of cosmology provides a robust description of the history of the Universe from $\sim 10^{-4}$ s after the Big Bang. This clearly depends on the validity of General Relativity, nuclear physics, and electromagnetic physics, all of which have never been contradicted. Moreover, we should remark that in this model the Universe is assumed to be initially radiation–dominated, which then evolves to a matter–dominated era, and finally, the model allows for either a Λ–dominated epoch or a curvature–dominated era.

1.2.1 The Friedmann–Lemaître–Robertson–Walker solution

We now discuss the mathematical construction of the standard model of cosmology within General Relativity, such that it will be in agreement with the observable Universe. As we described in section 1.1, the elementary ingredient of General Relativity is the space–time metric. In the standard model of cosmology, the basis of the metric formulation is the empirical observation that on appreciably large cosmic length scales, and at earlier times, the Universe is remarkably homogeneous and isotropic. This observational fact has been promoted to the cosmological principle which supposes that the Universe is spatially isotropic and homogeneous. Thus, this uniformity principle could be viewed as an extension to the Copernican principle, according to which we are not situated in a privileged place in the Universe. Indeed, by adding the Copernican principle with the isotropic hypothesis, the cosmological

principle follows.

The isotropic hypothesis, by which we mean that at every point the Universe can be seen as isotropic, is nowadays well–established throughout the observable Universe. For instance, spectroscopic surveys have illustrated this isotropy in the projected distribution of the locations of galaxies on the celestial sphere [66], along with the angular distributions of radio sources [67]. At earlier times, isotropy has been clearly illustrated by the reported tiny fluctuations in the temperature of the CMB radiation [65, 68], the linchpin of much present–day observational cosmology.

By homogeneity we mean that at every instant, each point of space is similar to any other one. This has also been verified via the three–dimensional maps of the galaxy locations in large volume galaxy catalogues [69, 70]. On the other hand, inhomogeneous models, for which the spherically–symmetric but inhomogeneous Lemaître–Tolman–Bondi [71–73] space–time is often adopted, have been shown [74] to fit current cosmological data without the use of the cosmological constant. However, it has been reported [75] that in such models, a violation of the blackbody CMB radiation energy spectrum is expected to severely constrain these models with prospective spectral distortions experiments. We will discuss and make use of spectral distortions in the CMB radiation spectrum in chapter 2.

The cosmological principle entails that the geometry of space–time be highly–symmetric and completely described by Friedmann's original solution, in which the ten arbitrary functions in the space–time metric are reduced to the scale factor function $a(t)$, and a pure number K. As already described, Friedmann's solution was studied by Lemaître, and it was later explored by Howard Percy Robertson [76] along with Arthur Geoffrey Walker [77] in the 1930s. This became known as the Friedmann–Lemaître–Robertson–Walker (FLRW) metric, which, in spatial comoving spherical coordinates, its line–element takes the general form

$$\mathrm{d}s^2 = -\mathrm{d}t^2 + a^2(t)\left(\frac{\mathrm{d}r^2}{1-Kr^2} + r^2\left(\mathrm{d}\theta^2 + \sin^2\theta\,\mathrm{d}\varphi^2\right)\right) , \tag{1.18}$$

where t is the physical cosmic time, whereas r, θ, and φ are the spatial comoving coordinates which label the points of the three–dimensional constant time–slice. These spatial comoving coordinates are insensitive to the expansion dynamics, where the expansion of the Universe is described by the evolution of the cosmic scale factor $a(t)$, which is encoded in Einstein's field equations. As a consequence of this expansion, the physical distances are weighted by the scale factor, and are thus increasing with time. Moreover, the scale factor is defined up to an arbitrary constant rescaling, which directly corresponds to a rescaling of the comoving variables. Unless stated otherwise, in this thesis we will be using the convention of $a_0 \equiv a(t_0) = 1$, where we denote parameter values at the present epoch by a 0–subscript.

The quantity K denotes the curvature of the three–dimensional space. By a

suitable redefinition of the radial coordinate r, this can be reduced to the canonical values $K = \{+1, 0, -1\}$, corresponding to a positive curvature three–space, a flat three–dimensional plane, and a negative curvature three–dimensional space, respectively. In the following, it will be convenient to adopt the conformal time η, which is related to the cosmic time by $\mathrm{d}t = a(t)\mathrm{d}\eta$. In this convention, the generic FLRW line–element can be expressed as follows

$$\mathrm{d}s^2 = a^2(\eta)\left(-\mathrm{d}\eta^2 + \frac{\mathrm{d}r^2}{1-Kr^2} + r^2\left(\mathrm{d}\theta^2 + \sin^2\theta\,\mathrm{d}\varphi^2\right)\right) . \tag{1.19}$$

Particularly, in the flat case, which will be frequently used in the following chapters, the FLRW line–element can be expressed in the usual spatial Cartesian coordinates by

$$\mathrm{d}s^2 = a^2(\eta)\left(-\mathrm{d}\eta^2 + \mathrm{d}x^2 + \mathrm{d}y^2 + \mathrm{d}z^2\right) . \tag{1.20}$$

An immediate consequence of the FLRW metric is Hubble's law. Indeed, in the physical space, the separation between two comoving observers with trajectories specified by $\boldsymbol{x} = \boldsymbol{x}_1$ and $\boldsymbol{x} = \boldsymbol{x}_2$, is given by $\boldsymbol{r}_{12} = a(t)(\boldsymbol{x}_1 - \boldsymbol{x}_2)$. Thus, its rate of change is given by

$$\dot{\boldsymbol{r}}_{12} = H\boldsymbol{r}_{12} , \tag{1.21}$$

where

$$H = \frac{\dot{a}}{a} , \tag{1.22}$$

is the Hubble parameter, and an over–dot denotes a derivative with respect to the cosmic time t. This illustrates that the farther the observers are from each other, the larger is their relative velocity. Since this applies for small separations, the Hubble parameter is often approximated by the Hubble constant, therefore recovering Hubble's law. The experimental determination of the Hubble constant H_0, is still continuously being refined, therefore it is often expressed in terms of its respective dimensionless parameter h as

$$H_0 = 100\,h\ \mathrm{km\,s^{-1}Mpc^{-1}} . \tag{1.23}$$

A current conservative mean value is found to be at $h \sim 0.7$ [65, 78, 79], with a few percent uncertainty.

A pivotal consequence of the expanding Universe is associated with the propagation of light, which emerges from Maxwell's equations in vacuum specified by $\nabla_\mu F^{\nu\mu} = 0$, where the antisymmetric Faraday tensor $F_{\mu\nu}$ satisfies $F_{\mu\nu;\alpha} + F_{\nu\alpha;\mu} + F_{\alpha\mu;\nu} = 0$. Maxwell's equations dictate that the trajectory of a light–ray $x^\mu(\lambda)$, is given by a null ($\mathrm{d}s^2 = 0$) geodesic with wave–vector $k^\mu = \mathrm{d}x^\mu/\mathrm{d}\lambda$, where λ is the affine parameter along the photon trajectory. Consequently, this wave–vector

is found to satisfy $k^\mu k_\mu = 0$ and $k^\mu \nabla_\mu k^\nu = 0$, from which one arrives to the key relationship of $\dot{E}/E = -H$. This shows that the energy of a photon E, measured by a comoving observer with four–velocity u^μ, is inversely proportional to the cosmic scale factor. Thus, this gives $E = h_{\rm pl}\,\nu = -k^\mu u_\mu \propto a^{-1}$, where $h_{\rm pl}$ is Planck's constant and ν is the photon frequency. This leads us to the definition of the redshift z, defined by

$$1 + z = \frac{a\,(t_{\rm rec})}{a\,(t_{\rm em})} = \frac{\nu_{\rm em}}{\nu_{\rm rec}} = \frac{\left(k_\mu u^\mu\right)_{\rm em}}{\left(k_\mu u^\mu\right)_{\rm rec}}\,, \tag{1.24}$$

where $\nu_{\rm em}$ and $\nu_{\rm rec}$ are the photon's emitted and received frequencies, respectively. Therefore, from redshift measurements one can deduce how much the Universe has expanded since light was emitted from a distant source. Indeed, from the definition of the Hubble parameter, one can easily show that time intervals are related to redshift intervals by $\mathrm{d}t = -\mathrm{d}z/[H(z)(1+z)]$. From the latter equation one can compute the age of the Universe by evaluating the following integral

$$t_0 = \int_0^\infty \frac{\mathrm{d}z}{H(z)\,(1+z)}\,, \tag{1.25}$$

along with its analogous conformal time, given by

$$\eta_0 = \int_0^1 \frac{\mathrm{d}a}{a^2 H(a)}\,. \tag{1.26}$$

With the above definition of the redshift, we now expand the scale factor around its current value as follows

$$a(t) = a_0 \left[1 + H_0\,(t - t_0) - \frac{1}{2}\,q_0\,H_0^2\,(t - t_0)^2 + \ldots\right]\,, \tag{1.27}$$

such that $0 < t_0 - t \ll t_0$. The third term in the square brackets introduces an important cosmological variable q_0, which is known as the deceleration parameter [80], and is defined by

$$q_0 = -\left.\frac{\ddot{a}}{aH^2}\right|_{t\,=\,t_0}\,. \tag{1.28}$$

Thus, the deceleration parameter determines whether the expansion of the Universe is either accelerating or decelerating via the sign of $\ddot{a}$. Remarkably, the negative sign that appears in the definition of the deceleration parameter was introduced since the Universe was thought [81, 82] to be undergoing a decelerating expansion so that $q_0 > 0$. Surprisingly, Allan Rex Sandage once described [83] cosmology as a quest for two numbers H_0 and q_0, a quest which is still ongoing with more involved

cosmological models that make use of more than two parameters. However, as we will see in this section (Fig. 1.1) and in the following chapters, there is an avalanche of cosmological data that robustly suggest $q_0 < 0$, indicating that the Universe is currently undergoing through an epoch of accelerated expansion.

1.2.2 Einstein's equations: A description of space–time dynamics

In order to explore the dynamics of the FLRW geometry, we need to look at the equations of motion that are dictated by Einstein's field equations (1.15). Apart from the specification of the space–time metric, one must also specify the energy–momentum tensor $T^{\mu\nu}$. Following the cosmological principle, the generic form of this tensor is that of a perfect fluid with time–dependent energy density ρ, and pressure P. Thus, for an i–th fluid with energy density ρ_i, and pressure P_i, we will adopt the following energy–momentum tensor

$$T_{\mu\nu} = (\rho_i + P_i)\, u_\mu u_\nu + P_i\, g_{\mu\nu} \,, \tag{1.29}$$

where the fluid's four–velocity is denoted by u^μ, and its trace reduces to $T^\mu{}_\mu = -\rho_i + 3P_i$. The only remaining freedom is the fluid's equation of state, that is the functional relationship between the fluid's pressure and energy density, $P_i = P_i\,(\rho_i)$.

The above perfect fluid energy–momentum tensor along with the computation of the Einstein tensor for the FLRW metric, leads to a relationship between the expansion rate and the total energy density, specified by the Friedmann [28, 84] equations

$$H^2 = \frac{\kappa^2}{3}\,\rho - \frac{K}{a^2} + \frac{\Lambda}{3} \,, \tag{1.30}$$

$$\frac{\ddot{a}}{a} = -\frac{\kappa^2}{6}\,(\rho + 3P) + \frac{\Lambda}{3} \,, \tag{1.31}$$

where ρ and P are the total energy density and pressure, summed over all species which fill the Universe, respectively. We recall that $\kappa^2 = 8\pi G$, and that an over–dot represents a derivative with respect to cosmic time. Moreover, the matter conservation equation (1.17) reduces to the continuity equation

$$\dot{\rho} + 3H\,(\rho + P) = 0 \,. \tag{1.32}$$

We remark that as a consequence of the Bianchi identities, Eqs. (1.30)–(1.32) are not independent. A necessary piece of information on the fluid under consideration is encoded into its equation of state w, which is often specified by a simple linear

relationship of

$$P = w\rho \ . \tag{1.33}$$

For instance, in the case of radiation (r), by which we describe the contributions from electromagnetic radiation and relativistic particles, its equation of state can be derived from the energy–momentum tensor for electromagnetism specified by

$$T_r^{\mu\nu} = F^{\mu\lambda}F^{\nu}{}_{\lambda} - \frac{1}{4}g^{\mu\nu}F^{\lambda\sigma}F_{\lambda\sigma} \ . \tag{1.34}$$

By equating the null trace of $T_r^{\mu\nu}$, with the trace of the energy–momentum tensor of Eq. (1.29), we get $w_r = 1/3$ for radiation.

On the other hand, non–relativistic particles with very small kinetic energy with respect to their rest mass, are therefore characterised by negligible pressure. Thus, the equation of state of dust, or simply matter (m), is specified by $w_m = 0$.

By bringing the cosmological constant contribution to the right–hand side of Einstein's field equations (1.15), the cosmological constant can now be considered as an additional matter constituent. This leads to the definition of an associated energy–momentum tensor given by

$$T_{\mu\nu}^{\Lambda} = -\frac{\Lambda}{\kappa^2}\, g_{\mu\nu} = -\rho_{\Lambda}\, g_{\mu\nu} \ , \tag{1.35}$$

where the last equality follows from Lorentz invariance or from the acceleration equation (1.31). By equating the trace of $T_{\mu\nu}^{\Lambda}$, with the trace of the energy–momentum tensor of a perfect fluid, it follows that the cosmological constant is characterised by a constant equation of state, specified by $w_{\Lambda} = -1$.

Moreover, by using the Friedmann equations, one can illustrate that the curvature term can be assimilated with a fluid with a characteristic equation of state of $w_K = -1/3$.

The solution of the continuity equation (1.32) for a perfect fluid with constant equation of state w_i, and energy density ρ_i, is given by

$$\rho_i \propto a^{-3\left(1+w_i\right)} \ . \tag{1.36}$$

Thus, the evolution of the radiation and matter energy densities are given by $\rho_r \propto a^{-4}$ and $\rho_m \propto a^{-3}$, respectively. For the case of the cosmological constant, it follows that its energy density remains constant, that is $\rho_{\Lambda} \propto a^0$.

We now express the Friedmann equations in a dimensionless form, by making use of the critical energy density, defined by

$$\rho_{\rm cr} = \frac{3H^2}{\kappa^2} \ , \tag{1.37}$$

where its current value is found to be $\rho_{\mathrm{cr},0} = 1.88 \times 10^{-29} h^2\,\mathrm{g\,cm^{-3}} = 8.10 \times 10^{-47} h^2\,\mathrm{GeV}^4$. We now write the total matter and radiation energy density in units of the critical density by introducing the energy density parameter

$$\Omega = \frac{\rho}{\rho_{\mathrm{cr}}} = \frac{\kappa^2 \rho}{3H^2} \,. \tag{1.38}$$

Similarly, we express the cosmological constant term and the curvature contribution in terms of the following dimensionless density parameters

$$\Omega_\Lambda = \frac{\Lambda}{3H^2} \,, \quad \Omega_K = -\frac{K}{H^2\, a^2} \,. \tag{1.39}$$

Thus, the Friedmann equation (1.30) takes the form of a constraint equation

$$\sum_i \Omega_i + \Omega_\Lambda + \Omega_K = 1 \,, \tag{1.40}$$

where we further decomposed the total energy density into a sum of its constituents. Thus, the spatial curvature is fixed by the sum of the total matter and radiation content in the Universe, and the cosmological constant contribution. This is illustrated in Fig. 1.1, in which we show that current cosmological data favours a spatially flat space–time in the concordance model. Consequently, we will be neglecting the non–flat FLRW cases in subsequent chapters.

The i–th energy density contribution appearing in Eq. (1.40) is characterised by its own equation of state w_i, and density parameter

$$\Omega_i = \frac{\kappa^2 \rho_i}{3H^2} = \Omega_{i,0}\, a^{-3\left(1+w_i\right)} \left(\frac{H_0}{H}\right)^2 \,, \tag{1.41}$$

where $\Omega_{i,0}$ denotes its present–day value, however we will later denote their current value without the 0–subscript depending on the situation. After substituting Eq. (1.41) in Eq. (1.40) we arrive at

$$\left(\frac{H}{H_0}\right)^2 = \sum_i \Omega_{i,0}\, a^{-3\left(1+w_i\right)} + \Omega_{\Lambda,0} + \Omega_{K,0}\, a^{-2} \,. \tag{1.42}$$

For a Universe fully described by its constituents of radiation, matter, cosmological constant, and curvature, Eq. (1.42) gives rise to the following Friedmann equation

$$H(a) = H_0 \left(\Omega_{r,0}\, a^{-4} + \Omega_{m,0}\, a^{-3} + \Omega_{K,0}\, a^{-2} + \Omega_{\Lambda,0}\right)^{1/2} \,. \tag{1.43}$$

Finally, we remark that for the ΛCDM model, the deceleration parameter defined

in Eq. (1.28), reduces to

$$q_0 = \frac{1}{2}\Omega_{m,0} - \Omega_{\Lambda,0} \ , \tag{1.44}$$

implying that an accelerated expansion of the Universe is possible when the inequality $\Omega_{\Lambda,0} > \Omega_{m,0}/2$ is satisfied. The latter argument still holds when one considers radiation, since its contribution is negligible today. On the other hand, for an arbitrary matter composition, the Friedmann equations give

$$q_0 = \frac{1}{2}\sum_i \Omega_{i,0}\,(1+3w_i) \ . \tag{1.45}$$

Therefore, the equation of state of the dominating cosmic fluid must satisfy the inequality $w_i < -1/3$, in order for the Universe to be currently undergoing through an epoch of accelerated expansion.

A major breakthrough in astronomy is attributed to Mark M. Phillips, who demonstrated [85] that supernovae Type Ia (SNIa) can be used as standard candles, which are simply objects of fixed absolute magnitude. SNIa appear in binary systems where one of the two stars is a white dwarf that accretes the mass of its companion. As a result, the white dwarf collapses and explodes in a supernova when it reaches the critical Chandrasekhar mass [86] of $1.4M_\odot$, where $M_\odot$ denotes one solar mass.

This led to the construction of the SNIa Hubble diagram for distant supernovae from two independent teams: the High–z Supernova Search Team (HZT) [87] and the Supernova Cosmology Project (SCP) [88] collaborations. The HZT collaboration conservatively reported that $q_0 < 0$ at the 2.8σ confidence level, with $\Omega_{\Lambda,0} > 0$ at the 3.0σ confidence level which becomes 7.0σ for the flat FLRW case. The SCP collaboration complemented the HZT results with their cosmological parameter constraint of $0.8\Omega_{m,0} - 0.6\Omega_{\Lambda,0} \approx -0.2 \pm 0.1$, strongly suggesting a non–zero cosmological constant contribution in an almost flat Universe. The SCP collaboration also reported that in a flat FLRW space–time, $\Omega_{m,0} = 0.28^{+0.09}_{-0.08}$ at the 68% confidence level. These cosmological parameter constraints further showed that the Universe became Λ–dominated after the epoch of matter–domination at a cross–over redshift of

$$z_{m-\Lambda} = \left(\frac{\Omega_{\Lambda,0}}{\Omega_{m,0}}\right)^{1/3} - 1 \approx 0.37 \ , \tag{1.46}$$

whereas the Universe entered into its current era of accelerated expansion at

$$z_{\text{dec}-\text{acc}} = \left(\frac{2\,\Omega_{\Lambda,0}}{\Omega_{m,0}}\right)^{1/3} - 1 \approx 0.73 \ . \tag{1.47}$$

Since these outstanding supernovae discoveries were announced in 1998, the field

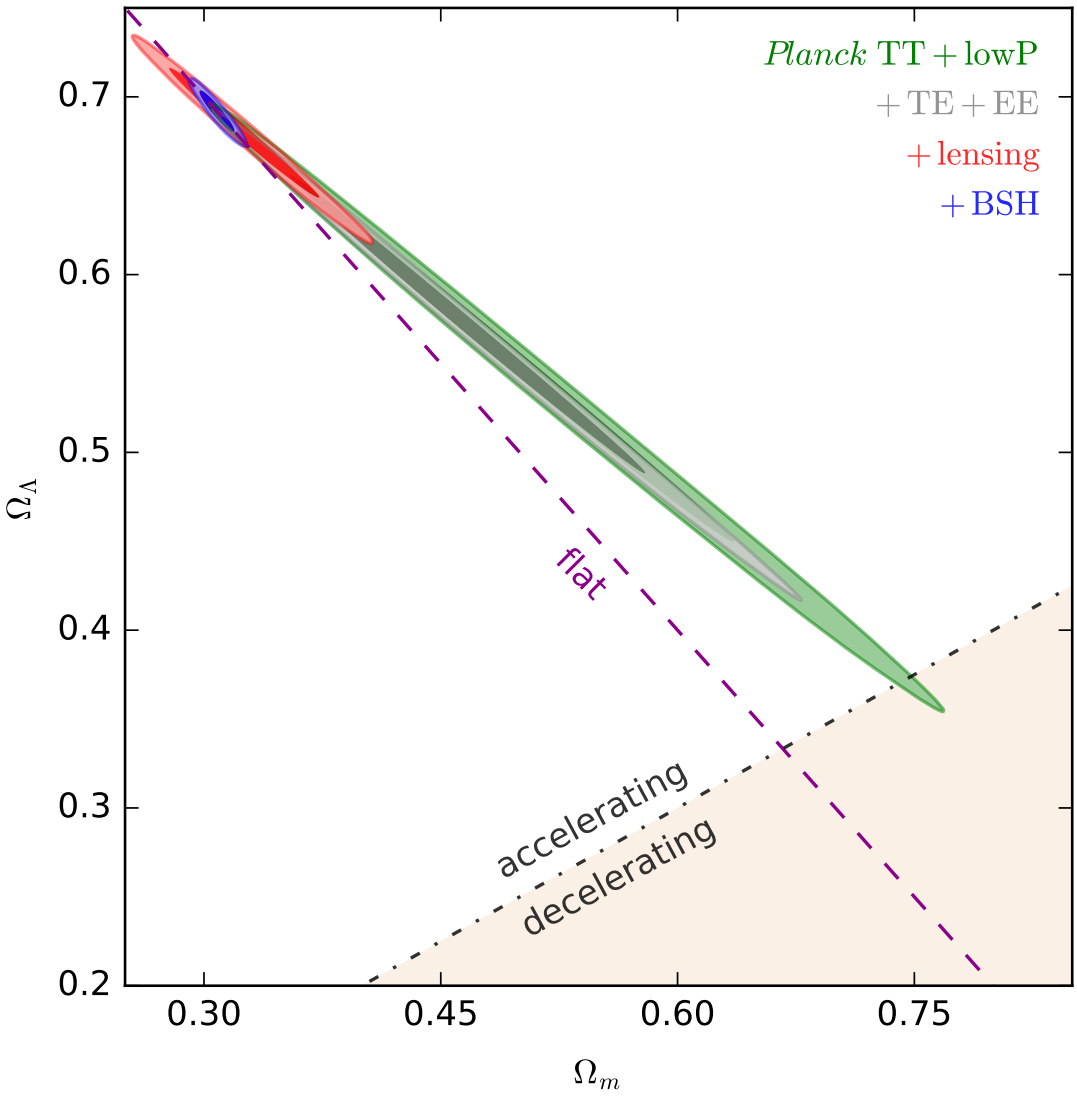

Figure 1.1: This figure shows the concordance model 68% and 95% credible regions in the Ω_m–Ω_Λ plane using the data sets indicated in the figure, which we describe in the text. The diagonal dot–dashed line labelled accelerating/decelerating is drawn for $q_0 = 0$, and divides the cosmological models with an accelerating or decelerating expansion at the present time. The diagonal dashed line labelled flat indicates the scenario of a spatially flat Universe.

of observational cosmology made huge steps forward, which consequently led to significantly stronger evidence for an accelerating Universe. We illustrate this in Fig. 1.1 where we make use of the *Planck* collaboration publicly [89] available Markov chain Monte Carlo samples for the ΛCDM model in curved FLRW space–time, which we analysed with `GetDist` [90]. Fig. 1.1 shows the 68% and 95% credible regions

for the present–day values of Ω_m and Ω_Λ, from which one concludes that current data sets favour a spatially flat FLRW metric, and that currently the Universe is undergoing an epoch of accelerated expansion. The constraints have been derived from the *Planck* temperature power spectrum along with information from the low–multipole polarisation (*Planck* TT + lowP), combined with the E–mode polarisation and its cross–correlation with the temperature spectrum (+ TE + EE). We also consider additional information from the effect of gravitational lensing by large–scale structures on the CMB temperature and polarisation spectra [91] (+ lensing), and we further add information from baryon acoustic oscillations data [92–94], a compilation of supernovae data [95], and a measurement of the Hubble constant [96] (+ BSH). We further discuss this statistical approach in chapter 2 where we place tight limits on the ΛCDM parameters.

1.2.3 Set of cosmological parameters

Our understanding of the underlying physics of the cosmos is strongly dependent on the empirical knowledge of our Universe via several observational experiments that are able to probe various epochs of its cosmic history. Consequently, observational cosmology is very influential on the choice of the cosmological parameters that characterise a given cosmological model. As already mentioned, the set of cosmological parameters that were of interest in the 1970s was limited to H_0 and q_0 [83]. Today's cosmological model is often chosen to be the ΛCDM model that is fully described by a minimal set of six parameters, however the choice of parameters is chosen according to the cosmological experiment. For instance, the *Planck* collaboration [97, 98] based their results on a baseline ΛCDM model, in which a spatially flat FLRW space–time is assumed along with six key parameters that are tightly constrained with *Planck* data sets [65, 99]. Throughout this thesis we will be using the definitions for the cosmological parameters as presented in this section, unless stated otherwise.

Nowadays, there is a substantial observational basis for estimates of the cosmic mean densities of all the known and more significant forms of matter and energy, even if their physical nature is still hypothetical. The cosmic energy inventory is now assumed to consist of around forty distinct elements [100], from which only three sectors in particular dominate the present energy budget of the Universe.

Cosmologists have now well–established that the largest portion of the present–day global energy density of the Universe is attributed to the dark sector, which is believed to be composed of cold dark matter and dark energy. The nature of both components of the dark sector still needs to be deciphered, however cosmological observations robustly indicate that around ninety–five percent of the total cosmic energy budget is contained in the dark sector [65]. We will discuss the current status of cold dark matter and dark energy in chapter 2 and chapter 3, respectively. In the

ΛCDM model dark energy is attributed to the cosmological constant, however this identification will change according to the cosmological model under consideration. Although we will denote the cold dark matter density parameter by Ω_c, it is customary to use the parameter $\Omega_c h^2$, where we recall that h is the dimensionless Hubble constant as defined by Eq. (1.23).

The second largest sector is the baryonic sector, which currently constitutes around five percent of the total energy budget of the Universe [65]. Tight limits have been placed on the baryonic sector via the abundance of light elements in the early Universe [101–104], along with the measurements of the CMB anisotropies [65]. Remarkably, the largest portion of baryonic matter is found in warm intergalactic plasma (around ninety percent of the total baryonic matter), rather than in stars (around six percent of the total baryonic matter), and planets (around 0.002 percent of the total baryonic matter) [100]. We denote the baryonic density parameter by Ω_b, however we often quote this quantity in terms of $\Omega_b h^2$. Thus, the total matter sector can now be expressed as $\Omega_m = \Omega_c + \Omega_b$.

The third major sector, although presently insignificant, is the radiation sector. Its major photon constituent is fixed by the well–determined CMB photon temperature $T_0 = 2.7255\,\mathrm{K}$ [105]. We also account for the neutrino contribution to the total radiation density via

$$\Omega_r h^2 = \Omega_\gamma h^2 \left(1 + \frac{7}{8}\left(\frac{4}{11}\right)^{4/3} N_{\rm eff}\right) \,, \tag{1.48}$$

where $\Omega_\gamma h^2$ denotes the photon contribution, and $N_{\rm eff}$ defines the effective number of neutrino species. Unless stated otherwise, we will adopt the value of $N_{\rm eff} = 3.046$ [106, 107]. We note that the first constraints [108] on $N_{\rm eff}$ were derived from Big Bang nucleosynthesis, via the helium mass fraction parametrisation of $Y_P = 4n_{He}/n_B$, with n_{He} being the number density of helium–4 and we denote the baryonic number density by n_B. This relationship easily follows from Eq. (1.43) in a radiation–dominated Universe which postulates that $H(a) \propto \sqrt{\Omega_r a^{-4}}$, where the radiation energy density is parametrised by the effective number of neutrino species as illustrated in Eq. (1.48). Thus, a larger $N_{\rm eff}$ leads to a speed–up of the expansion of the Universe, which in turn gives rise to a larger relic neutron abundance due to a modification of the onset of the nuclear processes [109], and thus, a higher yield[1] of helium–4. Standard nucleosynthesis predicts that $Y_P \sim 0.25$ [109], which is nowadays computed using sophisticated numerical codes such as `PArthENoPE` [110], that solve a set of coupled kinetic equations supplemented by Einstein's equations along with a

[1]Here we follow Ref. [109] and assume that to a very good approximation all neutrons which have not decayed at a temperature of around 0.07 MeV (which is set by the deuterium bottleneck constraint mentioned in section 1.2) are eventually bound into helium nuclei.

number of conservation equations. When required, we use interpolated results from this Big Bang nucleosynthesis code for our work.

Before we define other cosmological parameters, we will slightly digress in order to motivate the parameters that follow. For a comparison between the *Planck* measurements of the CMB temperature anisotropy spectrum and the theoretically predicted spectrum, an accurate solution for the CMB temperature anisotropy power spectrum is required. This can be achieved by solving a set of coupled equations that describe the perturbed evolution of matter and radiation in a perturbed FLRW space–time. We will quantitatively discuss the linearly perturbed Universe in the subsequent chapters, however we here mention the key parameters that characterise the profile of the CMB anisotropy temperature power spectrum. The linear theory of cosmological perturbations was first presented by Evgeny Mikhailovich Lifshitz [111] in 1946, and its application to the CMB anisotropies was implemented by Phillip James Edwin Peebles and J. T. Yu [112] in 1970. Later studies have extended this work in several ways, particularly by the inclusion of other matter and radiation constituents [113–116]. One of the main challenges is to solve an infinite hierarchy of coupled differential equations that emerge from the perturbed Boltzmann equation, which govern the evolution of photons. However, this brute–force approach [117] was overcome by a line–of–sight integral approach [118], in which a truncation in the Boltzmann hierarchy is possible. This line–of–sight approach was implemented for the first time in the Boltzmann code `CMBFAST` [118] by Uros Seljak and Matias Zaldarriaga in 1996, and this has been used by all modern codes such as `CAMB` [90], `CMBEASY` [119], and `CLASS` [120].

The first convincing evidence for the CMB anisotropy was reported [121] by George Fitzgerald Smoot and his collaborators in 1977, however the first measurements of higher–order anisotropies were recorded by the *Cosmic Background Explorer* (COBE) [122] in 1992. The CMB anisotropies were revisited by the *Wilkinson Microwave Anisotropy Probe* (WMAP) [123, 124] satellite in 2003, which clearly illustrated that this cosmological imprint is one of the most powerful probes of the Universe. Following COBE and WMAP, the third–generation space mission *Planck* [125], was launched in 2009 and its first results were published in 2013 [97]. *Planck* measurements of the CMB anisotropies are currently the most accurate measurements, which consequently led to overwhelmingly tight constraints on the parameters of the concordance model of cosmology.

The background ionisation history has to be calculated to high accuracy in order to precisely predict the theoretical CMB power spectrum. An important quantity for the study of the ionisation history of the Universe is the Thomson scattering rate, given by

$$\Gamma_T = \sigma_T \, a \, n_e \, X_e \ , \tag{1.49}$$

where σ_T is the Thomson scattering cross–section, n_e is the total electron number

density, X_e is the ionised electron fraction, and we recall that a is the cosmological scale factor. The ionised fraction is found to be close to unity at high redshifts, and at the time of recombination between electrons and nuclei, n_e drops suddenly to very small values. Consequently, Thomson scattering suddenly becomes very inefficient, and photons decouple from the electrons.

Since $n_e \propto a^{-3}$, the Thomson scattering rate evolves like $a^{-2}X_e$. Before recombination, the Thomson scattering rate dominates over the Hubble expansion rate, resulting in an opaque Universe. However, X_e abruptly decreases at the recombination epoch, thus enabling the Hubble expansion rate to overtake the Thomson scattering rate, leading to a transparent Universe. One can determine the time of recombination by considering the visibility function $\mathfrak{g}(\eta) = -e^{-\tau}\mathrm{d}\tau/\mathrm{d}\eta$, where the optical depth [118] is specified by

$$\tau(\eta) = \int_{\eta}^{\eta_0} \sigma_T \, a \, n_e \, X_e \, \mathrm{d}\eta \, . \tag{1.50}$$

The optical depth represents the opacity of the Universe at a given time when observed from the present time. On the other hand, the visibility function gives the probability that a CMB photon seen today experienced its last scattering at a time η. Due to the suppression from the $e^{-\tau}$ factor, the visibility function is negligible before recombination, then at the time of recombination it is characterised by a pronounced spike, which then falls again to negligible values due to the smallness of $\mathrm{d}\tau/\mathrm{d}\eta$. The time at which this spike occurs in the visibility function defines the decoupling redshift $z_{\rm dec}$, of the last–scattering surface, with the spike's width giving an indication on the thickness of this last–scattering surface.

Another important epoch in the ionisation history of the Universe takes place at $z \sim 10$, when star formation causes a reionization of the Universe due to their emission of ultra–violet photons. Despite of an increase in X_e at the time of reionization, Γ_T remains much smaller than the Hubble expansion rate due to the dilution of n_e. Thus, the Universe keeps being transparent, however a relatively smaller and wider spike than that observed at the time of decoupling develops around the time of reionization. This therefore indicates that although the CMB photons did not interact between the last–scattering surface and today, a minority of these photons were re–scattered at reionization. We approximate reionization as being relatively instantaneous [126], with its midpoint parametrised by a redshift $z_{\rm reio}$, and compute the reionization optical depth $\tau_{\rm reio}$ using Eq. (1.50). It is well known that small–scale fluctuations in the CMB temperature anisotropy power spectrum are suppressed by $e^{-2\tau_{\rm reio}}$, which therefore makes *Planck* sensitive to the reionization epoch.

We now define another cosmological parameter which quantifies the left–right sliding of the CMB temperature power spectrum. This is the angular scale of the sound horizon at last–scattering θ_s, which depends on the ratio of the sound horizon

at decoupling to the angular diameter distance to decoupling, such that

$$\theta_s = \frac{d_s\left(z_{\rm dec}\right)}{D_A\left(z_{\rm dec}\right)} \,. \tag{1.51}$$

In the tightly coupled limit of the perturbed Boltzmann equations, that is when Compton scattering caused the electron–proton fluid to be tightly coupled with the photons, baryons and photons can be considered as a single tightly coupled fluid. In this regime, we can define the sound speed of perturbations in this fluid as

$$c_s^2 = \frac{1}{3\left(1+R\right)} \,, \tag{1.52}$$

where $R = 3\rho_b/(4\rho_\gamma)$. Thus, primordial perturbations which could possibly be seeded by inflation (discussed in chapter 2), would propagate in this fluid with a velocity c_s. Starting from such perturbations, acoustic waves propagate causally within a distance called the sound horizon. This leads to the definition of the comoving distance travelled by a wavefront since some arbitrary time deep inside the radiation–dominated epoch, given by

$$r_s(\eta) = \int_{\eta_{\rm in}}^{\eta} c_s\left(\eta'\right)\, {\rm d}\eta' \,, \tag{1.53}$$

which is known as the comoving sound horizon, such that $d_s\left(\eta_{\rm dec}\right) = a\left(\eta_{\rm dec}\right) r_s\left(\eta_{\rm dec}\right)$. Evidently, the sound horizon at decoupling depends on the evolution of the Universe prior to the decoupling epoch. Thus, this makes θ_s sensitive to the expansion history and sound speed, which mainly depend on $\Omega_m h^2$ and $\Omega_b h^2$. Moreover, since the scale of these gravity–driven acoustic oscillations of the coupled photon–baryon fluid is set by the sound horizon at the epoch of recombination, the sound horizon scale provides a standard ruler [127] calibrated by the CMB anisotropy measurements. Due to the imprint of these sound waves in the baryon distribution and, through gravitational interactions, in the dark matter distribution as well, this scale appears as a series of relatively tiny oscillations [112, 128] in the galaxy power spectrum probed by baryon acoustic oscillations (BAO) experiments. Thus, information from BAO observations complement the CMB anisotropies measurements [129, 130], consequently allowing for a number of parameter degeneracies to be broken, leading to tighter constraints on the ΛCDM parameters as illustrated in Fig. 1.1.

On the other hand, the angular diameter distance to decoupling depends on the expansion and geometry of the Universe after decoupling, making it more sensitive to the dark energy content and the total matter content of the Universe at late–times.

The angular diameter distance in a flat FLRW space–time is given by

$$D_A(t) = a(t) \int_t^{t_0} \frac{\mathrm{d}t'}{a\,(t')} \,. \tag{1.54}$$

Provided that the reciprocity theorem [131], which imposes that the trajectories of photons satisfy the properties of null geodesics, is satisfied along with the condition that the number of photons is conserved, then we can define the luminosity distance D_L, via the distance–duality relation

$$D_L(z) = (1+z)^2 D_A(z) \,. \tag{1.55}$$

The above cosmological distances lie at the heart of SNIa observations, which particularly were used for the ground–breaking discovery of the accelerated expansion of the Universe [87, 88].

The final two cosmological parameters in this baseline ΛCDM model are attributed to the power–law parametrisation of the primordial curvature power spectrum of scalar perturbations, specified by $\Delta^2_\zeta(k) = A_s(k/k_0)^{n_s-1}$. In this parametrisation A_s denotes the spectrum's amplitude, n_s is referred to as the scalar spectral index, and k_0 is the pivot scale which we set to $k_0 = 0.05\,\mathrm{Mpc}^{-1}$. We will be extending this power–law form of the primordial power spectrum in chapter 2, in which we further discuss the limits on higher–order terms appearing in the exponent of $\Delta^2_\zeta(k)$.

The baseline ΛCDM model consists of other parameters which can be determined from the six cosmological parameters that we discussed above. One of these derived parameters is σ_8, which denotes the root–mean–square fluctuation in total matter in $8\,h^{-1}\,\mathrm{Mpc}$ spheres at $z = 0$. This parameter characterises the normalisation of the initial power spectrum, and is defined by

$$\sigma^2_{\mathfrak{R}} = \int \frac{\mathrm{d}k}{k} \Delta^2_m(k) \left[\frac{3 j_1(k\mathfrak{R})}{k\mathfrak{R}}\right]^2 \,, \tag{1.56}$$

where $\mathfrak{R} = 8\,h^{-1}\,\mathrm{Mpc}$, $\Delta^2_m(k)$ is the total matter power spectrum, and $j_1(X)$ is the spherical Bessel function of order unity. An important scale which determines the scale above which the linear theory of cosmological perturbations will start to break down is the non–linear scale k_{nl}, which is roughly set by $\Delta^2_m(k_{\mathrm{nl}}) \approx 1$.

We conclude this chapter by a remark on the definition of the power spectra that have been introduced in this section, and will be repeatedly used in subsequent chapters. The reason behind the introduction of power spectra in cosmology is related to the fact that the theory of cosmological perturbations is a stochastic theory, whose aim is to predict the statistical properties of perturbed quantities at some arbitrary time, provided that the statistical properties are known at an earlier

time. Most often, it is assumed that the initial conditions are set by Gaussian fluctuations predicted from inflationary cosmology. As long as perturbations remain linear, Gaussianity will be preserved and all fluctuations can be described by their two–point correlation function in Fourier space, which for an arbitrary quantity A, is denoted by $\langle A(\eta, \boldsymbol{k}) A^*(\eta, \boldsymbol{k}')\rangle$. In the FLRW space–time, statistical homogeneity imposes that the two–point correlation vanishes for $\boldsymbol{k} \neq \boldsymbol{k}'$, and statistical isotropy implies that the power spectrum of A only depends on the modulus $k = |\boldsymbol{k}|$. It follows that the power spectrum of A, is defined by

$$\langle A(\eta, \boldsymbol{k}) A^*(\eta, \boldsymbol{k}')\rangle = \delta_D^{(3)}(\boldsymbol{k} - \boldsymbol{k}')\mathcal{P}_A(k) \ , \tag{1.57}$$

where $\delta_D^{(3)}(\boldsymbol{k} - \boldsymbol{k}')$ is the Dirac distribution. Moreover, the dimensionless power spectrum of A, is given by

$$\Delta_A^2(k) = \frac{k^3}{2\pi^2}\mathcal{P}_A(k) \ . \tag{1.58}$$

These generic definitions specify the spectra of the quantities that we will be using throughout this thesis.

1.3 Conclusions

We devoted this chapter to an introduction of the standard pillars of the Big Bang model, and the emergence of the concordance model of cosmology. We first discussed the gravitational theory of General Relativity, and illustrated its success over several astrophysical and cosmological scales. We have then introduced the standard Big Bang model for the description of the Universe, where we highlighted the excellent agreement between its theoretical predictions and several experiments, which consequently led to the adoption of this model as the standard model of modern cosmology. In layman's terms, the Big Bang model postulates that the Universe emerged from a state where matter at high temperature was ionised and in thermodynamic equilibrium, which cooled down during its expansion allowing for the interactions that were efficient at high temperatures to decouple as soon as their reaction rate becomes smaller than the Hubble expansion rate. In this framework, the Universe is therefore assumed to evolve from a radiation–dominated era to a matter–dominated epoch, with the possibility for an era dominated by the cosmological constant or by the spatial curvature of the Universe. Moreover, we discussed the validity of the homogeneous and isotropic expanding Universe that is described by the FLRW metric.

Although the Big Bang model offers a convincing picture of the evolution of the Universe, it is well known that there are still some puzzling open problems that need

to be addressed. We will get back to this in chapter 3, where we discuss some of these issues. Particularly, we will be interested in the dark sector problems, which it is now well–established that this sector accounts to around ninety–five percent of the present–day global cosmic energy budget.

A new branch of science is born; the application of astronomical knowledge to find (or at least to constrain) the fundamental laws of physics in regions inaccessible to direct experiment. We are in the position of the palaeontologists, with only fossils or remnants to study directly.

Yakov B. Zel'dovich

2

Shedding light on primordial cosmology

As we discussed in chapter 1, an urge to unravel the primordial thermal history of our Universe gave rise to the standard Big Bang cosmological model, which has outlived any other proposed model to date. While George Gamow [39–43] together with Ralph Asher Alpher, Hans Bethe, and Robert Herman [44–52] were laying the foundations of primordial nucleosynthesis, they came up with the idea that the early Universe was once very hot and dense, which then expanded and cooled to its present state. Originally the primordial cosmic egg from which the elements formed was dubbed as *ylem* [132] (which was proposed to be composed of a gas of neutrons only), but then Fred Hoyle [133] (who was a critic of this idea) introduced the term *Big Bang* in order to describe an evolving and expanding Universe.

The first intimation of a hot and dense origin of the Universe was given in the so–called $\alpha\beta\gamma$ (Alpher–Bethe–Gamow) paper [47] in 1948, and later that year it was theoretically predicted [51] that in the proposed cosmological model, radiation was much more abundant than matter at very early times. Particularly, they showed that there should be a low temperature residual blackbody radiation suffusing the Universe [51, 52], which was predicted to be at $\sim 5\,\mathrm{K}$ [51]. This derived relic temperature of the cosmic microwave background (CMB) radiation was based on a simple density–pair relation $\left(\rho_\gamma \rho_b^{-4/3} = \text{constant}\right)$ between the baryonic matter energy density (ρ_b) and the CMB photon energy density (ρ_γ) at two distinct epochs, thus heavily dependent on the knowledge of the relevant cosmological parameters. Indeed, with a set of improved cosmological parameters, Alpher and Herman [49] obtained a temperature of $\sim 2.7\,\mathrm{K}$ for the CMB radiation.

It was in 1965 when Arno Allan Penzias and Robert Woodrow Wilson reported the existence of the CMB radiation at the Bell Telephone Laboratories, Crawford Hill, Holmdel, New Jersey using the 20–foot horn–reflector antenna [53, 54]. They serendipitously detected an excess isotropic antenna noise at a wavelength of 7.35 cm

corresponding to a temperature of $3.3 \pm 1.0\,\mathrm{K}$, which was immediately interpreted to be the relic blackbody radiation by Robert Henry Dicke and his collaborators [55].

In the current era of precision cosmology, it is imperative to test the concordance model of cosmology to its core before one starts to consider other promising cosmological models. The measurements of the CMB radiation anisotropies power spectrum placed very tight constraints on the parameters of the concordance cosmological model, and also provided firm evidence that inflation well–describes the dynamics of the early Universe.

In this chapter we will be focusing on possible small–scale departures in a generic profile of the primordial curvature power spectrum from the nearly scale–invariant spectrum that is very well–constrained on larger–scales. Such a deviation could be simply addressed by including higher–order parameters of the primordial curvature power spectrum which are often neglected, since, as we will show, the experiments that are probing the large–scales of the Universe are not very sensitive to these parameters. Most importantly, we will check for any anomalies within the framework of this cosmological model that could arise between the experiments that are probing the large–scales of the Universe, with other current and prospective experiments that are able to impose limits on the cosmic evolution on the small–scales. We will demonstrate that a joint analysis between the large–scale data and small–scale data, enables us to place robust constraints on the physics of the early Universe.

In section 2.1 we will be considering the cosmological consequences of infinitesimal departures from the Planck energy spectrum of the CMB radiation, where we look at two standard mechanisms by which the full thermodynamic equilibrium between photons and baryons in the early Universe is disrupted, giving rise to spectral distortions [134–138] in the CMB radiation spectrum. It is common practice to discern between the μ–type distortions which are characterised by a frequency–dependent chemical potential that is nearly a constant at high frequencies and diminishes at very low frequencies, and the y–type distortions which are associated with Sunyaev–Zel'dovich clusters [135] are characterised by a constant temperature decrement at low frequencies and an increment at high frequencies. Moreover, we will be considering the partially comptonized intermediate i–type [139] distortions.

The formation of primordial black holes (PBHs) will be discussed in section 2.2, in which we also review the relationship between PBHs and the current mystery of the origin of a major constituent of the Universe, dubbed dark matter. Thus, this analysis will enable us to look into the nature of dark matter and the inflationary paradigm that are interconnected via primordial density perturbations on the small–scales, which are created from the quantum fluctuations of the inflaton scalar field that drives inflation. We present and discuss the results of this analysis in section 2.3, and conclude in section 2.4. In the following we assume that the ΛCDM model applies, and adopt the spatially flat Friedmann–Lemaître–Robertson–Walker metric.

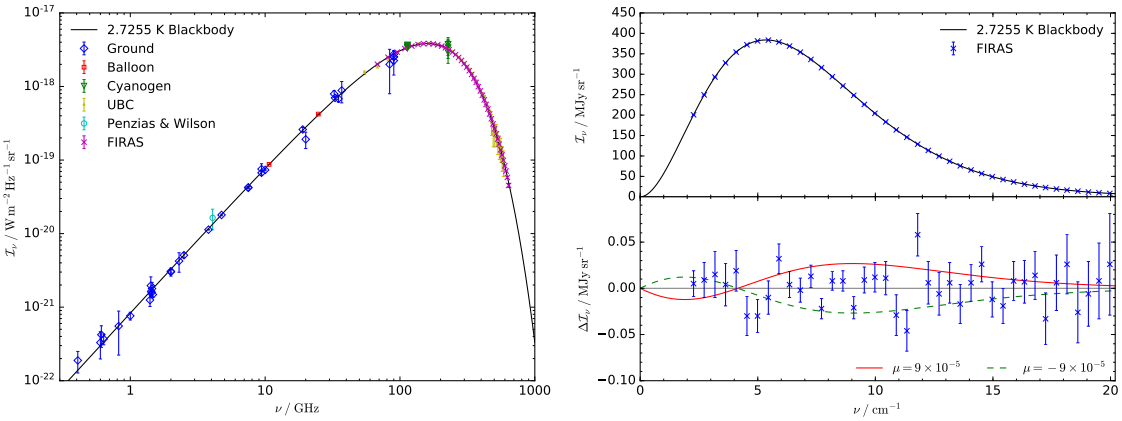

Figure 2.1: In the left panel we compare the measurements of the CMB energy spectrum [140] with a blackbody spectrum at a temperature of 2.7255 K, where we plot the intensity $\mathcal{I}_\nu = 2h_{Pl}\nu^3 c^{-2}(\exp(h_{Pl}\nu/k_B T_0) - 1)^{-1}$, against the frequency ν. In the top–right panel we show the same comparison with the FIRAS data only, whereas in the bottom–right panel we depict the maximum (95% CL) allowed μ–type spectral distortion by the FIRAS data [59] along with the actual residuals in units of MJy sr$^{-1} \equiv 10^{-20}$W m^{-2}Hz^{-1}sr^{-1}, as a function of ν.

2.1 Spectral distortions of the CMB spectrum

Apart from the cosmic signatures contained within the CMB anisotropies, which have now been extensively studied and without doubt paved the way to precision cosmology [65], the energy spectrum of the CMB provides us with invaluable information about the thermal history of the Universe at very early times. In the left panel of Fig. 2.1 we depict the current CMB energy spectrum measurements over a broad range of frequencies ν, together with a Planck spectrum at a temperature of $T_0 = 2.7255\,\mathrm{K}$ [105]. There are several physical mechanisms which could lead to an energy release in this primordial era, such as decaying relic particles [141, 142], and annihilating particles [143, 144]. We will be considering two scenarios that are present in the standard model of cosmology, the adiabatic cooling of electrons and baryons, together with the dissipation of acoustic waves. The latter mechanism arises from the Silk damping [145] of primordial small–scale fluctuations leading to an energy release in the early Universe. Consequently, inevitable spectral distortions of the CMB spectrum [134–138] are produced which are sensitive to the underlying functional form of the primordial power spectrum. In the top–right panel of Fig. 2.1 we compare the COBE/ Far Infrared Absolute Spectrophotometer (FIRAS) measurements [58, 59] of the CMB spectrum with a blackbody at a temperature T_0, clearly showing that the CMB spectrum is indeed a blackbody to a very high precision. In the bottom–right panel of Fig. 2.1 we show the residuals from the blackbody spectrum at a temperature T_0, leaving only a room for a μ–type spectral distortion of $|\mu| \lesssim 9 \times 10^{-5}$ at the 95% confidence level (CL) [59], also shown in the figure. Other

more recent measurements of the μ–type spectral distortion at lower frequencies have been reported by ARCADE [146] and TRIS [147]. FIRAS measurements also allow for a y–type spectral distortion of $|y| \lesssim 1.5 \times 10^{-5}$ at the 95% CL [59], however in this analysis we will be interested in those modes $\left(50\,\mathrm{Mpc}^{-1} \lesssim k \lesssim 10^4\,\mathrm{Mpc}^{-1}\right)$ which dissipate their energy during the μ–era $\left(5 \times 10^4 \lesssim z \lesssim 2 \times 10^6\right)$ producing a small residual chemical potential. As long as Compton scattering is still able to achieve full kinetic equilibrium with electrons, the CMB spectrum is able to regain a Bose–Einstein distribution with chemical potential μ, and occupation number $n_{\mathrm{BE}}(x \equiv h_{Pl}\nu/k_B T_\gamma) = 1/(e^{x+\mu} - 1)$, with T_γ denoting the CMB temperature, k_B is Boltzmann's constant, and h_{Pl} is Planck's constant. In general, the chemical potential will be frequency–dependent due to the creation of photons at low frequencies, however, proposed experiments like the Primordial Inflation Explorer (*PIXIE*) [148] will probe the high frequency spectrum ($30\,\mathrm{GHz} \leq \nu \leq 6\,\mathrm{THz}$), in which the chemical potential is constant [149, 150]. At higher redshifts ($z \gtrsim 2 \times 10^6$), double Compton scattering, bremsstrahlung, and Compton scattering are so efficient that the thermalisation process ensures that for nearly any arbitrary amount of energy injection, no spectral distortion should remain today [137]. At lower redshifts ($z \lesssim 10^4 - 10^5$), the Compton redistribution of photons over the entire spectrum is too weak to establish a Bose–Einstein spectrum, resulting in a y–type spectral distortion. Since y–type spectral distortions continue to be created throughout the late–time epoch of the Universe, for instance via the heating of CMB by electrons in the intergalactic medium during and after reionization, we will marginalise over it in our analysis.

At redshifts well before the recombination era ($z \gtrsim 10^4$), one can use the tight coupling approximation to compute the energy injection rate from the photon–baryon fluid acoustic wave dissipation, given by [151–153]

$$\left.\frac{\mathrm{d}Q}{\mathrm{d}z}\right|_{\mathrm{ac}} = \frac{9}{4}\frac{\mathrm{d}k_D^{-2}}{\mathrm{d}z}\int \frac{\mathrm{d}^3k}{(2\pi)^3} P_\zeta(k)\, k^2\, e^{-2k^2/k_D^2}\,, \tag{2.1}$$

where the primordial power spectrum is defined by $P_\zeta(k) = 4/(0.4R_\nu + 1.5)\mathcal{P}_\zeta \approx 1.45\mathcal{P}_\zeta$, with $R_\nu = \rho_\nu/(\rho_\gamma + \rho_\nu) \approx 0.41$ denoting the contributions of massless neutrinos (ρ_ν) to the energy density of relativistic species. The phenomenological parametrisation of the curvature power spectrum of scalar perturbations in the comoving gauge $\mathcal{P}_\zeta$, is given by [154]

$$\mathcal{P}_\zeta(k) = \frac{2\pi^2}{k^3} A_s \left(\frac{k}{k_0}\right)^{n_s - 1 + \frac{1}{2}\alpha_s \ln\left(k/k_0\right) + \frac{1}{6}\beta_s\left[\ln\left(k/k_0\right)\right]^2 + \frac{1}{24}\gamma_s\left[\ln\left(k/k_0\right)\right]^3}\,, \tag{2.2}$$

where A_s is the scalar amplitude and n_s, α_s, β_s, and γ_s are the scalar spectral index, the running of the scalar spectral index, the running–of–the–running of the scalar spectral index, and the running–of–the–running–of–the–running of the scalar

spectral index, respectively. We assume that these parameters are all specified at the pivot scale k_0, and are defined by

$$\begin{aligned} n_s - 1 &= \left.\frac{\mathrm{d}\ln\Delta^2_\zeta}{\mathrm{d}\ln k}\right|_{k=k_0}\,, \qquad \alpha_s = \left.\frac{\mathrm{d}\,n_s}{\mathrm{d}\ln k}\right|_{k=k_0}\,, \\ \beta_s &= \left.\frac{\mathrm{d}\,\alpha_s}{\mathrm{d}\ln k}\right|_{k=k_0}\,, \qquad \gamma_s = \left.\frac{\mathrm{d}\,\beta_s}{\mathrm{d}\ln k}\right|_{k=k_0}\,, \end{aligned} \tag{2.3}$$

where we defined the dimensionless primordial power spectrum by

$$\Delta^2_\zeta(k) = \frac{k^3\mathcal{P}_\zeta(k)}{2\pi^2}\,. \tag{2.4}$$

In general, one can further consider higher–order terms in the exponent of Eq. (2.2), however current cosmological data sets are unable to place tight constraints on these parameters. Indeed, in section 2.3 we neglect γ_s from our constraint analysis. Moreover, the photon damping scale is defined by [145, 155–157]

$$k_D^{-2}(z) = \int_z^\infty \mathrm{d}z' \frac{c(1+z')}{6H(1+R)n_e\sigma_T}\left(\frac{R^2}{1+R}+\frac{16}{15}\right)\,, \tag{2.5}$$

where n_e is the number density of electrons, σ_T is the Thomson scattering cross–section, c is the speed of light, H is the Hubble parameter, and $R = 3\rho_b/(4\rho_\gamma) \approx 673(1+z)^{-1}$ is the baryon loading with ρ_b and ρ_γ being the baryon and photon energy densities, respectively. For a given k–mode, energy release happens at $k \simeq k_D(z)$, where $k_D(z) \approx 4\times10^{-6}(1+z)^{3/2}\,\mathrm{Mpc}^{-1}$, well inside the horizon scale of $k_h \approx 2\times10^{-6}(1+z)\,\mathrm{Mpc}^{-1}$.

Apart from the Silk damping contribution to the effective μ–distortion, another relatively smaller contribution arises from the adiabatic cooling of ordinary matter which continuously extracts energy from the photon bath via Compton scattering in order to establish an equilibrium photon temperature. This leads to a negative μ–distortion of $\sim 10^{-9}$, which directly depends on the helium abundance $f_{\rm He} \simeq Y_P/4(1-Y_P)$, and the baryon density relative to the critical density Ω_b. The tiny magnitude of this energy extraction from the CMB is due to the fact that the heat capacity of the CMB is much larger than that of matter. For the μ–distortion epoch, this effective energy extraction history is given by [149, 158–160]

$$\left.\frac{\mathrm{d}Q}{\mathrm{d}z}\right|_{\mathrm{cool}} = -\frac{3}{2}\frac{k_B\left(n_{\mathrm{H}}+n_{\mathrm{He}}+n_e\right)}{a_R T_\gamma^3(1+z)}$$

$$\approx -\frac{5.75\times10^{-10}}{(1+z)}\left(\frac{1-Y_P}{0.7533}\right)\left(\frac{\Omega_b h^2}{0.02225}\right)\left(\frac{1+f_{He}+X_e}{2.246}\right)\left(\frac{T_0}{2.7255\,\mathrm{K}}\right)^{-3}, \tag{2.6}$$

where $a_R = 8\pi^5 k_B^4/(15c^3h_{Pl}^3)$ is the radiation constant, Y_P is the primordial helium mass fraction, X_e is the free electron fraction, h is defined by the Hubble constant via $H_0 = 100\,h\,\mathrm{km\,s^{-1}\,Mpc^{-1}}$, $T_\gamma = T_0(1+z)$ [161] such that T_0 is the current cosmic background radiation temperature, and the number densities of hydrogen and helium are denoted by n_{H} and n_{He}, respectively.

Several methods have been implemented in the literature in order to compute the μ-distortion parameter (see for instance Ref. [160] for a comparative analysis). Given the energy release history composed of the damping of primordial small–scale perturbations along with the adiabatic cooling of ordinary matter, we can compute the spectral distortion via [135, 136, 153, 162]

$$\mu = 1.4\left.\frac{\Delta\rho_\gamma}{\rho_\gamma}\right|_\mu = 1.4\int_{z_\mu}^{z_{\mathrm{max}}}\mathcal{J}_\mu\left(z'\right)\frac{dQ}{dz'}\,\mathrm{d}z'\,, \tag{2.7}$$

where $\Delta\rho_\gamma/\rho_\gamma|_\mu$ denotes the effective energy release in the μ–era, and $\mathrm{d}Q/\mathrm{d}z$ is the sum of $\mathrm{d}Q/\mathrm{d}z|_{\mathrm{ac}}$ and $\mathrm{d}Q/\mathrm{d}z|_{\mathrm{cool}}$. The upper integration limit of Eq. (2.7) should be taken sufficiently behind the thermalisation redshift in order to take into account that the thermalisation efficiency does not abruptly vanish at the thermalisation epoch, given by [163–166]

$$z_{th} \approx 1.98\times10^6\left(\frac{1-Y_P/2}{0.8767}\right)^{-2/5}\left(\frac{\Omega_b h^2}{0.02225}\right)^{-2/5}\left(\frac{T_0}{2.7255\,\mathrm{K}}\right)^{1/5}. \tag{2.8}$$

The transition redshift between the y–distortion epoch and the μ–distortion epoch is set by defining the transition redshift z_μ in Eq. (2.7). As described in Ref. [139], a (nearly) pure μ–distortion is created at $y_\gamma \gtrsim y_\gamma^{\mathrm{max}} = 2$, corresponding to $z_\mu \approx 2\times10^5$, where the Compton parameter is defined by

$$y_\gamma(z) = \int_0^z \mathrm{d}z'\frac{k_B\sigma_T}{m_e c}\frac{n_e T_\gamma}{H(1+z')}\,, \tag{2.9}$$

in which the electron mass is denoted by m_e. In the following, we will compute the μ–distortion amplitude by setting the transition redshift in Eq. (2.7) equal to the inferred redshift from Eq. (2.9), such that $y_\gamma(z_\mu) \approx y_\gamma^{\mathrm{max}}$. We will then compare

this with the μ–parameter which is evaluated with an approximate transition at $z_\mu \approx 5 \times 10^4$ [165]. A similar analysis has been carried out in Ref. [160], in which the contribution of r–type distortions has also been considered.

The distortion visibility function $\mathcal{J}_\mu = e^{-\tau(z)}$, where $\tau(z)$ is the effective blackbody optical depth, ensures that the small μ–distortion contribution produced at $z \gtrsim z_{th}$ is also taken into account. Following Ref. [150], we will be making use of the following expression for the blackbody optical depth

$$\begin{aligned}\tau(z) = 1.007 & \left[\left(\frac{1+z}{1+z_{DC}}\right)^5 + \left(\frac{1+z}{1+z_{BR}}\right)^{5/2}\right]^{1/2} \\ & + 1.007\epsilon \ln\left[\left(\frac{1+z}{1+z_\epsilon}\right)^{5/4} + \sqrt{1+\left(\frac{1+z}{1+z_\epsilon}\right)^{5/2}}\right] \\ & + \left[\left(\frac{1+z}{1+z'_{DC}}\right)^3 + \left(\frac{1+z}{1+z'_{BR}}\right)^{1/2}\right] ,\end{aligned} \tag{2.10}$$

where

$$\begin{aligned} & z_{DC} = \left(\frac{25\Omega_r H_0^2}{4C^2 a_C a_{DC}}\right)^{1/5} , \quad z_{BR} = \left(\frac{25\Omega_r H_0^2}{4C^2 a_C a_{BR}}\right)^{2/5} , \quad z_\epsilon = \left(\frac{a_{BR}}{a_{DC}}\right)^{2/5} , \\ & \epsilon = \left(\frac{4C^2 a_{BR}^2 a_C}{25 a_{DC}\Omega_r H_0^2}\right)^{1/2} , \quad z'_{DC} = \left(\frac{3\Omega_r^{1/2} H_0}{2.958 C a_{DC}}\right)^{1/3} , \quad z'_{BR} = \left(\frac{\Omega_r^{1/2} H_0}{5.916 C a_{BR}}\right)^2 , \end{aligned} \tag{2.11}$$

with $C = 0.7768$, and Ω_r being the current radiation density relative to the critical density. The Compton (a_C), double Compton (a_{DC}), and bremsstrahlung (a_{BR}) parameters are defined via the rate coefficients by [150]

$$K_C = n_e \sigma_T c \frac{k_b T_e}{m_e c^2} \equiv a_C (1+z)^4 , \tag{2.12}$$

$$K_{DC} = \frac{4\alpha}{3\pi} n_e \sigma_T c \left(\frac{k_B T_e}{m_e c^2}\right)^2 g_{DC}(x_e) I_{DC} \equiv a_{DC}(1+z)^5 , \tag{2.13}$$

$$\begin{aligned} K_{BR} &= \frac{\alpha n_B}{(24\pi^3)^{1/2}} n_e \sigma_T c \left(\frac{k_B T_e}{m_e c^2}\right)^{-7/2} \left(\frac{h_{Pl}}{m_e c}\right)^3 g_{BR}(x_e, T_e) \\ &\equiv a_{BR}(1+z)^{5/2} , \end{aligned} \tag{2.14}$$

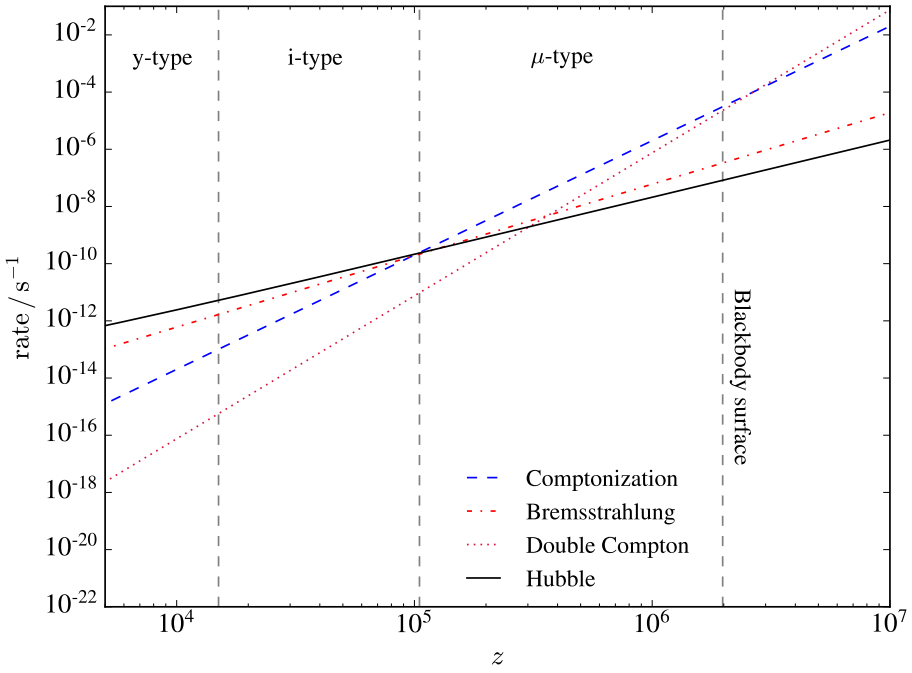

Figure 2.2: This figure illustrates the rates of comptonization, bremsstrahlung, and double Compton scattering, along with the Hubble rate in units of s^{-1}, as a function of redshift. For the comptonization rate we plot K_C, while we consider the bremsstrahlung and double Compton rates at the critical frequency of $x_e = 0.01$ [150] and plot $K_{BR}(e^{x_e} - 1)x_e^{-3}$ and $K_{DC}(e^{x_e} - 1)x_e^{-3}$, respectively. We also indicate the approximate y–distortion ($z \lesssim 1.5 \times 10^4$) and μ–distortion ($z \gtrsim 10^5$) epochs, along with an i–type distortion era ($1.5 \times 10^4 \lesssim z \lesssim 10^5$) during which the distortion has the shape in–between y–type and μ–type distortions. The blackbody surface is located at $z \approx z_{th}$ which defines the boundary of the blackbody photosphere, in which spectral distortions in the CMB spectrum are severely suppressed.

respectively. In Eqs. (2.12)-(2.14) the equilibrium electron temperature T_e, in a radiation field with occupation number $n(x)$, is given by [167, 168] $T_e/T_\gamma = \int (n+1) n x^4 \mathrm{d}x / (4 \int n x^3 \mathrm{d}x)$, and the corresponding dimensionless frequency is denoted by $x_e = h_{Pl}\nu/k_B T_e$. Moreover, α is the fine structure constant, n_B is the baryon number density, and $I_{DC} = \int (n+1) n x_e^4 \, \mathrm{d}x_e = 4\pi^4/15$ for a blackbody spectrum at temperature T_e with occupation number $n(x_e)$. The gaunt factors for bremsstrahlung and double Compton scattering will be assumed to be constant in the redshift range of interest, thus we will be using their fitting values [149, 150, 169] of $g_{DC} \approx 1.005$ and $g_{BR} \approx 2.99$, respectively.

We compare the rates of Compton scattering, double Compton scattering, and bremsstrahlung absorption with the Hubble rate in Fig. 2.2, clearly illustrating the dominant mechanism at any given epoch. We also indicate the blackbody surface for our Universe at $z \approx z_{th}$, which defines the epoch by which the CMB spectrum was created, and therefore cannot be considered as an initial condition. The temperature

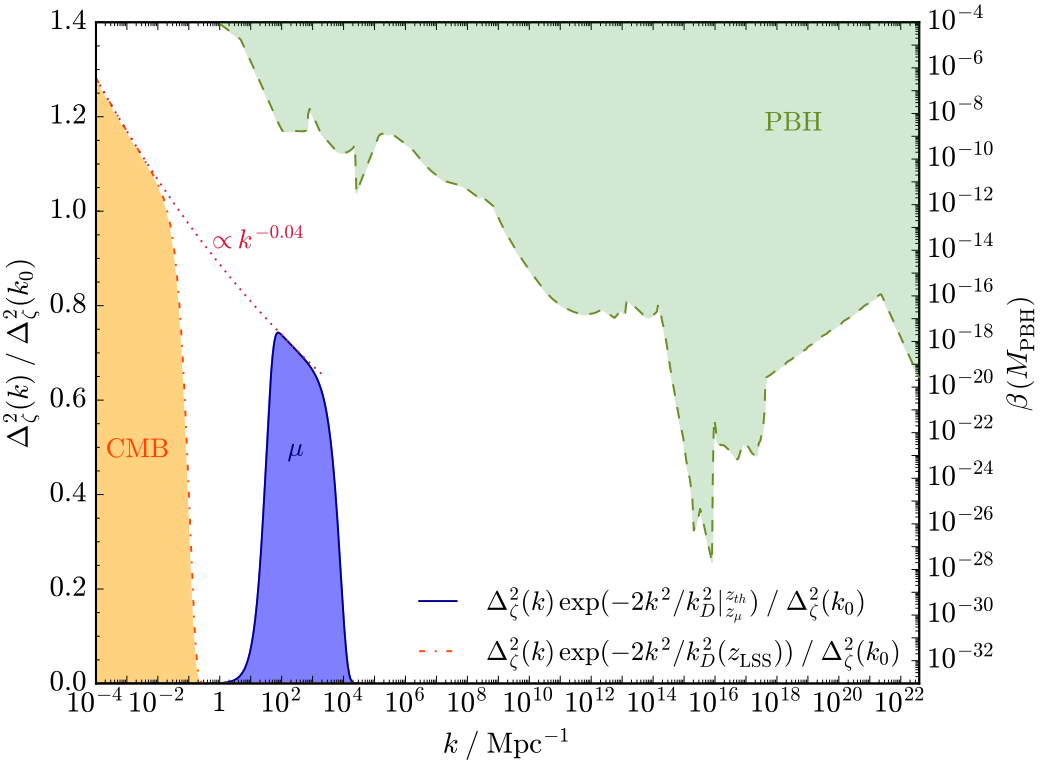

Figure 2.3: This figure depicts the distinct length scales that are probed by the CMB anisotropies, μ–distortion, and PBHs. For the CMB and μ–distortion shaded regions we plot $\Delta^2_\zeta(k)\exp\left(-2k^2/k_D^2\right)/\Delta^2_\zeta(k_0)$ at the redshift of the last–scattering surface $z_{\rm LSS} = 1100$, and its difference between z_{th} and z_μ, respectively. For the PBH shaded region, we illustrate the full compilation of the constraints on $\beta\,(M_{\rm PBH})$.

anisotropies of the CMB were later imprinted at $z_{\rm LSS} \approx 1100$, which defines an important cosmological boundary known as the last–scattering surface.

We illustrate the scales probed by the μ–distortion arising from the dissipation of primordial perturbations in Fig. 2.3, in which we also compare with the scales probed by the CMB anisotropies and by the PBHs that we discuss in the next section. In this figure we plot the normalised dimensionless primordial power spectrum (2.4), and we also use the k–space window function $W_\mu(k) \approx 2.3e^{-2k^2/k_D^2}$ [170, 171], which accounts for the thermalisation process. One can estimate the ensemble average of the effective μ–distortion by computing the log–integral of $\Delta^2_\zeta(k)W_\mu(k)$ [170–172], however we will be using the above procedure.

2.2 Dark matter & primordial black holes

Before considering the physics of PBHs, we will first review one of the puzzling cosmic components that presently makes up $\sim 84\%$ [65] of the global matter content in the Universe. In 1933, while Fritz Zwicky was taking measurements of the velocity dispersion of galaxies in the Coma cluster (Abell 1656), which is a large cluster of galaxies located in the constellation Coma Berenices, he found out that the inferred mass–to–light ratio exceeded the ratio in the solar neighbourhood by around two orders of magnitude [173]. Consequently, he attributed this to the presence of yet unseen *"dunkler Materie"* [173], or dark matter [174], as it is still known today. Similar studies have been carried out on clusters of galaxies, in which there was a constant reappearance of the mass discrepancy. For instance, Sinclair Smith, who was considering the Virgo cluster, noted [175] that *"The cause of the discrepancy is not clear"* and concluded his paper with *"Whatever the correct answer, it cannot be given with certainty at this time"*. However, at that time too few observations and theoretical constraints were available in order to reach a consensus on the interpretation of this reported discrepancy.

In the meantime, galactic rotation curves, which consider the orbital velocity of gas and stars in galaxies as a function of their radial separation from the galactic centre, were also being analysed. In the earliest studies, nearby galaxies such as M31 and M33 were considered by several astronomers [176–178], including the pioneering work of Jan Hendrik Oort [179]. In the early 1970s, an intriguing feature of these rotation curves was emerging: the galactic rotation curves tend to be flattening and stay flat even at the largest radial separation from the galactic centre, contrary to the Keplerian falloff behaviour which is expected at these scales where the mass should be monotonically decreasing beyond the optical disc. Similar to the discrepancy noted by Zwicky, this also indicates that there is a significant non–luminous mass contribution which was not being properly taken into account. Indeed, in an important study carried out by Kenneth Charles Freeman, he noted [180] that *"These data have relatively low spatial resolution; if they are correct, then there must be in these galaxies additional matter which is undetected"*, in which he was referring to the data acquired from NGC300 galaxy in the constellation Sculptor and M33 Triangulum galaxy in the constellation Triangulum.

Despite of this observational evidence of a hiding matter contribution, the two anomalies of flat rotation curves and the cluster mass discrepancy were seriously being considered after these anomalies came together in two landmark publications by Jeremiah P. Ostriker *et al.* [181] and Jaan Einasto *et al.* [182] in 1974, approximately four decades after Zwicky's observation. In the latter study they reported that due to these common discrepancies, *"the clusters of galaxies are stabilised by hidden matter"*. By the late 1970s there was a common consensus about the origin

of these anomalies, as for instance was reported in the review by Sandra M. Faber and John S. Gallagher in which they concluded [183] that *"After reviewing all the evidence, it is our opinion that the case for invisible mass in the Universe is very strong and getting stronger"*.

Apart from the galactic and galaxy cluster scales, currently the preponderant evidence for dark matter is attributed to cosmological and astrophysical measurements that ranges from the shape profiles of the CMB temperature anisotropies power spectrum and the linear matter power spectrum [184], to gravitational lensing [185], and the large–scale structure formation N–body simulations [186]. Thus, our direct evidence of the particle nature of dark matter is very limited. Indeed, with the current observations, one is allowed to consider dark matter to be as light as 10^{-22} eV or as heavy as hundred solar masses [187]. Consequently, there is no shortage of promising dark matter candidates, in fact it is often referred to as the non–baryonic candidate zoo [188].

In the standard cold dark matter model [189] it is assumed that dark matter consists of massive particles that weakly interact with each other and with other constituents of the Universe. It is also considered to be composed of long–lived particles, in a sense that their lifetime must be comparable to or greater than the present age of the Universe. These, as yet undiscovered, particles are better known under the generic name of weakly interacting massive particles (WIMPs) [190, 191], which are expected to be produced thermally in the primordial Universe and have been predicted by several theoretical extensions of the standard model of particle physics [192]. Several direct detection experiments have been carried out in order to search for these predicted particles, such as by observing the nuclear recoils produced by WIMP scattering off nucleons. This technique has been implemented by the XENON100 [193, 194], CDMS II [195, 196], SuperCDMS [197], LUX [198], and CDEX-1 [199] experiments, and is planned to be conducted with the currently proposed LUX–ZEPLIN [200], DARWIN [201], and XENON1T [202] experiments. Sufficiently light ($m_a \approx 20\mu\text{eV}$) axionic [203–205] dark matter, characterised by its energy density relative to the critical density by $\Omega_a \approx (6\,\mu\text{eV}/m_a)^{7/6}$ [206], has also been seriously considered and tested [207] as a promising dark matter candidate. Finally, we now have robust evidence that a minute part of the dark matter is attributed to massive neutrinos, which are considered as hot dark matter since these were relativistic at the time of decoupling from the cosmic plasma [208].

Chronologically the standard cold dark matter model superseded the hot dark matter model in the early 1980s. The hot dark matter model, being characterised by the top–down structure formation mechanism [209], was abandoned by the mid–1980s when there was enough observational evidence that if galaxies were to form sufficiently early, then their distribution would be much more inhomogeneous than it is observed to be. The main driving force behind this turning point was the successful

reconstruction of the formation of cosmic structure in the Universe. Although, to a very good accuracy, the Universe is found to be homogeneous and isotropic on its largest–scales, a variety of structures, such as stars and galaxy clusters, have been found on smaller–scales which would be impossible to form without the presence of dark matter. The tiny fluctuations at the very early times, which are well–motivated by the inflationary scenario, would have led to an inconsistent CMB signal if only baryonic matter were to enhance these fluctuations in order to create the observed cosmic structures. On the other hand, cold dark matter did not directly interact with photons, thus enabling these seeded primordial fluctuations to grow for a much longer time before baryonic matter decoupled from radiation. Consequently, the cosmic structures will then naturally be created once the ordinary matter decouples from radiation and is drawn to the relatively dense clumps of cold dark matter.

Contrary to the top–down structure formation mechanism observed in the hot dark matter model, in which the smaller structures form via fragmentation, the cold dark matter model is characterised by the hierarchical mechanism of structure formation in which the small structures are formed before the largest structures. This was the main motivation behind the rejection of the hot dark matter model. This hierarchical mechanism is possible in a cold dark matter scenario, because the smallest–scales are the first to enter into the non–linear regime, with the large–scales being still linear today. Thus, the smallest structures are therefore the oldest, in accordance with observations [210, 211]. This process carries on and larger–scales will eventually become non–linear, leading to the merger of small overdense regions to merge into larger galaxies and superclusters. This non–linearity length scale at $z \sim 0.3$ was found to be $\sim 70\,h^{-1}$ Mpc [69]. At this scale the Universe has a complex spatial pattern of sophisticated inter–connected structures with multiple morphologies and a rich geometry, better known as the cosmic web [212]. However, on the large–scales, this is smoothed and the Universe becomes homogeneous again.

Motivated by the small–scales ($\lesssim 1$ Mpc) related problems of the standard cold dark matter model, such as the prediction of more substructures, several alternatives have been proposed [213]. For instance, a mixed model consisting of cold dark matter along with hot dark matter was explored and turned out to be a very promising model when confronted with data available at the late 1990s [214]. Other models include warm dark matter [215], decaying dark matter [216], and repulsive dark matter [217]. However, with the avalanche of more recent cosmological data, an extended model of the standard cold dark matter model, the so–called ΛCDM (Λ–cold–dark–matter) model or the concordance model of cosmology, has been shown to be in an excellent agreement with all the observations to date. The major present day constituent of the ΛCDM model is found within another mysterious component, dubbed as dark energy, represented by the Λ term which we discussed in chapter 1.

We will now turn our attention to PBHs which are an alternative dark matter

candidate that are created in the very early Universe. Given that PBHs formed in the radiation–dominated epoch, just after the end of the inflation, they evade the Big Bang nucleosynthesis baryonic constraint. Thus, along with their dynamical similarities with cold dark matter, PBHs could be classified as a non–baryonic form of matter [218]. PBHs are on an equal footing with the other cold dark matter candidates, since there is still no compelling evidence that PBHs may constitute a fraction or, perhaps, all of the dark matter. The link between PBHs and dark matter was explored by George F. Chapline [219], and previously proposed in Refs. [220–223].

Interest in PBHs as dark matter candidates has flourished after the first direct detection of gravitational waves which were emitted from a binary black hole merger [11]. Motivated by the possibility to test General Relativity in the dynamic strong–field regime, led to gravitational waves detection experiments which were pioneered by Joseph Weber's resonant mass detectors [224] in the 1960s. The existence of gravitational waves was already indirectly demonstrated [225] through the radiative energy loss of the $\sim$ 59–millisecond binary pulsar system PSR B1913+16 that was discovered [226] by Russell Alan Hulse and Joseph Hooton Taylor in 1974 at the Arecibo observatory. The first detection of gravitational waves was revealed by the two detectors of the Laser Interferometer Gravitational–Wave Observatory (LIGO) in 2015, in which they reported [11] that the source corresponds to two black holes with masses of $36^{+5}_{-4}\,M_\odot$ and $29^{+4}_{-4}\,M_\odot$ located at a redshift of $z = 0.09^{+0.03}_{-0.04}$, and with a final black hole mass of $62^{+4}_{-4}\,M_\odot$, where $M_\odot$ denotes one solar mass. The enormous amount of energy being liberated in gravitational waves was reported to be $3.0^{+0.5}_{-0.5}\,M_\odot c^2$. The order of magnitude of the source's black hole masses initiated this interest in PBHs, since these values are much higher than the typical masses of binary black holes that are created from the final stages of the stellar evolution of Population I or Population II main sequence stars [227–230]. After the detection of other similar binary black hole mergers [12–15], this plausible detection of PBHs was gaining ground. Moreover, the link between PBHs and the possible explanation that these partially, or even totally, constitute the dark matter in our Universe [231] made this alternative explanation more intriguing.

The mechanism behind the formation of these PBHs is most likely to be the same phenomenon that shaped the large–scale structure in the Universe, where the latter arose from the growth of small density fluctuations via the process of gravitational instability. Cosmological inflation is an attractive and very promising scenario which is able to produce primordial quantum fluctuations from the inflaton field which is itself driving inflation. One possibility for the formation of PBHs is indeed from the gravitational collapse of significantly large density fluctuations ($\delta = \delta\rho/\rho \sim \mathcal{O}(1)$) that re–enter the horizon during the radiation–dominated era and cannot be overcome by the pressure forces.

Since cosmological observations are able to probe the nearly large–scale scale–invariant spectrum of the quantum fluctuations, PBH formation opens a new window on the small–scales to confront inflation, which is independent from the large–scale CMB and large–scale structure data. This is the main motivation behind the analysis presented in section 2.3.

It is well–known that with a *blue* spectrum one can produce PBHs, since in this case there is an increase in power on the smallest–scales, especially on the length scales relevant for PBH formation [232, 233]. In our case we will be using the runnings of the scalar spectral index (refer to Eq. (2.2)) so that the amplitude of the fluctuations is allowed to increase on the small–scales.

We now briefly discuss the procedure that we implemented in section 2.3 where we used the current PBH constraints, which we also present at the end of this section. Provided that at horizon crossing ($R = (aH)^{-1}$), the relative mass excess inside an overdense region with smoothed density contrast $\delta_{\rm hor}(R)$, is greater than a critical threshold $\delta_c \sim 1/3$ [234], the region will collapse to form a PBH. We will be using $\delta_c = 1/3$ in our analysis, however other derived values can be found in Refs. [235, 236] in which they report that this threshold value is sensitive to the initial perturbation profile. Moreover, we introduce an upper limit for the density contrast of $\delta_{\rm hor}(R) \lesssim 1$ that arises from the possibility of very large density perturbations to close up upon themselves and form separate Universes [221, 223, 234, 237]. However, this has been revisited in Ref. [238] in which they showed that the no separate Universe condition does not pose a constraint on the density perturbations, although the choice of this upper limit does not alter the abundance of PBHs due to the rapidly decreasing integrands above δ_c. We also consider Gaussian perturbations with the probability distribution of the smoothed density contrast $P_\delta(\delta_{\rm hor}(R))$, which is given by

$$P_\delta\left(\delta_{\rm hor}(R)\right) = \frac{1}{\sqrt{2\pi}\sigma_\delta(R)} \exp\left(-\frac{\delta^2_{\rm hor}(R)}{2\sigma^2_\delta(R)}\right) , \tag{2.15}$$

where the mass variance of the above probability distribution function is given by

$$\sigma^2_\delta(R) = \int_0^\infty W^2(kR)\mathcal{P}_\delta(k)\frac{{\rm d}k}{k} , \tag{2.16}$$

with $W(kR)$ being the Fourier transform of the window function that is used to smooth the density contrast, and $\mathcal{P}_\delta(k)$ denotes the power spectrum of the density contrast. In this work we will be using a Gaussian window function (see for instance Refs. [239, 240] for other functional forms of the window function) specified by $W(kR) = \exp\left(-k^2R^2/2\right)$.

We then use the relationship between the power spectra of the density contrast

and that of the primordial curvature perturbation $\mathcal{P}_{\mathcal{R}}(k)$, given by [241]

$$\mathcal{P}_{\delta}(k) = \frac{16}{3}\left(\frac{k}{aH}\right)^{2} j_1^2\left(\frac{k}{\sqrt{3}aH}\right)\mathcal{P}_{\mathcal{R}}(k)\,, \tag{2.17}$$

where $j_1(X)$ is the spherical Bessel function of the first kind. We note that the last quantity in Eq. (2.17) is identical to the dimensionless power spectrum $\Delta^2_{\zeta}(k) = k^3\mathcal{P}_{\zeta}(k)/(2\pi^2)$ of section 2.1. However, since the integral of the mass variance of Eq. (2.16) is dominated by the scales of $k \sim 1/R$, we will assume that over this restricted range of local k–values being probed by a specific PBH abundance constraint, the primordial curvature perturbation power spectrum is assumed to be given by a power–law [242, 243]

$$\mathcal{P}_{\mathcal{R}}(k) = \mathcal{P}_{\mathcal{R}}(k_R)\left(\frac{k}{k_R}\right)^{n_s(R)-1}\,, \tag{2.18}$$

with $k_R = 1/R$ and

$$\mathcal{P}_{\mathcal{R}}(k_R) = A_s\left(\frac{k_R}{k_0}\right)^{n(R)-1}\,. \tag{2.19}$$

The effective spectral indices $n_s(R)$ and $n(R)$ describe the slope of the power spectrum at the local scales of $k \sim k_R$, and the normalisation of the spectrum at $k_R \gg k_0$, respectively. These are related to the primordial curvature power spectrum parameters defined at the pivot scale k_0, as follows

$$n(R) = n_s - \frac{1}{2}\alpha_s \ln\left(k_0 R\right) + \frac{1}{6}\beta_s\left[\ln\left(k_0 R\right)\right]^2 - \frac{1}{24}\gamma_s\left[\ln\left(k_0 R\right)\right]^3\,, \tag{2.20}$$

$$n_s(R) = n(R) - \frac{1}{2}\alpha_s \ln\left(k_0 R\right) + \frac{1}{3}\beta_s\left[\ln\left(k_0 R\right)\right]^2 - \frac{1}{8}\gamma_s\left[\ln\left(k_0 R\right)\right]^3\,, \tag{2.21}$$

where Eq. (2.20) is derived by comparing Eq. (2.19) with Eq. (2.2), whereas for the definition of $n_s(R)$ we used the derived expression of $n(R)$ along with the condition of $\mathrm{d}\ln\mathcal{P}_{\mathcal{R}}(k_R)/\mathrm{d}\ln k_R = \mathrm{d}\ln\mathcal{P}_{\mathcal{R}}(k)/\mathrm{d}\ln k|_{k=k_R}$. We found that this approach significantly speeds up the calculations of section 2.3, where we also checked that the final results remain consistent when using this approximation in the analysis of that section. The final link in the chain is the relationship between the initial PBH mass fraction $\beta\left(M_{\rm PBH}\right) = \rho_{\rm PBH}(t_i)/\rho_{\rm cr}(t_i)$, at the time of PBH formation t_i, and the mass variance. We remark that in the latter definition the critical energy density was denoted by $\rho_{\rm cr}$. In the Press–Schechter formalism [244], this relationship between

the PBH initial mass fraction and the mass variance, is given by

$$\begin{aligned}\beta\left(M_{\rm PBH}\right) &= 2\frac{M_{\rm PBH}}{M_{\rm H}}\int_{\delta_c}^{1} P_\delta\left(\delta_{\rm hor}(R)\right)\,{\rm d}\delta_{\rm hor}(R)\\ &= \frac{2\gamma}{\sqrt{2\pi}\sigma_\delta(R)}\int_{\delta_c}^{1}\exp\left(-\frac{\delta^2_{\rm hor}(R)}{2\sigma^2_\delta(R)}\right)\,{\rm d}\delta_{\rm hor}(R)\\ &\approx \gamma\,{\rm erfc}\left(\frac{\delta_c}{\sqrt{2}\sigma_\delta(R)}\right)\,,\end{aligned} \tag{2.22}$$

where ${\rm erfc}(X)$ is the complementary error function. In Eq. (2.22) we adopted the assumption that the PBHs form at a single epoch and that their mass is a fixed fraction γ, of the horizon mass $M_{\rm H} = (4\pi/3)\rho H^{-3}$, such that $M_{\rm PBH} = \gamma\, M_{\rm H}$. The Friedmann equation in a radiation–dominated era reduces to $H^2 \approx (8\pi G/3)\rho$, with ρ denoting the total radiation energy density and G is Newton's gravitational constant, leading to the approximate relationship of $M_{\rm PBH} \approx 1.97\times10^5\,\gamma\,(t/1\,{\rm s})M_\odot$. The latter relationship clearly shows that PBHs span a huge mass range, that is determined by their time of formation, which will feature in the PBH abundance constraints. Moreover, we make use of $\gamma \approx 3^{-3/2}$ [234], which is derived from simple analytical calculations, however its numerical value depends on the details of the gravitational collapse.

Finally, the above Friedmann equation in the radiation–dominated epoch along with cosmic expansion at constant entropy ($\rho \propto g_*^{-1/3}a^{-4}$ [245], with g_* denoting the number of relativistic degrees of freedom), imply that

$$M_{\rm PBH} = \gamma M_{\rm H,eq}\left(\frac{g_{*,\rm eq}}{g_*}\right)^{1/3}\left(k_{\rm eq}R\right)^2\,, \tag{2.23}$$

where $M_{\rm H,eq}$ is the horizon mass at matter–radiation equality, the comoving wavenumber at equality is denoted by $k_{\rm eq}$, and $a_{\rm eq} = (1+z_{\rm eq})^{-1}$ is the scale factor at equality. This leads to the crucial relationship between the PBH mass and the comoving smoothing scale R, given by

$$\frac{R}{1\,{\rm Mpc}} \approx 3.70\times10^{-23}\gamma^{-1/2}\left(\Omega_r h^2\right)^{-1/2} a_{\rm eq}^{1/2}\left(\frac{k_{\rm eq}}{1\,{\rm Mpc}^{-1}}\right)^{1/2}\left(\frac{M_{\rm PBH}}{1\,{\rm g}}\right)^{1/2}\,, \tag{2.24}$$

where we used the number of relativistic degrees of freedom at the time of matter radiation equality of $g_{*,\rm eq} \approx 3.36$.

We now derive a relationship between the current cold dark matter non–evaporated PBH fraction $f_{\rm PBH}$, and $\beta\left(M_{\rm PBH}\right)$. By rewriting the radiation–dominated Friedmann equation in terms of the radiation temperature as $H^2 = (4\pi^3 G/45)g_* T^4$, we get that

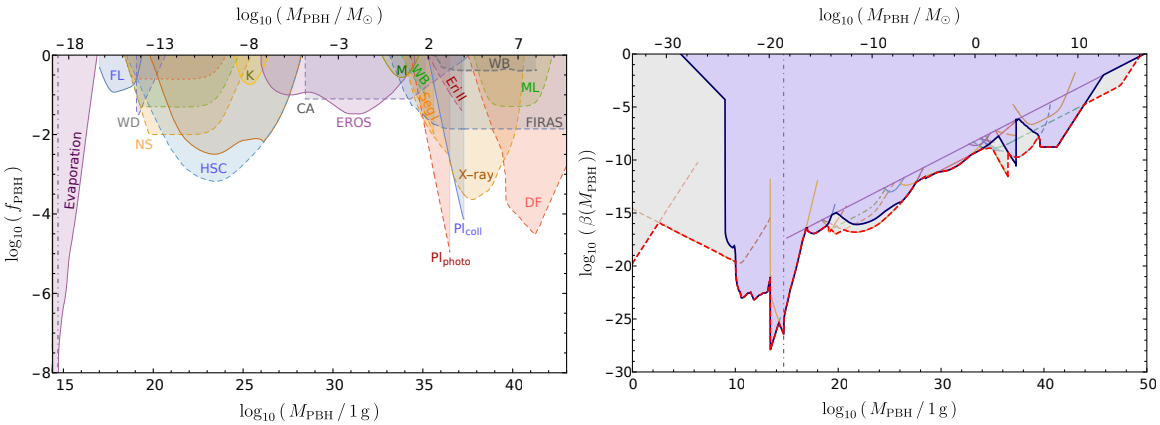

Figure 2.4: The shaded regions in the left panel of this figure illustrate the constraints from different observations on the fraction of PBH dark matter $f_{\rm PBH}$, as a function of their mass $M_{\rm PBH}$. The depicted regions are excluded by the consequences of PBH evaporation [246], femtolensing of γ–ray bursts (FL) [247], white dwarf explosions (WD) [248], neutron star capture (NS) [249], microlensing search of the Subaru Hyper Suprime–Cam data (HSC) [250], *Kepler* microlensing data (K) [251], EROS microlensing data (EROS) [252], caustic crossing (CA) [253], MACHO microlensing limits (M) [254], the disruption of wide binaries (WB) [255, 256], distribution of stars in Segue I dwarf galaxy (Seg I) [257], *Planck* constraints from CMB photoionisation ($\rm Pl_{photo}$) and collisional ionisation ($\rm Pl_{coll}$) [258], limits from the survival of the star cluster near the core of Eridanus II dwarf galaxy (Eri II) [259], luminosity function of X-ray binaries (X-ray) [260], millilens search (ML) [261], accretion effects on the CMB by FIRAS data (FIRAS) [246], and dynamical friction (DF) [246]. In the right panel we show the full compilation of constraints on $\beta(M_{\rm PBH})$, for the mass range $1{\rm g} \leq M_{\rm PBH} \leq 10^{50}{\rm g}$. We use the constraints on the non–evaporating PBHs ($M_{\rm PBH} \gtrsim M^*_{\rm PBH}$) of the left panel, along with the current epoch constraint on $\Omega_{\rm PBH}$ [65, 262] and PBH evaporation constraints from Planck–mass relics [232, 246], entropy [246], lightest supersymmetric particle production [263], Big Bang nucleosynthesis [246], damping of CMB anisotropies [246], extragalactic photon–background [246], galactic γ–ray emission [264, 265], and 21 cm observations [266]. We remark that these constraints have varying degrees of certainty and they are all associated with various caveats. The relatively robust constraints are denoted by solid lines, whereas dashed lines denote less secure constraints.

$t \approx 0.74(g_*/10.75)^{-1/2}(T/(1\,{\rm MeV}))^{-2}\,{\rm s}$. We further assume that the PBHs have a monochromatic mass function, by which we mean that they share a common mass of $M_{\rm PBH}$, therefore we can write $\beta\,(M_{\rm PBH}) = M_{\rm PBH} n_{\rm PBH}(t_i)/\rho(t_i)$. Assuming the conservation of the ratio of the PBH number density to the total entropy density in relativistic species $n_{\rm PBH}/s$, along with the fact that $\rho = 3sT/4$ and adopting a current value of the entropy of $s(t_0) = 8.55 \times 10^{85}\,{\rm Gpc}^{-3}$, we arrive at

$$f_{\rm PBH} = \frac{\Omega_{\rm PBH}}{\Omega_c} \approx \frac{\beta\,(M_{\rm PBH})}{2.70 \times 10^{-9}} \gamma^{1/2} \left(\frac{g_{*,i}}{106.75}\right)^{-1/4} \left(\frac{\Omega_c h^2}{0.12}\right)^{-1} \left(\frac{M_{\rm PBH}}{M_\odot}\right)^{-1/2}, \quad (2.25)$$

where $g_{*,i} \approx 106.75$ [262] is the number of relativistic degrees of freedom at the time of PBH formation deep in the radiation era, and $\Omega_{\rm PBH}$ and Ω_c denote the current unevaporated PBH density in units of the critical density and the cold dark matter density relative to the critical density, respectively.

We show the current PBH constraints expressed in terms of $\beta\,(M_{\rm PBH})$ and $f_{\rm PBH}$ in the panels of Fig. 2.4 as a function of their mass $M_{\rm PBH}$. In the left panel of Fig. 2.4 we focus on the constraints arising from the present–day consequences of non–evaporating PBHs, while in the right panel we show the full compilation of all the PBH constraints. The vertical dot–dashed lines in these panels indicate the critical PBH mass of $M^*_{\rm PBH} \approx 5 \times 10^{14}$ g [265, 267], below which a PBH would have evaporated by the present epoch of the Universe through the emission of Hawking radiation [222, 268] in which black holes radiate thermally with a temperature of $T_{\rm PBH} \approx 106(10^{14}{\rm g}/M_{\rm PBH})$ MeV.

In section 2.3 we use the full compilation of the $\beta\,(M_{\rm PBH})$ constraints presented in Fig. 2.4, from which we derive an upper bound on $\sigma_\delta(R)$ by inverting Eq. (2.22). We then compute the mass variance for the given set of cosmological parameter values using Eqs. (2.16)–(2.21), and check if the inferred scale–dependent upper bound on the mass variance is satisfied over all PBH mass scales.

2.3 Constraints on the concordance model

We here present and discuss our results, particularly focusing on how one can place more robust limits on the profile of the primordial curvature power spectrum, with respect to the current constraints inferred from the CMB anisotropies alone. We will demonstrate this by performing a joint analysis of the inflationary paradigm and the dark matter sector by considering the current limits on PBH formation, along with prospective μ–distortion measurements. We will show that when we combine the PBH and μ–distortion small–scale constraints with the large–scale CMB anisotropies data, the derived constraints will be much tighter than when one treats each sector in isolation. Various studies have illustrated this in a number of distinct perspectives (see for instance Refs. [151, 153, 160, 170, 172, 241–243, 269–289]), which we now reconsider and extend in several ways.

We perform a global analysis in which we infer the posterior distributions along with the respective confidence limits on the primordial power spectrum parameters of Eq. (2.2), together with the baryon density parameter $\Omega_b h^2$, the cold dark matter density parameter $\Omega_c h^2$, the ratio of the sound horizon to the angular diameter distance at decoupling θ_s, and the reionization optical depth $\tau_{\rm reio}$. Thus, our baseline set of parameters consists of $\Theta = \{\Omega_b h^2,\, \Omega_c h^2,\, 100\,\theta_s,\, \tau_{\rm reio},\, \ln(10^{10} A_s),\, n_s,\, \alpha_s,\, \beta_s\}$.

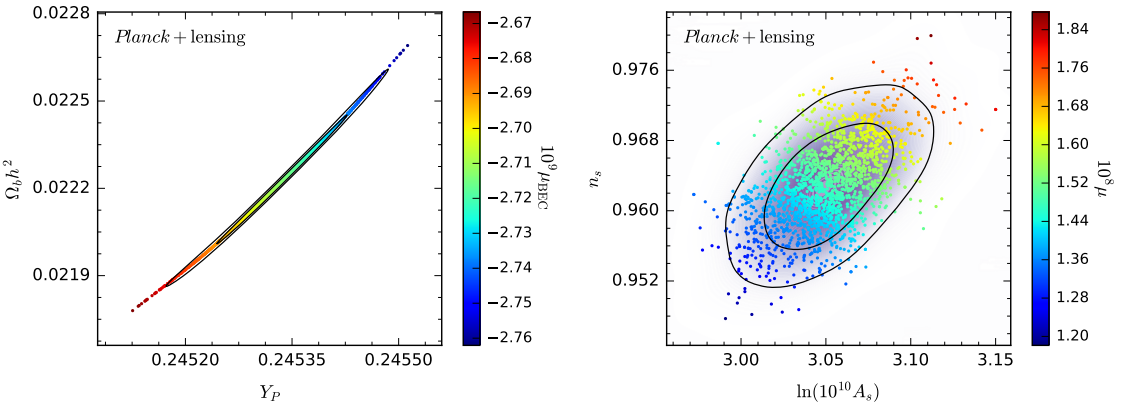

Figure 2.5: The panels of this figure show the ΛCDM model 68% and 95% CRs in the Y_P–$\Omega_b h^2$ (left) and $\ln\left(10^{10}A_s\right)$–$n_s$ (right) planes using the *Planck* + lensing data sets. We also illustrate a number of samples coloured by the μ–distortion parameters $\mu_{\rm BEC}$ (left), and μ (right).

We specify the following flat priors on the floating parameters: $\Omega_b h^2 = [0.005,\, 0.100]$, $\Omega_c h^2 = [0.01,\, 0.99]$, $100\,\theta_s = [0.5,\, 10.0]$, $\tau_{\rm reio} = [0.01,\, 0.80]$, $\ln(10^{10}A_s) = [2.0,\, 4.0]$, $n_s = [0.8,\, 1.2]$, $\alpha_s = [-0.5,\, 0.5]$, and $\beta_s = [-0.1,\, 0.1]$.

We will be fixing the pivot scale to $k_0 = 0.05\,{\rm Mpc}^{-1}$, the CMB temperature to $T_0 = 2.7255\,{\rm K}$, along with the neutrino effective number to $N_{\rm eff} = 3.046$ [106, 107], and Y_P is derived via standard Big Bang nucleosynthesis.

Moreover, we also compute several derived parameters, including H_0, the reionization redshift $z_{\rm reio}$, the root–mean–square fluctuation in total matter in $8\,h^{-1}\,{\rm Mpc}$ spheres σ_8, the dark energy density relative to the critical density Ω_Λ, and the total matter density relative to the critical density Ω_m. We have excluded the primordial power spectrum parameter γ_s from this analysis, since we found that this parameter is not very well constrained with the considered data sets, however we believe that the inclusion of γ_s would lead to an interesting study if one includes more information on the small–scales.

We also derive several parameters related to the μ–distortion using a modified `IDISTORT` code [139, 153], that implements the procedure described in section 2.1. We infer these parameters via importance sampling of the Markov chain Monte Carlo (MCMC) samples implemented in the `GetDist` routine [90]. In the μ–distortion computation, we accurately calculated the free electron fraction X_e, by interfacing the modified `IDISTORT` code with the primordial recombination `HyRec` code [290]. We report the total effective μ–distortion (μ^{z_2}) together with the μ–distortion resulting only from the adiabatic cooling of electrons and baryons ($\mu^{z_2}_{\rm BEC}$) using the inferred transition redshift z_2, which we compute as described in section 2.1. In order to show the dependence of the μ–distortion on the transition redshift, we further calculated the total effective μ–distortion (μ) and its adiabatic cooling contribution ($\mu_{\rm BEC}$) adopting a fixed transition redshift of $z_\mu = 5 \times 10^4$. We created the MCMC

samples using a customised version of the cosmological Boltzmann code `CLASS` [120] along with `Monte Python` [291], and then fully analysed the chains with `GetDist`.

Parameter	*Planck* + lensing	+ BSH
$100\ \Omega_b h^2$ ..	$2.2225^{+0.0162}_{-0.0161}$	$2.2242^{+0.0145}_{-0.0134}$
$\Omega_c h^2$	$0.11938^{+0.00147}_{-0.00151}$	$0.11927^{+0.00100}_{-0.00102}$
$100\ \theta_s$	$1.0418^{+0.0003}_{-0.0003}$	$1.0418^{+0.0003}_{-0.0003}$
$\tau_{\rm reio}$	$0.059230^{+0.014143}_{-0.014549}$	$0.059897^{+0.011265}_{-0.011270}$
$\ln\left(10^{10} A_s\right)$	$3.0507^{+0.0256}_{-0.0274}$	$3.0517^{+0.0208}_{-0.0216}$
n_s	$0.96292^{+0.00510}_{-0.00497}$	$0.96342^{+0.00402}_{-0.00412}$
H_0	$67.969^{+0.666}_{-0.684}$	$68.022^{+0.458}_{-0.448}$
Ω_Λ	$0.69327^{+0.00928}_{-0.00869}$	$0.69401^{+0.00612}_{-0.00593}$
Ω_m	$0.30664^{+0.00869}_{-0.00927}$	$0.30590^{+0.00593}_{-0.00612}$
σ_8	$0.82441^{+0.00919}_{-0.00939}$	$0.82459^{+0.00809}_{-0.00854}$
$z_{\rm reio}$	$8.1349^{+1.4669}_{-1.3310}$	$8.2179^{+1.1847}_{-1.0369}$
$10^8 \mu^{z_2}$	$0.82610^{+0.05743}_{-0.06688}$	$0.82663^{+0.04631}_{-0.05273}$
$10^{-5} z_2$	$2.05285^{+0.00715}_{-0.00710}$	$2.05239^{+0.00650}_{-0.00636}$
$10^9 \mu^{z_2}_{\rm BEC}$ ...	$-1.5837^{+0.0111}_{-0.0109}$	$-1.5844^{+0.0101}_{-0.0099}$
$10^8 \mu$	$1.48329^{+0.09362}_{-0.10831}$	$1.4839^{+0.0755}_{-0.0856}$
$10^9 \mu_{\rm BEC}$ ...	$-2.7135^{+0.0160}_{-0.0159}$	$-2.7145^{+0.0147}_{-0.0144}$

Table 2.1: For each model parameter we report the 68% CLs for the ΛCDM model with null runnings of the scalar spectral index. The Hubble constant is given in units of $\mathrm{km\,s^{-1}\,Mpc^{-1}}$.

We now summarise the data sets that will be used in the following analysis. In all data set combinations, we will be using the *Planck* 2015 temperature and polarisation (TT, TE, EE) high–ℓ and low–ℓ likelihoods [292], along with the lensing likelihood [91]. We will refer to the *Planck* joint likelihoods by *Planck* + lensing. Moreover, we will occasionally further consider a background data set which we denote by BSH. This consists of baryon acoustic oscillations (BAO) measurements, a supernovae Type Ia (SNIa) sample, and a cosmic chronometers data set. For the BAO measurements we make use of the measurements reported by the six degree Field Galaxy Survey [92], the SDSS DR7 Main Galaxy Sample [93], SDSS–IV DR14 eBOSS [293], SDSS–III DR12 Lyα–forests [294], and SDSS–III DR12 Baryon Oscillation Spectroscopic Survey [295]. In the latter BAO data set we make use of the full likelihood which includes information on the growth rate. For the SNIa data set we use the SDSS–II/ SNLS3 Joint Light–curve Analysis [95] data compilation, and for the Hubble parameter measurements we make use of the measurements reported in Refs. [296–301].

Furthermore, we will be using the compiled PBH constraints shown in the right panel of Fig. 2.4 of section 2.2 by employing a step–function likelihood, similar to the implementation of Ref. [302]. We derived the following results using the optimistic PBH upper bound on $\beta(M_{\rm PBH})$, however we checked that with the conservative

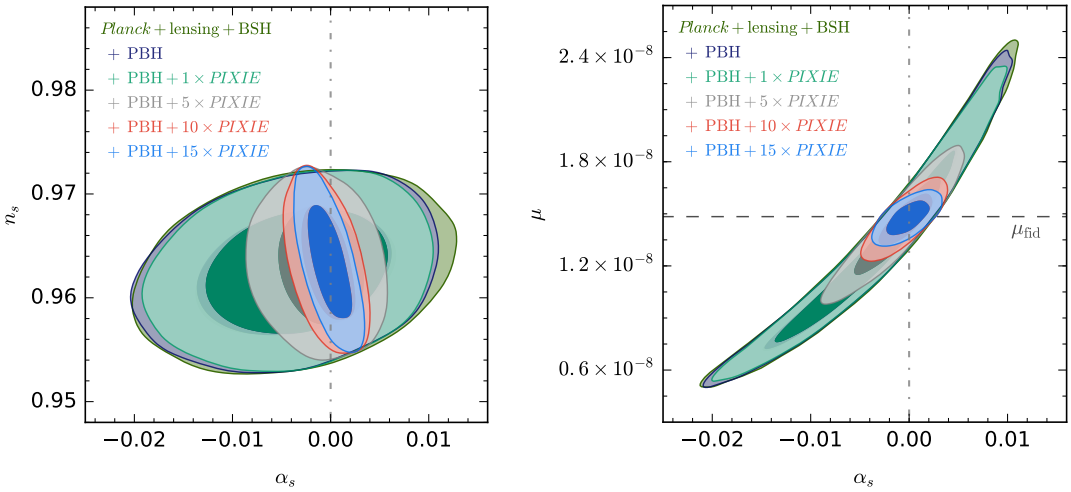

Figure 2.6: The panels of this figure show the ΛCDM + α_s model 68% and 95% CRs in the α_s–n_s (left) and α_s–μ (right) planes. The vertical dot–dashed lines and the horizontal dashed line indicate the null running assumed in the ΛCDM model, and the mean of the derived fiducial μ–distortion in the ΛCDM model, respectively.

upper bound, the final constraints are unaltered. In order to study the implications of prospective measurements of the μ–distortion, we make our forecast around the ΛCDM prediction [281, 282], in which we post–process the Markov chains with a Gaussian likelihood considering $\mu_{\rm fid} = (1.48 \pm 1.00/n) \times 10^{-8}$ for an $n\times$*PIXIE* sensitivity, where we set the fiducial mean value to coincide with the derived mean–fit value in the ΛCDM scenario. We have set the 1σ error of $\mu_{\rm fid}$ to be in agreement with the reported $1\times$*PIXIE*–type experiment uncertainty of Refs. [148, 162], whereas a $10\times$*PIXIE* spectral sensitivity could possibly be reached by a *PRISM*–like [303] experiment. We also examine an optimistic $15\times$*PIXIE*–type experiment in order to discuss its quantitative improvement over the other *PIXIE*–type experiments.

We present the 68% CLs for the ΛCDM model parameters in Table 2.1, where we confront the model with the *Planck* + lensing data sets, and in combination with the BSH data set. Clearly, the ΛCDM model parameters are very well constrained with only the large–scale data sets, in which we are also able to indirectly derive a very tight constraint on the μ–distortion related parameters. One can clearly see that the concordance model of cosmology predicts a positive μ–distortion of $\sim 10^{-8}$, along with a negative baryon cooling contribution with an absolute magnitude of $\sim 10^{-9}$. We also find a very mild improvement in the predicted μ–distortion parameters when we combine the CMB anisotropies data sets with the BSH data set, since the latter data set is able to break some of the parameter degeneracies. In the left panel of Fig. 2.5, we show the ΛCDM 68% and 95% credible regions (CRs) for Y_P and $\Omega_b h^2$, in which we also illustrate some samples coloured with $\mu_{\rm BEC}$. This clearly illustrates

Parameter	*Planck* + lensing	+ BSH	+ BSH + PBH
$100\ \Omega_b h^2 \ldots\ldots$	$2.2255^{+0.0169}_{-0.0179}$	$2.2255^{+0.0147}_{-0.0152}$	$2.2259^{+0.0150}_{-0.0152}$
$\Omega_c h^2 \ldots\ldots\ldots$	$0.11931^{+0.00155}_{-0.00152}$	$0.11933^{+0.00101}_{-0.00104}$	$0.11934^{+0.00102}_{-0.00104}$
$100\ \theta_s \ldots\ldots\ldots$	$1.0418^{+0.0003}_{-0.0003}$	$1.0418^{+0.0003}_{-0.0003}$	$1.0418^{+0.0003}_{-0.0003}$
$\tau_{\rm reio} \ldots\ldots\ldots$	$0.061534^{+0.014560}_{-0.014711}$	$0.060162^{+0.012545}_{-0.012478}$	$0.060029^{+0.012253}_{-0.012202}$
$\ln\left(10^{10} A_s\right) \ldots$	$3.0555^{+0.0273}_{-0.0272}$	$3.0530^{+0.0241}_{-0.0237}$	$3.0529^{+0.0236}_{-0.0229}$
$n_s \ldots\ldots\ldots\ldots$	$0.96273^{+0.00511}_{-0.00527}$	$0.96248^{+0.00423}_{-0.00440}$	$0.96247^{+0.00429}_{-0.00431}$
$\alpha_s \ldots\ldots\ldots\ldots$	$-0.0034670^{+0.0071233}_{-0.0072554}$	$-0.0036051^{+0.0070979}_{-0.0071759}$	$-0.0039201^{+0.0069935}_{-0.0065348}$
$H_0 \ldots\ldots\ldots\ldots$	$68.020^{+0.684}_{-0.723}$	$68.011^{+0.467}_{-0.456}$	$68.012^{+0.478}_{-0.461}$
$\Omega_\Lambda \ldots\ldots\ldots$	$0.69379^{+0.00956}_{-0.00908}$	$0.69374^{+0.00622}_{-0.00596}$	$0.69373^{+0.00630}_{-0.00602}$
$\Omega_m \ldots\ldots\ldots\ldots$	$0.30611^{+0.00908}_{-0.00955}$	$0.30617^{+0.00596}_{-0.00622}$	$0.30618^{+0.00602}_{-0.00630}$
$\sigma_8 \ldots\ldots\ldots\ldots$	$0.82530^{+0.00920}_{-0.00956}$	$0.82426^{+0.00898}_{-0.00905}$	$0.82416^{+0.00884}_{-0.00873}$
$z_{\rm reio} \ldots\ldots\ldots\ldots$	$8.3536^{+1.5214}_{-1.3066}$	$8.2359^{+1.2893}_{-1.1500}$	$8.2232^{+1.2804}_{-1.1157}$

Table 2.2: For each model parameter we report the 68% CLs for the ΛCDM + α_s scenario.

the correlation between the parameters that are being considered in this plot, as we already remarked in Eq. 2.6. In the right panel of Fig. 2.5, we show the 68% and 95% CRs for $\ln\left(10^{10} A_s\right)$ and n_s, which fully describe the primordial curvature power spectrum in the ΛCDM model. We also depict some samples coloured with the total effective μ–type spectral distortion parameter, in which, as expected, it is evident that there is a correlation between μ and the primordial power spectrum parameters.

We then considered an extension to the concordance model, in which we allowed for a varying non–zero running of the scalar spectral index. We report the 68% CLs for the ΛCDM + α_s model parameters in Table 2.2. As clearly shown, the *Planck* data is able to place tight limits on this extended model. Moreover, we see that the inferred constraints from the *Planck* + lensing data sets are consistent with those obtained when we further include the BSH and PBH data sets. Furthermore, we do not find any significant changes between the inferred constraints of the ΛCDM model and this extended model. However, we observe that a negative running of the scalar spectral index is more favoured than a positive one, albeit being consistent with a null running. This is clearly illustrated in the panels of Fig. 2.6 where we show the 68% and 95% CRs in the α_s–n_s and α_s–μ planes. Since the *Planck* data sets exclude the possibility of a relatively large positive running of the scalar spectral index that is needed to overshoot the PBH abundance constraint, the resulting constraint from *Planck* + BSH + PBH joint data set on α_s is found to be consistent

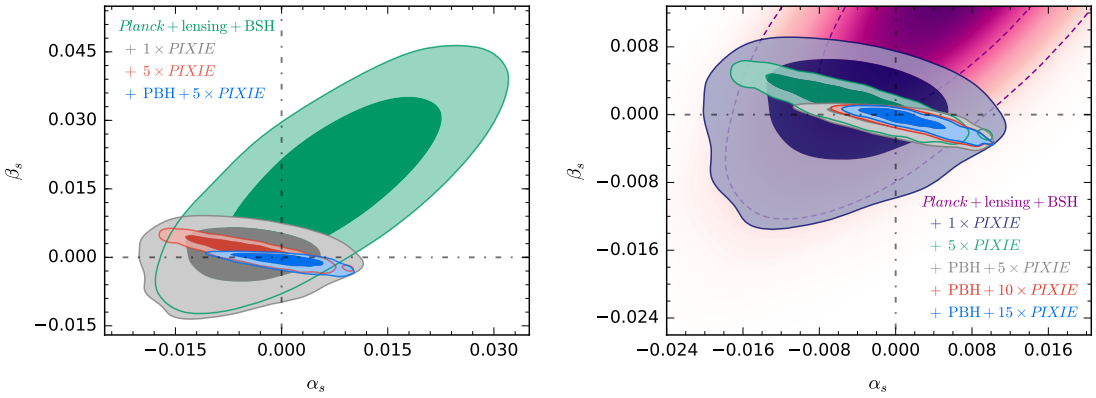

Figure 2.7: The panels of this figure show the ΛCDM + α_s + β_s model 68% and 95% CRs in the α_s–β_s plane. In the right panel we show the tightest constraints on the runnings of the scalar spectral index inferred from the joint data sets of the experiments which independently probe the small–scales and large–scales of the Universe, whereas in the left panel we show the relatively weaker large–scale constraints for comparison. The dot–dashed lines indicate the null runnings of the scalar spectral index assumed in the ΛCDM model.

with the one derived from the CMB anisotropies data. As illustrated in Fig. 2.8, the predicted μ–distortion in the ΛCDM model strongly rules out the possibility of a null μ–distortion, which could possibly arise from a total cancellation between the negative μ–distortion attributed to adiabatic cooling and the positive μ–distortion from Silk damping. To a lesser extent, this balanced injection scenario [304] is also found to be excluded in the ΛCDM + α_s model. Moreover, when we further include information from prospective μ–distortion experiments, we find that these would be able to place tighter constraints on the running of the scalar spectral index. From the results of Table 2.4, we observe that an experiment with the spectral sensitivity of at least $5\times$*PIXIE* could significantly improve the limits on α_s. This is also illustrated in the panels of Fig. 2.6, in which there is a significant shrinking in the inferred contours. We also observe that negative values of α_s inevitably lead to a suppression of the positive μ–distortion contribution attributed to the damping of acoustic waves, paving the way for a partial cancellation from the negative μ–distortion arising from baryon cooling, which consequently pushes the effective distortion to zero. This gives rise to the non–ellipsoidal contours in the α_s–μ plane, which also shows a significant correlation between α_s and μ. Our results are in agreement with a similar analysis of Ref. [282], where they also discussed the implications of the detection of the μ–type distortion on the parameters of the ΛCDM + α_s model.

Parameter	*Planck* + lensing	+ BSH	+ BSH + PBH
$100\ \Omega_b h^2$	$2.2181^{+0.0180}_{-0.0187}$	$2.2198^{+0.0155}_{-0.0161}$	$2.2269^{+0.0148}_{-0.0154}$
$\Omega_c h^2$	$0.11969^{+0.00153}_{-0.00159}$	$0.11951^{+0.00105}_{-0.00109}$	$0.11930^{+0.00105}_{-0.00104}$
$100\ \theta_s$	$1.0418^{+0.0003}_{-0.0003}$	$1.0418^{+0.0003}_{-0.0003}$	$1.0418^{+0.0003}_{-0.0003}$
$\tau_{\rm reio}$	$0.060051^{+0.015261}_{-0.014980}$	$0.059761^{+0.012937}_{-0.012909}$	$0.060019^{+0.012369}_{-0.012633}$
$\ln\left(10^{10} A_s\right)$ ...	$3.0520^{+0.0283}_{-0.0278}$	$3.0511^{+0.0248}_{-0.0245}$	$3.0531^{+0.0233}_{-0.0242}$
n_s	$0.95933^{+0.00595}_{-0.00569}$	$0.95970^{+0.00479}_{-0.00467}$	$0.96320^{+0.00442}_{-0.00446}$
α_s	$0.007771^{+0.010908}_{-0.010770}$	$0.007163^{+0.010571}_{-0.010708}$	$-0.006865^{+0.007763}_{-0.007370}$
β_s	$0.017953^{+0.012813}_{-0.012869}$	$0.017216^{+0.012773}_{-0.012553}$	$-0.004964^{+0.006862}_{-0.001530}$
H_0	$67.815^{+0.712}_{-0.721}$	$67.897^{+0.486}_{-0.483}$	$68.034^{+0.468}_{-0.466}$
Ω_Λ	$0.69126^{+0.01003}_{-0.00904}$	$0.69244^{+0.00651}_{-0.00629}$	$0.69399^{+0.00625}_{-0.00609}$
Ω_m	$0.30865^{+0.00904}_{-0.01003}$	$0.30747^{+0.00629}_{-0.00651}$	$0.30592^{+0.00609}_{-0.00625}$
σ_8	$0.82811^{+0.00994}_{-0.01017}$	$0.82709^{+0.00956}_{-0.00943}$	$0.82330^{+0.00874}_{-0.00928}$
$z_{\rm reio}$	$8.2243^{+1.5794}_{-1.3513}$	$8.2099^{+1.3588}_{-1.1979}$	$8.2170^{+1.2722}_{-1.1740}$

Table 2.3: For each model parameter we report the 68% CLs for the ΛCDM + α_s + β_s scenario.

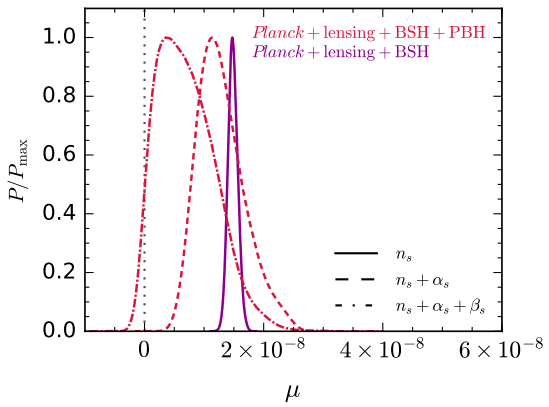

Figure 2.8: This figure shows the marginalised posterior distributions for the μ–type spectral distortion in the ΛCDM model (solid), ΛCDM + α_s model (dashed), and ΛCDM + α_s + β_s model (dot–dashed) using the joint data sets as indicated in the figure. The vertical dotted line illustrates the balanced injection scenario.

We now turn our attention to the extended ΛCDM + α_s + β_s model, where we find that the large–scale data sets favour positive runnings of the scalar spectral index. In the case of α_s, the derived constraint is in a very good agreement with a null running of the scalar spectral index ($< 1\sigma$), however β_s is found to be greater than zero at ~ 1.4 standard deviations. The significant shift of the constraint on α_s which is evident between the ΛCDM + α_s model and the ΛCDM + α_s + β_s model is due to the strong correlation between α_s and β_s, as clearly shown in the left panel of Fig. 2.7. Consequently, the running of the scalar spectral index is pushed towards a positive value, along with a positive running–of–the–running of the scalar spectral index. Thus, in this extended model, it is evident that these positive values of α_s and β_s will be able to significantly

Parameter	*Planck* + lensing + BSH + PBH	+ 1 × *PIXIE*	+ 5 × *PIXIE*	+ 10 × *PIXIE*	+ 15 × *PIXIE*
$\ln(10^{10}A_s)$	$3.0529^{+0.0236}_{-0.0229}$	$3.0528^{+0.0220}_{-0.0220}$	$3.0518^{+0.0218}_{-0.0218}$	$3.0513^{+0.0221}_{-0.0218}$	$3.0511^{+0.0223}_{-0.0220}$
n_s	$0.96247^{+0.00429}_{-0.00431}$	$0.96251^{+0.00396}_{-0.00400}$	$0.96312^{+0.00376}_{-0.00384}$	$0.96335^{+0.00366}_{-0.00375}$	$0.96343^{+0.00361}_{-0.00374}$
α_s	$-0.00392^{+0.00699}_{-0.00653}$	$-0.00363^{+0.00644}_{-0.00579}$	$-0.00107^{+0.00315}_{-0.00266}$	$-0.00035^{+0.00177}_{-0.00180}$	$-0.00019^{+0.00145}_{-0.00143}$
$10^8\mu^{z_2}$	$0.69490^{+0.18070}_{-0.33222}$	$0.70280^{+0.18278}_{-0.30951}$	$0.78586^{+0.12272}_{-0.13540}$	$0.81423^{+0.06751}_{-0.06974}$	$0.82105^{+0.04570}_{-0.04636}$
$10^{-5}z_2$	$2.05131^{+0.00655}_{-0.00654}$	$2.05140^{+0.00650}_{-0.00652}$	$2.05210^{+0.00630}_{-0.00636}$	$2.05222^{+0.00624}_{-0.00630}$	$2.05221^{+0.00623}_{-0.00632}$
$10^9\mu^{z_2}_{\rm BEC}$ ...	$-1.5861^{+0.0102}_{-0.0102}$	$-1.5860^{+0.0101}_{-0.0102}$	$-1.5849^{+0.0098}_{-0.0099}$	$-1.5847^{+0.0097}_{-0.0098}$	$-1.5847^{+0.0097}_{-0.0098}$
$10^8\mu$	$1.28530^{+0.28563}_{-0.47539}$	$1.29788^{+0.28617}_{-0.44087}$	$1.42440^{+0.18621}_{-0.18692}$	$1.46636^{+0.09444}_{-0.09848}$	$1.47637^{+0.06269}_{-0.06460}$
$10^9\mu_{\rm BEC}$ ...	$-2.7170^{+0.0148}_{-0.0148}$	$-2.7168^{+0.0147}_{-0.0148}$	$-2.7152^{+0.0142}_{-0.0144}$	$-2.7149^{+0.0141}_{-0.0142}$	$-2.7150^{+0.0141}_{-0.0142}$

Parameter	*Planck* + lensing + BSH + PBH	+ 1 × *PIXIE*	+ 5 × *PIXIE*	+ 10 × *PIXIE*	+ 15 × *PIXIE*
$\ln(10^{10}A_s)$	$3.0531^{+0.0233}_{-0.0242}$	$3.0528^{+0.0228}_{-0.0223}$	$3.0515^{+0.0233}_{-0.0228}$	$3.0510^{+0.0240}_{-0.0232}$	$3.0509^{+0.0244}_{-0.0235}$
n_s	$0.96320^{+0.00442}_{-0.00446}$	$0.96321^{+0.00415}_{-0.00422}$	$0.96386^{+0.00393}_{-0.00387}$	$0.96411^{+0.00387}_{-0.00379}$	$0.96418^{+0.00384}_{-0.00375}$
α_s	$-0.00687^{+0.00776}_{-0.00737}$	$-0.00537^{+0.00680}_{-0.00668}$	$0.00023^{+0.00398}_{-0.00439}$	$0.00113^{+0.00266}_{-0.00402}$	$0.00131^{+0.00217}_{-0.00397}$
β_s	$-0.00496^{+0.00686}_{-0.00153}$	$-0.00364^{+0.00451}_{-0.00108}$	$-0.00069^{+0.00142}_{-0.00052}$	$-0.00059^{+0.00125}_{-0.00045}$	$-0.00058^{+0.00122}_{-0.00042}$
$10^8\mu^{z_2}$	$0.30067^{+0.15096}_{-0.40717}$	$0.38766^{+0.21911}_{-0.39351}$	$0.74783^{+0.12415}_{-0.13644}$	$0.79708^{+0.06746}_{-0.06845}$	$0.80709^{+0.04623}_{-0.04673}$
$10^{-5}z_2$	$2.05083^{+0.00652}_{-0.00663}$	$2.05119^{+0.00647}_{-0.00660}$	$2.05245^{+0.00659}_{-0.00644}$	$2.05257^{+0.00672}_{-0.00638}$	$2.05255^{+0.00685}_{-0.00646}$
$10^9\mu^{z_2}_{\rm BEC}$ ...	$-1.5869^{+0.0101}_{-0.0103}$	$-1.5863^{+0.0101}_{-0.0103}$	$-1.5843^{+0.0103}_{-0.0099}$	$-1.5841^{+0.0105}_{-0.0098}$	$-1.5842^{+0.0107}_{-0.0010}$
$10^8\mu$	$0.69783^{+0.34355}_{-0.61329}$	$0.83785^{+0.42550}_{-0.53172}$	$1.38239^{+0.17983}_{-0.19287}$	$1.45371^{+0.10120}_{-0.09405}$	$1.46812^{+0.05527}_{-0.07180}$
$10^9\mu_{\rm BEC}$ ...	$-2.7181^{+0.0147}_{-0.0150}$	$-2.7173^{+0.0146}_{-0.0150}$	$-2.7144^{+0.0150}_{-0.0144}$	$-2.7141^{+0.0153}_{-0.0143}$	$-2.7141^{+0.0156}_{-0.0145}$

Table 2.4: For each model parameter we report the 68% CLs for the ΛCDM + α_s (top) and ΛCDM + α_s + β_s (bottom) cases. The inferred constraints from $n\times$*PIXIE* are obtained by post–processing the Markov chains with a Gaussian likelihood of $\mu = (1.48 \pm 1.00/n) \times 10^{-8}$, where its mean value is fixed to the derived mean value of the μ–type spectral distortion parameter in the ΛCDM model presented in Table 2.1.

increase the power on the small–scales. As a result, the PBH constraint is crucial in this case since the PBH abundance constraint, although relatively weak, will not allow for these positive values of the runnings of the scalar spectral index. Indeed, when we confront the ΛCDM + α_s + β_s model with the *Planck* + BSH + PBH joint likelihoods, the PBH upper bound is able to push the constraints on both α_s and β_s to negative values, which are found to be consistent with zero at less than one

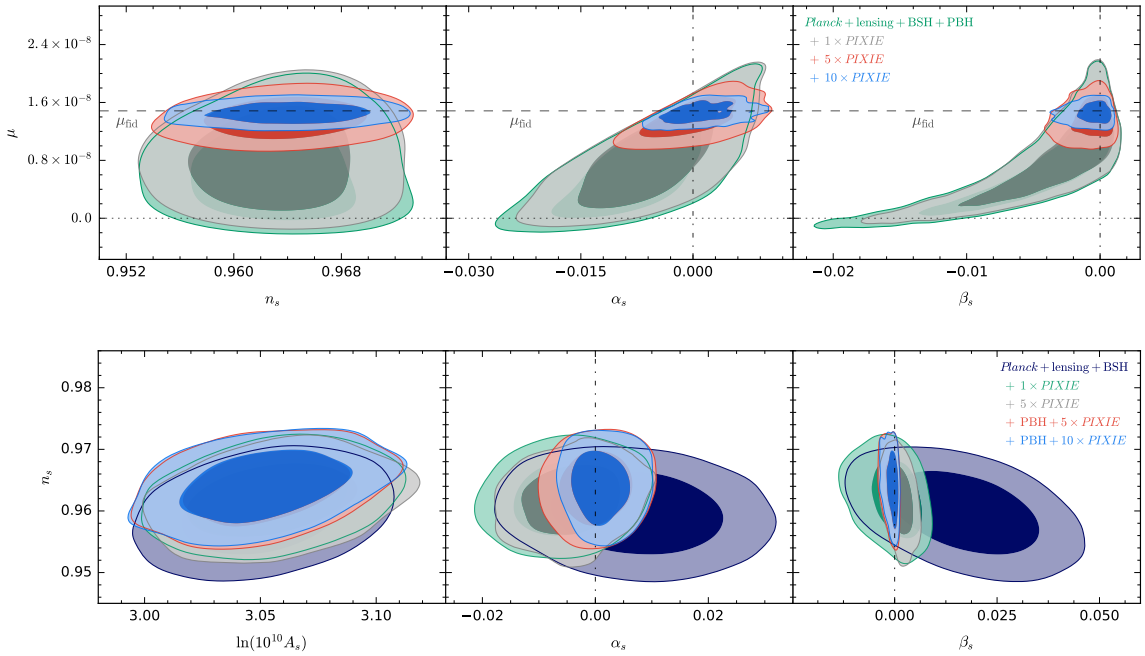

Figure 2.9: The panels of this figure show the ΛCDM + α_s + β_s model 68% and 95% CRs. The vertical dot–dashed lines indicate the null runnings of the scalar spectral index assumed in the ΛCDM model. The horizontal dotted and dashed lines indicate the balanced injection scenario, and the mean of the derived fiducial μ–distortion in the ΛCDM model, respectively.

standard deviation.

We present the 68% CLs for the ΛCDM + α_s + β_s model parameters in Table 2.3 which were inferred from the *Planck* + lensing data sets, in combination with the BSH and PBH data sets. In Table 2.4 we present the 68% CLs for this model, in which we further add the information from the μ–distortion, where we assume a fiducial ΛCDM model value for μ. In Figs. 2.7 and 2.9 we illustrate the remarkable shrinking of the marginalised contours when we consider the large–scale data sets along with the crucial information from the small–scales. The 68% CLs on the running–of–the–running of the scalar spectral index are $-5 \times 10^{-3} \lesssim \beta_s \lesssim 9 \times 10^{-4}$ (*Planck* + lensing + BSH + PBH + 1×*PIXIE*), or $-1.2 \times 10^{-3} \lesssim \beta_s \lesssim 7.3 \times 10^{-4}$ (*Planck* + lensing + BSH + PBH + 5×*PIXIE*), or $-1.0 \times 10^{-3} \lesssim \beta_s \lesssim 6.4 \times 10^{-4}$ (*Planck* + lensing + BSH + PBH + 15×*PIXIE*), implying that the small–scale data can robustly constrain the higher–order parameters of the primordial curvature power spectrum.

Since β_s is the dominant parameter which determines the magnitude of the μ–distortion resulting from the dissipation of acoustic waves, in the top panel of Fig. 2.9 the very strong correlation between μ and β_s could easily be noticed. Similar to the correlation between μ and α_s in the ΛCDM + α_s model, we also find non–

ellipsoidal contours in the β_s–μ plane, which occur for the same physical reason. Furthermore, in the ΛCDM + α_s + β_s model we find that the balanced injection scenario is very mildly ruled out at ~ 1.1 standard deviations when not including constraints from the μ–distortion. Consequently, this would be more challenging for prospective μ–distortion experiments at a spectral sensitivity of $\sim 10^{-9}$, however even if a null detection of the μ–distortion is reported by such an experiment, this would shed some light on the possible mechanisms that are counter–balancing the energy injection in the CMB. Thus, a better understanding of the physics of PBHs along with future experiments that would be able to probe the thermal history of our early Universe, for instance via μ–distortion measurements, are paramount for the study of our primordial Universe.

2.4 Conclusions

In this chapter we had a close look at the current status of the concordance cosmological model, where we confronted this model and two other extended models with large–scale and small–scale cosmological data. We devoted section 2.1 to the creation of the CMB spectral distortions, particularly focusing on the μ–type spectral distortion. We considered the cooling of photons due to energy transfer to baryons and electrons, together with the heating of the CMB via Silk damping, by which a μ–type spectral distortion is expected to arise in the very early Universe. The Silk damping μ–distortion which results from the dissipation of acoustic waves in the photon–baryon–electron plasma, was found to be a crucial probe for the shape of the small–scale primordial power spectrum, particularly when we allowed for more freedom in the phenomenological parametrisation of the primordial power spectrum.

After we presented a brief overview of the, yet not fully understood, puzzling dark matter constituent of the Universe, in section 2.2 we also discussed the formation of PBHs, which are considered as a macroscopic candidate for cold dark matter. We compiled the present constraints on the abundance of PBHs from a number of experiments, which, at face value, nearly rule out the possibility that all of cold dark matter could be contained within PBHs. However, a small fraction of cold dark matter could still be found in PBHs, especially if one takes into account the several caveats that exist in these constraints. Moreover, it is important to remark that the constraints on $f_{\rm PBH}$ get stronger when one considers an extended PBH mass function [305] rather than our assumed monochromatic PBH mass function, however this is beyond the scope of this analysis. Since our full compilation of PBH constraints spans fifty orders of magnitude in PBH masses, our aim was to confront the ΛCDM model and its extensions with this constraint that is able to probe a very wide range of length scales.

Indeed, in section 2.3 we presented our results, particularly focusing on the in-

ferred limits that we placed on the parameters that describe the shape of the primordial power spectrum. We showed that when the CMB anisotropies data is complemented by the small–scale constraints from the abundance of PBHs along with prospective μ–distortion measurements, tight limits on the higher–order parameters of the primordial power spectrum could be placed. This clearly shows the importance of a better understanding of the formation and evolution of PBHs, along with prospective direct measurements of the μ–distortion. We have illustrated that these independent probes are able to exclude a significantly large portion of the currently viable region of the primordial power spectrum parameter space that is inferred from large–scale experiments.

It should not be forgotten that all this talk about the Universe involves a tremendous extrapolation, which is a very dangerous operation.

Willem de Sitter

3 Discordance in ΛCDM?

The expansion of the Universe has constantly been revisited by numerous astrophysical and cosmological observations. Evidently, the existence of the dark sector is now well–established through its gravitational effects on the expansion of the Universe, which itself is being observed solely via the properties of baryonic matter and electromagnetic radiation. As we have already discussed in the previous chapters, the evolution of the Hubble parameter requires the introduction of additional degrees of freedom in order to agree with current observational data. Indeed, one cannot reconstruct the observed Hubble expansion rate by a mixture of pressureless cold dark matter and radiation. In the elementary framework of the concordance model of cosmology, we saw that this model was capable of reproducing the observed accelerated cosmic expansion with the aid of the cosmological constant term. The simplicity of this model along with its current remarkable agreement with observations, which we illustrated in the previous chapter, the ΛCDM model has now been adopted as the reference model of cosmology.

Before we turn our attention to the dark sector problems that arise in the ΛCDM model, we will first discuss the shortcomings of the hot Big Bang model prior to the onset of the radiation–dominated epoch. Around the Grand Unification energy scale, the laws of physics are found to be less reliable since these need to be hugely extrapolated to regimes where they have not been tested. However, we will see that a period of cosmic inflation would in principle provide a tentative solution to the several problems of the hot Big Bang model, which we discuss in section 3.1. Remarkably, these cosmological problems turn out to be similar to the currently open problems of the late–time Universe.

Despite the success of the ΛCDM model, cosmologists are still puzzled with the present–day theoretical understanding of several aspects of this model, particularly the dark sector constituents of dark matter and dark energy. Generically we call

dark energy any model which probes the recent cosmic epoch of accelerated expansion of the Universe, independently of its physical origin. The simplistic choice of dark energy is the cosmological constant Λ, which lies at the heart of the ΛCDM model. However, the cosmological constant is characterised by two main open problems which we will discuss in section 3.2, while in section 3.3 we will address the currently reported tensions within the concordance model and their implications on our understanding of dark energy in general. We draw our final remarks in section 3.4.

3.1 The flatness and horizon Big Bang problems

Since the Big Bang model postulates that there is a finite amount of time since the Big Bang singularity, this puts a constraint on the finite distance that photons can travel within the age of the Universe. At the same time, we have seen that we should also satisfy the cosmological principle. Although the Friedmann–Lemaître–Robertson–Walker (FLRW) space–time embraces the above conditions, the FLRW solution does not explain the origin of this homogeneity and isotropy, for which observational evidence is becoming stronger. Thus, it is imperative to physically motivate this hypothesis rather than imposing it in the standard model of cosmology.

In a decelerated Universe, such as in a matter–dominated or a radiation–dominated epoch, if photons are causally disconnected at some redshift, then it follows that they were never in contact before, since the comoving particle horizon

$$\chi_P = \int_0^a \frac{\mathrm{d}a'}{a'^2 H(a')} \sim a^{(1+3w)/2} \,, \tag{3.1}$$

is a monotonically growing function of the scale factor a, when $1 + 3w > 0$ (see Eq. (1.45)). We recall that the Hubble parameter is denoted by H, and the equation of state of the dominating fluid is denoted by w. Consequently, if the expansion was always decelerating in the early Universe, the particle horizon at the time of decoupling $z_{\rm dec} \approx 1090$ [65], would be too small relative to the size of the observable Universe. Thus, two widely–separated regions of the cosmic microwave background (CMB) will have non–overlapping horizons, such that these will be causally disconnected at recombination. Indeed, by taking the ratio of the comoving distance between a point on the last–scattering surface and an observer on Earth, to the comoving particle horizon distance for such a point, we find that the number of regions in causal contact at decoupling is around

$$N_{\rm causal} \sim \left(\frac{\eta_0 - \eta_{\rm dec}}{\eta_{\rm dec}} \right)^3 \sim 10^4 \,, \tag{3.2}$$

where in the last step we assumed that the conformal time $\eta \propto a^{1/2}$, as in a matter–dominated epoch. We remark that the above argument also follows from the counting of non–overlapping past light cones on a space–time diagram. Surprisingly, the scale of such a causal region on the last–scattering surface should now be observed under an angle of $\theta_{\text{causal}} \lesssim 2^\circ$. Therefore, larger angular scales should correspond to regions which were causally disconnected at the decoupling epoch. However, as we have already anticipated in chapter 1, the temperature of the CMB radiation is found to be the same on the whole 4π solid angle, up to tiny temperature fluctuations of $\delta T \sim 10^{-5} T_0$ [65], where T_0 is the current temperature of the CMB radiation. This cosmological conundrum became known as the horizon problem, which in itself is deeply related with the state of the Universe's thermodynamic equilibrium.

Another cosmological puzzle arises from the fact that, although the contribution of the spatial curvature to the Universe's expansion quickly increases with time if $\ddot{a} < 0$, where we recall that a dot represents a derivative with respect to cosmic time, observations strongly favour a spatially–flat Universe. This can be easily shown by considering the evolution of $\Omega_K = -K/(H^2 a^2)$, given by

$$\frac{\mathrm{d}\Omega_K}{\mathrm{d}\ln a} = -2\,\Omega_K \left(\frac{\ddot{a}}{aH^2}\right) \ , \tag{3.3}$$

which in the absence of the cosmological constant contribution, the acceleration equation (1.31) leads to

$$\frac{\mathrm{d}\Omega_K}{\mathrm{d}\ln a} = \Omega_K \left(1 - \Omega_K\right)\left(1 + 3w\right) \ , \tag{3.4}$$

where w denotes the equation of state of the dominating fluid. Moreover, for a constant w, this equation can be integrated to give

$$\Omega_K(z) = \frac{\Omega_{K,0}}{(1+z)^{1+3w}\left(1 - \Omega_{K,0}\right) + \Omega_{K,0}} \ , \tag{3.5}$$

where the current value of Ω_K is represented by $\Omega_{K,0}$. From Eq. (3.5) along with a conservative limit of $|\Omega_{K,0}| < 0.1$ [65], we require that $|\Omega_K(z_{\text{dec}})| < 10^{-4}$, $|\Omega_K(z_{\text{eq}})| < 3 \times 10^{-5}$, and $|\Omega_K(z_{\text{BBN}})| \lesssim 10^{-11}$, where we denoted the redshift of matter–radiation equality by $z_{\text{eq}} \approx 3365$ [65] and the redshift at Big Bang nucleosynthesis by $z_{\text{BBN}} \sim 10^{10}$. Therefore, an explanation for the reported small value of the present–day spatial curvature requires significant fine–tuning of Ω_K down to unnaturally tiny values in the very early cosmic epoch. Again, the Big Bang model does not address this issue, which is dubbed as the flatness problem.

The main driving force behind the proposal of an inflationary era just before the onset of the Big Bang radiation–dominated epoch was to resolve the above flatness

and horizon problems. However, other similar ideas to the inflationary mechanism have been proposed as early as 1965 by E. B. Gliner [306], and the model by R. Brout, F. Englert, and E. Gunzig that they proposed in 1978 [307].

The first semi–realistic model of an inflationary cosmic era was presented by Alexei Alexandrovich Starobinsky [308] in 1979, whereas the first physically motivated inflationary model that directly addressed the Big Bang problems was proposed by Alan Harvey Guth in 1980 [309]. This was soon followed by the work of Andrei Dmitriyevich Linde [310], and the crucial link between the origin of the large–scale structures of the Universe to quantum fluctuations generated during the inflationary epoch was reported by Viatcheslav Fyodorovich Mukhanov and Gennady Chibisov in 1981 [311].

Before we demonstrate how inflation is capable of solving the horizon and flatness problems, we will first show that inflation is a phase of accelerated expansion of the Universe. In the absence of the cosmological constant, the Friedmann equation (1.30) can be written as follows

$$\left(\Omega^{-1} - 1\right) \rho a^2 = -\frac{3K}{8\pi G} \,, \tag{3.6}$$

where we recall that $\Omega = 8\pi G\rho/(3H^2)$, with ρ being the energy density of the dominating fluid. We now consider an inflationary period during the time interval $[t_i,\, t_f]$, where $t_f > t_i$ represents the time at the end of inflation, whereas t_i is the time at the beginning of inflation. From Eq. (3.6), it follows that

$$\left(\Omega_i^{-1} - 1\right) \rho_i a_i^2 = \left(\Omega_f^{-1} - 1\right) \rho_f a_f^2 \,, \tag{3.7}$$

which implies that the flatness problem can be resolved if $\rho_i a_i^2 \ll \rho_f a_f^2$ is satisfied, such that we can naturally explain the smallness of the spatial curvature at very early times. We recall that the evolution of a perfect fluid with a constant equation of state w, is given by $\rho a^2 \propto a^{-1-3w}$ (see Eq. (1.36)). Since ρa^2 must be an increasing function of the scale factor to resolve the flatness problem, this implies that $w < -1/3$. We know from Eq. (1.45) that this imposes an epoch of accelerating expansion of the Universe, that is $\ddot{a} > 0$. Therefore, the inflationary era must be characterised by a period of accelerating expansion.

We now quantify the minimal length of this inflationary epoch, such that it will be able to resolve the horizon problem and the flatness problem. For this we define the e–fold number which measures the growth in the scale factor during the accelerating phase, given by

$$N = \ln\left(\frac{a_f}{a_i}\right) \,, \tag{3.8}$$

where a_f and a_i are the values of the scale factor at the end and beginning of

inflation, respectively. On assuming a quasi–de Sitter inflationary period during which the Hubble parameter can be assumed to be almost constant, we arrive at

$$\left|\frac{\Omega_K\left(t_f\right)}{\Omega_K\left(t_i\right)}\right| = \left(\frac{a_f}{a_i}\right)^{-2} = e^{-2N} \ . \tag{3.9}$$

We now assume that inflation ends at the Grand Unification scale characterised by $T_f \sim 10^{16}\,\mathrm{GeV}$ [309], which leads to $a_f \sim 2.35 \times 10^{-29}$, where we have further used the fact that the temperature of the Universe varies as $T \propto a^{-1}$, and used a present–day cosmic temperature of $T_0 = 2.7255\,\mathrm{K} = 2.3488 \times 10^{-13}\,\mathrm{GeV}$ [105]. Thus, we can now estimate the spatial curvature contribution at the end of inflation by using Eq. (3.5), given by

$$\left|\Omega_K\left(t_f\right)\right| \sim 6.13 \times 10^{-59} \ , \tag{3.10}$$

where we conservatively assumed that $|\Omega_{K,0}| = 0.1$ [65], and that the Universe is radiation–dominated. Finally, in order to have $\left|\Omega_K\left(t_f\right)\right| \lesssim 6.13 \times 10^{-59}$ and $\left|\Omega_K\left(t_i\right)\right| \sim \mathcal{O}(1)$, we require

$$N \gtrsim 67 \ , \tag{3.11}$$

for the resolution of the flatness problem. We now consider the horizon problem, from which we derive another lower bound on the length of the inflationary period. Since $\ddot{a} > 0$ must be satisfied during inflation, this implies that the comoving Hubble radius $(aH)^{-1}$, decreases in time according to

$$\frac{\mathrm{d}}{\mathrm{d}t}(aH)^{-1} < 0 \ . \tag{3.12}$$

Consequently, one can conclude that the entire observable Universe would emerge out of the same causal region before the onset of inflation, thus resolving the mystery behind the observed isotropy in the CMB radiation. At the very least, we require that the present–day observable Universe fits in the comoving Hubble radius at the beginning of inflation, that is

$$(a_0 H_0)^{-1} < (a_i H_i)^{-1} \ . \tag{3.13}$$

By assuming that at the end of inflation the Universe was radiation–dominated, the Friedmann equation (1.30) reduces to

$$H_f^2 = \frac{8\pi G}{3}\left(\frac{\pi^2}{30}\right) g_*\, T_f^4 \ , \tag{3.14}$$

where $g_* \sim 10^2$ represents the effective number of relativistic degrees of freedom.

This leads to

$$\frac{a_0 H_0}{a_f H_f} \sim 4.67 \times 10^{-28} \left(\frac{h}{0.7}\right) , \tag{3.15}$$

where we recall that $h \sim 0.7$ [65, 78, 79] is the dimensionless Hubble constant defined in Eq. (1.23). Thus, in a quasi–de Sitter inflationary epoch, from the condition specified in Eq. (3.13) along with Eq. (3.15), it follows that we require

$$N \gtrsim 63 , \tag{3.16}$$

in order to solve the horizon problem. Extraordinarily, the length of the primordial accelerated expansion period that is required to resolve the horizon problem, is well–suited to clarify the flatness problem of the hot Big Bang model.

3.2 Problems of the dark sector

The observational evidence for the current deceleration parameter satisfying $q_0 < 0$, only relies on the fact that the Universe is described by an FLRW space–time, which is a manifestation of the cosmological principle. As we have seen in chapter 1, if the theory of gravitation is assumed to be Einstein's theory of General Relativity, then such an acceleration can only be explained if the matter content of the Universe is dominated by a fluid whose equation of state satisfies $w < -1/3$.

In the simplistic scenario of the ΛCDM model, such a component is described by the cosmological constant, that is itself characterised by a constant equation of state of $w = -1$. One of the well–known triumphs of the cosmological constant was demonstrated in the early 1990s, when it was used to resolve the so–called age problem. The introduction of a non–zero cosmological constant contribution to the expansion of the Universe provided a ready solution to resolve the tension between the independent measurements of the Hubble constant and the age of the Universe. At the time, measurements of the Hubble constant ranged between $60 - 90\,\mathrm{km\,s^{-1}Mpc^{-1}}$, whereas the age of the oldest globular clusters implied an age of the Universe in the range of $13 - 15\,\mathrm{Gyr}$ [312, 313]. These limits led to relatively high values of the expansion age $H_0\,t_0$, when compared to the Einstein–de Sitter model, for which $H_0\,t_0 = 2/3$. Indeed, by integrating Eq. (1.25) in a spatially–flat Universe solely composed of non–relativistic matter (m) and the cosmological constant, such that $\Omega_{m,0} + \Omega_{\Lambda,0} = 1$, we get

$$H_0\, t_0 = \int_0^1 \frac{\mathrm{d}a}{a\sqrt{\Omega_{m,0}\, a^{-3} + \Omega_{\Lambda,0}}} = \frac{2}{3\sqrt{\Omega_{\Lambda,0}}} \ln\left(\frac{1+\sqrt{\Omega_{\Lambda,0}}}{\sqrt{\Omega_{m,0}}}\right), \tag{3.17}$$

which easily allows for an increase in the dimensionless age of the Universe as the contribution from the cosmological constant increases. The asymptotic values of Eq. (3.17) are of $H_0\, t_0 \to 2/3$ for $\Omega_{\Lambda,0} \to 0$, and $H_0\, t_0 \to \infty$ for $\Omega_{\Lambda,0} \to 1$, corresponding to the Einstein–de Sitter and de Sitter solutions, respectively. By using Eq. (1.23) along with the normalisation of the dimensionless Hubble constant and the age of the Universe to their currently favoured values [65, 78, 79], we arrive at

$$H_0\, t_0 = 0.987 \left(\frac{h}{0.7}\right)\left(\frac{t_0}{13.8\,\mathrm{Gyr}}\right), \tag{3.18}$$

from which we clearly observe that for $\Omega_{m,0} \approx 0.275$ and $\Omega_{\Lambda,0} \approx 0.725$, the ΛCDM model can easily reproduce the dimensionless age of the Universe reported in Eq. (3.18).

Without doubt, as already remarked in the previous chapters, cosmologists converted rather abruptly from scepticism about the recent cosmic epoch of accelerating expansion to a tentative acceptance after the ground–breaking supernovae results [87, 88]. Evidently, further studies [124, 314] have complemented these pioneering results, which consequently led to the ΛCDM model to sideline its alternatives.

Although the introduction of the non–zero cosmological constant seems to be a very promising explanation for the very recent cosmic epoch of the accelerated expansion, cosmologists are still confronted with two prominent open problems attributed to the cosmological constant itself. Similar to the flatness problem that is addressed with the primordial inflationary era, by construction, the ratio of the energy density of the cosmological constant to the energy density of the total non–relativistic matter is found to evolve as $\rho_\Lambda/\rho_m \propto a^3$. Consequently, the contribution from the cosmological constant in the early Universe is negligible in comparison to the matter and radiation contributions, while at late–times the cosmological constant dominates the energy budget of the Universe. Surprisingly, although the Universe has expanded by a factor of approximately 10^{29} (see section 3.1) from the onset of the radiation–dominated epoch, the present–day ratio between the baryonic (b), cold

dark matter (c), and cosmological constant contributions is reported [65] to be

$$\Omega_{b,0} \,:\, \Omega_{c,0} \,:\, \Omega_{\Lambda,0} \approx 1 \,:\, 5 \,:\, 14 \,. \tag{3.19}$$

Evidently, the cosmic inventory at the current cosmic epoch seems to be very fine–tuned, particularly when one considers the time–scale of the Universe. This, yet unresolved, puzzle of why such distinct matter constituents of the Universe, come with such a ratio, became known as the coincidence problem. A direct implication of the present–day abundances of these matter components follows from the deceleration–acceleration transition redshift equation (1.47), which peculiarly shows that the Universe entered into an epoch of accelerating expansion very recently at a redshift of less than unity.

To put the coincidence problem into perspective, we consider a transitional period between the total non–relativistic matter ($\Omega_m = \Omega_b + \Omega_c$) and the cosmological constant to include the time from $\Omega_\Lambda/\Omega_m = 0.01$ to $\Omega_\Lambda/\Omega_m = 5$, during which the Universe would only expand by a factor of around $10^{0.9}$. This clearly shows that there needs to be a significant amount of fine–tuning in order to presently have these very distinct components of the Universe at the same order of magnitude. However, we should finally mention that due to our lack of understanding of the dark sector of the Universe, observations infer the dark matter and dark energy abundances via the observations of luminous matter. Thus, these conclusions strongly depend on the validity of General Relativity on cosmological scales, which up to now has always been proven to be correct. This therefore leaves a small room for the modification of the theory of General Relativity, implying that it is imperative to confront this theory on cosmological scales.

We now revisit Einstein's field equations (1.15), from which we observe that the cosmological constant term, with natural units of $[Length^{-2}]$, could either be interpreted as a geometrical term or as a matter contribution to the energy–momentum tensor. Indeed, from Eq. (1.35) it follows that we can represent the cosmological constant contribution to the expansion of the Universe by a fluid with constant energy density

$$\rho_\Lambda = \frac{\Lambda}{8\pi G} \,. \tag{3.20}$$

Within the framework of General Relativity the Λ–term is a completely free parameter and there is no theoretical constraint which can be imposed on its value. From the perspective of non–classical physics, we know that Lorentz invariance implies that in the vacuum, the energy–momentum tensor must take the form of $\langle T^{\mu\nu}\rangle_{\text{vac}} = -\langle\rho\rangle_{\text{vac}}\, g^{\mu\nu}$, where the minus sign follows from our choice of space–time signature. From Einstein's field equations (1.15), we observe that this vacuum energy–momentum tensor can be represented by adding the term $8\pi G\langle\rho\rangle_{\text{vac}}$ to an effective cosmological constant $\Lambda_{\text{eff}} = \Lambda + 8\pi G\langle\rho\rangle_{\text{vac}}$. In terms of an effective vacuum energy

density, this can be written as follows

$$\rho_{\rm eff}^{\Lambda} = \frac{\Lambda_{\rm eff}}{8\pi G} = \langle\rho\rangle_{\rm vac} + \frac{\Lambda}{8\pi G} \,. \tag{3.21}$$

As we have illustrated in chapter 1, current cosmological observations favour a spatially–flat FLRW space–time with the present–day energy density being dominated by the cosmological constant. With the aid of the Friedmann equation (1.30), we can place a rough upper bound on the magnitude of the cosmological constant from the perspective of cosmology, given by

$$|\Lambda_{\rm eff}| \lesssim H_0^2 = 2.23 \times 10^{-84} \left(\frac{h}{0.7}\right)^2 \,{\rm GeV}^2 \,, \tag{3.22}$$

where we recall that h is the dimensionless Hubble constant. This corresponds to an upper bound on the total effective vacuum energy of

$$\left|\rho_{\rm eff}^{\Lambda}\right| \lesssim 1.32 \times 10^{-47} \left(\frac{h}{0.7}\right)^2 \,{\rm GeV}^4 \,. \tag{3.23}$$

As long as we consider classical physics, this value does not create any issues with our understanding of Nature. However, the introduction of Quantum Mechanics changes this story somewhat. The quantum aspects of the cosmological constant were first visited by Wolfgang Ernst Pauli in the early 1920s when he was wondering whether the zero–point energy, whose concept was proposed by Max Planck in 1911 [315], of the radiation field could be gravitationally effective. For decades, the contribution of quantum fluctuations to the cosmological constant was sidelined by particle physicists, even after the demonstration [316] in the Casimir effect [317] of the reality of zero–point energies. In 1967 Yakov B. Zel'dovich returned to this idea when he considered [318, 319] quantum fluctuations to account for a non–zero vacuum energy density, although he found that this approach predicted an effective vacuum energy density of around nine orders of magnitude larger than the cosmological upper bound. Indeed, from a quantum point of view, we expect that by summing the zero–point energies of all normal modes of some field with mass m up to a wavenumber cutoff $k_{\rm max} \gg m$, the vacuum energy density receives a total contribution of

$$\langle\rho\rangle_{\rm vac} = \frac{1}{2}\int_0^{k_{\rm max}} \frac{{\rm d}^3\boldsymbol{k}}{(2\pi)^3}\sqrt{k^2+m^2} = \frac{1}{4\pi^2}\int_0^{k_{\rm max}} {\rm d}k\, k^2\sqrt{k^2+m^2} \simeq \frac{k_{\rm max}^4}{16\pi^2} \,, \tag{3.24}$$

where the cutoff frequency of $k_{\rm max}$, needs to be implemented due to an ultraviolet divergence ($k_{\rm max} \to \infty$) of the integral. This approach is justified with the fact

that all the energy scales probed by experiments to date agree with a description of Nature as a set of quantum fields. In order to account for the vacuum contribution from smaller wavelengths we require a more complete theory of Nature, however if we believe that the theory of General Relativity remains valid up to the Planck scale, then we can set the cutoff frequency to this scale. We observe that at the Planck scale of $k_{\rm max} = m_{\rm Pl} = 1.22 \times 10^{19}\,{\rm GeV}$, the theoretically expected value for the vacuum energy density, is given by

$$\langle\rho\rangle_{\rm vac}^{\rm Pl} \approx 1.40 \times 10^{74}\,{\rm GeV}^4\ . \tag{3.25}$$

Since we deduced that $|\langle\rho\rangle_{\rm vac} + \Lambda/(8\pi G)| \lesssim 10^{-47}\,{\rm GeV}^4$, this cosmological upper bound implies that the two terms must cancel each other to better than 121 decimal places. This extraordinary fine–tuning of around 120–orders of magnitude is the so–called cosmological constant problem [320].

A number of different approaches have tried to shed some light on this cosmological constant problem, although none of these proposals were able to alleviate this conundrum of the dark sector. One of the most elegant resolutions was proposed by supersymmetry, in which the vacuum energy vanishes as long as supersymmetry is not broken [321]. This follows from the fact that exact supersymmetry implies an equal number of fermionic and bosonic degrees of freedom, thus quantum effects will not change this conclusion due to the boson–fermion symmetry which exactly cancels all the loop corrections. However, the elegance of supersymmetry is broken today, leading to $\langle\rho\rangle_{\rm vac} > 0$. It turns out that, if this vacuum energy were the only contribution to the effective cosmological constant, then it will convert the problem of the cosmological constant to a catastrophe. Indeed, if supersymmetry is broken at around 1 TeV, then this leads to $\rho_\Lambda \sim -(1\,{\rm TeV})^4$ during the entire cosmic history. Finally, we remark that any globally supersymmetric theory that involves gravity is inevitably a locally supersymmetric supergravity theory. However, in this scenario a significant amount of fine–tuning is required in order to explain the cosmological constant problem [320]. Thus, it is not a trivial task to see how any property of supergravity or superstring theory could make the effective cosmological constant sufficiently small in order to be in agreement with the upper bound inferred from cosmological observations.

Another approach has been taken via the so–called anthropic principle [322]. There are several versions of this principle, however they mainly rely on the idea that a set of parameters directly influence other physical phenomena such that if these parameters had a different value, these phenomena would not take place or be observable. Thus, this approach looks into the consequences of the modification of these constants of Nature, rather than the computation of their exact values. For instance, Steven Weinberg was able to predict [323] a non–zero present–day value for the cosmological constant by considering the effects of the vacuum energy

on the possible existence of life. His argument followed from the fact that if the vacuum energy was large and positive, then galaxies would not form due to the rapid acceleration of the Universe, whereas if the cosmological constant contribution was large and negative then the Universe would re–collapse. Time will tell if this, rather philosophical, idea would be embraced by cosmologists as the solution to the cosmological problems within the dark sector.

Finally, we should mention that the above dark sector problems have been explored with several modifications in the theory of General Relativity, which led to a very active area of research in modern cosmology. In the subsequent chapters we will be focusing on a modified dark sector scenario in which the cosmological constant will be replaced by a dynamical scalar field with a canonical kinetic term. Moreover, in this class of models we will allow for an interaction between cold dark matter and this dark energy scalar field. However, before we turn our attention to these models, we will now discuss some parametrisations for the equation of state of dark energy as well as the currently reported mild tensions arising from different cosmological probes.

3.3 What can we learn from observational cosmology?

In order to decipher the characteristics of the puzzling dark sector, especially of the dark energy constituent, one should confront the numerous alternatives to the standard cosmological constant with observational data. The simplest, rather generic, phenomenological extension of the cosmological constant that appears in the ΛCDM model is to parametrise [324] the equation of state for a dark energy fluid which replaces the cosmological constant itself. Since the equation of state is a relation between the fluid's pressure and energy density, the equation of state is therefore closely related to the underlying physics. This approach might shed some light on the possible dynamical features of dark energy, which, if confirmed, will eventually exclude the cosmological constant. There are several cosmological models in which dark energy is considered to be a dynamical quantity rather than a constant throughout the history of the Universe. For instance, a slowly–rolling dynamical scalar quintessence [325–329] field has been exhaustively explored in the literature, and we will be discussing extended models of quintessence in the subsequent chapters. A similar model which makes use of a dynamical scalar field, but with a non–canonical kinetic term in the Lagrangian, is the model of k–essence [330–332].

We will here consider a standard N–th order Taylor expansion of a time–dependent dark energy equation of state of the form [333]

$$w_X(a) = \sum_{n=0}^{N} w_n x_n(a) \ , \tag{3.26}$$

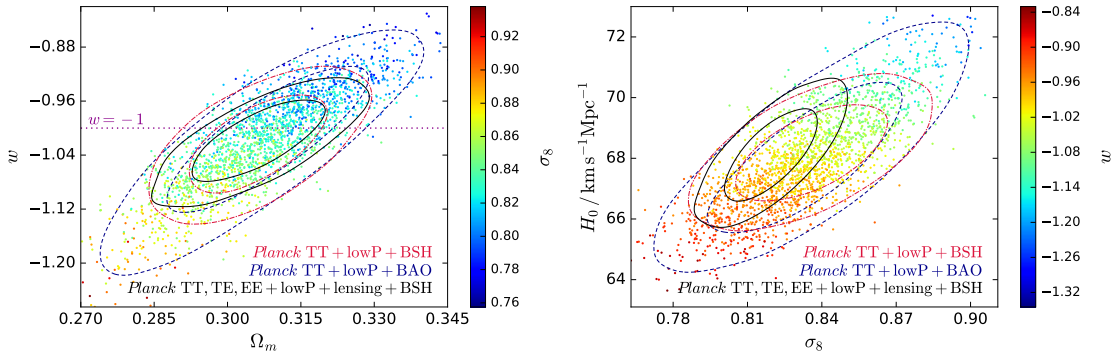

Figure 3.1: This figure shows the wCDM parametrised model 68% and 95% credible regions in the Ω_m–w plane (left) and σ_8–H_0 / km s^{-1}Mpc^{-1} plane (right) using the data sets indicated in the figure, which we describe in the text. The samples are coloured with the values of σ_8 in the left panel, whereas w is used in the right panel. The dotted line in the left panel indicates the equation of state of the cosmological constant.

where several choices for the expansion function $x_n(a)$, have been explored [334–340]. In our case, we will adopt an expansion in terms of the scale factor of $x_n(a) = (1-a)^n$ [336, 339], and consider its zeroth–order ($N = 0$) and first–order ($N = 1$) terms. Thus, at the zeroth–order we end up with a constant equation of state of dark energy, which for simplicity will be denoted by w. In this wCDM scenario, the scale factor at the matter–dark energy equality is given by

$$a_{m-X}^{-3w} = \frac{\Omega_{m,0}}{\Omega_{X,0}} \,, \tag{3.27}$$

where $\Omega_{m,0}$ and $\Omega_{X,0}$ denote the present-day total matter and dark energy abundances, respectively. From the Friedmann equation (1.31) which now takes into account the dark energy fluid with a constant equation of state w, along with a non–relativistic matter component, we get the transitional redshift between decelerated and accelerated cosmic expansion at a scale factor of

$$a_{\rm dec-acc}^{-3w} = -\frac{1}{1+3w}\frac{\Omega_{m,0}}{\Omega_{X,0}} \,. \tag{3.28}$$

At first–order, we have a two–parameter expansion of the parametrised equation of state which corresponds to the $\{w_0, w_a\}$ case, specified by

$$w_X(a) = w_0 + (1-a)w_a \,, \tag{3.29}$$

where both w_0 and w_a are constants, and w_a measures the time evolution of the dark energy density. This parametrisation is also known as the Chevallier–Polarski–Linder (CPL) parametrisation. The CPL time–dependent parametrisation is obviously more

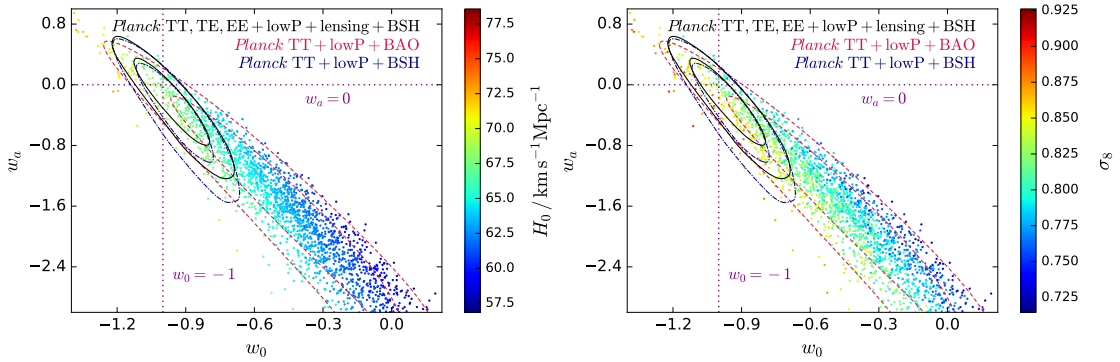

Figure 3.2: This figure shows the CPL parametrised model 68% and 95% credible regions in the w_0–w_a plane using the data sets indicated in the figure, which we describe in the text. The samples are coloured with the values of H_0 / km s^{-1}Mpc^{-1} in the left panel, whereas σ_8 is used in the right panel. The point of intersection of the dotted lines indicate the equation of state of the cosmological constant.

applicable to modified theories of gravity which are characterised by a dynamical dark energy equation of state.

Similar to chapter 1, we here make use of the *Planck* collaboration publicly [89] available Markov chain Monte Carlo samples for the wCDM and CPL parametrised models, which we then analyse with `GetDist` [90]. These constraints have been derived from the *Planck* temperature power spectrum along with information from the low–multipole polarisation (*Planck* TT + lowP), combined with the E–mode polarisation and its cross–correlation with the temperature spectrum (*Planck* TT, TE, EE + lowP). We also consider additional information from the effect of gravitational lensing by large–scale structures on the CMB temperature and polarisation spectra [91] (+ lensing), and we further add information from baryon acoustic oscillations data [92–94] (+ BAO), a compilation of supernovae data [95], and an independent local measurement of the Hubble constant [96] (+ BSH).

In the left panel of Fig. 3.1 we show the 68% and 95% credible regions for the present–day total matter abundance Ω_m, along with the parametrised dark energy equation of state w. We also illustrate a number of samples coloured with the values of the root–mean–square fluctuation in total matter in $8\,h^{-1}\,\mathrm{Mpc}$ spheres σ_8, as defined in chapter 1. The corresponding w_0–w_a parametrised model constraints are illustrated in the panels of Fig. 3.2, where we show the 68% and 95% credible regions for the dark energy equation of state $\{w_0, w_a\}$ parameters. In the left and right panels of Fig. 3.2 we also depict some samples coloured with the values of H_0, and σ_8, respectively. In Figs. 3.1 and 3.2, the cosmological constant is indicated by the dotted lines, where in the zeroth–order expansion it is simply depicted by the horizontal line at $w = -1$, whereas in the first–order expansion the intersection point of the two lines at $w_0 = -1$ and $w_a = 0$ reduces to the cosmological constant.

Evidently, Figs. 3.1 and 3.2 show that current cosmological data sets are consis-

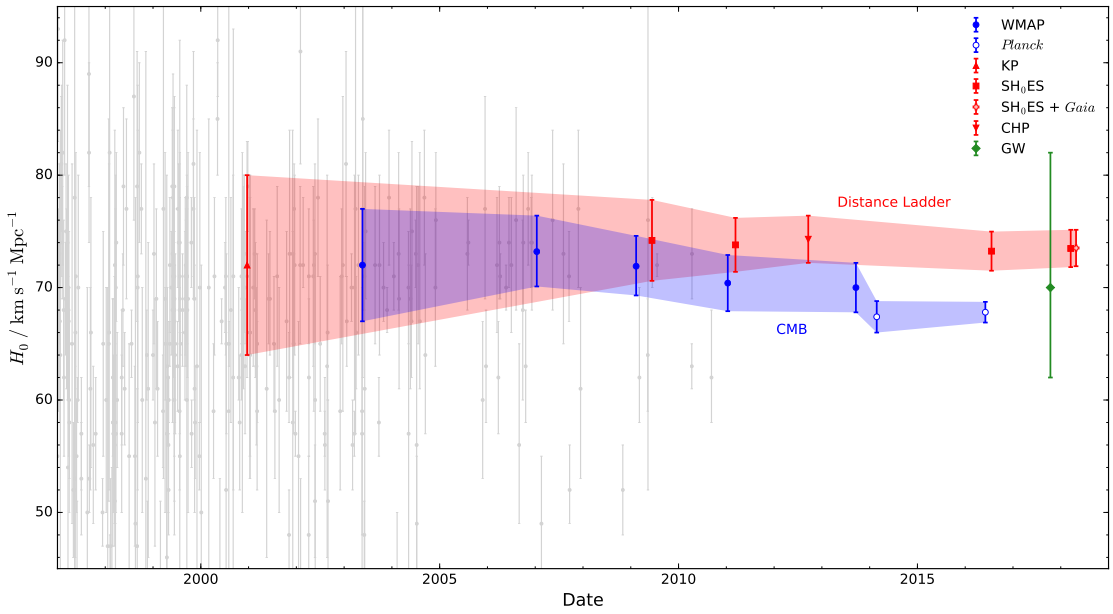

Figure 3.3: This figure shows the discordance between the determination of the Hubble constant from the Cepheid distance ladder (red) [78, 79, 351–355] and the inferred Hubble constant values from CMB (blue) observations under the assumption of the ΛCDM model [65, 99, 124, 356–359], as a function of publication date. We also include the first measurement of the Hubble constant from gravitational–wave astronomy (green) [360], along with a compilation (gray) of other reported values of H_0 [361]. The coloured error bars represent the 1σ error as quoted at the time of publication.

tent with the cosmological constant description of dark energy when the equation of state of dark energy is considered as a variable parameter. Indeed, the tightest 68% (95%) confidence levels that are inferred from the full joint data set combination are of $w = -1.019^{+0.039(0.075)}_{-0.040(0.080)}$ in the wCDM model, and of $w_0 = -0.955^{+0.101(0.215)}_{-0.120(0.201)}$ and $w_a = -0.251^{+0.448(0.677)}_{-0.334(0.799)}$ in the CPL parametrised model. However, a number of different cosmological probes have recently been reporting [341–350], yet unresolved, tensions in comparative analyses of their data. Although this apparent disagreement between different data sets at the 2–3σ level is not yet alarming for the ΛCDM model, forthcoming data might enhance this disagreement, consequently turning this tension into an actual discrepancy.

Two currently actively investigated tensions that perhaps attract the most attention of cosmologists as well as astronomers, are attributed to the inferred values of H_0 and σ_8. The H_0 tension stems from the disagreement between the inferred model–dependent Hubble constant from CMB observations [65, 99, 124, 356–359] and the direct local measurements of the Hubble constant [78, 79, 351–355]. We illustrate this H_0 discordance in Fig. 3.3, where we compare a number of recent values of the Hubble constant determined in the nearby galaxies with several derived values

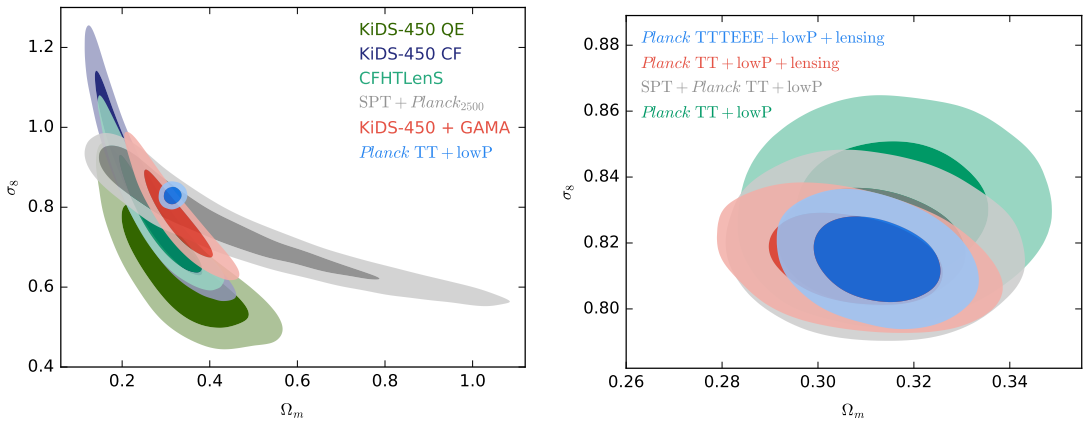

Figure 3.4: The panels of this figure show the concordance model 68% and 95% credible regions in the Ω_m–σ_8 plane using the data sets indicated in each respective panel, which we describe in the text. The left panel illustrates the current tension between large–scale structure surveys (KiDS–450 QE/CF, KiDS–450 + GAMA, CFHTLenS) and CMB observations (*Planck*, SPT), whereas in the right panel we illustrate the currently tightest constraints in the Ω_m–σ_8 plane from CMB measurements only.

of the Hubble constant based on the adopted concordance cosmological model. On the other hand, the σ_8 tension arises from a comparison between the ΛCDM extrapolated value of σ_8 from measurements of the spectrum of temperature anisotropies of the CMB [65] which typically probe the large–scales, with the more direct small–scale constraints from low–redshift large–scale structure experiments [344, 362–370]. This σ_8 tension was recently illustrated with the weak gravitational lensing data from the Kilo Degree Survey (KiDS–450) when compared with the *Planck* satellite measurements of the CMB radiation temperature anisotropy power spectrum in the Ω_m–σ_8 plane, thus this tension is commonly referred to as the Ω_m–σ_8 tension. This choice of parameters emerges from the fact that the cosmic shear power spectrum of KiDS–450 is mostly sensitive to these parameters, along with their combination of $\sigma_8\sqrt{\Omega_m/0.3}$.

These tensions have been confronted with rigorous statistical analyses [350, 371–375] in order to determine whether systematics could alleviate these tensions, however the currently known systematic effects are not solely able to solve these tensions. We depict the 68% and 95% credible regions in the Ω_m–σ_8 plane in Fig. 3.4, whereas the corresponding marginalised contours in the Ω_m–$\sigma_8\sqrt{\Omega_m/0.3}$ plane and σ_8–$\sigma_8\sqrt{\Omega_m/0.3}$ plane are shown in Fig. 3.5. For these figures, we used the publicly available chains of the large–scale structure probes from KiDS–450 quadratic estimator (KiDS–450 QE) [376] and correlation function (KiDS–450 CF) [344] analyses, KiDS + GAMA [377], and CFHTLenS [378]. Moreover, we further included a number of CMB publicly available chains from the *Planck* collaboration [89] as described above, along with the SPT chains that adopt a 2500 deg^2 CMB gravitational lensing

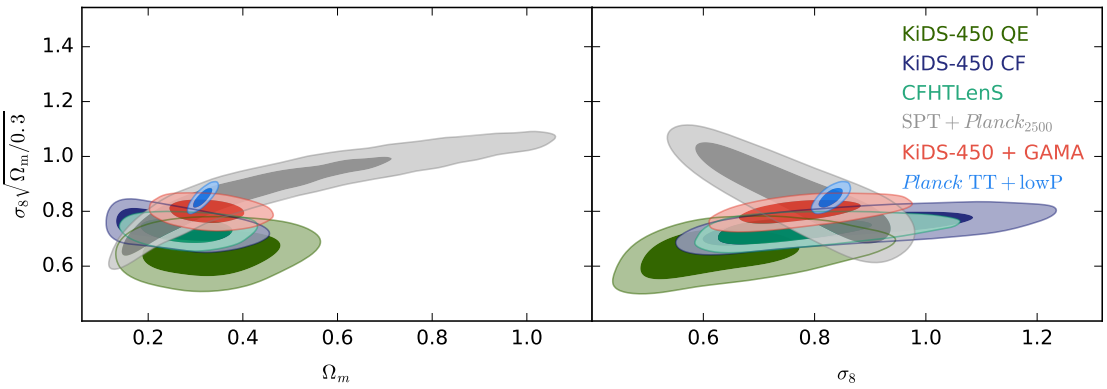

Figure 3.5: In the left panel we show the concordance model 68% and 95% credible regions in the Ω_m–$\sigma_8\sqrt{\Omega_m/0.3}$ plane, whereas in the right panel we illustrate the credible regions in the σ_8–$\sigma_8\sqrt{\Omega_m/0.3}$ plane, using the data sets indicated in the figure. Similar to Fig. 3.4, these panels illustrate the mild tension between large–scale structure observations and CMB measurements.

potential map (SPT + *Planck*$_{2500}$ or SPT) [379] as opposed to the full–sky *Planck* lensing data (+ lensing) [91].

Among the most physically motivated attempts to solve these tensions, there is the inclusion of massive neutrinos to the concordance model [380–382]. This approach might be the most sensible one, since we now have enough evidence that massive neutrinos exist, and that the introduction of massive neutrinos in the ΛCDM model is well–known to be characterised by a reduction in the amount of small–scale power relative to the large–scales in the observed matter power spectrum, a characteristic that is directly linked to the σ_8 tension. However, further studies showed that the H_0–σ_8 tension is very unlikely [383] to be entirely solved by adding massive neutrinos to the concordance model.

Although a constant equation of state of dark energy satisfying $w < -1$, is able to alleviate the H_0 tension between the inferred CMB values and the local measurements [384–389], it is unlikely that this can also address the σ_8 tension. As illustrated in the right panel of Fig. 3.1 it is clear that a phantom–like dark energy equation of state of $w < -1$, can accommodate [384–389] large values of the Hubble constant that are consistent with local measurements of H_0. However, due to the correlation between H_0 and σ_8, phantom–like dark energy prefers higher values of σ_8 than the currently favoured values reported by large–scale structure observations, although it was recently reported that the wCDM model is slightly favoured over the ΛCDM model when a joint analysis between the discordant data sets is performed [383]. Moreover, the CPL parametrised model of dark energy was also found [383] to bring substantial concordance between large–scale structure data and CMB measurements. Although the results in Fig. 3.2 are consistent with a cosmological constant description of dark energy, the data sets under consideration still allow for an appreciable amount of freedom for the case of a dynamical dark

energy equation of state, which could be interpreted as a window of opportunity for alternative models to ΛCDM. A more generic non–constant dynamical dark energy equation of state has been recently explored in Ref. [390], in which they found that this model has the potential to alleviate the currently reported tensions. Thus, a better understanding of the dark energy evolution via forthcoming data sets along with other phenomenological parametrisations, should shed some light on the true model of this puzzling dark sector constituent.

3.4 Conclusions

In this chapter we have looked at the currently open problems of modern cosmology, and the reported tensions within the concordance model. We have discussed the flatness and horizon problems, along with their currently best known solution given by a postulated inflationary primordial epoch. We have demonstrated the elegance of this inflationary period that is able to solve both problems at the same time. Obviously, one needs to construct physically motivated models of inflation, and work out its relationship with the rest of the Big Bang model.

At late times, we have seen that there needs to be a significant amount of fine–tuning in order to entirely describe the period of accelerated expansion with the cosmological constant. One can view the cosmological constant problem as a price that we need to pay for dumping too much into the mysterious vacuum. If the vacuum energy density was as large as theories of elementary particle physics suggest, then the Universe would be dramatically different, with properties we would find both bizarre and unsettling. Thus, it is our task to repair a number of our theoretical faulty foundations without destroying the towering edifice we have built on it.

As we have discussed in the last section of this chapter, although the ΛCDM model appears to provide an excellent fit to the wide range of data, as we previously demonstrated in chapter 2, the race is on to accumulate sufficient evidence for extensions to this model and a contribution to this goal is the objective of the subsequent chapters. Clearly, under the strong presumption that all the current and forthcoming cosmological data is accurate and relatively free from systematics, current tensions might turn into a number of significant disagreements with the present–day concordance model of cosmology. Consequently, the well–established ΛCDM model could potentially require a crucial amount of new physics, which could naturally be embedded in an alternative model. Thus, in light of our incomplete understanding of the cosmic evolution of our Universe, the consideration of alternative models of dark energy is a rational step towards a more comprehensive view of the cosmos.

I think – to really make some headway – one would have to find another general principle eavesdropped from Nature.

Albert Einstein

4

Dynamics & cosmological implications of multifluid dark energy interactions

The elegance, comprehensibility, and longevity characteristics of the theory of General Relativity inflict a non–trivial task for any alternative theory of gravitation to set it aside. As we discussed in chapter 1, this currently adopted standard theory of gravitation still requires experimental confrontation from galactic scales upwards. Nevertheless, the theory of General Relativity has so far been able to superbly describe our Universe, which we clearly illustrated in chapter 2. However, this theoretically robust description of our Universe comes at the price of accepting that around ninety–five percent [65] of the present–day energy–matter content of the Universe is of obscure nature. This unfamiliar territory became known as the dark sector of the cosmos, which is believed to be composed of dark matter and dark energy. Albeit the simplistic cosmological constant could well play the role of dark energy, we have seen in chapter 3 that the cosmological constant is characterised by the cosmological constant problem and the coincidence problem.

Although this puzzling dark sector of the Universe has recently been the main driving force behind the motivation for alternative theories of gravitation, the proposal of theories of modified gravity dates back to the very early days after Einstein's publication [6, p. 245] of his theory of General Relativity in 1915. Indeed, fourth–order metric theories of gravitation were introduced as a specialisation of Hermann Weyl's [391] non–integrable relativity theory from 1918, while he was working on a unified theory of gravitation and electromagnetism which laid the foundation for the modern gauge–field interpretation of electromagnetism [392–394]. This class of theories became known as $f(R)$ theories of gravity [395], in which the gravitational part of the action is generalised to a function of the Ricci scalar R, instead of the simple linear term that is considered in the Einstein–Hilbert action. This generic

class of modified gravity has been used for a tentative description of the inflationary period at the early Universe [396], as well as for the late–time accelerated cosmic expansion [397–401]. These ideas have been exhaustively explored (see Refs. [402–404] for recent review articles) and other combinations of higher–order curvature invariants that further include the Ricci tensor $R_{\mu\nu}$, and the Riemann tensor $R_{\alpha\beta\gamma\delta}$, such as R^2, $R_{\mu\nu}R^{\mu\nu}$, and $R_{\alpha\beta\gamma\delta}R^{\alpha\beta\gamma\delta}$, have been studied in a cosmological context [405–411].

Shortly after Weyl's theory, Theodor Kaluza proposed [412] another unified theory of gravity and electromagnetism in 1921, in which he envisioned five–dimensional space–time to which General Relativity was applied in the usual four–dimensional space–time, along with a vector field that is attributed to the vector potential of electromagnetism and a scalar field which would be responsible for a new interaction. In his theory, Kaluza made use of the cylinder condition, which was later justified [413, 414] by Oskar Klein as long as one considers the fifth–dimension to be topologically compact with the topology of a circle, and consequently led to the so–called Kaluza–Klein theory. From this interpretation, the scale of compactification is represented by the radius of the fifth–dimension, which turns out [414] to be very small when compared to all other characteristic lengths, implying that this can only be probed by enormously high energies.

Kaluza–Klein theory along with the idea that the fundamental constants of Nature might be variable quantities in cosmological time, where the latter idea is attributed to Paul Dirac's Large Numbers Hypothesis [415, 416], inspired Pascual Jordan's work [417] on the so–called scalar–tensor theory of gravitation. However, the nascency of scalar–tensor theories of gravitation dates back to 1941 with Willy Scherrer's proposal [418], in which his motivation for the introduction of a scalar field was ascribed to a new approach for scalar relativistic mechanics. In fact, Scherrer presented [418] his Lagrangian, which corresponds to that of Jordan, on which he imposed a similar constraint that is used for the norming of a Schrödinger wave equation. Although it might appear as if Nordström's [19] idea of scalar gravity was being revived, the concept behind scalar–tensor theories of gravitation is not simply to amalgamate the metric tensor field with the scalar field. Alternative gravitational theories of this kind embrace the solid foundation of General Relativity, and the scalar field comes into play in a non–trivial manner via the so–called non–minimal coupling.

On the other hand, while Jordan was adopting the projective relativity [417, 419] four–dimensional space approach for the five–dimensional space Kaluza–Klein theory, he identified [420] the scalar field variable that appears in Kaluza–Klein theory with the function to replace the gravitational constant, in accordance with Dirac's argument [415, 416]. The resulting field equations for the gravitational field, the electromagnetic four–potential, and the scalar field were given by Jordan and Claus

Müller [421] and in a subsequent paper [422], Jordan considered five–dimensional cosmology. Independently from Jordan's work, Ives Thiry together with André Lichnerowicz also arrived at the same field equations [423, 424], although they missed the physical interpretation of the scalar field.

Jordan's scalar function was reinterpreted [425] by Markus Fierz as the permittivity of the vacuum, and Fierz pointed out the difficulty of coupling the scalar field to the energy–momentum tensor of matter. Indeed, the latter remark by Fierz was embraced by Carl H. Brans and Robert H. Dicke [426, 427] who considered the matter Lagrangian to be independent from the scalar field, consequently distinguishing their proposal from Jordan's scalar–tensor theory formulation. Brans and Dicke presented their alternative theory of gravitation as an extension to Einstein's theory of General Relativity, and did not make the connection with five–dimensional spaces or with a unified field theory. Moreover, Brans and Dicke developed their theory on the weak equivalence principle, Mach's principle, and a varying gravitational constant, which they published in 1961 [426] and in a subsequent paper by Brans [427]. Indeed, the matter–scalar coupling chosen by Brans and Dicke ensured that all matter constituents universally couple to the same metric, such that they are considered as freely–falling in this universal metric in accordance with the weak equivalence principle. Dicke immediately referred [428] to this alternative theory of gravitation by the name of Brans–Dicke theory, which has remained unchanged since then. Surprisingly, the reported Lagrangian of Brans–Dicke theory was identical to that of Scherrer's expression [418], while the respective field equations were already presented in a slightly different notation by Günther Ludwig and Müller [429]. Since the Brans–Dicke scalar field $\phi_{\rm BD}$, corresponds to the reciprocal of Jordan's theory scalar field, the evolution of the scalar field in Brans–Dicke theory is governed by a simple wave equation of $\nabla^{\mu}\nabla_{\mu}\phi_{\rm BD} \propto T_{\rm BD}$ [426, 427]. The non–zero constant of proportionality arises from the coupling between the scalar field and matter, where the latter is denoted by the trace of its energy–momentum tensor $T_{\rm BD}$. We remark that although the Brans–Dicke scalar field was chosen to be decoupled from the matter Lagrangian in accordance with the universality of free–fall, the scalar field does couple to matter in the field equations. Thus, the field equations of General Relativity are modified, such that General Relativity can be considered as a limiting case of when the Brans–Dicke matter–scalar coupling vanishes. Eventually, this simplistic and elegant approach of Brans and Dicke led to what is still considered as the archetypal scalar–tensor theory of gravitation, despite the fact that their theory was presented two decades after the first proposal.

The natural extension of scalar–tensor theories with a similar formulation to the Brans–Dicke theory, is encapsulated in the Horndeski Lagrangian [430] that was presented by Gregory Walter Horndeski in 1974. This is the most general gravitational sector Lagrangian that involves a metric tensor field along with a single classical

scalar field, providing second order equations of motion in four–dimensions. Thus, gravity is mediated by a massless spin–2 graviton field and by a spin–0 scalar field. On assuming that the weak equivalence principle holds, such that all excitations of each matter field $\chi_m^{(i)}$ are minimally and universally coupled to the scalar field, leads us to the following scalar–tensor theory action

$$\mathcal{S} = \int \mathrm{d}^4x\,\sqrt{-g}\left[\sum_{i=2}^{5}\mathcal{L}_i + \mathcal{L}_m\Big(g_{\mu\nu},\,\chi_m^{(i)}\Big)\right] , \tag{4.1}$$

where the global matter sector is described by the Lagrangian $\mathcal{L}_m$, which is only a functional of the matter fields and the metric $g_{\mu\nu}$, such that it does not involve the scalar field ϕ. We further recall that g is the determinant of $g_{\mu\nu}$. In the modern language of generalised Galileons [431], the four Lagrangian functions arising from the gravitational sector specified by the Horndeski theory, are given by [432]

$$\mathcal{L}_2 = K(\phi, X) , \tag{4.2}$$

$$\mathcal{L}_3 = -\,G_3(\phi,\,X)\Box\phi , \tag{4.3}$$

$$\mathcal{L}_4 = G_4(\phi,\,X)R + G_{4,X}(\phi,\,X)\Big[\,(\Box\phi)^2 - \big(\nabla_\mu\nabla_\nu\phi\big)^2\Big] , \tag{4.4}$$

$$\begin{aligned}\mathcal{L}_5 =\,& G_5(\phi,\,X)G_{\mu\nu}\nabla^\mu\nabla^\nu\phi \\ & - \frac{1}{6}G_{5,X}(\phi,\,X)\Big[\,(\Box\phi)^3 - 3\,(\Box\phi)\,\big(\nabla_\mu\nabla_\nu\phi\big)^2 + 2\,\big(\nabla_\mu\nabla_\nu\phi\big)^3\Big] .\end{aligned} \tag{4.5}$$

The four functions $K(\phi,\,X)$ and $G_{i\,\in\,\{3,\,4,\,5\}}(\phi,\,X)$ are arbitrary functions of the scalar field and its canonical kinetic term $X = -\nabla^\mu\phi\nabla_\mu\phi/2$, and a derivative with respect to the scalar field's kinetic energy is denoted by $G_{i,X} = \partial G_i/\partial X$. Moreover, the d'Alembertian is denoted by $\Box = \nabla^\mu\nabla_\mu$, $\big(\nabla_\mu\nabla_\nu\phi\big)^2 = \nabla_\mu\nabla_\nu\phi\nabla^\mu\nabla^\nu\phi$, $\big(\nabla_\mu\nabla_\nu\phi\big)^3 = \nabla_\mu\nabla_\nu\phi\nabla^\nu\nabla^\lambda\phi\nabla_\lambda\nabla^\mu\phi$, R denotes the Ricci scalar, and $G_{\mu\nu}$ is the Einstein tensor. In the Horndeski theory, one can easily observe that the non–minimal couplings between the scalar field and gravity are completely fixed by $\mathcal{L}_4$ and $\mathcal{L}_5$. It is worth noting that, even though Horndeski's Lagrangian includes second order derivatives of the fields, it evades the Ostrogradskian instability [433] since it does not satisfy the non–degeneracy assumption [434, 435], where we identify degenerate theories with those theories in which the highest derivative term can not be written as a function of canonical variables, such as General Relativity. Furthermore, the Einstein–Hilbert Lagrangian is recovered when one only considers the non–vanishing contribution of $G_4 = M_{\mathrm{Pl}}^2/2$ (see Eq. (1.14)), where $M_{\mathrm{Pl}}^{-1} = \kappa = \sqrt{8\pi G}$ denotes the

reciprocal of the reduced Planck mass, with G being the gravitational constant. Brans–Dicke theory [426, 427] is also a subclass of the Horndeski theory, which is retrieved when one sets $G_3 = G_5 = 0$, $G_4 = \phi_{\rm BD}$, and the generalised k–essence term to $K = -\omega_{\rm BD}\phi_{\rm BD}^{-1}\nabla_\mu\phi_{\rm BD}\nabla^\mu\phi_{\rm BD}$, with $\omega_{\rm BD}$ being the classical Brans–Dicke matter–scalar coupling parameter.

We further remark that, in the generic Horndeski theory, the propagation speed of gravitational–waves deviates from the speed of light whenever the coupling G_4 depends on the kinetic energy of the scalar field, and the coupling G_5 is not constant [436]. After the almost simultaneous multi–messenger gravitational–wave astronomy observations of a binary neutron star merger with gravitational–waves [16] and its electromagnetic counterpart [17], unequivocally fixed the speed of gravitational–waves to be the same as the speed of light with deviations of around 10^{-15} [18] (see section 1.1). Provided that in the general Horndeski framework, this is not achieved by a severe tuning of the coupling parameters in order to unnaturally cancel the characteristic deviation between the speed of gravitational–waves and the speed of light, we require the severe restriction on the Horndeski theory of $G_5 = 0$ and $G_4 = G_4(\phi)$ [437–444]. Thus, the currently physically motivated viable Horndeski model belongs to the class of kinetic gravity braiding models [445] augmented by a non–minimal coupling to the Ricci scalar. Particularly, the dark energy models that we will be considering in this thesis are an extended subclass of these viable Horndeski type models, thus evading the mentioned gravitational–waves stringent constraint.

In this chapter and in the subsequent chapters, we will be particularly interested in extensions of the so–called quintessence models. This terminology was coined by Robert R. Caldwell, Rahul Dave, and Paul J. Steinhardt [328], however the first quintessence models were presented in the late 1980s by Bharat Ratra and Phillip James Edwin Peebles [326] along with Christof Wetterich [325]. Quintessence models are generically ascribed to a specific, rather phenomenological, type of Horndeski scalar–tensor theory with a minimally coupled scalar field, such that the adopted scalar field acts like a dynamical cosmological constant with a time–dependent pressure to energy density ratio. Consequently, the quintessence scalar field ϕ, is often referred to as the dark energy scalar field, since it was originally introduced as an alternative mechanism to explain the nature of dark energy. Therefore, the quintessence scalar field must be slowly–rolling down a potential $V(\phi)$, such that the energy scale of the quintessence potential is of the order of around 10^{-47} GeV^4 today (see Eq. (3.23)).

The generic Brans–Dicke type universally coupled model of quintessence, with non–minimally coupled scalar field, is recovered from the Horndeski theory by setting $G_3 = G_5 = 0$, $G_4 = (M_{\rm Pl}^2/2)\, f(\phi)$, and $K = \omega(\phi)X - V(\phi)$, where $\omega(\phi)$ can be considered as a generalised Brans–Dicke coupling parameter. However, the formulation of quintessence models is often expressed in terms of a minimally coupled

quintessence scalar field. This can be easily achieved in these Brans–Dicke type theories by employing a conformal transformation [428], in which the metric is rescaled by a function of the field, such that $g_{\mu\nu} \to f^{-1}(\phi) g_{\mu\nu}$.

This transformation allows for a different representation of the same theory in a different frame. Indeed, the original formulation in which the non–canonical quintessence scalar field was non–minimally coupled to gravity is normally referred to as the Jordan frame, where the matter Lagrangian only depends on the metric with no direct interaction between the scalar field and the matter fields.

After the implementation of the conformal transformation, the theory is now said to be expressed in the Einstein frame, in which the scalar field is now minimally coupled to gravity, thus recovering the standard Einstein–Hilbert formulation in the presence of the scalar field's canonical kinetic term and its potential function. However, in the Einstein frame, matter fields are found to be explicitly coupled to the scalar field through the coupling function $f^{-1}(\phi)$. This can be viewed [428, 446] as an interchange of a space–time varying gravitational constant in the Jordan frame, with a General Relativity type gravitational sector associated to a matter action with field dependent mass and coupling constants in the Einstein frame.

More generally, Horndeski's action has been shown [447] to be formally invariant under a more extensive relation, the so–called disformal transformation, given by

$$g_{\mu\nu} \to C(\phi) g_{\mu\nu} + D(\phi) \partial_\mu \phi \, \partial_\nu \phi \, , \tag{4.6}$$

where the function $C(\phi)$ is the conformal coupling that stems from Brans–Dicke type scalar–tensor theories, whereas the new function $D(\phi)$ is known as the disformal coupling, first introduced by Jacob D. Bekenstein [448]. Therefore, such a generic transformation is mathematically natural to be considered as one of the characteristics of Horndeski's theory. We should point out that, when the disformal transformation was introduced in the context of Finsler geometry [448], a more general disformal transformation was presented, namely

$$g_{\mu\nu} \to C(\phi, X) g_{\mu\nu} + D(\phi, X) \partial_\mu \phi \, \partial_\nu \phi \, . \tag{4.7}$$

Motivated by the simpler case that a disformally–transformed gravitational theory still belongs to a class of Horndeski's theory [447], we will adopt the disformal relation specified in Eq. (4.6).

From the perspective of scalar–tensor theories, the elementary quintessence models can be considered as phenomenological in their origin[1]. This is due to the fact

[1] A more simplistic approach to the quintessence model formulation is to consider $G_3 = G_5 = 0$, $G_4 = M_{\rm Pl}^2/2$, and $K = X - V(\phi)$ in the Horndeski action, in which matter is automatically decoupled from the scalar field. We decided to adopt the approach described in the main text, in order to introduce the coupling functions from the conventional scalar–tensor theories.

that, although the scalar–gravitational sector of the Lagrangian is simply assumed to have the same formulation as the Einstein frame Brans–Dicke type scalar–tensor theory, the matter Lagrangian is further assumed to be completely decoupled from the quintessence scalar field. Thus, minimally coupled quintessence models can be viewed as the conformally transformed Einstein frame Brans–Dicke type scalar–tensor theories, but without the non–minimal coupling to the matter fields. These minimally coupled quintessence models were shown to shed some light on the classical problems attributed to the cosmological constant as described in chapter 3, particularly the coincidence problem. Certain enticing formulations of the minimally coupled quintessence models, were able to partially alleviate the coincidence problem via the tracker [329, 449] and scaling [450–453] attractor solutions. These solutions allow for a wide range of initial conditions such that the dynamical evolution of the scalar field will rapidly join a well–defined late–time behaviour in accordance with cosmological observations. Moreover, non–minimally coupled quintessence [453–456] along with a number of high energy physics inspired quintessence models, such as in the frameworks of cosmic strings [457], pseudo–Nambu–Goldstone bosons [458], supersymmetry [459, 460], and supergravity [461–464], have been put forward.

From the field–theoretical side, there is no reason to believe that the quintessence scalar field is decoupled from the rest of the world, unless there is a symmetry which forbids coupling to the standard model fields [465]. In the simplest scenario, the scalar field only couples non–minimally to dark matter, which is addressed with the so–called coupled quintessence models that will thoroughly be discussed in chapters 5 and 6.

In this chapter we will examine the possibility of a quintessence scalar field to be coupled differently to two different fluids, such as dust and radiation or two dust components. The first proposals which considered the possibility of a scalar field directly coupled to matter were reported in Refs. [466–469]. To couple the scalar field in a non–trivial way to matter, it is usually assumed that matter feels a different metric than the one that describes the gravitational sector. For instance, dark matter particles could propagate such that their geodesics are with respect to a metric $\tilde{g}_{\mu\nu}$, which is related to the gravitational metric via the above conformal and disformal transformations.

The aim of this chapter is to provide a comprehensive dynamical systems analysis of models which allow for disformal couplings of a scalar field to matter, along with the cosmological implications. Dynamical systems techniques provide powerful tools to classify all solutions of the system in terms of fixed points that are independent of the initial conditions. Thus, one could analytically determine the final state of the Universe from a given set of initial conditions. Thence, we will derive the fixed points for the different cases that will be considered in the following sections, and evaluate the conditions for their existence and stability. In particular, we will recover

all results from the literature, but extend those where necessary, and discuss the two–fluid case in the presence of disformal couplings, which we reported for the first time in Ref. [1].

In the next section, we present the model and the equations of motion in full generality. In section 4.2 we introduce the equations of the dynamical system, and solve for a single fluid case with arbitrary equation of state in section 4.3. In section 4.4 we present the different cases with two fluids. The cosmological consequences are discussed in section 4.5, and in section 4.6 we present and analyse a model which predicts a variation of the electromagnetic fine–structure constant, to which we also apply our fixed point solutions. We give our conclusions in section 4.7.

4.1 Cosmological model

We consider a scalar–tensor theory in the Einstein frame with action

$$\mathcal{S} = \int \mathrm{d}^4x\sqrt{-g}\left[\frac{M_{\rm Pl}^2}{2}R - \frac{1}{2}g^{\mu\nu}\partial_\mu\phi\partial_\nu\phi - V(\phi)\right] + \sum_i \mathcal{S}_i\left[\tilde{g}^i_{\mu\nu}, \chi_i\right], \tag{4.8}$$

where the fields χ_i propagate on geodesics defined by the metrics

$$\tilde{g}^i_{\mu\nu} = C_i(\phi)g_{\mu\nu} + D_i(\phi)\partial_\mu\phi\partial_\nu\phi\,, \tag{4.9}$$

with $C_i(\phi)$, $D_i(\phi)$ being the conformal and disformal coupling functions, respectively. The introduction of disformal couplings is the simplest extension of the models discussed in the literature which are based on conformal couplings only. But we should mention that the simple look of the action above is deceiving: if we were to study the theory in the frame in which ordinary matter is decoupled from the scalar field, the theory in this frame is a Horndeski type theory, in which the scalar field is in general coupled disformally to all other matter forms [447, 470]. Furthermore, the action above can also be motivated from a higher–dimensional setup, in which dark matter is confined on a slow–moving brane moving in a higher–dimensional space [471]. In such a model, which is studied in the next chapter, the scalar field describes the position of the brane and dark matter is coupled disformally. Moreover, working in the Einstein frame will significantly simplify our computations. Hopefully, this will become clear as we unveil the calculations. Variation of the action (4.8) with respect to the metric $g_{\mu\nu}$, leads to the field equations in the Einstein frame

$$G_{\mu\nu} = R_{\mu\nu} - \frac{1}{2}g_{\mu\nu}R = \kappa^2\left(T^\phi_{\mu\nu} + \sum_i T^i_{\mu\nu}\right)\,, \tag{4.10}$$

where we recall that $G_{\mu\nu}$ is the Einstein tensor, $R_{\mu\nu}$ is the Ricci tensor, R is the Ricci scalar, and $\kappa^2 = M_{\rm Pl}^{-2} = 8\pi G$, such that $M_{\rm Pl} = 2.4 \times 10^{18}$ GeV is the reduced Planck mass. The energy–momentum tensors for the scalar field ϕ, and the other fields χ_i, are defined by

$$T^{\phi}_{\mu\nu} = \partial_\mu\phi\partial_\nu\phi - g_{\mu\nu}\left(\frac{1}{2}g^{\rho\sigma}\partial_\rho\phi\partial_\sigma\phi + V(\phi)\right) , \tag{4.11}$$

$$T^{i}_{\mu\nu} = -\frac{2}{\sqrt{-g}}\frac{\delta\left(\sqrt{-\tilde{g}^i}\tilde{\mathcal{L}}_i\right)}{\delta g^{\mu\nu}} , \tag{4.12}$$

respectively. The equation of motion of the scalar field simplifies to the following equation

$$\Box\phi = V_{,\phi} - \sum_i Q_i , \tag{4.13}$$

where $V_{,\phi} = {\rm d}V/{\rm d}\phi$, and

$$Q_i = \frac{C_{i,\phi}}{2C_i}T_i + \frac{D_{i,\phi}}{2C_i}T_i^{\mu\nu}\nabla_\mu\phi\nabla_\nu\phi - \nabla_\mu\left[\frac{D_i}{C_i}T_i^{\mu\nu}\nabla_\nu\phi\right] , \tag{4.14}$$

such that T_i is the trace of $T_i^{\mu\nu}$. The Einstein tensor is divergenceless (see chapter 1), but in our theory this does not imply that all $(i+1)$ energy–momentum tensors on the right hand side of Eq. (4.10) are independently conserved. Indeed, we find the following conservation equation for each i–component

$$\nabla^\mu T^i_{\mu\nu} = Q_i\nabla_\nu\phi . \tag{4.15}$$

On specifying a perfect fluid energy–momentum tensor for each i–component,

$$T_i^{\mu\nu} = (\rho_i + p_i)u^\mu u^\nu + p_i g^{\mu\nu} , \tag{4.16}$$

where ρ_i and p_i are the Einstein frame $i^{\rm th}$ fluid energy density and pressure respectively, we find the following modified conservation equation

$$u^\mu\nabla_\mu\rho_i + (\rho_i + p_i)\nabla_\mu u^\mu = -Q_i u^\mu\nabla_\mu\phi , \tag{4.17}$$

after projecting Eq. (4.15) along the four–velocity u^μ. From now on we will consider the standard flat Friedmann–Lemaître–Robertson–Walker (FLRW) metric, such that ${\rm d}s^2 = -{\rm d}t^2 + a^2(t)\delta_{ij}{\rm d}x^i{\rm d}x^j$ (see section 1.2.1), as our Einstein frame metric, with cosmic scale factor $a(t)$. Furthermore, for background cosmology, a time–dependent scalar field is considered, and we denote a coordinate time derivative by a dot. In

this setting, the modified Klein–Gordon equation, fluid conservation equation, and Friedmann equations simplify as follows

$$\ddot{\phi} + 3H\dot{\phi} + V_{,\phi} = \sum_i Q_i \,, \tag{4.18}$$

$$\dot{\rho}_i + 3H\rho_i(1+w_i) = -Q_i\dot{\phi} \,, \tag{4.19}$$

$$H^2 = \frac{\kappa^2}{3}\left(\rho_\phi + \sum_i \rho_i\right), \tag{4.20}$$

$$\dot{H} = -\frac{\kappa^2}{2}\left(\rho_\phi(1+w_\phi) + \sum_i \rho_i(1+w_i)\right), \tag{4.21}$$

where we define the field's energy density as $\rho_\phi = \frac{1}{2}\dot{\phi}^2 + V(\phi)$, its pressure as $p_\phi = \frac{1}{2}\dot{\phi}^2 - V(\phi)$, and the equation of state parameters for the field and fluids are $w_\phi = p_\phi/\rho_\phi$, and $w_i = p_i/\rho_i$, respectively. Since we will be interested in the Einstein frame dynamics of the scalar field in the presence of radiation and matter, we remark that for an FLRW cosmology with two perfect fluids coupled to the scalar field, it can be found that [472]

$$Q_1 = \frac{\mathcal{A}_2}{\mathcal{A}_1\mathcal{A}_2 - D_1D_2\rho_1\rho_2}\left(\mathcal{B}_1 - D_1\rho_1\frac{\mathcal{B}_2}{\mathcal{A}_2}\right) \,, \tag{4.22}$$

$$Q_2 = \frac{\mathcal{A}_1}{\mathcal{A}_1\mathcal{A}_2 - D_1D_2\rho_1\rho_2}\left(\mathcal{B}_2 - D_2\rho_2\frac{\mathcal{B}_1}{\mathcal{A}_1}\right) \,, \tag{4.23}$$

where

$$\mathcal{A}_i = C_i + D_i\left(\rho_i - \dot{\phi}^2\right) \,, \tag{4.24}$$

$$\mathcal{B}_i = \left[\frac{1}{2}C_{i,\phi}(-1+3w_i) - \frac{1}{2}D_{i,\phi}\dot{\phi}^2 + D_i\left(3(1+w_i)H\dot{\phi} + V_{,\phi} + \frac{C_{i,\phi}}{C_i}\dot{\phi}^2\right)\right]\rho_i \,. \tag{4.25}$$

4.2 Dynamical system analysis

We are now going to reduce the above system of equations to a set of first order autonomous differential equations. We first introduce the variables

$$x^2 \equiv \frac{\kappa^2\phi'^2}{6}\,, \qquad y^2 \equiv \frac{\kappa^2 V}{3H^2}\,, \qquad z_i^2 \equiv \frac{\kappa^2\rho_i}{3H^2}\,, \qquad \lambda_V \equiv -\frac{1}{\kappa}\frac{V_{,\phi}}{V}\,, \tag{4.26}$$

$$\lambda_C^i \equiv -\frac{1}{\kappa}\frac{C_{i,\phi}}{C_i}\,, \qquad \lambda_D^i \equiv -\frac{1}{\kappa}\frac{D_{i,\phi}}{D_i}\,, \qquad \sigma_i \equiv \frac{D_i H^2}{\kappa^2 C_i}\,, \tag{4.27}$$

where we use the number of e–folds $N = \ln a(t)$, instead of the Einstein frame coordinate time t, as the time coordinate, and denote derivatives with respect to N by a prime. In these new variables the Friedmann–scalar field system of equations can be written as follows

$$x' = -\left(3 + \frac{H'}{H}\right)x + \sqrt{\frac{3}{2}}\left(\lambda_V y^2 + \frac{\kappa Q_1}{3H^2} + \frac{\kappa Q_2}{3H^2}\right)\,, \tag{4.28}$$

$$y' = -\sqrt{\frac{3}{2}}\left(\lambda_V x + \sqrt{\frac{2}{3}}\frac{H'}{H}\right)y\,, \tag{4.29}$$

$$z_i' = -\frac{3}{2}\left(1 + w_i + \frac{2}{3}\frac{H'}{H} + \frac{1}{3}\sqrt{\frac{2}{3}}\frac{\kappa Q_i}{H^2}\frac{x}{z_i^2}\right)z_i\,, \tag{4.30}$$

$$\sigma_i' = \left(\sqrt{6}\left(\lambda_C^i - \lambda_D^i\right)x + 2\frac{H'}{H}\right)\sigma_i\,, \tag{4.31}$$

where

$$\frac{H'}{H} = -\frac{3}{2}\left(2x^2 + \sum_{i=1}^{2}(1+w_i)z_i^2\right)\,, \tag{4.32}$$

subject to the Friedmann equation constraint

$$x^2 + y^2 + \sum_{i=1}^{2} z_i^2 = 1\,. \tag{4.33}$$

For two species coupled to the scalar field, we can write

$$\frac{Q_1}{H^2} = \frac{3A_2}{A_1A_2 - 9\sigma_1\sigma_2 z_1^2 z_2^2}\left(\frac{\nu_1}{3z_1^2} - \frac{\nu_2\sigma_1}{A_2}\right) z_1^2 \,, \tag{4.34}$$

$$\frac{Q_2}{H^2} = \frac{3A_1}{A_1A_2 - 9\sigma_1\sigma_2 z_1^2 z_2^2}\left(\frac{\nu_2}{3z_2^2} - \frac{\nu_1\sigma_2}{A_1}\right) z_2^2 \,, \tag{4.35}$$

where

$$A_i \equiv \frac{\mathcal{A}_i}{C_i} = 1 + 3\sigma_i\left(z_i^2 - 2x^2\right) \,, \tag{4.36}$$

$$\nu_i \equiv \frac{\mathcal{B}_i}{C_i H^2} = 3\left[\frac{1}{2}\lambda_C^i(1-3w_i) + 3\sigma_i\left(\left(\lambda_D^i - 2\lambda_C^i\right)x^2 + \sqrt{6}(1+w_i)x - \lambda_V y^2\right)\right]\frac{z_i^2}{\kappa}. \tag{4.37}$$

In what follows, we will be considering exponential forms for C_i, D_i, and V. This ensures that the autonomous system of equations is closed. Indeed, if we choose a different functional form for either one of them, we require a set of evolution equations for the functions $\lambda_{V,C,D}$ [449, 473, 474], or alternatively include the equation $\phi' = \sqrt{6}x/\kappa$ [475] (see appendix A.4). Furthermore, an exponential disformal coupling is motivated from the simplistic conformally coupled quintessence model with an exponential conformal coupling and potential, which is conformally equivalent to Brans–Dicke type Lagrangians [476]. Such exponential potentials occur in a number of particle physics theories [477–479], and have also been studied in the context of cosmological inflation [450, 473]. Other useful quantities are the following

$$\Omega_\phi = x^2 + y^2 \,, \tag{4.38}$$

$$w_\phi = \frac{x^2 - y^2}{x^2 + y^2} \,, \tag{4.39}$$

$$Z_i = \sqrt{1 - 6\sigma_i x^2} \,, \tag{4.40}$$

$$w_i = \tilde{w}_i\left(1 - 6\sigma_i x^2\right) \,, \tag{4.41}$$

where $\tilde{w}_i$ is the equation of state parameter of fluid $i = 1, 2$ in the frame defined by the metric $\tilde{g}^i_{\mu\nu}$. For example, in the case of dust and radiation, $\tilde{w}_i = 0$ and $\tilde{w}_i = 1/3$, respectively. We define Z_i in Eq. (4.40) as follows

$$\sqrt{\frac{-\tilde{g}^i}{-g}} = C_i^2\sqrt{1 + \frac{D_i}{C_i}g^{\mu\nu}\phi_{,\mu}\phi_{,\nu}} = C_i^2 Z_i \,. \tag{4.42}$$

A potential problem for the theory is when $Z_i = 0$ due to a metric singularity. This has been discussed in Ref. [480]. We also define an effective equation of state parameter $w_{\rm eff}$ [481, 482], such that

$$\frac{H'}{H} \equiv -\frac{3}{2}\left(1 + w_{\rm eff}\right) \ , \tag{4.43}$$

which implies that

$$w_{\rm eff} = x^2 - y^2 + w_1 z_1^2 + w_2\left(1 - x^2 - y^2 - z_1^2\right) \ . \tag{4.44}$$

We require $w_{\rm eff} < -1/3$ in order to obtain an accelerated expansion of the Universe (see chapter 1). At a fixed point $(x^c,\ y^c,\ z_i^c,\ \sigma_i^c)$, the dynamical system is at rest, and furthermore the acceleration equation (4.43) implies a power law solution of the scale factor

$$a \propto (t - t_0)^{2/\left[3\left(1+w_{\rm eff}^c\right)\right]} \ , \tag{4.45}$$

where $w_{\rm eff}^c = w_{\rm eff}\left(x^c,\ y^c,\ z_i^c,\ \sigma_i^c\right)$, and t_0 is a constant of integration. When $w_{\rm eff}^c = -1$, the Universe is undergoing eternal de Sitter exponential expansion with a constant Hubble parameter.

4.3 Single fluid–Arbitrary equation of state

For a single fluid with an Einstein frame equation of state parameter w, the relevant equations reduce to the following

$$\begin{aligned} x' =& -3x + \frac{3}{2}\left(1 + \left(\frac{1-w}{1+w}\right)x^2 - y^2\right)(1+w)x + \sqrt{\frac{3}{2}}\lambda_V y^2 \\ &+ \sqrt{\frac{3}{2}}\frac{1 - x^2 - y^2}{1 + 3\sigma\left(1 - 3x^2 - y^2\right)}\left(\frac{1}{2}\lambda_C(1-3w)\right. \\ &\left. + 3\sigma\left(\sqrt{6}x(1+w) - \lambda_V y^2 + (\lambda_D - 2\lambda_C)x^2\right)\right) \ , \end{aligned} \tag{4.46}$$

$$y' = -\sqrt{\frac{3}{2}}\lambda_V xy + \frac{3}{2}\left(1 + \left(\frac{1-w}{1+w}\right)x^2 - y^2\right)(1+w)y \ , \tag{4.47}$$

$$\sigma' = \sqrt{6}\left(\lambda_C - \lambda_D\right)x\sigma - 3\left(1 + \left(\frac{1-w}{1+w}\right)x^2 - y^2\right)(1+w)\sigma \ , \tag{4.48}$$

Name	x	y	σ
(1)	-1	0	0
(2)	1	0	0
(3)	$\frac{\sqrt{2}\beta-\sqrt{2\beta^2-3}}{\sqrt{3}}$	0	$\frac{1}{18}\left(2\beta\left(2\beta+\sqrt{4\beta^2-6}\right)-3\right)$
(4)	$\frac{\sqrt{2}\beta+\sqrt{2\beta^2-3}}{\sqrt{3}}$	0	$\frac{1}{18}\left(2\beta\left(2\beta-\sqrt{4\beta^2-6}\right)-3\right)$
(5)	$\frac{\sqrt{\frac{3}{2}}\gamma}{\alpha(4-3\gamma)+2\beta}$	0	$\frac{(\alpha(4-3\gamma)+2\beta)^2\left(2\alpha^2(4-3\gamma)^2+4\alpha\beta(4-3\gamma)-3(\gamma-2)\gamma\right)}{9(\gamma-1)\gamma(3(6\alpha^2-1)\gamma^2-24\alpha\gamma(2\alpha+\beta)+8(2\alpha+\beta)^2)}$
(6)	$\frac{\sqrt{\frac{2}{3}}\alpha(4-3\gamma)}{\gamma-2}$	0	0
(7)	$\frac{\lambda}{\sqrt{6}}$	$\sqrt{1-\frac{\lambda^2}{6}}$	0
(8)	$\frac{\sqrt{\frac{3}{2}}\gamma}{(4-3\gamma)\alpha+\lambda}$	$\frac{\sqrt{2\alpha^2(4-3\gamma)^2+\alpha(8-6\gamma)\lambda-3(\gamma-2)\gamma}}{\sqrt{2(\alpha(4-3\gamma)+\lambda)^2}}$	0

Table 4.1: Fixed points of the system (4.46)–(4.48) for the single fluid case.

with the Friedmann equation constraint

$$x^2 + y^2 + z^2 = 1 \,, \tag{4.49}$$

where the other variables have the same definition as in the general two fluid case discussed in section 4.2. We remark that for the special case of a pressureless fluid, characterised by $w = 0$, with the following couplings and scalar field potential

$$C(\phi) = e^{2\alpha\kappa\phi} \,, \qquad D(\phi) = \frac{e^{2(\alpha+\beta)\kappa\phi}}{M^4} \,, \qquad V(\phi) = V_0^4 e^{-\lambda\kappa\phi} \,, \tag{4.50}$$

where α, β, λ, M, and V_0 are all considered to be constant, we recover the dynamical system studied in Ref. [480]. The latter parameter V_0, is a mass scale associated with the scalar potential. We will be considering the couplings and scalar field potential as defined in Eq. (4.50), and we will re–parametrise our single fluid equation of state parameter to $\gamma \equiv \tilde{w} + 1$, such that $0 \leq \gamma \leq 2$. We remark that, the above system coincides with the conformally coupled case of Refs. [476, 483] in the limit $\beta \to -\infty$, and the uncoupled system presented in Ref. [450] is recovered when $\beta \to -\infty$ and $\alpha = 0$.

Name	Ω_ϕ	w_ϕ	Z
(1)	1	1	1
(2)	1	1	1
(3)	$\frac{1}{3}\left(\sqrt{2\beta^2-3}-\sqrt{2}\beta\right)^2$	1	0
(4)	$\frac{1}{3}\left(\sqrt{2\beta^2-3}+\sqrt{2}\beta\right)^2$	1	0
(5)	$\frac{3\gamma^2}{2(\alpha(4-3\gamma)+2\beta)^2}$	1	$\sqrt{\frac{\gamma\left(-2\alpha^2(4-3\gamma)^2+4\alpha\beta(3\gamma-4)+3(\gamma-2)\gamma\right)}{(\gamma-1)\left(3\left(6\alpha^2-1\right)\gamma^2-24\alpha\gamma(2\alpha+\beta)+8(2\alpha+\beta)^2\right)}}+1$
(6)	$\frac{2\alpha^2(4-3\gamma)^2}{3(\gamma-2)^2}$	1	1
(7)	1	$\frac{1}{3}\left(\lambda^2-3\right)$	1
(8)	$\frac{\alpha^2(4-3\gamma)^2+\alpha(4-3\gamma)\lambda+3\gamma}{(\alpha(4-3\gamma)+\lambda)^2}$	$\frac{3\gamma^2}{\alpha^2(4-3\gamma)^2+\alpha(4-3\gamma)\lambda+3\gamma}-1$	1

Table 4.2: The cosmological parameters Ω_ϕ and w_ϕ, together with the quantity Z, as respectively defined by Eqs. (4.38), (4.39), and (4.40), for the single fluid case described by the system (4.46)–(4.48).

4.3.1 Fixed points

The fixed points for a single fluid with an arbitrary constant equation of state parameter γ, are found by setting Eqs. (4.46)–(4.48) equal to zero. The fixed points for this system, labelled (1)–(8), are tabulated in Table 4.1. We list the cosmological parameters Ω_ϕ and w_ϕ, along with the variable Z, in Table 4.2. In Table 4.3 we explicitly write down the equation of state parameter dependent fixed points for the particular cases of dust and radiation, since the remaining fixed points are identical to the generic case of Table 4.1. We use the same numbering system for radiation and dust fixed points and label the radiation fixed points by a subscript (r) and the dust fixed points by a subscript (d). For simplicity, we do not rename (1), (2) and (7) for the radiation and dust cases, although we relabel (3) and (4) for the specific cases of dust and radiation, as described above, in order to use them in the two fluid cases discussed in section 4.4. In Table 4.4 we give the effective equation of state together with the required parameter values for accelerated expansion for all dust fixed points. Fixed point (5) is obtained when considering $y = 0$, $\sigma \neq 0$ in Eqs. (4.46) and (4.48) giving, in the generic case, fixed points (3), (4), and (5). For the specific case of dust, only fixed points $(3)_{(d)}$ and $(4)_{(d)}$ are obtained, ending up with seven fixed points which coincide with the fixed points found in Ref. [480]. As expected, for radiation, characterised by $\gamma = 4/3$, we obtain the full set of eight fixed points.

4.3.1.1 Existence conditions

For this analysis we will be using the fact that $0 \leq \Omega_\phi \leq 1$, such that the fluid energy density is non–negative $\rho \geq 0$. As already mentioned, we will be considering $0 \leq \gamma \leq 2$, and that $\{x,\ y,\ \sigma,\ Z\} \in \mathbb{R}$.

Arbitrary equation of state

We will now make some remarks on the existence of the fixed points (1)–(8) found in Table 4.1.

- *Kination*: Fixed points (1) and (2) always exist as they are independent of the introduced parameters. These scalar field kinetic dominated solutions are characterised by a stiff equation of state of $w_\phi = 1$, and as expected there is no metric singularity as $Z = 1$.

- *Disformal*: For the disformal fixed points (3) and (4), we find that $\beta \geq \sqrt{3/2}$ for (3) and $\beta \leq -\sqrt{3/2}$ for (4). Both points give a stiff fluid with a metric singularity as $Z = 0$, and they are found to be independent from the fluid equation of state parameter, although, as we will see, their stability does depend on γ.

- *Mixed*: As already remarked in the beginning of this section, (5) is not defined for dust, and this fixed point does not exist for the choice of $\gamma = 0$. The allowed parameter values of α, β and γ must satisfy the inequality $3\gamma^2 < 2\left(\alpha(4-3\gamma)+2\beta\right)^2$ together with the condition $Z \in \mathbb{R}$. This disformal fixed point is also characterised by a stiff fluid ($w_\phi = 1$), although in this case we can avoid the metric singularity if we choose the right parameter values, such that $Z \in \mathbb{R} \setminus \{0\}$.

- *Conformal kinetic*: In order to define a finite x–coordinate of (6), we restrict the range of γ to $0 \leq \gamma < 2$. For $\gamma = 4/3$, all parameter values are allowed, although we end up with an indeterminate value of w_ϕ. For $\gamma \neq 4/3$, the solution is characterised by a stiff fluid. The existence of this fixed point is as

Name	x	y	σ	Ω_ϕ	w_ϕ	Z
$(5)_{(r)}$	$\frac{\sqrt{\frac{2}{3}}}{\beta}$	0	$\frac{\beta^2}{3\beta^2-2}$	$\frac{2}{3\beta^2}$	1	$\sqrt{1+\frac{4}{2-3\beta^2}}$
$(6)_{(d)}$	$-\sqrt{\frac{2}{3}}\alpha$	0	0	$\frac{2\alpha^2}{3}$	1	1
$(6)_{(r)}$	0	0	0	0	-	1
$(8)_{(d)}$	$\sqrt{\frac{3}{2}}\frac{1}{\alpha+\lambda}$	$\frac{\sqrt{3+2\alpha(\alpha+\lambda)}}{\sqrt{2(\alpha+\lambda)^2}}$	0	$\frac{3+\alpha(\alpha+\lambda)}{(\alpha+\lambda)^2}$	$-1+\frac{3}{3+\alpha(\alpha+\lambda)}$	1
$(8)_{(r)}$	$2\sqrt{\frac{2}{3}}\frac{1}{\lambda}$	$\frac{2}{\sqrt{3\lambda^2}}$	0	$\frac{4}{\lambda^2}$	$\frac{1}{3}$	1

Table 4.3: The equation of state parameter dependent fixed points of the system (4.46)–(4.48), in the single fluid case, specified for dust and radiation, along with the respective cosmological parameters.

follows

$$\text{For } \gamma \in [0, 4/3) \cup (4/3, 2) \,, \qquad \alpha^2 < \frac{3(\gamma-2)^2}{2(4-3\gamma)^2} \,,$$
$$\text{For } \gamma = \frac{4}{3} \,, \qquad \forall \alpha \,.$$

- *Scalar field dominated*: For fixed point (7) we find that this is defined if $\lambda^2 < 6$. This is a scalar field dominated solution ($\Omega_\phi = 1$) with a scalar field equation of state parameter $w_\phi = -1 + \lambda^2/3$.

- *Conformal scaling*: For the last fixed point (8), we require the following inequalities to be satisfied in order to be defined

$$\alpha^2(4-3\gamma)^2 + \alpha(4-3\gamma)\lambda > -\frac{3}{2}\gamma(2-\gamma) \,,$$
$$\alpha(4-3\gamma)\lambda > 3\gamma - \lambda^2 \,.$$

  In the absence of the conformal coupling ($\alpha = 0$), (8) is a cosmological scaling solution [325, 450, 483], such that $w_\phi = \gamma - 1$.

Quantity	(1)	(2)	$(3)_{(d)}$	$(4)_{(d)}$	$(6)_{(d)}$	(7)	$(8)_{(d)}$
w_{eff}	1	1	Ω_ϕ	Ω_ϕ	$\frac{2\alpha^2}{3}$	$\frac{\lambda^2}{3}-1$	$\frac{-\alpha}{\alpha+\lambda}$
Acceleration	No	No	No	No	No	$\lambda^2<2$	$\lambda \leq -\sqrt{2}\,,\ \alpha<\lambda/2$, or, $-\sqrt{2}<\lambda<0\,,\ \alpha<\left(3-\lambda^2\right)/\lambda$, or, $0<\lambda<\sqrt{2}\,,\ \alpha>\left(3-\lambda^2\right)/\lambda$, or, $\lambda \geq \sqrt{2}\,,\ \alpha>\lambda/2$

Table 4.4: The effective equation of state w_{eff}, together with the required parameter values for an accelerated expansion, for all dust fixed points $(1)-(8)_{(d)}$. We take into consideration the existence of the fixed point when determining the required parameters for acceleration.

We shall now consider the existence of the dust ($\gamma=1$) fixed points, denoted by the index (d), and radiation ($\gamma=4/3$) fixed points, denoted by the index (r);

Dust ($\gamma=1$)

The existence arguments for fixed points (1)–(4) found in Table 4.1 also hold for (1), (2), $(3)_{(d)}$, $(4)_{(d)}$, respectively. Furthermore, the existence of (7) is equivalent to the general case. Regarding the conformal kinetic dominated fixed point $(6)_{(d)}$, we require that $\alpha^2<3/2$. For the last fixed point $(8)_{(d)}$, we require that $\alpha(\alpha+\lambda)>-3/2$ and $\lambda(\alpha+\lambda)>3$. We note that for non–negative values of α, λ and β, this analysis coincides with that of Ref. [480].

Radiation ($\gamma=4/3$)

Similar to the dust case, the first four radiation fixed points and (7) are respectively equivalent to (1)–(4) and (7) found in Table 4.1, hence the existence of these fixed points follows from the general fluid discussion. For fixed point $(5)_{(r)}$, we find that we require $\beta^2>2$ in order to satisfy the condition $\Omega_\phi<1$, and that the coupling between the two disformally related metrics Z, is made sure to be real valued. This solution is characterised by a stiff fluid equation of state, and for $\beta^2>2$, the radiation and Einstein frame metrics are both well–defined without a singularity. The radiation fluid dominated solution $(6)_{(r)}$, always exists, irrespective of the parameter values. It is characterised by an indeterminate scalar field equation of state. The last radiation fixed point $(8)_{(r)}$, is a scaling solution which exists when $\lambda^2>4$.

4.3.1.2 Stability conditions

We now study the stability of the fixed points by analysing the eigenvalues of the matrix $\mathcal{M}$, which is constructed after considering a small perturbation around each fixed point. In what follows, no zero eigenvalues are obtained, and hence the Hartman–Grobman theorem [484] guarantees that the stability around a fixed point can be studied by the linear approximation (see for example Refs. [474, 480]).

We here briefly point out the adopted method for the computation of the eigenvalues that is implemented for all the cases that are considered in this chapter. For this purpose, we will consider a general system of n first–order ordinary differential equations for n variables X_i, as a function of some arbitrary coordinate t. Since all considered systems are autonomous, we will consider this generic system to be of the same type. Hence, the generic system can be expressed as follows

$$\frac{\mathrm{d}X_i}{\mathrm{d}t} = f_i(\{X_j\}) \,. \tag{4.51}$$

We define the fixed points $\{X_j^c\}$, of our system to be the solutions of the n algebraic equations when we set $f_i = 0\ \forall i$. By considering a small perturbation δX_i, around a fixed point X_i^c, thence considering a point $X_i = X_i^c + \delta X_i$, one obtains, up to first order

$$\frac{\mathrm{d}\delta X_i}{\mathrm{d}t} = \mathcal{M}_{ij}\delta X_j, \text{ where, } \mathcal{M}_{ij} = \frac{\partial f_i}{\partial X_j} \,. \tag{4.52}$$

The eigenvalues that are used in order to study the stability of the fixed points correspond to the eigenvalues of the $n \times n$ matrix $\mathcal{M}_{ij}$, evaluated at the fixed point X_i^c. For example, for the single fluid system with equation of state parameter γ, described by the system (4.46)–(4.48) together with Eq. (4.50), the matrix elements of the 3×3 matrix $\mathcal{M}_{ij}$, reduce to the following

$$\begin{aligned}
\mathcal{M}_{11} = &-3 + \frac{3}{2}\left(1 - x^2 - y^2\right)\left(\gamma - 18(\gamma-1)\sigma x^2\right) + 3x^2\left(3 - \gamma + 6(\gamma-1)\sigma x^2\right) \\
&+ \sqrt{\frac{3}{2}}\frac{-2x + 12\sigma x(1-y^2)}{(1 + 3\sigma(1 - 3x^2 - y^2))^2}\Bigg((3\gamma - 18(\gamma-1)\sigma x^2 - 4)\alpha \\
&+3\sigma\left(\sqrt{6}x(\gamma - 6(\gamma-1)\sigma x^2) - \lambda y^2 + 2(\alpha-\beta)x^2\right)\Bigg) \\
&+ \sqrt{\frac{3}{2}}\frac{1 - x^2 - y^2}{1 + 3\sigma(1 - 3x^2 - y^2)}\Bigg(-36(\gamma-1)\alpha x\sigma \\
&+3\sigma\left(\sqrt{6}(\gamma - 18(\gamma-1)\sigma x^2) + 4(\alpha-\beta)x\right)\Bigg) \,,
\end{aligned}$$

$$\mathcal{M}_{12} = 3xy\left(6(\gamma-1)\sigma x^2-\gamma\right)+\sqrt{6}\lambda y$$
$$+\sqrt{\frac{3}{2}}\frac{-2y+12\sigma y x^2}{\left(1+3\sigma(1-3x^2-y^2)\right)^2}\Big(\left(3\gamma-18(\gamma-1)\sigma x^2-4\right)\alpha$$
$$+3\sigma\left(\sqrt{6}x\left(\gamma-6(\gamma-1)\sigma x^2\right)-\lambda y^2+2(\alpha-\beta)x^2\right)\Big)$$
$$+3\sqrt{6}\frac{\left(x^2+y^2-1\right)\lambda\sigma y}{1+3\sigma\left(1-3x^2-y^2\right)}\,,$$

$$\mathcal{M}_{13} = 9(\gamma-1)\left(x^2+y^2-1\right)x^3+\sqrt{\frac{3}{2}}\frac{1-x^2-y^2}{1+3\sigma\left(1-3x^2-y^2\right)}\Big(-18(\gamma-1)\alpha x^2$$
$$-36\sqrt{6}(\gamma-1)\sigma x^3+3\left(\sqrt{6}\gamma x-\lambda y^2+2(\alpha-\beta)x^2\right)\Big)$$
$$-\sqrt{\frac{3}{2}}\frac{3\left(1-3x^2-y^2\right)\left(1-x^2-y^2\right)}{\left(1+3\sigma\left(1-3x^2-y^2\right)\right)^2}\Big(\left(3\gamma-18(\gamma-1)\sigma x^2-4\right)\alpha$$
$$+3\sigma\left(\sqrt{6}x\left(\gamma-6(\gamma-1)\sigma x^2\right)-\lambda y^2+2(\alpha-\beta)x^2\right)\Big)\,,$$

$$\mathcal{M}_{21} = -\sqrt{\frac{3}{2}}\lambda y-18(\gamma-1)\sigma xy\left(1-x^2-y^2\right)+3xy\left(2-\gamma+6(\gamma-1)\sigma x^2\right)\,,$$

$$\mathcal{M}_{22} = -\sqrt{\frac{3}{2}}\lambda x+\frac{3}{2}\left(\gamma-6(\gamma-1)\sigma x^2\right)\left(1-3y^2\right)+\frac{3}{2}\left(2-\gamma+6(\gamma-1)\sigma x^2\right)x^2\,,$$

$$\mathcal{M}_{23} = 9(\gamma-1)\left(x^2+y^2-1\right)x^2y\,,$$

$$\mathcal{M}_{31} = 2\sqrt{6}\beta\sigma+36(\gamma-1)\sigma^2x\left(1-x^2-y^2\right)+6\sigma x\left(\gamma-2-6(\gamma-1)\sigma x^2\right)\,,$$

$$\mathcal{M}_{32} = 6\sigma y\left(\gamma-6(\gamma-1)\sigma x^2\right)\,,$$

$$\mathcal{M}_{33} = 2\sqrt{6}\beta x-6x^2-3\left(1-x^2-y^2\right)\left(\gamma-12(\gamma-1)\sigma x^2\right)\,.$$

For completeness, we further present the full generic set of eigenvalues denoted by $e_{1,2,3}$, in appendix A.1. Since our system is three–dimensional and not two–

dimensional, as in the purely conformal scenario, the stability analysis will be different from the lower dimensional system. In the following, we will restrict our stability analysis to the dust and radiation cases only, as in the general fluid case there is freedom in four parameters. This is due to the fact that, even if the fixed points are independent from the disformal coupling, the eigenvalues can still contain β.

Dust ($\gamma = 1$)

- (1): this can either be a stable node, an unstable node or a saddle point depending on the chosen values of α, β and λ. It is a stable node if $\beta > -\sqrt{3/2}$, $\lambda < -\sqrt{6}$ and $\alpha > \sqrt{3/2}$. Consequently, this fixed point can become stable when a disformal coupling is introduced. Also, in our analyses we find that the introduction of a disformal coupling widens up the region of parameter space that renders a fixed point stable. In the following, we consider a fixed point to be unstable whenever it is neither stable nor a saddle point.

- (2): similarly, the other scalar field kinetic dominated fixed point can either be a stable node, an unstable node or a saddle point according to the chosen parameter values. It is a stable node if $\beta < \sqrt{3/2}$, $\lambda > \sqrt{6}$ and $\alpha < -\sqrt{3/2}$.

- $(3)_{(d)}$: it is either a stable node or a saddle point. Indeed, we find that this is a stable point if $\beta > \sqrt{3/2}$, $\alpha < -\beta + \sqrt{(-3+2\beta^2)/2}$ and $\lambda > 2\beta$.

- $(4)_{(d)}$: the remaining disformal fixed point can either be a stable node or a saddle point. It is stable if $\beta < -\sqrt{3/2}$, $\alpha > -\beta - \sqrt{(-3+2\beta^2)/2}$ and $\lambda < 2\beta$.

- $(6)_{(d)}$: the conformal kinetic dust solution can either be a stable node or a saddle point. It cannot be an unstable fixed point as $e_1 < 0$ when $-\sqrt{3/2} < \alpha < \sqrt{3/2}$. It is found to be stable in the following regions

$$-\sqrt{\frac{3}{2}} < \alpha < 0\,, \qquad \lambda > \frac{-3-2\alpha^2}{2\alpha}\,, \qquad \beta < \frac{-3-2\alpha^2}{4\alpha}\,,$$

$$\text{or,} \qquad 0 < \alpha < \sqrt{\frac{3}{2}}\,, \qquad \lambda < \frac{-3-2\alpha^2}{2\alpha}\,, \qquad \beta > \frac{-3-2\alpha^2}{4\alpha}\,.$$

- (7): for parameter values satisfying either one of the following inequalities

$$-\sqrt{6} \;<\; \lambda < 0\,, \qquad \beta > \frac{\lambda}{2}\,, \qquad \alpha > \frac{3-\lambda^2}{\lambda}\,,$$

$$\text{or,} \qquad 0 \;<\; \lambda < \sqrt{6}\,, \qquad \beta < \frac{\lambda}{2}\,, \qquad \alpha < \frac{3-\lambda^2}{\lambda}\,,$$

  we have a stable node, otherwise it is a saddle point. This dust fixed point cannot be unstable, since $e_2 < 0$ for $-\sqrt{6} < \lambda < \sqrt{6}$.

- $(8)_{(d)}$: the conformal scaling fixed point is found to be either a saddle point, a stable spiral, a stable node or a spiral saddle. We show all four distinct natures of this fixed point when $\beta = -0.9,\ 0.5,\ 5$ in Fig. 4.1.

The three–dimensional single fluid system is invariant under $y \to -y$ and furthermore, the $(x,\ y,\ \sigma)$–phase space is non–compact, since $-1 \leq x \leq 1,\ 0 \leq y \leq \sqrt{1-x^2},\ 0 \leq \sigma < \infty$. We restrict the range of σ to non–negative values due to stability problems [480, 485]. We compactify this phase space by introducing the variable $\Sigma = \arctan\sigma$. The phase space is now compact, with $x,\ y,\ \Sigma$ lying in the range $-1 \leq x \leq 1,\ 0 \leq y \leq \sqrt{1-x^2},\ 0 \leq \Sigma < \pi/2$. We are also aware of fixed points at $\Sigma = \pi/2$ [480], although this is beyond the scope of our study. The compactified phase space is described by a semi–circular prism of length $\pi/2$. Furthermore, we can at most have six fixed points for any parameter choice. This is due to the fact that for a particular choice of β, either $(3)_{(d)}$ or $(4)_{(d)}$ exists, but not both at the same time. Two illustrations containing some solution trajectories with different attractors are shown in Fig. 4.2. The $x-y$ plane in these three–dimensional phase spaces, depict the purely conformal case.

Radiation ($\gamma = 4/3$)

- (1): since $e_2 = 2$, then this kination fixed point cannot be stable. Indeed, it can either be an unstable node or a saddle point. It is found to be an unstable node if $\lambda > -\sqrt{6}$ and $\beta < -\sqrt{3/2}$, and it is a saddle point if either $\lambda < -\sqrt{6}$ and $\beta \neq -\sqrt{3/2}$, or if $\lambda > -\sqrt{6}$ and $\beta > -\sqrt{3/2}$.

- (2): the other kination fixed point is found to be an unstable node if $\lambda < \sqrt{6}$ and $\beta > \sqrt{3/2}$. It can also be a saddle point if $\lambda < \sqrt{6}$ and $\beta < \sqrt{3/2}$, or if $\lambda > \sqrt{6}$ and $\beta \neq \sqrt{3/2}$.

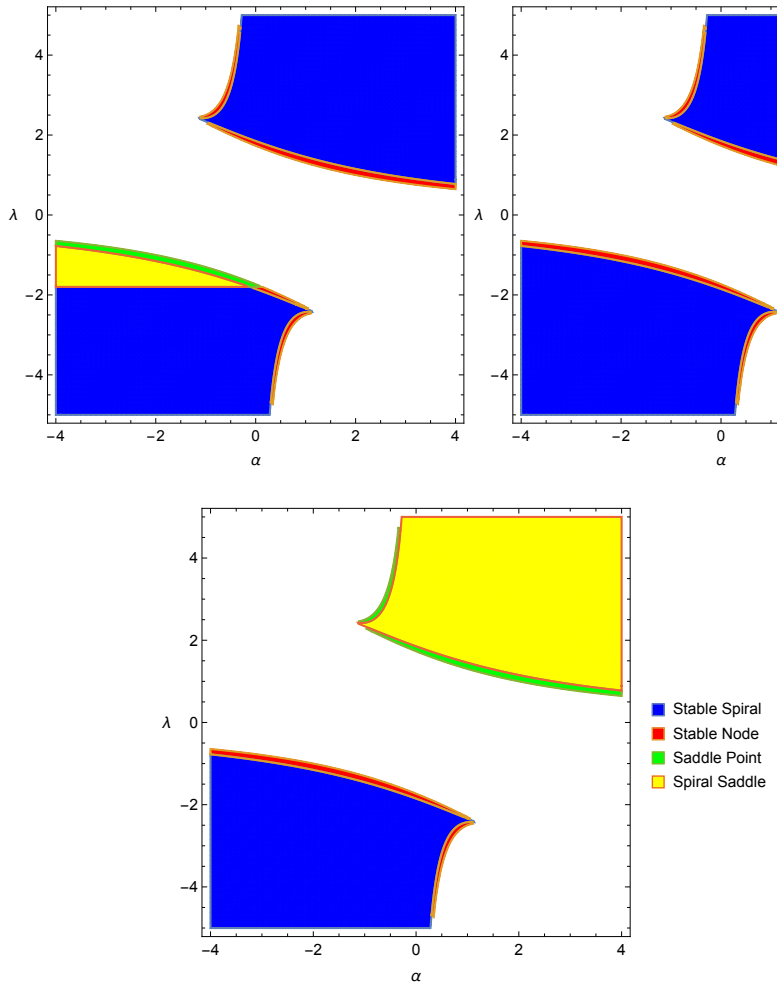

Figure 4.1: The regions show an illustration of the parameter values of α and λ for the dust fixed point $(8)_{(d)}$ when $\beta = -0.9$ (left), $\beta = 0.5$ (right), and $\beta = 5$ (bottom), with each region corresponding to a distinct nature of the fixed point.

- $(3)_{(r)}$: in this case, we can have a stable node for $\beta > \sqrt{2}$ and $\lambda > 2\beta$. It can also be a saddle point for $\beta > \sqrt{2}$ and $\lambda < 2\beta$, or if $\sqrt{3/2} < \beta < \sqrt{2}$, then it is a saddle point when $\lambda \neq 2\beta$.

- $(4)_{(r)}$: this disformal fixed point is a stable node when $\beta < -\sqrt{2}$ and $\lambda < 2\beta$. For $\beta < -\sqrt{2}$ and $\lambda > 2\beta$, together with the other choice of $-\sqrt{2} < \beta < -\sqrt{3/2}$ and $\lambda \neq 2\beta$, we find that $(4)_{(r)}$ is a saddle point.

- $(5)_{(r)}$: the mixed fixed point, which is missing in the case of dust, is found

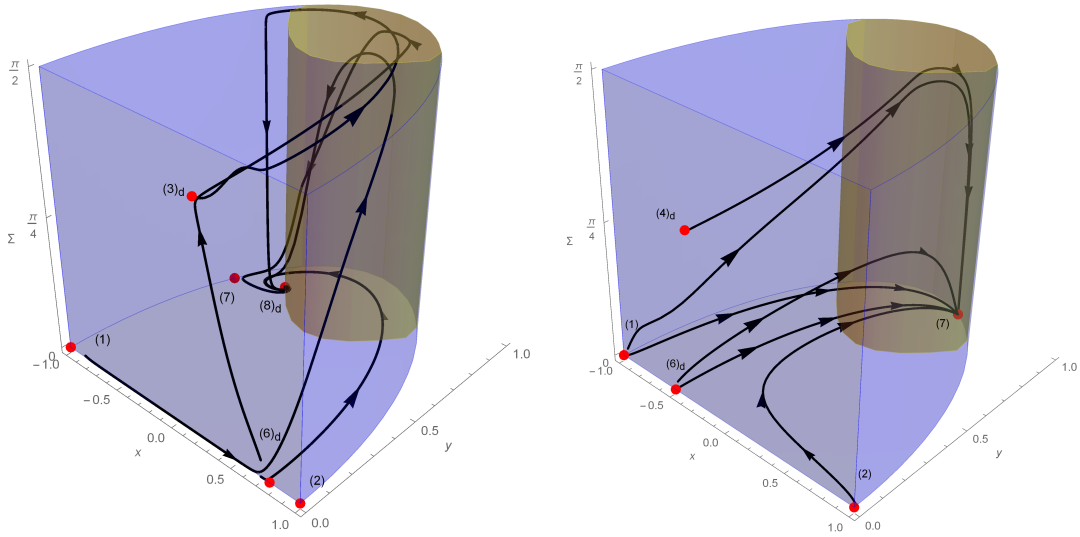

Figure 4.2: In this figure we show the phase space for the single dust case with different attractors. The different solution trajectories correspond to different initial conditions. The blue region is the allowed region, whereas the yellow region is where the Universe undergoes an accelerated expansion. On the left the attractor is $(8)_{(d)}$ with $\alpha = -0.94,\ \beta = 3,\ \lambda = -1.88$, and on the right the attractor is (7) with $\alpha = 0.6,\ \beta = -2,\ \lambda = 0.7$.

to be only a saddle point, since e_1 and e_2 have opposite signs in the available range of β. Indeed, this is true for $\beta < -\sqrt{2}$ such that $\lambda \neq 2\beta$, and for the choice $\beta > \sqrt{2}$ and $\lambda \neq 2\beta$.

- $(6)_{(r)}$: this radiation dominated fixed point is a saddle point, as its eigenvalues are $e_1 = -1,\ e_2 = -4$ and $e_3 = 2$.

- (7): this scalar field dominated fixed point is either a stable node or a saddle point, since $e_2 < 0$ in the fixed point existence range of $-\sqrt{6} < \lambda < \sqrt{6}$. It is found to be stable for $-2 < \lambda < 0$ and $\beta > \lambda/2$, and also when $0 < \lambda < 2$ such that $\beta < \lambda/2$.

- $(8)_{(r)}$: the conformal scaling fixed point cannot be unstable as $\Re(e_2) < 0$ and $\Re(e_3) < 0\ \forall\lambda \in \mathbb{R} \setminus [-2, 2]$. We find that for $2 < \lambda \leq 8/\sqrt{15}$ and $-8/\sqrt{15} \leq \lambda < -2$, it is a stable node for $\beta < \lambda/2$ and $\beta > \lambda/2$ respectively, and it is a saddle point if $\beta > \lambda/2$ and $\beta < \lambda/2$ respectively. For $\lambda > 8/\sqrt{15}$, it is found to be a stable spiral when $\beta < \lambda/2$, and a spiral saddle if $\beta > \lambda/2$.

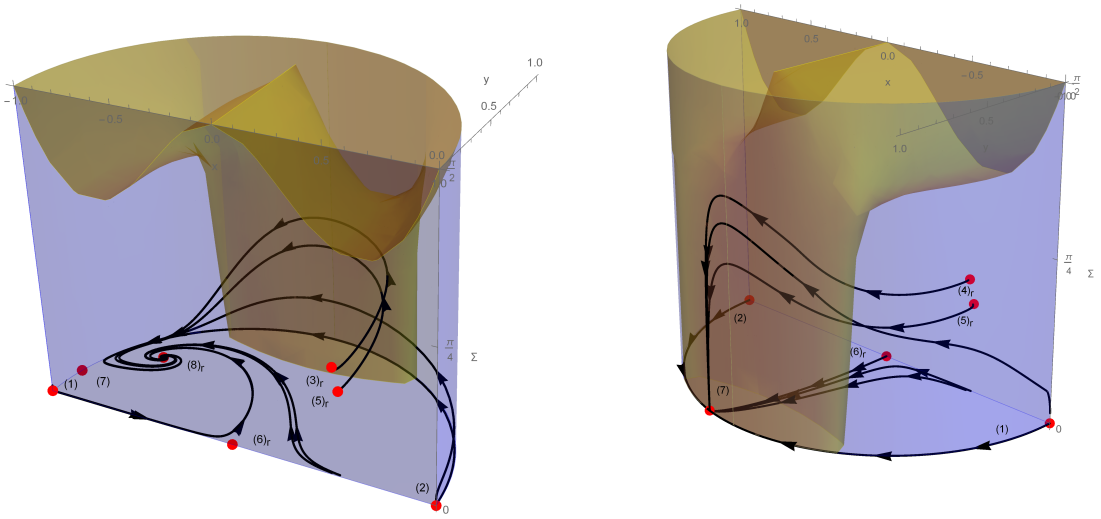

Figure 4.3: In this figure we show the phase space for the radiation single fluid case with different attractors. The different solution trajectories correspond to different initial conditions. The blue region is the allowed region, whereas the yellow region is where the Universe undergoes an accelerated expansion. On the left the attractor is $(8)_{(r)}$ with $\beta = 1.5,\ \lambda = -2.395$, and on the right the attractor is (7) with $\beta = -1.5,\ \lambda = 0.448$.

Similarly, for $\lambda < -8/\sqrt{15}$, $(8)_{(r)}$ is a stable spiral when $\beta > \lambda/2$, and a spiral saddle if $\beta < \lambda/2$.

Similar to the single fluid dust case, we show the phase space together with some solution trajectories in Fig. 4.3. In this case, for any particular choice of the parameters, we can at most have seven fixed points, where two of them are disformal fixed points. We should remark that when either one of the disformal fixed points is the global attractor of the system, it is found that the solution converges very slowly, in agreement with the results found in Ref. [480].

4.4 Two fluids

We will now investigate the dynamical system presented in section 4.2 for a two fluid scenario. Three different particular cases are studied in the sections that follow. In each case, we will be considering at least one conformally–disformally coupled fluid. When the obtained fixed point can be generated from a single fluid system, we will use an identical label to that corresponding to a single fluid fixed point. Despite the fact that the majority of the two fluid fixed points reduce to the single fluid fixed points, our aim is to generalise the conformally coupled fluid system [476, 482, 486] to a conformally–disformally coupled fluid system. Because a generic treatment is

very cumbersome, we will consider in what follows, dust and radiation fluids only.

4.4.1 Two fluids-Conformal–disformal dust & conformal–disformal radiation

In this section, we study the full solution of the two fluid conformal–disformal system presented in section 4.2 for the particular case of dust and radiation perfect fluids, in which we set $\gamma_1 = 1,\ \gamma_2 = 4/3$. This system will be five–dimensional, in which we choose our dynamical variables to be $x,\ y,\ z_1,\ \sigma_1$ and σ_2. In the absence of disformal couplings, this system reduces to the three–dimensional conformally coupled case presented in Ref. [476]. We choose our couplings and scalar field potential to be of exponential forms

$$C_i(\phi) = e^{2\alpha_i \kappa \phi}, \qquad D_i(\phi) = \frac{e^{2(\alpha_i+\beta_i)\kappa\phi}}{M_i^4}, \qquad V(\phi) = V_0^4 e^{-\lambda\kappa\phi}. \tag{4.53}$$

For completeness, we list all fixed points in Table 4.5 together with the corresponding cosmological parameters in Table 4.6. We also include z_2 in Table 4.5 in order to link the single fluid cases studied in section 4.3 with this scenario. We label the new fixed points for this two fluid system which cannot be retrieved from a single fluid system by (a) and (b). We shall refer to fixed point (a) as the *conformal dust radiation* fixed point, which was obtained in Ref. [476], and refer to fixed point (b) as the *disformal dust radiation* fixed point.

4.4.1.1 Existence conditions

In this section we will only comment on the existence of the conformal dust radiation fixed point and the disformal dust radiation fixed point, since the existence of the other fixed points follows from section 4.3.1.1. Indeed, we find that fixed point (a) exists when $\alpha_1^2 > 1/2$, and fixed point (b) exists whenever $\beta_1^2 > 2$.

For the disformal fixed points (b), $(3)_{(d)}$, $(4)_{(d)}$, $(3)_{(r)}$, $(4)_{(r)}$, we can clearly observe that whenever fluid i has a non–zero value of σ_i, the disformal metric transformation reduces to $Z_i = 0$. The mixed disformal fixed point $(5)_{(r)}$, however, avoids the singularity for both metrics.

Name	x	y	z_1	z_2	σ_1	σ_2
(1)	-1	0	0	0	0	0
$(6)_{(r)}$	0	0	0	1	0	0
(2)	1	0	0	0	0	0
(a)	$-\frac{1}{\sqrt{6}\alpha_1}$	0	$\frac{1}{\sqrt{3\alpha_1^2}}$	$\sqrt{1-\frac{1}{2\alpha_1^2}}$	0	0
$(6)_{(d)}$	$-\sqrt{\frac{2}{3}}\alpha_1$	0	$\sqrt{1-\frac{2\alpha_1^2}{3}}$	0	0	0
(b)	$\frac{\sqrt{\frac{2}{3}}}{\beta_1}$	0	$\frac{2}{\sqrt{3\beta_1^2}}$	$\sqrt{1-\frac{2}{\beta_1^2}}$	$\frac{\beta_1^2}{4}$	0
$(3)_{(d)}$	$\frac{\sqrt{2}\beta_1-\sqrt{2\beta_1^2-3}}{\sqrt{3}}$	0	ϵ_1^d	0	ϵ_2^d	0
$(4)_{(d)}$	$\frac{\sqrt{2}\beta_1+\sqrt{2\beta_1^2-3}}{\sqrt{3}}$	0	ϵ_3^d	0	ϵ_4^d	0
$(5)_{(r)}$	$\frac{\sqrt{\frac{2}{3}}}{\beta_2}$	0	0	$\sqrt{1-\frac{2}{3\beta_2^2}}$	0	$\frac{\beta_2^2}{3\beta_2^2-2}$
$(3)_{(r)}$	$\frac{\sqrt{2}\beta_2-\sqrt{2\beta_2^2-3}}{\sqrt{3}}$	0	0	ϵ_1^r	0	ϵ_2^r
$(4)_{(r)}$	$\frac{\sqrt{2}\beta_2+\sqrt{2\beta_2^2-3}}{\sqrt{3}}$	0	0	ϵ_3^r	0	ϵ_4^r
$(8)_{(r)}$	$\frac{2\sqrt{\frac{2}{3}}}{\lambda}$	$\frac{2}{\sqrt{3\lambda^2}}$	0	$\sqrt{1-\frac{4}{\lambda^2}}$	0	0
(7)	$\frac{\lambda}{\sqrt{6}}$	$\sqrt{1-\frac{\lambda^2}{6}}$	0	0	0	0
$(8)_{(d)}$	$\sqrt{\frac{3}{2}}\frac{1}{\alpha_1+\lambda}$	$\sqrt{\frac{3+2\alpha_1(\alpha_1+\lambda)}{2(\alpha_1+\lambda)^2}}$	$\sqrt{\frac{\lambda(\alpha_1+\lambda)-3}{(\alpha_1+\lambda)^2}}$	0	0	0

Table 4.5: The fixed points for the case of conformally–disformally coupled dust and conformally–disformally coupled radiation. The $\epsilon^{d,r}$ terms are as follows: $\epsilon_1^d \equiv \sqrt{\frac{2}{3}}\sqrt{\beta_1\left(\sqrt{4\beta_1^2-6}-2\beta_1\right)+3}$, $\epsilon_2^d \equiv \frac{1}{18}\left(2\beta_1\left(2\beta_1+\sqrt{4\beta_1^2-6}\right)-3\right), \epsilon_3^d \equiv \sqrt{6-2\beta_1\left(2\beta_1+\sqrt{4\beta_1^2-6}\right)}/\sqrt{3}$, $\epsilon_4^d \equiv \frac{1}{18}\left(2\beta_1\left(2\beta_1-\sqrt{4\beta_1^2-6}\right)-3\right), \epsilon_1^r \equiv \sqrt{\frac{2}{3}}\sqrt{\beta_2\left(\sqrt{4\beta_2^2-6}-2\beta_2\right)+3}, \epsilon_2^r \equiv \frac{1}{18}\left(2\beta_2\left(2\beta_2+\sqrt{4\beta_2^2-6}\right)-3\right), \epsilon_3^r \equiv \sqrt{6-2\beta_2\left(2\beta_2+\sqrt{4\beta_2^2-6}\right)}/\sqrt{3}$, and $\epsilon_4^r \equiv \frac{1}{18}\left(2\beta_2\left(2\beta_2-\sqrt{4\beta_2^2-6}\right)-3\right)$.

Name	Ω_ϕ	w_ϕ	Z_1	Z_2	w_{eff}
(1)	1	1	1	1	1
$(6)_{(r)}$	0	-	1	1	$\frac{1}{3}$
(2)	1	1	1	1	1
(a)	$\frac{1}{6\alpha_1^2}$	1	1	1	$\frac{1}{3}$
$(6)_{(d)}$	$\frac{2}{3}\alpha_1^2$	1	1	1	$\frac{2\alpha_1^2}{3}$
(b)	$\frac{2}{3\beta_1^2}$	1	0	1	$\frac{1}{3}$
$(3)_{(d)}$	$\frac{1}{3}\left(-\sqrt{2}\beta_1+\sqrt{2\beta_1^2-3}\right)^2$	1	0	1	$\frac{1}{3}\left(2\beta_1\left(2\beta_1-\sqrt{4\beta_1^2-6}\right)-3\right)$
$(4)_{(d)}$	$\frac{1}{3}\left(\sqrt{2}\beta_1+\sqrt{2\beta_1^2-3}\right)^2$	1	0	1	$\frac{1}{3}\left(2\beta_1\left(2\beta_1+\sqrt{4\beta_1^2-6}\right)-3\right)$
$(5)_{(r)}$	$\frac{2}{3\beta_2^2}$	1	1	$\sqrt{1+\frac{4}{2-3\beta_2^2}}$	$\frac{1}{3}$
$(3)_{(r)}$	$\frac{1}{3}\left(-\sqrt{2}\beta_2+\sqrt{2\beta_2^2-3}\right)^2$	1	1	0	$\frac{1}{3}\left(2\beta_2\left(2\beta_2-\sqrt{4\beta_2^2-6}\right)-3\right)$
$(4)_{(r)}$	$\frac{1}{3}\left(\sqrt{2}\beta_2+\sqrt{2\beta_2^2-3}\right)^2$	1	1	0	$\frac{1}{3}\left(2\beta_2\left(2\beta_2+\sqrt{4\beta_2^2-6}\right)-3\right)$
$(8)_{(r)}$	$\frac{4}{\lambda^2}$	$\frac{1}{3}$	1	1	$\frac{1}{3}$
(7)	1	$\frac{\lambda^2}{3}-1$	1	1	$\frac{\lambda^2}{3}-1$
$(8)_{(d)}$	$\frac{3+\alpha_1(\alpha_1+\lambda)}{(\alpha_1+\lambda)^2}$	$\frac{3}{3+\alpha_1(\alpha_1+\lambda)}-1$	1	1	$-\frac{\alpha_1}{\alpha_1+\lambda}$

Table 4.6: Listed are, respectively, the cosmological parameters Ω_ϕ and w_ϕ, together with Z_1, Z_2, and the effective equation of state parameter w_{eff}, for the fixed points of conformally–disformally coupled dust and conformally–disformally coupled radiation.

4.4.1.2 Stability conditions

We will now discuss the region in which the above fixed points are found to be stable by using the eigenvalues $e_{1,2,3,4,5}$ [2]. We only discuss the regions in which the fixed point is found to be stable.

[2] These eigenvalues are not all included in the text due to the length of the algebraic expressions. We only write down the eigenvalues of the new fixed points (a) and (b) in appendix A.2.1.

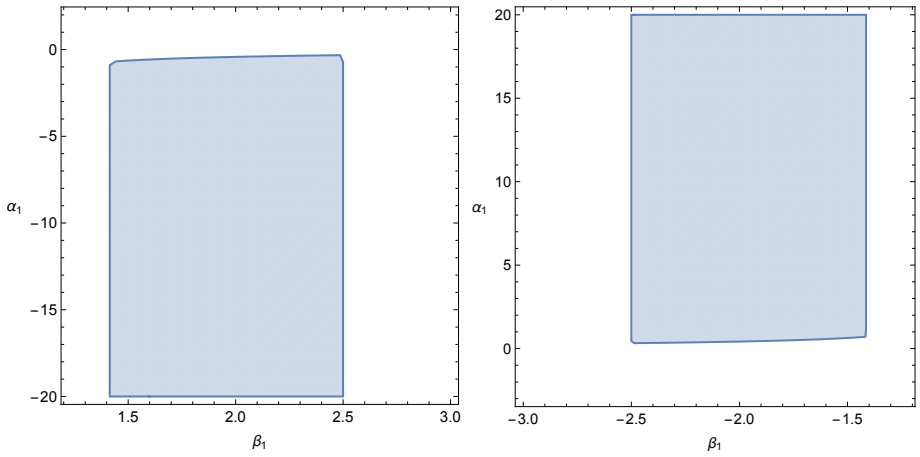

Figure 4.4: The stable node regions for the case of conformal–disformal dust and conformal–disformal radiation, illustrating the parameter values of α_1 and β_1 for fixed points $(3)_{(d)}$ (left), and $(4)_{(d)}$ (right). The other free parameters for $(3)_{(d)}$ are chosen to be $(\beta_2, \lambda) = (0.5, 5)$, and we set the parameters for $(4)_{(d)}$ to $(\beta_2, \lambda) = (0.5, -5)$, so that all eigenvalues have a negative real part.

- The kinetic dominated fixed points (1) and (2) cannot be stable since $e_1 = 2$, for both of them. Also, the radiation dominated fixed point $(6)_{(r)}$, is found to be a saddle point since $e_1,\ e_2,\ e_4 < 0$ and $e_3,\ e_5 > 0$.

- The conformal dust radiation fixed point (a), can either be a stable node or a stable spiral. Indeed, it is found to be a stable node when either of the following conditions are satisfied

$$-\sqrt{\frac{2}{3}} \leq \alpha_1 < -\frac{1}{\sqrt{2}}\,, \qquad \beta_1 < -2\alpha_1\,, \qquad \beta_2 < -2\alpha_1\,, \qquad \lambda > -4\alpha_1\,,$$

$$\text{or,} \qquad \frac{1}{\sqrt{2}} < \alpha_1 \leq \sqrt{\frac{2}{3}}\,, \qquad \beta_1 > -2\alpha_1\,, \qquad \beta_2 > -2\alpha_1\,, \qquad \lambda < -4\alpha_1\,,$$

and is a stable spiral when either of the following holds

$$\alpha_1 < -\sqrt{\frac{2}{3}}\,, \qquad \beta_1 < -2\alpha_1\,, \qquad \beta_2 < -2\alpha_1\,, \qquad \lambda > -4\alpha_1\,,$$

$$\text{or,} \qquad \alpha_1 > \sqrt{\frac{2}{3}}\,, \qquad \beta_1 > -2\alpha_1\,, \qquad \beta_2 > -2\alpha_1\,, \qquad \lambda < -4\alpha_1\,.$$

- The conformal dust kinetic fixed point $(6)_{(d)}$, is a stable node when either of the following conditions is satisfied

$$-\frac{1}{\sqrt{2}} < \alpha_1 < 0\,, \quad \lambda > \frac{-3-2\alpha_1^2}{2\alpha_1}\,, \quad \beta_1 < \frac{-3-2\alpha_1^2}{4\alpha_1}\,, \quad \beta_2 < \frac{-3-2\alpha_1^2}{4\alpha_1}\,,$$

or,

$$0 < \alpha_1 < \frac{1}{\sqrt{2}}\,, \quad \lambda < \frac{-3-2\alpha_1^2}{2\alpha_1}\,, \quad \beta_1 > \frac{-3-2\alpha_1^2}{4\alpha_1}\,, \quad \beta_2 > \frac{-3-2\alpha_1^2}{4\alpha_1}\,.$$

- For the disformal dust radiation fixed point (b), we know that this exists if $\beta_1^2 > 2$. Furthermore, this two fluid disformal fixed point is found to be a saddle point.

- The existence of fixed point $(3)_{(d)}$, requires $\beta_1 \geq \sqrt{3/2}$. By imposing that $e_{1,2} < 0$, we get that $\beta_2 < \beta_1$, and $\lambda > 2\beta_1$. The constraint on α_1 in terms of β_1, is obtained from $e_{3,4,5}$. An illustration of some allowed parameter values is shown in Fig. 4.4.

- The existence of the other disformal fixed point $(4)_{(d)}$, implies that $\beta_1 \leq -\sqrt{3/2}$. Furthermore, e_1, $e_2 < 0$, give $\beta_2 > \beta_1$, and $\lambda < 2\beta_1$. From $e_{3,4,5}$, we get constraints on the choice of α_1 in terms of β_1. An illustration of some values is given in Fig. 4.4.

- The only non–singular disformal fixed point $(5)_{(r)}$, is a saddle point when $\beta_2^2 > 2$. This is due to the opposite signs of e_3 and e_4.

- For the next disformal fixed point $(3)_{(r)}$, we find that this is a stable node when the following inequalities are satisfied

$$\beta_2 > \sqrt{2}\,, \qquad \beta_1 < \beta_2\,, \qquad \alpha_1 < -\beta_2 + \sqrt{\frac{2\beta_2^2-3}{2}}\,, \qquad \lambda > 2\beta_2\,.$$

- Similarly, fixed point $(4)_{(r)}$, is found to be a stable node when the chosen parameters satisfy the following inequalities

$$\beta_2 < -\sqrt{2}\,, \qquad \beta_1 > \beta_2\,, \qquad \alpha_1 > -\beta_2 - \sqrt{\frac{2\beta_2^2-3}{2}}\,, \qquad \lambda < 2\beta_2\,.$$

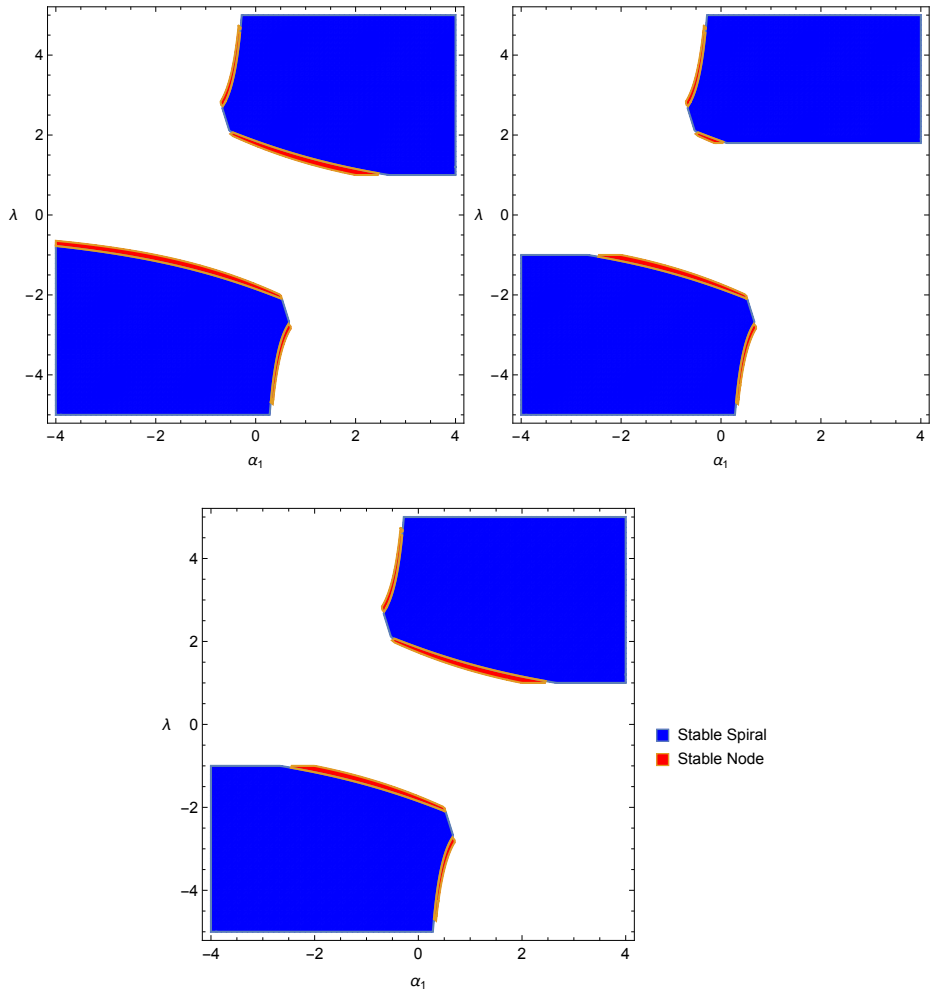

Figure 4.5: The stable regions for the conformal–disformal dust and conformal–disformal radiation scenario, illustrating the parameter values of α_1 and λ, for fixed point $(8)_{(d)}$, when $(\beta_1, \beta_2) = (0.1, 0.5)$ (left), $(\beta_1, \beta_2) = (-0.5, 0.9)$ (right), and $(\beta_1, \beta_2) = (-0.5, 0.5)$ (bottom).

- The conformal radiation scaling fixed point $(8)_{(r)}$, is found to be a stable node when either of the following holds

$$-\frac{8}{\sqrt{15}} \leq \lambda < -2\,, \qquad \beta_1 > \frac{\lambda}{2}\,, \qquad \beta_2 > \frac{\lambda}{2}\,, \qquad \alpha_1 > -\frac{\lambda}{4}\,,$$

$$\text{or,} \qquad 2 < \lambda \leq \frac{8}{\sqrt{15}}\,, \qquad \beta_1 < \frac{\lambda}{2}\,, \qquad \beta_2 < \frac{\lambda}{2}\,, \qquad \alpha_1 < -\frac{\lambda}{4}\,,$$

and is a stable spiral when either of the following is satisfied

$$\lambda < -\frac{8}{\sqrt{15}}\,, \qquad \beta_1 > \frac{\lambda}{2}\,, \qquad \beta_2 > \frac{\lambda}{2}\,, \qquad \alpha_1 > -\frac{\lambda}{4}\,,$$

$$\text{or,} \qquad \lambda > \frac{8}{\sqrt{15}}\,, \qquad \beta_1 < \frac{\lambda}{2}\,, \qquad \beta_2 < \frac{\lambda}{2}\,, \qquad \alpha_1 < -\frac{\lambda}{4}\,.$$

- The scalar field dominated fixed point (7), is a stable node in the following regions

$$-2 < \lambda < 0\,, \qquad \beta_1 > \frac{\lambda}{2}\,, \qquad \beta_2 > \frac{\lambda}{2}\,, \qquad \alpha_1 > \frac{3-\lambda^2}{\lambda}\,,$$

$$\text{or,} \qquad 0 < \lambda < 2\,, \qquad \beta_1 < \frac{\lambda}{2}\,, \qquad \beta_2 < \frac{\lambda}{2}\,, \qquad \alpha_1 < \frac{3-\lambda^2}{\lambda}\,.$$

- For the conformal dust scaling fixed point $(8)_{(d)}$, an illustration of the possible values of α_1 and λ, for some fixed values of the other parameters that render this point stable, is given in Fig. 4.5. Indeed, we find that this point can either be a stable node, or a stable spiral.

We will be interested in cosmologically acceptable trajectories, by which we mean that the trajectory should start in the radiation era, then evolve to a matter dominated era, and finally reproduce our present day accelerating Universe (as discussed in chapter 1). In our examples, we will use $\Omega_{m,0} \simeq 0.308$, $\Omega_{\phi,0} \simeq 0.692$, $H_0 \simeq 67.8\,\mathrm{km\,s^{-1}\,Mpc^{-1}}$, and $w_{\phi,0} \simeq -1$, as our present day cosmological parameters [65]. These imply that, the present values of the dynamical system variables should be $x_0 \simeq 0$, $y_0 \simeq 0.832$, $z_{0,1} \simeq 0.555$. Furthermore, since the scalar field plays an important role in the late–time Universe, the trajectories in the radiation dominated epoch should start near $x = y = 0$. We give an example in Fig. 4.6, showing the evolution of Ω_i and ρ_i, such that the future attractor is the scalar field dominated fixed point (7). In this plot we compare the conformally coupled scenario with the disformally coupled case by evolving the equations from the same initial conditions. We also define a time–dependent effective mass scale,

$$M_{\rm eff} = (|D_r - D_m|)^{-1/4}\,, \tag{4.54}$$

which we also show in Fig. 4.6.

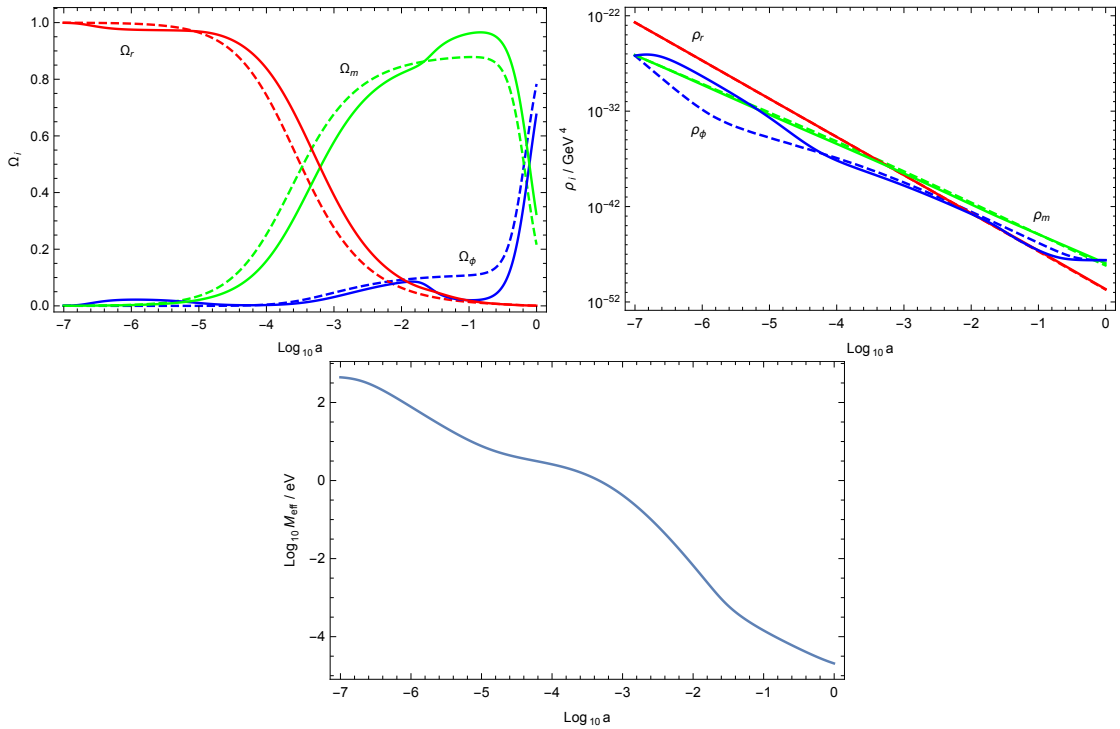

Figure 4.6: The above plots show the evolution of $\Omega_{r,m,\phi}$ (left), and $\rho_{r,m,\phi}$ (right), when the future attractor is fixed point (7), of the conformal–disformal dust and conformal–disformal radiation case. In each plot we use the same initial conditions and compare the conformally coupled dust case (dashed line) with the conformally–disformally coupled dust–radiation case (solid line), as discussed in section 4.4.1. The bottom plot shows the evolution of the effective mass scale defined in Eq. (4.54). The parameters are fixed to $\alpha_1 = -0.41,\ \beta_1 = 5.81,\ \beta_2 = 5.11$, and $\lambda = -0.08$.

By assuming standard Big Bang Nucleosynthesis (BBN), we can use a conservative constraint of[3] $\Omega_\phi(\sim \text{MeV}) < 0.2$ [452, 488] to limit the range of the parameters α_1, β_2, and λ. If we further assume that, the non–singular fixed points (a), $(5)_{(r)}$, and $(8)_{(r)}$, are reached by BBN, the constraint of $\Omega_\phi < 0.2$ at the BBN epoch implies that, $\alpha_1^2 > 5/6$, $\beta_2^2 > 10/3$, and $\lambda^2 > 20$, respectively.

4.4.2 Two fluids-Conformal dust & conformal–disformal radiation

In this section we consider another particular case of the generic system, which was presented in section 4.2. Thence, we will be interested in a conformally coupled perfect fluid with equation of state parameter γ_1, defined in the conformal frame by the metric $\tilde{g}^1_{\mu\nu}$, in the presence of a distinct conformally–disformally coupled perfect

[3] A tighter constraint of $\Omega_\phi(\sim \text{MeV}) < 0.045$ was reported in Ref. [487], however, we decided to make use of a more conservative constraint.

fluid with equation of state parameter γ_2, defined in the disformal frame by the metric $\tilde{g}^2_{\mu\nu}$. As in the single fluid case, we will be considering exponential couplings and scalar field potential, namely

$$C_i(\phi) = e^{2\alpha_i \kappa\phi}, \qquad D_1(\phi) = 0, \qquad D_2(\phi) = \frac{e^{2(\alpha_2+\beta)\kappa\phi}}{M^4}, \qquad V(\phi) = V_0^4 e^{-\lambda\kappa\phi}. \tag{4.55}$$

This system can be viewed as a reduced phase space analysis of the previous higher–dimensional system of section 4.4.1. As a matter of fact, this dynamical system is four–dimensional, hence, one dimension less than the previous case. One might think that the results could simply be obtained from the previous case by setting $\beta_1 \to -\infty$. We will see in the following that, if we do this, then we would be missing out some of the stability conditions. For simplicity, we choose to eliminate z_2 from our system of differential equations, and hence, we end up with four ordinary differential equations for $x,\ y,\ z_1$, and σ_2. The fixed points for this system are listed in Table A.1. This is a generalisation of the fixed points found in the single fluid case with equation of state parameter γ, collected in Table 4.1.

We will now specify this system to conformally coupled dust and conformally–disformally coupled radiation, where we set $\gamma_1 = 1$ and $\gamma_2 = 4/3$. As expected, the fixed points for this particular system are found to be contained in the fixed points discussed in the previous case when we considered radiation and dust to be both conformally and disformally coupled. Indeed, the fixed points for this system are (1), $(6)_{(r)}$, (2), (a), $(6)_{(d)}$, $(5)_{(r)}$, $(3)_{(r)}$, $(4)_{(r)}$, $(8)_{(r)}$, (7), and $(8)_{(d)}$. Since the existence analysis of these fixed points coincides with that presented in section 4.4.1.1, we only discuss the stability of these fixed points. All the eigenvalues $e_{1,2,3,4}$, for each fixed point can be found in appendix A.2.2.

4.4.2.1 Stability conditions

We will now discuss the stability of the fixed points of this reduced system. This analysis will be slightly different from the previous, since we now have four eigenvalues. In the stability analysis that follows, we will only comment on those regions where the fixed point is stable.

- The scalar field kinetic energy dominated fixed points (1) and (2), both have $e_1 > 0$, and hence, cannot be stable. The radiation fluid dominated fixed point $(6)_{(r)}$, can only be a saddle point, since $e_1,\ e_3 < 0$ and $e_2,\ e_4 > 0$.

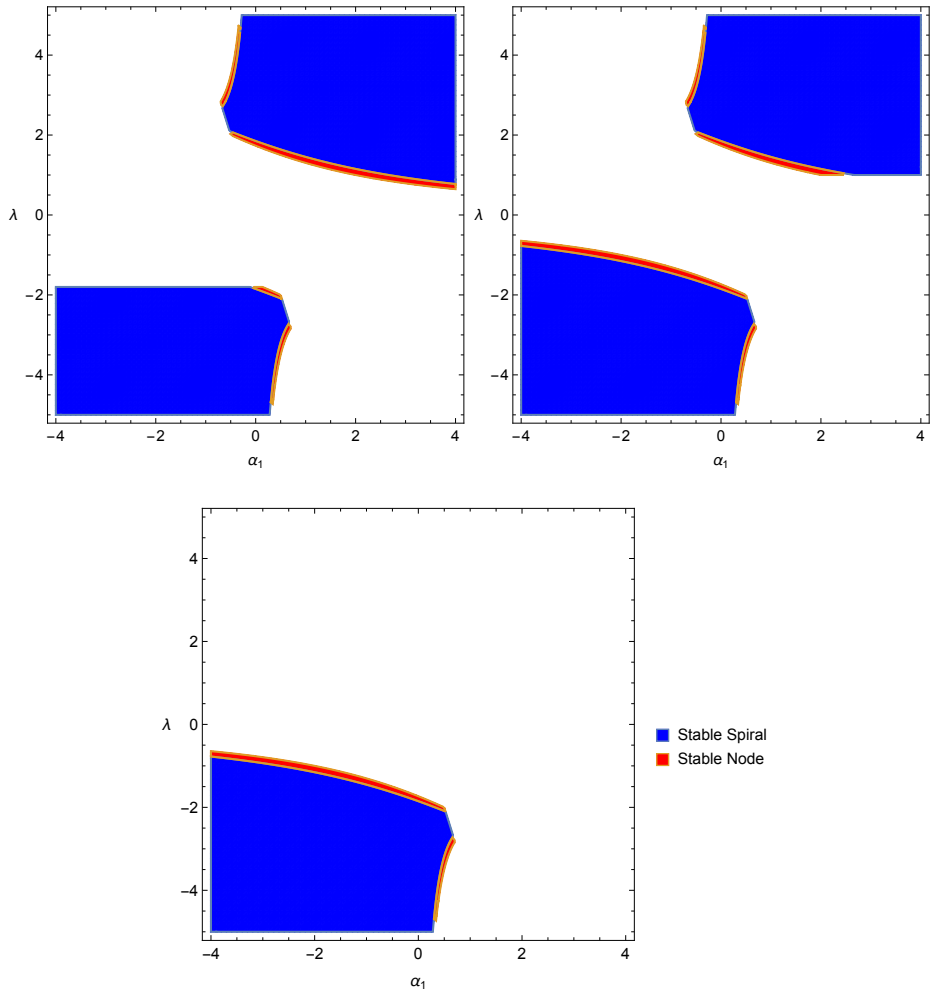

Figure 4.7: The stable regions for the case of conformal dust and conformal–disformal radiation, illustrating the parameter values of α_1 and λ for fixed point $(8)_{(d)}$, when $\beta = -0.9$ (left), $\beta = 0.5$ (right), and $\beta = 5$ (bottom).

- Fixed point (a), is found to be a stable node when

$$-\sqrt{\frac{2}{3}} \leq \alpha_1 < -\frac{1}{\sqrt{2}}\,, \qquad \lambda > -4\alpha_1\,, \qquad \beta < -2\alpha_1,$$

$$\text{or,} \qquad \frac{1}{\sqrt{2}} < \alpha_1 \leq \sqrt{\frac{2}{3}}\,, \qquad \lambda < -4\alpha_1\,, \qquad \beta > -2\alpha_1\,,$$

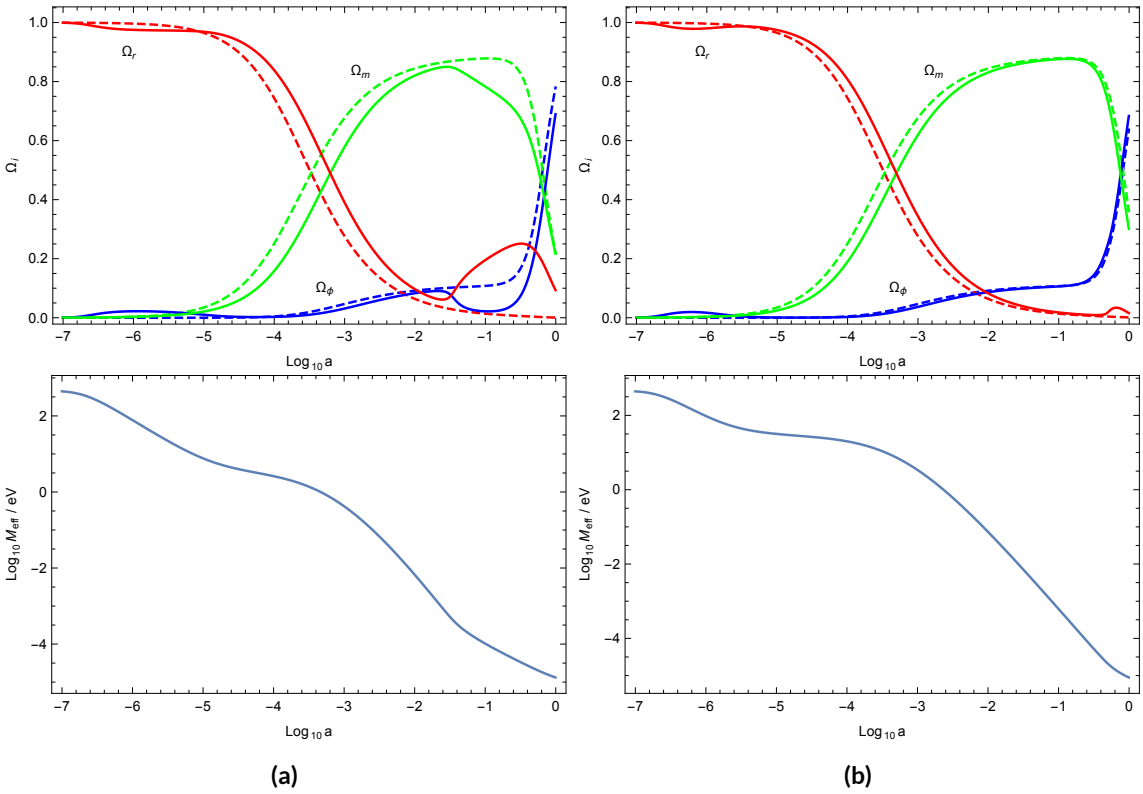

Figure 4.8: The above plots show the evolution of $\Omega_{r,m,\phi}$ and M_{eff}, when the future attractor is fixed point (7), of the conformal dust and conformal–disformal radiation case. In (a) we use the same parameters as those adopted in Fig. 4.6, where we set $\alpha_1 = -0.41,\ \beta = 5.11,\ \lambda = -0.08$, whereas in (b) we use $\alpha_1 = -0.41,\ \beta = 4.41,\ \lambda = -0.08$. In each plot we adopt the same initial conditions and compare the purely conformal case (dashed line) with the conformal dust and conformal–disformal radiation case (solid line), as discussed in section 4.4.2.

and a stable spiral when

$$\alpha_1 < -\sqrt{\frac{2}{3}}\,, \qquad \beta < -2\alpha_1\,, \qquad \lambda > -4\alpha_1,$$

$$\text{or,} \qquad \alpha_1 > \sqrt{\frac{2}{3}}\,, \qquad \beta > -2\alpha_1\,, \qquad \lambda < -4\alpha_1\,.$$

- Fixed point $(6)_{(d)}$, is a stable node when one of the following set of inequalities is satisfied

$$-\frac{1}{\sqrt{2}} < \alpha_1 < 0\,, \qquad \lambda > \frac{-3-2\alpha_1^2}{2\alpha_1}\,, \qquad \beta < \frac{-3-2\alpha_1^2}{4\alpha_1}\,,$$

$$\text{or,} \qquad 0 < \alpha_1 < \frac{1}{\sqrt{2}}\,, \qquad \lambda < \frac{-3-2\alpha_1^2}{2\alpha_1}\,, \qquad \beta > \frac{-3-2\alpha_1^2}{4\alpha_1}\,.$$

- The mixed fixed point $(5)_{(r)}$, can only be a saddle point in the existence range of $\beta^2 > 2$. The other disformal fixed point $(3)_{(r)}$, is found to be a stable node when

$$\beta > \sqrt{2}\,, \qquad \alpha_1 < -\beta + \sqrt{\frac{2\beta^2-3}{2}}\,, \qquad \lambda > 2\beta\,.$$

The last disformal fixed point $(4)_{(r)}$, can also be a stable node if the following inequalities are satisfied

$$\beta < -\sqrt{2}\,, \qquad \alpha_1 > -\beta - \sqrt{\frac{2\beta^2-3}{2}}\,, \qquad \lambda < 2\beta\,.$$

- The radiation scaling fixed point $(8)_{(r)}$, is a stable node when

$$-\frac{8}{\sqrt{15}} \leq \lambda < -2\,, \qquad \beta > \frac{\lambda}{2}\,, \qquad \alpha_1 > -\frac{\lambda}{4},$$

$$\text{or,} \qquad 2 < \lambda \leq \frac{8}{\sqrt{15}}\,, \qquad \beta < \frac{\lambda}{2}\,, \qquad \alpha_1 < -\frac{\lambda}{4}\,,$$

and it can also be a stable spiral when the following inequalities are satisfied

$$\lambda < -\frac{8}{\sqrt{15}}\,, \qquad \beta > \frac{\lambda}{2}\,, \qquad \alpha_1 > -\frac{\lambda}{4},$$

$$\text{or,} \qquad \lambda > \frac{8}{\sqrt{15}}\,, \qquad \beta < \frac{\lambda}{2}\,, \qquad \alpha_1 < -\frac{\lambda}{4}\,.$$

- The scalar field dominated fixed point (7), is a stable node in the following

regions

$$-2 < \lambda < 0\,, \qquad \beta > \frac{\lambda}{2}\,, \qquad \alpha_1 > \frac{3-\lambda^2}{\lambda},$$

$$\text{or,} \qquad 0 < \lambda < 2\,, \qquad \beta < \frac{\lambda}{2}\,, \qquad \alpha_1 < \frac{3-\lambda^2}{\lambda}\,.$$

- The conformal dust scaling fixed point $(8)_{(d)}$, can either be a stable node or a stable spiral, as depicted in Fig. 4.7. Although this fixed point also appears in the previous two fluid and single fluid cases, the stable regions differ from those presented in Fig. 4.1 and Fig. 4.5.

We illustrate two examples in Fig. 4.8, showing the evolution of Ω_i, and the effective mass $M_{\rm eff}$. In Fig. 4.8 (a) we adopt the same parameters and initial conditions as those used in the example shown in Fig. 4.6. It is evident that, the radiation disformal coupling gives rise to a larger contribution to the radiation energy density at late times. Indeed, when the radiation disformal coupling exponent parameter is reduced, as depicted in Fig. 4.8 (b), this enhanced contribution is diluted.

4.4.3 Two fluids-Two conformal–disformal dust components

In this section, we study the full solution of the two fluid conformal–disformal system presented in section 4.2 for the particular case of two dust components. Similar to the system discussed in section 4.4.1, this system is also five–dimensional, in which we choose our dynamical variables to be x, y, z_1, σ_1, and σ_2. Furthermore, the couplings and scalar field potential are identical to those in Eq. (4.53). As expected, we recover the single fluid dust case fixed points for both components, although we obtain a *conformal dust dominated* fixed point (c), in which neither of the fluids is subdominant. We list this fixed point in Table 4.7. Fixed point (c) is characterised by $x = y = \sigma_i = 0$, and

$$\sum_{i=1}^{2} z_i^2 \lambda_C^i (4 - 3\gamma_i) = 0\,. \tag{4.56}$$

Moreover, the radiation dominated fixed point $(6)_{(r)}$ is also obtained in this way, although in that case the radiation fluid dominates the solution. This dust dominated fixed point has already been studied in Refs. [482, 486, 489]. The fixed points for this system are found to be the following: (1), (c), (2), $(6)^1_{(d)}$, $(6)^2_{(d)}$, $(3)^1_{(d)}$, $(4)^1_{(d)}$, $(3)^2_{(d)}$, $(4)^2_{(d)}$, (7), $(8)^1_{(d)}$, and $(8)^2_{(d)}$. We use a superscript with the

Name	x	y	z_1	z_2	σ_1	σ_2	Ω_ϕ	w_ϕ	Z_1	Z_2	w_{eff}
(c)	0	0	$\sqrt{\frac{\alpha_2}{\alpha_2-\alpha_1}}$	$\sqrt{\frac{\alpha_1}{\alpha_1-\alpha_2}}$	0	0	0	-	1	1	0

Table 4.7: The relevant quantities of the conformal dust dominated fixed point obtained when considering two conformally–disformally coupled dust components.

single fluid dust fixed point labels to indicate the dominant fluid, such that, for superscript i we have $z_i \neq 0$. We only comment on the existence of (c), since for the other fixed points, this analysis follows directly from section 4.3.1.1. This conformal dust dominated fixed point exists when either of the following holds

$$\alpha_2 > 0,\ \alpha_1 \leq 0,\ \ \text{or},\ \ \alpha_2 = 0,\ \alpha_1 \neq 0,\ \ \text{or},\ \ \alpha_2 < 0,\ \alpha_1 \geq 0\ .$$

4.4.3.1 Stability conditions

As was done in the previous cases, we also present the stability analysis of these fixed points, in which we only discuss the regions where the fixed point is found to be stable. For completeness, we list all eigenvalues in appendix A.2.3. For each fixed point we have five eigenvalues $e_{1,2,3,4,5}$, which, in general depend on all five model parameters: $\alpha_{1,2}$, $\beta_{1,2}$, λ. This is in contrast with the dust–radiation case, in which, although we have the same number of eigenvalues, the eigenvalues in that case did not depend on α_2. This is due to the fact that radiation is conformally invariant.

- For this case, the two kinetic dominated fixed points can be stable. Indeed, (1) is stable when the following holds

$$\alpha_1 > \sqrt{\frac{3}{2}}\,,\quad \alpha_2 > \sqrt{\frac{3}{2}}\,,\quad \beta_1 > -\sqrt{\frac{3}{2}}\,,\quad \beta_2 > -\sqrt{\frac{3}{2}}\,,\quad \lambda < -\sqrt{6}\,,$$

  and (2) is a stable node whenever the following inequalities are satisfied

$$\alpha_1 < -\sqrt{\frac{3}{2}}\,,\quad \alpha_2 < -\sqrt{\frac{3}{2}}\,,\quad \beta_1 < \sqrt{\frac{3}{2}}\,,\quad \beta_2 < \sqrt{\frac{3}{2}}\,,\quad \lambda > \sqrt{6}\,.$$

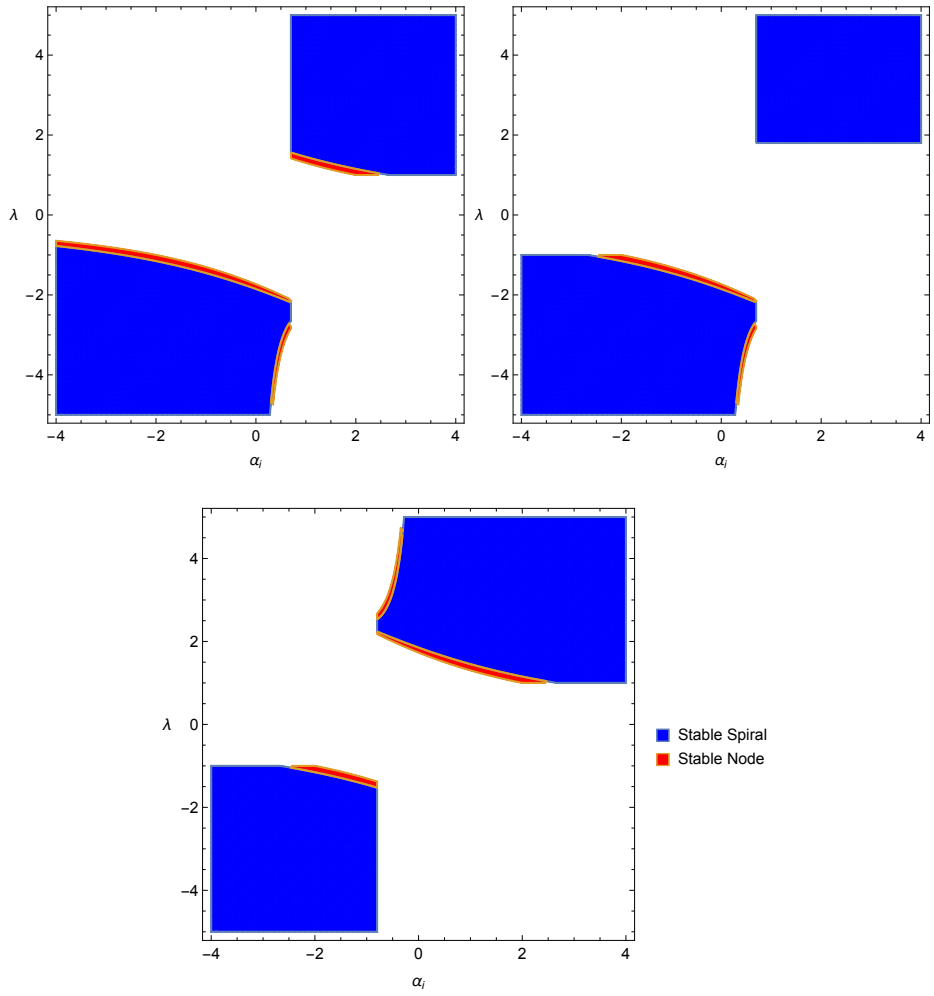

Figure 4.9: The stable regions for a two conformal–disformal dust case, show an illustration of the parameter values of α_i and λ, for fixed points $(8)^{i=1,2}_{(d)}$, when $(\beta_1, \beta_2, \alpha_{j\neq i}) = (0.1, 0.5, 0.7)$ (left), $(\beta_1, \beta_2, \alpha_{j\neq i}) = (-0.5, 0.9, 0.7)$ (right), and $(\beta_1, \beta_2, \alpha_{j\neq i}) = (-0.5, 0.5, -0.8)$ (bottom).

- The conformal dust dominated fixed point (c), is found to be a saddle when satisfying the existence condition.
- The conformal kinetic fixed point $(6)^1_{(d)}$, is a stable node when the parameters satisfy the following inequalities

$$-\sqrt{\frac{3}{2}} < \alpha_1 < 0, \quad \alpha_2 < \alpha_1, \quad \beta_1 < \frac{-2\alpha_1^2 - 3}{4\alpha_1}, \quad \beta_2 < \frac{-2\alpha_1^2 - 3}{4\alpha_1}, \quad \lambda > \frac{-2\alpha_1^2 - 3}{2\alpha_1},$$

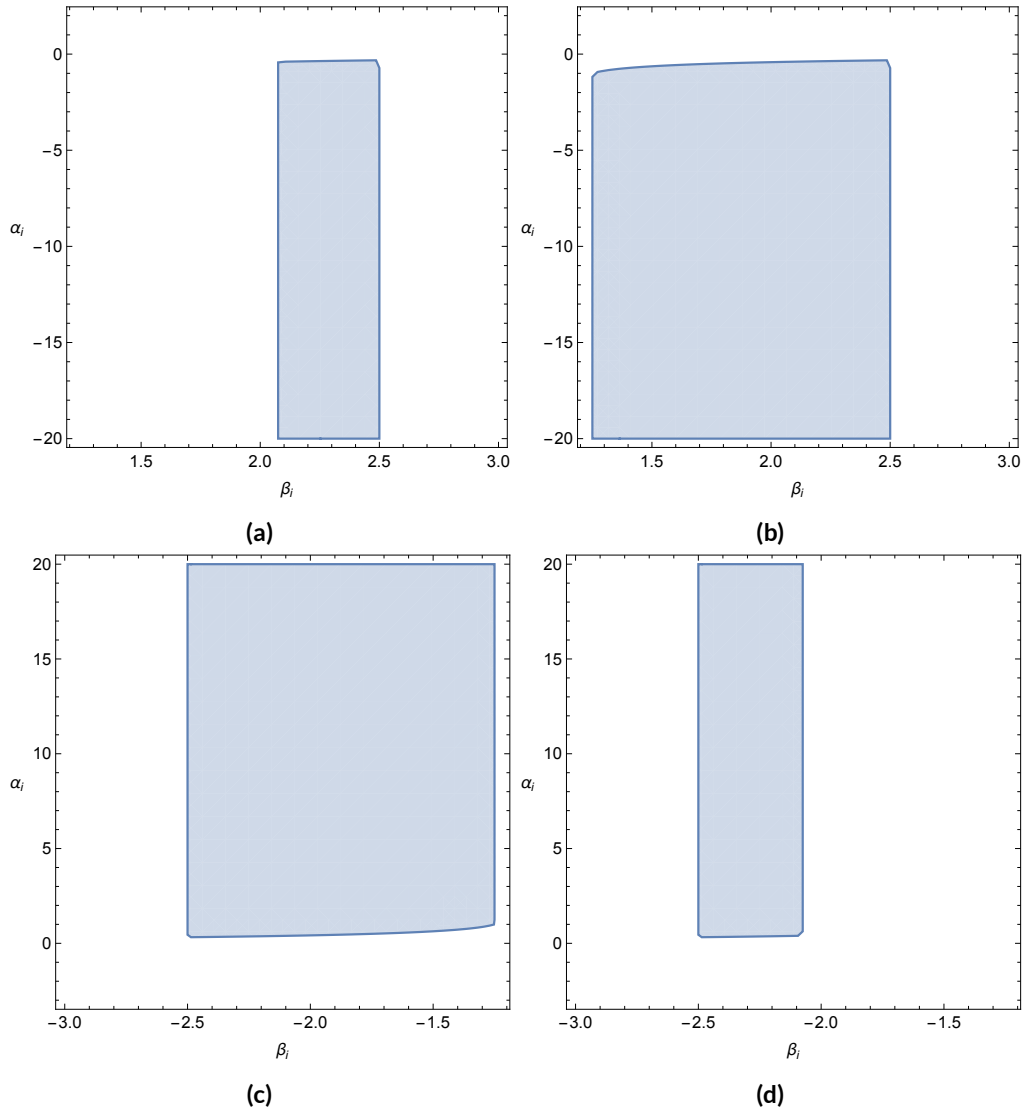

Figure 4.10: The stable node regions for a two conformal–disformal dust case, show an illustration of the parameter values of α_i and β_i, for fixed points $(3)^{i=1,2}_{(d)}$ in (a), (b); and $(4)^{i=1,2}_{(d)}$ in (c), (d), respectively. The other free parameters are chosen to be as follows: (a) – $(\beta_{j\neq i}, \alpha_{j\neq i}, \lambda) = (0.5, -0.4, 5)$, (b) – $(\beta_{j\neq i}, \alpha_{j\neq i}, \lambda) = (0.5, -1, 5)$, (c) – $(\beta_{j\neq i}, \alpha_{j\neq i}, \lambda) = (0.5, 1, -5)$, and (d) – $(\beta_{j\neq i}, \alpha_{j\neq i}, \lambda) = (0.5, 0.4, -5)$.

or,

$$0 < \alpha_1 < \sqrt{\frac{3}{2}}, \quad \alpha_2 > \alpha_1, \quad \beta_1 > \frac{-2\alpha_1^2 - 3}{4\alpha_1}, \quad \beta_2 > \frac{-2\alpha_1^2 - 3}{4\alpha_1}, \quad \lambda < \frac{-2\alpha_1^2 - 3}{2\alpha_1},$$

Case	λ	α_1	β_1	α_2	β_2
I	$\sqrt{\frac{3}{2}}$	-1.5	–	0	-5
Ic	$\sqrt{\frac{3}{2}}$	-1.5	–	0.035	–
II	$\sqrt{\frac{3}{2}}$	-1.5	–	1	-5
IIc	$\sqrt{\frac{3}{2}}$	-1.5	–	1	–
III	$\sqrt{\frac{3}{2}}$	-1.5	0.5	1	-5
IV	$\sqrt{\frac{3}{2}}$	0	0.5	0	-5

Table 4.8: Listed are, respectively, the cases considered in Fig. 4.11 together with the respective parameter values. Cases I, II, III, and IV are all disformally coupled cases, whereas cases Ic and IIc are conformally coupled cases.

and the other conformal kinetic dust fixed point $(6)^2_{(d)}$, is a stable node when either one of the following conditions is satisfied

$$-\sqrt{\frac{3}{2}} < \alpha_2 < 0, \quad \alpha_1 < \alpha_2, \quad \beta_1 < \frac{-2\alpha_2^2-3}{4\alpha_2}, \quad \beta_2 < \frac{-2\alpha_2^2-3}{4\alpha_2}, \quad \lambda > \frac{-2\alpha_2^2-3}{2\alpha_2},$$

or,

$$0 < \alpha_2 < \sqrt{\frac{3}{2}}, \quad \alpha_1 > \alpha_2, \quad \beta_1 > \frac{-2\alpha_2^2-3}{4\alpha_2}, \quad \beta_2 > \frac{-2\alpha_2^2-3}{4\alpha_2}, \quad \lambda < \frac{-2\alpha_2^2-3}{2\alpha_2}.$$

The regions of stability for the conformal scaling fixed points $(8)^{1,2}_{(d)}$, are shown in Fig. 4.9. The regions of stability differ from the previous cases, since the eigenvalues now depend on all five model parameters, leading to more degrees of freedom in the (α_i, λ)–parameter space.

- The regions of stability for the four disformal fixed points $(3)^{1,2}_{(d)}$ and $(4)^{1,2}_{(d)}$, are illustrated in Fig. 4.10.

- The scalar field dominated fixed point (7), is a stable node when the parameters satisfy either one of the following conditions

$$-\sqrt{6} < \lambda < 0\,, \quad \alpha_1 > \frac{3-\lambda^2}{\lambda}\,, \quad \alpha_2 > \frac{3-\lambda^2}{\lambda}\,, \quad \beta_1 > \frac{\lambda}{2}\,, \quad \beta_2 > \frac{\lambda}{2}\,,$$

$$\text{or,} \quad 0 < \lambda < \sqrt{6}\,, \quad \alpha_1 < \frac{3-\lambda^2}{\lambda}\,, \quad \alpha_2 < \frac{3-\lambda^2}{\lambda}\,, \quad \beta_1 < \frac{\lambda}{2}\,, \quad \beta_2 < \frac{\lambda}{2}\,.$$

We illustrate some examples in Fig. 4.11, in which we consider different coupling cases as described in Table 4.8. The purely conformal cases are denoted by Ic, and IIc. We use these conformal cases to compare with the disformal cases I, II, III, and IV. In case I, we consider the first dust component to be conformally coupled, and the second component to be purely disformally coupled. In case II, the first dust component is conformally coupled, whereas the second component is conformally–disformally coupled. In case III, the two dust components are both conformally–disformally coupled, whereas in case IV, the two components are purely disformally coupled. We remark that, when we neglect the disformal coupling, we consider $M_i \to \infty$ in Eq. (4.53), hence β_i is arbitrary in these circumstances.

4.5 Cosmological consequences

In this section, we will summarise our findings and present some cosmological consequences of the discussed fixed points. The only fixed points that admit accelerated solutions are points (7) and $(8)_{(d)}$. When the attractor of the system is the scalar field dominated fixed point (7), the matter and radiation sectors vanish completely, as soon as this point is reached. Hence, in order to account for the present–day non–zero matter and radiation densities, the initial conditions should be fine–tuned in such a way that the scalar field dominated attractor is not reached at the present time. On the other hand, the conformal dust scaling fixed point $(8)_{(d)}$, is a solution for which the matter and scalar field energy density parameters $\Omega_{m,\phi}$, stabilise to a constant finite value and remain indefinitely constant. The values of these energy density parameters are fixed when the conformal coupling strength parameter α, and the scalar field potential exponent λ, are specified, and are independent from the choice of initial conditions. Consequently, the coincidence of the current values of the energy density parameters is solved when the attractor of the system is point $(8)_{(d)}$. However, trajectories with this global attractor are known to lack a matter dominated epoch (see for example Ref. [476]) which could lead to negative consequences on the growth of perturbations.

All trajectories starting deep in the radiation era depart from the neighbourhood

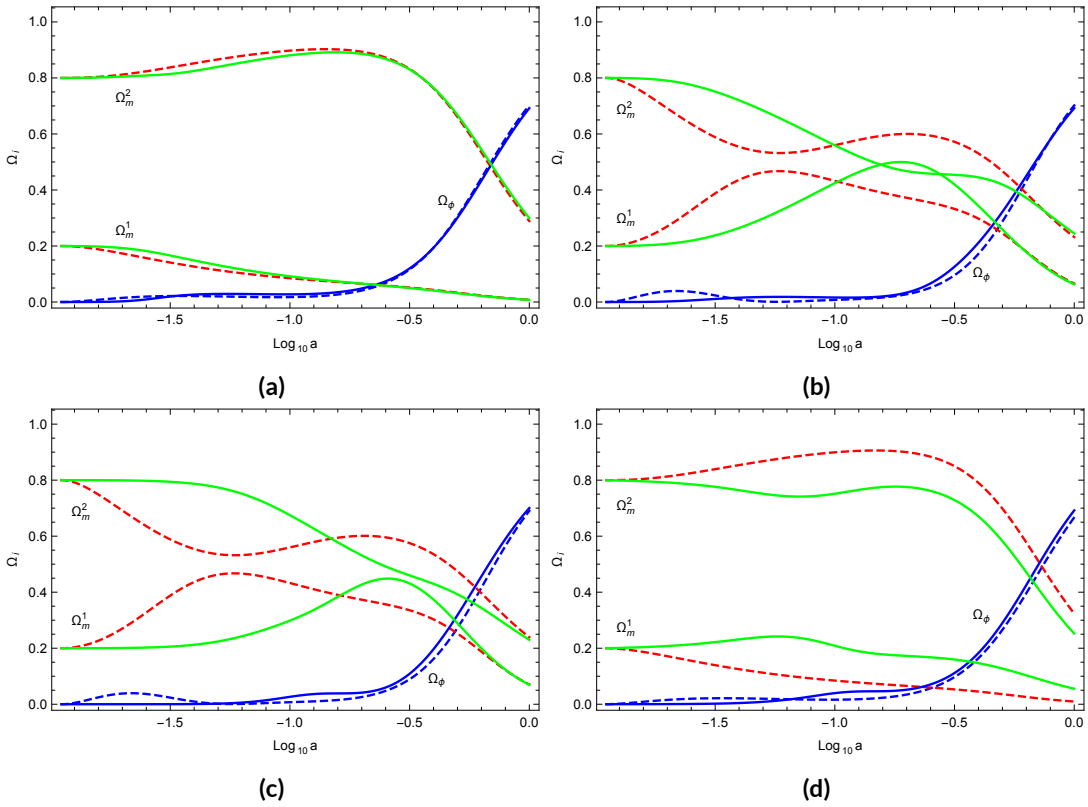

Figure 4.11: In (a), (b), (c), and (d) we compare disformally coupled cases (solid line) with conformally coupled scenarios (dashed line). Thence, in (a) cases I and Ic are compared, in (b) cases II and IIc are compared, in (c) we compare III with IIc, and in (d) we compare IV with Ic.

of the radiation dominated fixed point $(6)_{(r)}$, even if initially the field's kinetic energy dominated, such that the trajectory is near the kination fixed points (1) and (2), as the system would quickly evolve towards the saddle point $(6)_{(r)}$. After leaving the radiation dominated fixed point, the trajectory could pass near the radiation disformal fixed point, mixed fixed point, and the disformal dust radiation fixed point. The existence of these transient saddle points depends on the parameter choice of a given model. Indeed, in Fig. 4.6 all three saddle points are present in the field–radiation–dominated era (ϕRDE), while in Fig. 4.8 only the points $(5)_{(r)}$ and $(3)_{(r)}$ exist, with $(5)_{(r)}$ being the transient fixed point in the ϕRDE. In this ϕRDE, energy is transferred from radiation to the coupled scalar field as the trajectory passes near these transient fixed points. A further energy transfer to the coupled matter sector is also possible if the trajectory evolves temporarily towards point (b). As a consequence, radiation–matter equivalence happens at a different e–fold number when compared with the purely conformal system, which is missing the mentioned fixed points.

In the matter dominated era, conformally coupled models are known to enter a field–matter–dominated era, or ϕMDE [476], characterised by an energy transfer from matter to the coupled scalar field. This happens as the trajectory passes near the conformal dust kinetic saddle point $(6)_{(d)}$, before it is attracted towards the scalar field dominated fixed point (7). In the uncoupled case, fixed point $(6)_{(d)}$ is fixed at $x = y = 0$, and hence does not lead to the energy transfer observed in the conformally coupled model. When matter and radiation are disformally coupled, the ϕMDE could be modified due to an evolution of the trajectory towards one of the disformal fixed points. This is clearly seen in Fig. 4.6 in which the system, after leaving the point $(6)_{(d)}$, passes near the disformal saddle point $(3)_{(d)}$. As a result, there is a transfer of energy from the coupled scalar field to matter; the reverse process of the conformally coupled model. An increase in the radiation energy density could also appear in the ϕMDE. This is illustrated in Fig. 4.8, in which radiation is disformally coupled while matter is only conformally coupled to the scalar field. The energy transfer from matter and the scalar field to radiation occurs, because of a dynamical evolution of the trajectory towards the disformal radiation saddle point $(3)_{(r)}$, before the trajectory is attracted towards fixed point (7).

The conformal dust radiation fixed point could also be a transient fixed point, although this requires a large conformal coupling ($\alpha^2 > 1/2$). This might be in conflict with local observations in the purely conformal scenario, however such constraints could be relaxed when considering multiple couplings, such as the additional disformal coupling [3–5]. We will discuss this possibility in more detail in the subsequent chapters.

The conformal dust dominated fixed point, although it is not able to give an accelerated expansion of the Universe, it could be a transient fixed point for the evolution of two coupled dust fluids. In conformally coupled models, the trajectory first evolves towards the conformal dust kinetic fixed point, resulting in an increase of the scalar field energy density parameter, and then the trajectory evolves towards saddle point (c), as it is attracted towards the global attractor point (7). The transition towards the conformal dust dominated fixed point is clearly seen in case IIc depicted in Fig. 4.11, characterised by a decrease in the scalar field energy density before the system evolves towards the dark energy dominated era. On the other hand, in the presence of a disformal coupling, the disformal fixed point of the disformally coupled dust component $(4)_{(d)}$, delays the evolution towards the conformal dust kinetic and the conformal dust dominated fixed points. As shown in Fig. 4.11, this disformal fixed point can even force the system to evolve directly towards point (c), and hence no transfer of energy to the coupled scalar field takes place, which would then shift the field–matter equivalence e–fold number.

4.6 Disformally induced variation of the fine–structure constant

As we briefly alluded in the introduction of this chapter, the idea on the variation of the fundamental constants of Nature was first raised by Dirac in his Large Numbers Hypothesis [415, 416]. The advent of higher–dimensional theories [490, 491], in which the effective $(3+1)$–dimensional constants can vary in space and time, has led to an increased interest in Nature's fundamental constants and their variation. Despite this, we have seen in chapter 1 that Einstein's equivalence principle, and hence local position invariance, is one of the building blocks of gravitational metric theories, which include amongst others the well–known gravitational theory of General Relativity. Thence, the link between the constancy of fundamental constants and the equivalence principle is a natural one. Here we focus on space–time variations of the electromagnetic fine–structure constant[4] $\alpha \equiv e^2/(4\pi\varepsilon_0\hbar c) \simeq 1/137$ [492], where e is the electron charge, ε_0 is the permittivity of the vacuum, $\hbar$ is the reduced Planck's constant, and c is the speed of light in vacuum.

Since the constraints on possible space–time variations of the electromagnetic fine–structure constant are becoming tighter (see for instance Ref. [493]), it is imperative to confront those theoretical models which predict such a variation. Stringent constraints on such a variation have been reported at low redshifts from astrophysical [494–505], geochemical [506–508], and laboratory [509] observations, while relatively weaker constraints have been derived from BBN at a redshift of $z \sim 10^9$ [510], and the cosmic microwave background (CMB) radiation at $z \sim 10^3$ [511].

Theoretically, the most immediate way to obtain a space–time variation of the electromagnetic fine–structure constant[5] is to introduce a non–minimal coupling between the scalar field and electromagnetic fields [512–516]. It has been shown that such a non–minimal coupling gives rise to nonconservation of the photon number along geodesics [517] which results in a modification of the distance–duality relation [131, 512, 518–522] (see chapter 1) and CMB spectrum distortions [512, 523, 524], where the latter was thoroughly discussed in chapter 2. Similar results have also been reported in disformal scalar–tensor theories [472, 525–527]. We will now show that such non–minimal coupling is not necessary to instigate a non–zero variation of α, as we can reproduce a varying electromagnetic fine–structure coupling purely by the introduced disformally related metrics. We presented this model in Ref. [2].

Similar to the set–up that was introduced in section 4.1, here we consider the following action, respectively consisting of a gravitational sector, a matter sector,

[4] We remark that, since the variable α was used in the previous sections in a different context, we chose to adopt the same variable to denote the electromagnetic fine–structure constant in accordance with its standard notation.

[5] Since the electromagnetic fine–structure constant is now a dynamical quantity, we will often refer to the space–time varying α by the fine–structure coupling instead of a constant.

and an electromagnetic sector:

$$\mathcal{S} = \mathcal{S}_{\text{grav}}\left(g_{\mu\nu}, \phi\right) + \mathcal{S}_{\text{matter}}\left(\tilde{g}^{(m)}_{\mu\nu}\right) + \mathcal{S}_{\text{EM}}\left(A_{\mu}, \tilde{g}^{(r)}_{\mu\nu}\right). \tag{4.57}$$

The metrics $\tilde{g}^{(m)}_{\mu\nu}$ and $\tilde{g}^{(r)}_{\mu\nu}$, are related to $g_{\mu\nu}$, via a disformal transformation:

$$\tilde{g}^{(m)}_{\mu\nu} = C_m g_{\mu\nu} + D_m \phi_{,\mu}\phi_{,\nu} \ , \tag{4.58}$$

$$\tilde{g}^{(r)}_{\mu\nu} = \ C_r g_{\mu\nu} + D_r \phi_{,\mu}\phi_{,\nu} \ . \tag{4.59}$$

Here, $C_{r,m}$ and $D_{r,m}$ are functions of the scalar field ϕ, and we recall that, the functions $C_{r,m}$ are conformal factors, whereas the functions $D_{r,m}$ are disformal couplings. At this point, we do not specify the gravitational sector. Instead, we study the consequences of the disformally coupled scalar field on the propagation of electromagnetic waves. We aim to work in the Jordan frame, by which we mean the frame in which matter is decoupled from the scalar degree of freedom. We therefore perform a disformal transformation of the action above such that all parts of the action are written in terms of the metric $\tilde{g}^{(m)}_{\mu\nu}$. The electromagnetic sector is specified by

$$\mathcal{S}_{\text{EM}} = -\frac{1}{4}\int \mathrm{d}^4x\sqrt{-\tilde{g}^{(r)}}h(\phi)\tilde{g}^{\mu\nu}_{(r)}\tilde{g}^{\alpha\beta}_{(r)}F_{\mu\alpha}F_{\nu\beta} - \int \mathrm{d}^4x\sqrt{-\tilde{g}^{(m)}}\tilde{g}^{\mu\nu}_{(m)}j_{\mu}A_{\nu} \ , \tag{4.60}$$

where $F_{\mu\nu}$ is the standard antisymmetric Faraday tensor, specified by $F_{\mu\nu} = \partial_{\mu}A_{\nu} - \partial_{\nu}A_{\mu}$, with A^{μ} and j^{μ} being the electromagnetic vector potential and four–current, respectively. The function $h(\phi)$, is the direct coupling between the electromagnetic field and the scalar. A useful expression for $\tilde{g}^{(r)}_{\mu\nu}$, is given by

$$\tilde{g}^{(r)}_{\mu\nu} = \frac{C_r}{C_m}\tilde{g}^{(m)}_{\mu\nu} + \left(D_r - \frac{C_r D_m}{C_m}\right)\phi_{,\mu}\phi_{,\nu} \equiv A\tilde{g}^{(m)}_{\mu\nu} + B\phi_{,\mu}\phi_{,\nu} \ . \tag{4.61}$$

Thence, in terms of this metric, the electromagnetic sector becomes

$$\begin{aligned}\mathcal{S}_{\text{EM}} = &-\frac{1}{4}\int \mathrm{d}^4x\sqrt{-\tilde{g}^{(m)}}h(\phi)Z_{\alpha}\left[\tilde{g}^{\mu\nu}_{(m)}\tilde{g}^{\alpha\beta}_{(m)} - 2\gamma^2\tilde{g}^{\mu\nu}_{(m)}\phi^{,\alpha}\phi^{,\beta}\right]F_{\mu\alpha}F_{\nu\beta} \\ &- \int \mathrm{d}^4x\sqrt{-\tilde{g}^{(m)}}\tilde{g}^{\mu\nu}_{(m)}j_{\mu}A_{\nu} \ ,\end{aligned} \tag{4.62}$$

where we raise the indices with the metric $\tilde{g}^{(m)}_{\mu\nu}$, and define

$$Z_{\alpha} = \left(1 + \frac{B}{A}\tilde{g}^{\mu\nu}_{(m)}\partial_{\mu}\phi\partial_{\nu}\phi\right)^{1/2} , \tag{4.63}$$

along with

$$\gamma^2 = \frac{B}{A + B\tilde{g}^{\mu\nu}_{(m)}\partial_\mu\phi\partial_\nu\phi} \ . \tag{4.64}$$

Note that the term proportional to γ^4 vanishes due to the antisymmetry of $F_{\mu\nu}$. Furthermore, note that gauge invariance implies $\widetilde{\nabla}_\mu j^\mu = 0$, where the covariant derivative is compatible with the metric $\tilde{g}^{(m)}_{\mu\nu}$. The field equations can be readily obtained by varying the action with respect to A_μ, which results in

$$\widetilde{\nabla}_\epsilon \left(h(\phi) Z_\alpha F^{\epsilon\rho}\right) - \widetilde{\nabla}_\epsilon \left(h(\phi) Z_\alpha \gamma^2 \phi^{,\beta} \left(\tilde{g}^{\epsilon\nu}_{(m)}\phi^{,\rho} - \tilde{g}^{\rho\nu}_{(m)}\phi^{,\epsilon}\right) F_{\nu\beta}\right) = j^\rho \ , \tag{4.65}$$

where we again raise the indices with $\tilde{g}^{(m)}_{\mu\nu}$. The first term in the action (4.62) contains two parts: the first part consists of the kinetic term for the vector potential A_μ; the second part is an interaction term between the disformally coupled scalar field and A_μ. The latter vanishes in the case of vanishing disformal couplings. From the form of the action (4.62) we might naively think that, the fine–structure coupling is simply given by $\alpha \propto 1/(h(\phi)Z_\alpha)$. This is not the case, as we shall show.

To identify the effective electromagnetic coupling (or the fine–structure constant) α, we start by deriving the field equation for the electric field in Minkowski space, where we set $\tilde{g}^{(m)}_{\mu\nu} = \eta_{\mu\nu}$, and further consider the bare speed of light $c = 1$. We also assume that the scalar field is a function of time only. From the obtained field equation (4.65), and using the fact that the electric field is identified by $E^i = F^{i0}$, we find that the field equation for the electric field reduces to

$$\nabla \cdot \boldsymbol{E} = \frac{Z_\alpha \rho}{h(\phi)} \ , \tag{4.66}$$

where $\rho = j^0$ is the charge density. By integrating this equation over a volume $\mathcal{V}$, it is straightforward to derive the electrostatic potential $V_E(r)$ (for which $\boldsymbol{E} = -\nabla V_E$) at a distance r, which is found to be $V_E(r) = Z_\alpha Q/(4\pi h(\phi) r)$, where Q is the total charge contained in $\mathcal{V}$. Comparing this to the standard expression for the tree–level–potential from Quantum Electrodynamics, one finds that α has the following simple dependence on Z_α and $h(\phi)$:

$$\alpha \propto \frac{Z_\alpha}{h(\phi)} \ . \tag{4.67}$$

Note that if matter and radiation couple in the same way to the scalar field (in which $\tilde{g}^{(m)}_{\mu\nu} = \tilde{g}^{(r)}_{\mu\nu}$, such that $A = 1$ and $B = 0$) we have $Z_\alpha = 1$, and we recover the usual form of $\alpha \propto 1/h(\phi)$ [469, 512, 528–534].

4.6.1 Cosmological evolution

For clarity, we rewrite the adopted gravitational–scalar action

$$\mathcal{S}_{\text{grav}}\left(g_{\mu\nu},\phi\right)=\int \mathrm{d}^4x\sqrt{-g}\left(\frac{M_{\text{Pl}}^2}{2}R-\frac{1}{2}g^{\mu\nu}\partial_\mu\phi\partial_\nu\phi-V(\phi)\right)\,, \tag{4.68}$$

where R is the Ricci scalar calculated with respect to the metric $g_{\mu\nu}$. For simplicity, in this section we will adopt the reduced Planck units by setting $M_{\text{Pl}}=1$. Hence, the theory we consider is given in the Einstein frame by the following action

$$\begin{aligned}\mathcal{S}=&\int \mathrm{d}^4x\sqrt{-g}\left(\frac{1}{2}R-\frac{1}{2}g^{\mu\nu}\partial_\mu\phi\partial_\nu\phi-V(\phi)\right)+\mathcal{S}_{\text{matter}}\left(\tilde{g}^{(m)}_{\mu\nu}\right)\\&-\frac{1}{4}\int \mathrm{d}^4x\sqrt{-\tilde{g}^{(r)}}h(\phi)\tilde{g}^{\mu\nu}_{(r)}\tilde{g}^{\alpha\beta}_{(r)}F_{\mu\alpha}F_{\nu\beta}\,.\end{aligned} \tag{4.69}$$

The last term in the action above describes the dynamics of the CMB photons. From now on, we will refer to the three distinctive frames as the Einstein frame, radiation frame, and Jordan frame, corresponding to the metrics $g_{\mu\nu}$, $\tilde{g}^{(r)}_{\mu\nu}$, and $\tilde{g}^{(m)}_{\mu\nu}$, respectively. We define the radiation frame as the frame in which all electromagnetic quantities are defined in their standard way. Furthermore, we define the Jordan frame as the frame in which matter is decoupled from the scalar field. As we have seen in the previous sections of this chapter, the gravity–scalar part of the action is written in its simplest form in the Einstein frame, thus, we will be working in this frame and not in the other two frames where in general this part of the action has a non–standard form.

By the variation of the action (4.69) with respect to the metric $g_{\mu\nu}$, we obtain the Einstein field equations

$$G^{\mu\nu}=T^{\mu\nu}_{\phi}+T^{\mu\nu}_{(m)}+T^{\mu\nu}_{(r)}\,, \tag{4.70}$$

where $G_{\mu\nu}=R_{\mu\nu}-\frac{1}{2}g_{\mu\nu}R$ is the usual Einstein tensor in the Einstein frame, with the Ricci tensor denoted by $R_{\mu\nu}$. We recall that, the energy–momentum tensors of the scalar field, matter, and radiation are denoted by $T^{\mu\nu}_{\phi}$, $T^{\mu\nu}_{(m)}$, and $T^{\mu\nu}_{(r)}$, respectively. We specify these energy–momentum tensors as follows

$$T^{\phi}_{\mu\nu} = \partial_\mu\phi\partial_\nu\phi - g_{\mu\nu}\left(\frac{1}{2}g^{\rho\sigma}\partial_\rho\phi\partial_\sigma\phi + V(\phi)\right) , \tag{4.71}$$

$$T^{(m)}_{\mu\nu} = -\frac{2}{\sqrt{-g}}\frac{\delta\left(\sqrt{-\tilde{g}^{(m)}}\widetilde{\mathcal{L}}_m\right)}{\delta g^{\mu\nu}} , \tag{4.72}$$

$$T^{(r)}_{\mu\nu} = -\frac{2}{\sqrt{-g}}\frac{\delta\left(\sqrt{-\tilde{g}^{(r)}}\widetilde{\mathcal{L}}_{EM}\right)}{\delta g^{\mu\nu}} , \tag{4.73}$$

where we define the electromagnetic Lagrangian by $\widetilde{\mathcal{L}}_{EM} = -\frac{1}{4}h(\phi)\tilde{g}^{\mu\nu}_{(r)}\tilde{g}^{\alpha\beta}_{(r)}F_{\mu\alpha}F_{\nu\beta}$, and denote the matter Lagrangian by $\widetilde{\mathcal{L}}_m$. We now use the variation of the action (4.69) with respect to the scalar field, which leads us to the Klein–Gordon equation

$$\Box\phi - V' = -Q_m - Q_r , \tag{4.74}$$

where, in this section, we denote a derivative with respect to the scalar field by a prime. Moreover, we have introduced a matter coupling strength Q_m, and a radiation coupling strength Q_r, given by

$$Q_m = \frac{C'_m}{2C_m}T_{(m)} + \frac{D'_m}{2C_m}\phi_{,\mu}\phi_{,\nu}T^{\mu\nu}_{(m)} - \nabla_\mu\left[\frac{D_m}{C_m}\phi_{,\nu}T^{\mu\nu}_{(m)}\right] , \tag{4.75}$$

$$Q_r = \frac{C'_r}{2C_r}T_{(r)} + \frac{D'_r}{2C_r}\phi_{,\mu}\phi_{,\nu}T^{\mu\nu}_{(r)} + \frac{h'}{h}C_r^2\sqrt{1+\frac{D_r}{C_r}g^{\mu\nu}\phi_{,\mu}\phi_{,\nu}}\,\widetilde{\mathcal{L}}_{EM} - \nabla_\mu\left[\frac{D_r}{C_r}\phi_{,\nu}T^{\mu\nu}_{(r)}\right] , \tag{4.76}$$

where $T_{(r)}$ and $T_{(m)}$, are the trace of $T^{\mu\nu}_{(r)}$ and $T^{\mu\nu}_{(m)}$, respectively. We note that for Eq. (4.76) we have also used Eq. (B.4), which we give in appendix B along with other useful variable transformations. As a result of the Bianchi identities, the total energy–momentum tensor in the Einstein frame is covariantly conserved with respect to the Einstein frame metric, leading to the following conservation equation

$$\nabla_\mu\left(T^{\mu\nu}_{\phi} + T^{\mu\nu}_{(m)} + T^{\mu\nu}_{(r)}\right) = 0 . \tag{4.77}$$

Although this holds for the total energy–momentum tensor, the couplings under consideration do not allow each of the energy–momentum tensors to be individually conserved. Indeed, by using Eqs. (4.71), (4.74), and (4.77), we find that the matter

and radiation conservation equations now read as follows

$$\nabla_{\mu} T^{\mu}_{(m)\nu} = Q_m \phi_{,\nu} \ , \tag{4.78}$$

$$\nabla_{\mu} T^{\mu}_{(r)\nu} = Q_r \phi_{,\nu} \ , \tag{4.79}$$

where a similar derivation is described in Refs. [470, 472, 535–537]. We shall now consider perfect fluid energy–momentum tensors for radiation and matter in the Einstein frame

$$T^{\mu\nu}_{(r)} = (\rho_r + p_r) u^{\mu} u^{\nu} + p_r g^{\mu\nu}, \tag{4.80}$$

$$T^{\mu\nu}_{(m)} = (\rho_m + p_m) u^{\mu} u^{\nu} + p_m g^{\mu\nu}, \tag{4.81}$$

where ρ_r and p_r, are the Einstein frame radiation energy density and pressure, respectively. Similarly, ρ_m and p_m are the Einstein frame matter energy density and pressure, respectively, and u^{μ} is the Einstein frame four–velocity. By projecting the matter and radiation conservation equations along the four–velocity, we obtain the following modified conservation equations

$$u^{\mu} \nabla_{\mu} \rho_r + (\rho_r + p_r) \nabla_{\mu} u^{\mu} = -Q_r u^{\mu} \phi_{,\mu} \ , \tag{4.82}$$

$$u^{\mu} \nabla_{\mu} \rho_m + (\rho_m + p_m) \nabla_{\mu} u^{\mu} = -Q_m u^{\mu} \phi_{,\mu} \ . \tag{4.83}$$

These modified conservation equations show that energy is transferred from the scalar field, depicted by the term projecting the field gradient along the four–velocity. We also define a perfect fluid energy–momentum tensor for both radiation and matter in the respective radiation frame and Jordan frame, given by

$$\widetilde{T}^{\mu\nu}_{(r)} = (\tilde{\rho}_r + \tilde{p}_r) \tilde{u}^{\mu} \tilde{u}^{\nu} + \tilde{p}_r \tilde{g}^{\mu\nu}_{(r)} \ , \tag{4.84}$$

$$\widetilde{T}^{\mu\nu}_{(m)} = (\tilde{\rho}_m + \tilde{p}_m) \tilde{u}^{\mu} \tilde{u}^{\nu} + \tilde{p}_m \tilde{g}^{\mu\nu}_{(m)} \ . \tag{4.85}$$

Following the adopted approach of the previous sections, we will be considering a time–dependent scalar field, and a spatially flat FLRW Einstein frame metric, with expansion scale factor $a(t)$. Furthermore, we introduce the following electromagnetic parametrisation[6] [514]

$$\eta \equiv \frac{\widetilde{\mathcal{L}}_{EM}}{\tilde{\rho}_r} \ , \tag{4.86}$$

where η could be positive or negative and have a modulus between 0 and ≈ 1.

[6] Not to be confused with the conformal time variable of chapter 1.

We should note that in Ref. [514] they associate the η parameter with matter energy density and not with radiation energy density. Also, by setting $\eta = 1$ in the introduced electromagnetic parametrisation, and considering the special case of $C_r(\phi) = C_m(\phi) = 1$, together with $D_r(\phi) = D_m(\phi) = 0$, we recover all the relevant equations given in Ref. [512], in which a statistical microscopic approach was employed. Using Eq. (B.10), we obtain the following relationship between the energy density in the radiation frame and that in the Einstein frame

$$\tilde{\rho}_r = \frac{\rho_r}{C_r^2}\sqrt{1 + \frac{D_r}{C_r}\phi_{,\mu}\phi^{,\mu}}\,. \tag{4.87}$$

Hence, we can now write the radiation coupling parameter Q_r, in terms of this η–parametrisation, as follows

$$Q_r = \frac{C_r'}{2C_r}T_{(r)} + \frac{D_r'}{2C_r}\phi_{,\mu}\phi_{,\nu}T^{\mu\nu}_{(r)} + \frac{h'(\phi)}{h(\phi)}\left[1 + \frac{D_r}{C_r}\phi_{,\mu}\phi^{,\mu}\right]\eta\rho_r - \nabla_\mu\left[\frac{D_r}{C_r}\phi_{,\nu}T^{\mu\nu}_{(r)}\right]. \tag{4.88}$$

For FLRW cosmology, we find that the Klein–Gordon equation (4.74), together with the conservation equations (4.78)–(4.79), reduce to the following set of equations

$$\ddot{\phi} + 3H\dot{\phi} + V' = Q_m + Q_r\,, \tag{4.89}$$

$$\dot{\rho}_m + 3H(\rho_m + p_m) = -Q_m\dot{\phi}\,, \tag{4.90}$$

$$\dot{\rho}_r + 3H(\rho_r + p_r) = -Q_r\dot{\phi}\,, \tag{4.91}$$

where $H = \dot{a}/a$ is the Hubble parameter, and a dot represents an Einstein frame time derivative. By using Eqs. (4.89), (4.90), and (4.91), we can rewrite Eq. (4.75) and Eq. (4.88) in an analogous form to Eqs. (4.22)–(4.25), as follows

$$Q_m = \frac{A_r}{A_rA_m - D_rD_m\rho_r\rho_m}\left[B_m - \frac{D_mB_r}{A_r}\rho_m\right]\,, \tag{4.92}$$

$$Q_r = \frac{A_m}{A_rA_m - D_rD_m\rho_r\rho_m}\left[B_r - \frac{D_rB_m}{A_m}\rho_r\right]\,, \tag{4.93}$$

where

$$A_r = C_r + D_r\left(\rho_r - \dot{\phi}^2\right) , \tag{4.94}$$

$$A_m = C_m + D_m\left(\rho_m - \dot{\phi}^2\right) , \tag{4.95}$$

$$\begin{aligned} B_r = &\left\{\frac{1}{2}C_r'\left(3w_r - 1\right) - \frac{1}{2}D_r'\dot{\phi}^2 + \frac{h'(\phi)}{h(\phi)}\left(C_r - D_r\dot{\phi}^2\right)\eta\right. \\ &\left. + D_r\left[\frac{C_r'}{C_r}\dot{\phi}^2 + V' + 3H\dot{\phi}\left(1 + w_r\right)\right]\right\}\rho_r , \end{aligned} \tag{4.96}$$

$$B_m = \left\{\frac{1}{2}C_m'\left(3w_m - 1\right) - \frac{1}{2}D_m'\dot{\phi}^2 + D_m\left[\frac{C_m'}{C_m}\dot{\phi}^2 + V' + 3H\dot{\phi}\left(1 + w_m\right)\right]\right\}\rho_m . \tag{4.97}$$

Using Eq. (B.12), it follows that for pressureless matter, the equation of state parameter in both frames is identically zero. However, according to Eq. (B.12), the equation of state parameter for radiation in the Einstein frame is now modified to [472, 485]

$$w_r = \frac{1}{3}\left(1 - \frac{D_r}{C_r}\dot{\phi}^2\right), \tag{4.98}$$

where we have used the fact that in the radiation frame $\widetilde{w}_r = 1/3$. We find that the respective exact solutions for Eq. (4.90) and Eq. (4.91), are given by

$$\rho_m \propto \frac{C_m^2}{Y_m}\left(aC_m^{\frac{1}{2}}\right)^{-3}, \tag{4.99}$$

$$\rho_r \propto \frac{C_r^2}{h^\eta Y_r}\left(aC_r^{\frac{1}{2}}\right)^{-4}, \tag{4.100}$$

where we define $Y_m^2 = 1 - (D_m/C_m)\dot{\phi}^2$, $Y_r^2 = 1 - (D_r/C_r)\dot{\phi}^2$, and assume constant η in Eq. (4.100). As expected, we find that $\tilde{\rho}_m \propto \tilde{a}_{(m)}^{-3}$, where $\tilde{a}_{(m)}$ is the scale factor in the Jordan frame, and that $\tilde{\rho}_r \propto h^{-\eta}\tilde{a}_{(r)}^{-4}$, where $\tilde{a}_{(r)}$ is the radiation frame scale factor.

From the field equations (4.70), we derive the Friedmann equations in the Einstein frame, given by

$$H^2 = \frac{1}{3}\left(\rho_m + \rho_r + \rho_\phi\right), \tag{4.101}$$

$$\dot{H} = -\frac{1}{6}\left[3\left(\rho_m + \dot{\phi}^2\right) + \rho_r\left(4 - \frac{D_r}{C_r}\dot{\phi}^2\right)\right], \tag{4.102}$$

where we have also used Eq. (4.98), and defined the energy–momentum tensor of the scalar field as that of a perfect fluid with $\rho_\phi = (1/2)\dot{\phi}^2 + V(\phi)$, and $p_\phi = (1/2)\dot{\phi}^2 - V(\phi)$. We admit that the scalar field characterising the disformal coupling is also responsible for the current accelerated expansion of the Universe, thence, it is the dark energy. In order to compare our model's dark energy equation of state parameter to a supernovae Type Ia (SNIa) data set [538], we need to derive an effective equation of state parameter[7] $w_{\rm eff}$, following Refs. [485, 539]. We remark that, experimental constraints on dark energy assume a non–interacting dark sector. Thence, on assuming that dark energy is given by a non–interacting perfect fluid, described by its equation of state parameter $w_{\rm eff}$, we can write the energy conservation equation as follows

$$\dot{\rho}^{\rm eff}_{\rm DE} = -3H\left(1 + w_{\rm eff}\right)\rho^{\rm eff}_{\rm DE}\,. \tag{4.103}$$

By our dark sector assumption, dark matter is also assumed to be non–interacting, hence we can write the following Friedmann equation

$$H^2 = \frac{1}{3}\left(a^{-4}\rho_{r,0} + a^{-3}\rho_{m,0} + \rho^{\rm eff}_{\rm DE}\right), \tag{4.104}$$

where we recall that, we denote present–day quantities by a 0–subscript. By comparing Eq. (4.104) with Eq. (4.101), we get the energy density of the effective dark energy fluid

$$\rho^{\rm eff}_{\rm DE} = \rho_m + \rho_r + \rho_\phi - a^{-4}\rho_{r,0} - a^{-3}\rho_{m,0}\,. \tag{4.105}$$

After taking the Einstein frame time derivative of Eq. (4.105), substituting the Klein–Gordon equation (4.89), the matter conservation equation (4.90), the radiation conservation equation (4.91), and comparing the final equation with Eq. (4.103), we arrive at the effective equation of state parameter

$$w_{\rm eff} = \frac{p_\phi + \rho_r\left(w_r - \frac{1}{3}a^{-4}\frac{\rho_{r,0}}{\rho_r}\right)}{\rho^{\rm eff}_{\rm DE}}\,, \tag{4.106}$$

where w_r is the equation of state parameter for radiation in the Einstein frame, specified by Eq. (4.98). We should mention that, in the absence of the radiation,

[7] We remark that, this should not be confused with the variable defined in section 4.2.

matter, and electromagnetic couplings, w_{eff} reduces to the usual equation of state parameter for a quintessence scalar field of $w_\phi = p_\phi/\rho_\phi$.

4.6.2 Observational constraints

We will only consider a choice of parameters for our models in accordance with the reported cosmological, astrophysical, geochemical, and laboratory measurements. Since we now have identified the fine–structure coupling $\alpha \propto Z_\alpha/h(\phi)$, we can also define the temporal variation of α, which we denote by $\dot{\alpha}/\alpha$, where dot refers to the temporal derivative. As we are interested in solving our equations in a spatially flat FLRW metric, with a time–dependent scalar field, we here give the temporal variation of α in the mentioned setting. In this scenario, the coupling function Z_α, defined in Eq. (4.63), reduces to

$$Z_\alpha = \left(\frac{1 - \frac{D_r}{C_r}\dot{\phi}^2}{1 - \frac{D_m}{C_m}\dot{\phi}^2}\right)^{\frac{1}{2}} . \tag{4.107}$$

Furthermore, by considering the electromagnetic coupling $h(\phi)$, along with the scalar field dependent conformal and disformal couplings, it follows that $Z_\alpha = Z_\alpha\big(\phi, \dot{\phi}\big)$. We then arrive to the equation for the temporal variation of the fine–structure coupling, given by

$$\frac{\dot{\alpha}}{\alpha} = \frac{1}{Z_\alpha}\left(\frac{\partial Z_\alpha}{\partial \phi}\dot{\phi} + \frac{\partial Z_\alpha}{\partial \dot{\phi}}\ddot{\phi}\right) - \frac{1}{h}\frac{dh}{d\phi}\dot{\phi} . \tag{4.108}$$

Also, the redshift evolution of the fine–structure coupling is specified by the quantity[8]

$$\frac{\Delta\alpha}{\alpha}(z) \equiv \frac{\alpha(z) - \alpha(z=0)}{\alpha(z=0)} = \frac{h(\phi_0)Z_\alpha(z)}{h(\phi(z))Z_{\alpha,0}} - 1 , \tag{4.109}$$

where ϕ_0 is the present–day scalar field value, and $Z_{\alpha,0}$ is the current value of Z_α. In the absence of disformal couplings, we recover the usual forms of the temporal variation and evolution of the fine–structure coupling, as reported in Refs. [469, 512, 528–534]. In order to choose our parameters, we will make use of the following:

1. the Union2.1 SNIa data set [538] and the *Planck* collaboration results [65], such that the present time cosmic parameter values are in accordance with our final time boundary conditions. These results are summarised in Table 4.9. Since we are using a spatially flat FLRW Einstein frame metric, it follows that $\Omega_{\phi,0} \approx 0.7$.

[8] Note that the redshift is frame–invariant; see Ref. [472] and Ref. [526] for more details.

Parameter	Estimated value	Ref.
$w_{\phi,0}$	-1.006 ± 0.045	[65]
H_0	(67.8 ± 0.9) km s^{-1} Mpc^{-1}	[65]
$\Omega_{m,0}$	0.308 ± 0.012	[65]

Table 4.9: Listed are, respectively, the cosmological parameter, its estimated value, and the original reference.

2. the currently, most stringent atomic clock (AC) constraint on the present temporal variation of α [509]

$$\left.\frac{\dot{\alpha}}{\alpha}\right|_0 = (-1.6 \pm 2.3) \times 10^{-17}\ \mathrm{yr}^{-1}, \tag{4.110}$$

3. an Oklo natural reactor constraint, in which self–sustained natural fission reactions took place at around 2 Gyr ago ($z \approx 0.16$) [507, 508]

$$\frac{|\Delta\alpha|}{\alpha} < 1.1 \times 10^{-8}, \tag{4.111}$$

4. the ^{187}Re meteorite constraint over the age of the solar system of around 4.6 Gyr ($z \approx 0.43$) [506]

$$\frac{\Delta\alpha}{\alpha} = (-8 \pm 8) \times 10^{-7}, \tag{4.112}$$

5. astrophysical data, including the eleven data points from the recently reported data set, which contains the results of the Ultraviolet and Visual Echelle Spectrograph (UVES) [499, 500]. We list these measurements in Table 4.10, and plot the corresponding data points for the redshift evolution of $\Delta\alpha/\alpha$ in the figures of section 4.6.3. We also use the large data set from Keck telescope and ESO's Very Large Telescope (VLT) surveys [494]. By assuming that $\Delta\alpha/\alpha$ measurements are specified by a simple weighted mean, it is found that $(\Delta\alpha/\alpha)_{\mathrm{w}} = (-0.57 \pm 0.11) \times 10^{-5}$ [504] for the Keck quasi–stellar object (QSO) observations, while for the VLT quasar spectra observations, we have

$(\Delta\alpha/\alpha)_{\rm w} = (0.208 \pm 0.124) \times 10^{-5}$ [502]. These results differ from one another at around 4.7σ, suggesting a dipole–like variation in α. The binned many–multiplet (MM) VLT + Keck combined sample is also used in our $\Delta\alpha/\alpha$ redshift evolution plots, in which the statistical errors for certain points have been increased prior to binning, as described in Ref. [502]. We also use the weighted mean of the twenty–one Si IV doublets of $(\Delta\alpha/\alpha)_{\rm w} = (-0.5 \pm 1.3) \times 10^{-5}$ [505], where the alkali–doublet (AD) method was implemented. Moreover, we include two other measurements of $\Delta\alpha/\alpha = (-0.10 \pm 0.22) \times 10^{-5}$ at $z = 0.25$, and $\Delta\alpha/\alpha = (-0.08 \pm 0.27) \times 10^{-5}$ at $z = 0.68$, for which HI 21 cm absorption lines were used [501]. Other consistent results can be found in Ref. [503], and a detailed review on the constraints of $\Delta\alpha/\alpha$ is given in Refs. [493, 534, 540].

6. the CMB radiation constraint ($z \sim 10^3$) of [511]

$$\frac{\Delta\alpha}{\alpha} = (3.6 \pm 3.7) \times 10^{-3}, \tag{4.113}$$

7. and finally, constraints coming from axion–like particle searches, such as shining–light–through–a–wall experiments, which are capable of putting a constraint on D_r. For instance, when matter fields and photons are coupled in the same way to the scalar field, an upper bound on a constant radiation coupling of $D_r^{-1/4} \lesssim 10^{-11}$ GeV was placed [525]. We remark that, we fulfil[9] this upper bound in our examples of section 4.6.3.

The models presented in section 4.6.3 satisfy the above constraints, even though, there are parameter combinations that lead to cases which do not respect the Oklo bound. For example, some models in Fig. 4.12 do not pass the Oklo bound.

Before we compare our models with observational data, we remark that, in terms of the dynamical system variables introduced in Eqs. (4.26)–(4.27), the fine–structure coupling simplifies to

$$\alpha \propto \frac{Z_r}{Z_m}\,, \tag{4.114}$$

[9] Following the reported observations of gravitational–waves [16] along with its optical counterpart [17] from the binary neutron star merger GW170817 [18], very stringent constraints are now placed [439] on a constant radiation disformal coupling. Other constraints have been reported in Refs. [527, 541].

Object	z	$(\Delta\alpha/\alpha) \times 10^6$	Spectrograph	Ref.
Three sources	1.08	4.3 ± 3.4	HIRES	[495]
HS1549+1919	1.14	-7.5 ± 5.5	UVES/HIRES/HDS	[500]
HE0515-4414	1.15	-0.1 ± 1.8	UVES	[496]
HE0515-4414	1.15	0.5 ± 2.4	HARPS/UVES	[497]
HS1549+1919	1.34	-0.7 ± 6.6	UVES/HIRES/HDS	[500]
HE0001-2340	1.58	-1.5 ± 2.6	UVES	[498]
HE1104-1805A	1.66	-4.7 ± 5.3	HIRES	[495]
HE2217-2818	1.69	1.3 ± 2.6	UVES	[499]
HS1946+7658	1.74	-7.9 ± 6.2	HIRES	[495]
HS1549+1919	1.80	-6.4 ± 7.2	UVES/HIRES/HDS	[500]
Q1101-264	1.84	5.7 ± 2.7	UVES	[496]

Table 4.10: Listed are, respectively, the object along each line of sight, the redshift of the absorber, the measurements of $\Delta\alpha/\alpha$, the spectrograph, and the original reference. The first measurement is the weighted average from eight absorbers in the redshift range $0.73 < z < 1.53$, along the lines of sight of three quasars reported in Ref. [495].

where the variable Z_i is defined by Eq. (4.40), and we use subscripts r and m for radiation and matter, respectively. Thence, the evolution of the fine–structure coupling can be written as

$$\frac{\Delta\alpha}{\alpha} = \left(\frac{Z_r}{Z_m}\right)\left(\frac{Z_m^0}{Z_r^0}\right) - 1 \,, \tag{4.115}$$

where $Z_m^0 = Z_m(z = 0)$ and $Z_r^0 = Z_r(z = 0)$. From Eq. (4.114), it is evident that for a disformal fixed point which is characterised by a metric singularity in either the radiation metric or the matter metric, the fine–structure coupling cannot be defined. This observation supports the arguments presented in Ref. [480], in which such fixed points were considered as unviable fixed points. However, one could consider a trajectory such that the system discussed in section 4.4.1 reaches

$(5)_{(r)}$ at BBN, and evolve towards the attractor $(8)_{(d)}$, in which case Eq. (4.115) reduces to $\Delta\alpha/\alpha = \sqrt{1+4/\left(2-3\beta_r^2\right)}-1$. By considering this evolution, and by using a conservative BBN constraint of $|\Delta\alpha/\alpha| < 6\times10^{-2}$ [488, 540], we get that $|\beta_r| > 3.48$.

4.6.3 Current status

For the following analyses, we will adopt these specific forms of couplings and scalar field potential:

$$C_i(\phi) = \Upsilon_i e^{x_i\phi}\ , \tag{4.116}$$

$$D_i(\phi) = M_i^{-4} e^{y_i\phi}\ , \tag{4.117}$$

$$h(\phi) = 1-\zeta\left(\phi-\phi_0\right)\ , \tag{4.118}$$

$$V(\phi) = M_V^4 e^{-\lambda\phi}\ . \tag{4.119}$$

The introduced mass scales M_i and M_V, are tuned in order to obtain the correct present–day cosmological parameters as listed in Table 4.9, and ensure that we satisfy the constraint on the temporal variation of the fine–structure coupling of Eq. (4.110). Typically, we find that $M_i \sim M_V \sim$ meV. In our models, we will only consider disformally coupled radiation, thence we set $C_r(\phi) = 1$ for all the models under consideration. On the other hand, whenever we consider a scalar field dependent conformal matter coupling, we also tune the dimensionless parameter Υ_m, together with the other mass scales, in order to agree with the reported cosmological parameters of Table 4.9, and the temporal variation of the fine–structure coupling stringent constraint. Following the symmetry breaking argument of Ref. [542] for a slowly evolving time–dependent scalar field, we only consider a linear electromagnetic coupling function. We are constrained on the magnitude of the introduced dimensionless electromagnetic coupling parameter ζ, from local tests of the equivalence principle, which imply that [534]

$$|\zeta_{\rm local}| < 10^{-3}\ . \tag{4.120}$$

Another constraint on ζ was obtained in Ref. [543] using the CMB and large–scale structure data in combination with direct measurements of the expansion of the Universe, and more recently, another tighter constraint was obtained in Ref. [544], in which they reported that $|\zeta| < 5\times10^{-6}$.

We will now consider several models specified by different sets of model parameters. From our numerical results we found that, a change in the magnitude of $|\eta|$ between 0 and 1 has negligible effect on the results, so we set $\eta = 1$ in all the models. We summarise the different parameter values for each specific model in Table

Fig.	M_r	M_m	Υ_m	x_m	$\lvert\zeta\rvert$	M_V	λ	$(\dot{\alpha}/\alpha)\lvert_0 \times 10^{17}$
4.12	$\sim$ meV	$\sim$ meV	1	0	$< 5 \times 10^{-6}$	2.69 meV	0.45	$-2.14 \sim -1.62$
4.13	$\sim$ meV	15 meV	8	0.14	0	2.55 meV	0.45	$-2.41 \sim 0.70$
4.14	$\sim$ meV	15 meV	8	0.14	$< 5 \times 10^{-6}$	2.55 meV	0.45	$-2.10 \sim -1.24$

Table 4.11: Listed are, respectively, the figure reference, the parameter values for each specific model, and the range of $(\dot{\alpha}/\alpha)\lvert_0$, corresponding to the range of parameter values considered in each figure.

4.11, where we have neglected the parameters y_m and y_r, from the table since these parameters are both set to zero for the models shown in Figs. 4.12–4.14, although we do discuss a model with exponential disformal couplings in section 4.6.3.1.

The data points shown in Figs. 4.12–4.14 depicting the redshift evolution of $\Delta\alpha/\alpha$, were taken from section 4.6.2, as described therein. The respective data sets are indicated in the legend of each plot, where UVES + HIRES + HDS + HARPS refers to the compiled data points of Table 4.10. Moreover, for the illustrated limits on $w_{\rm eff}$, we make use of the constraints which were reported with (orange), and without (yellow) SNIa systematics [538]. The dotted and dot–dashed horizontal lines shown in the yellow regions depicting the $w_{\rm eff}$ constraints, indicate the central values of the reported constraints with and without SNIa systematics in each redshift bin, respectively. Although we start integrating our equations from $z = 10^3$, at which we set $\phi_{\rm ini} = 1.5\, M_{\rm Pl}$ as our initial condition, we restrict our plots to the redshift range where observational data is mostly concentrated.

4.6.3.1 Disformal couplings

In our first scenario, we consider disformally coupled radiation and matter in the absence of matter and radiation conformal couplings. Moreover, we set $\zeta = 0$, in order to get a purely disformal case without the addition of an electromagnetic coupling. This purely disformal case is an interesting model to consider, since it still predicts a non–zero variation of the fine–structure coupling, without the need of the conventional electromagnetic coupling. The redshift evolution of $\Delta\alpha/\alpha$, is shown in Fig. 4.12, in which we consider constant matter and radiation disformal couplings. We have also considered a purely disformal case with exponential disformal couplings, by setting $M_m = M_r = 100$ meV, $y_m = 23.5$, and $y_r = 1$, together with $M_V = 4.75$ meV and $\lambda = 2$. The latter two parameters were changed from those presented in

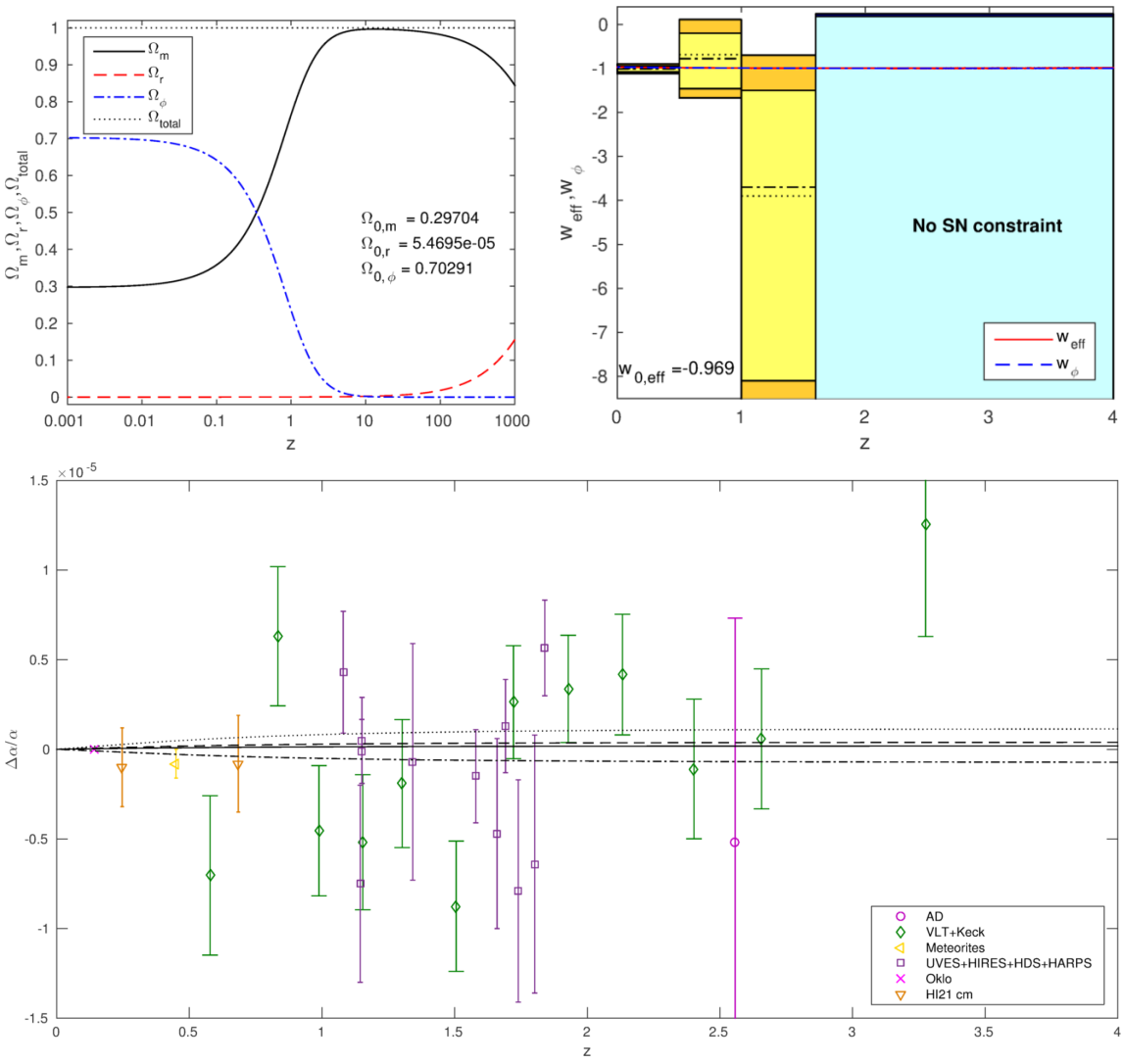

Figure 4.12: Redshift evolution of Ω_i's (left), w_{eff}, w_ϕ (right), and $\Delta\alpha/\alpha$ (bottom) when considering disformally coupled matter and radiation, with and without an electromagnetic coupling. In the bottom plot, the solid line depicts the purely disformal case, whereas the dot–dashed, dashed, and dotted lines correspond to $\zeta = -4.9\times10^{-6},\ 1\times10^{-6},\ 4.9\times10^{-6}$, respectively. The other model parameters are summarised in Table 4.11.

Table 4.11 in order to satisfy the current cosmological parameter constraints, whereas the exponential disformal coupling parameters were chosen such that the calculated temporal variation of the fine–structure coupling lies within the tight bounds of the atomic clock constraint. Since the redshift evolutions of $\Delta\alpha/\alpha$, Ω_i's, w_{eff}, and w_ϕ, for constant disformal and exponential disformal couplings are indistinguishable, we only show the constant disformal couplings case in Fig. 4.12.

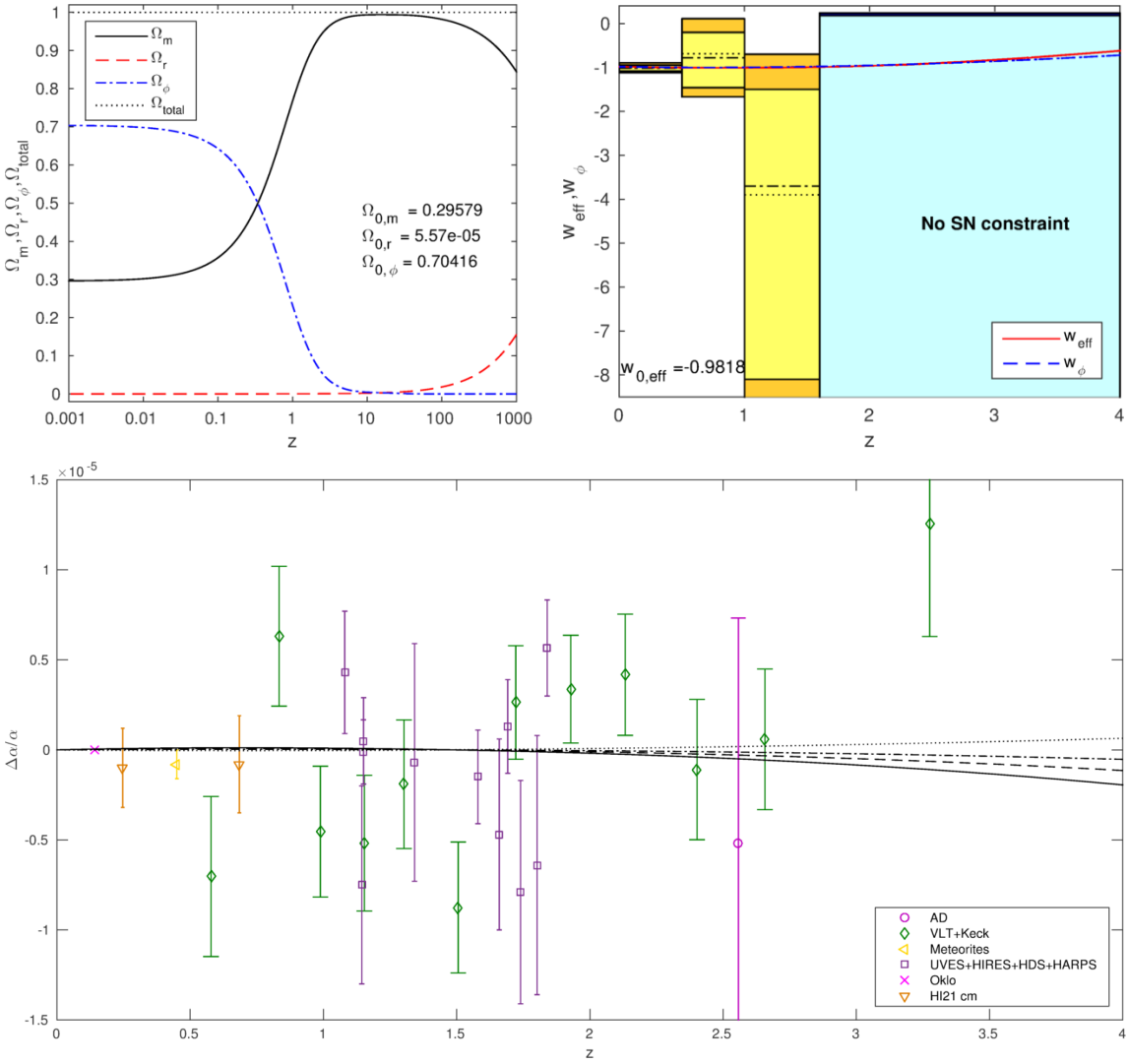

Figure 4.13: Redshift evolution of Ω_i's (left), w_{eff}, w_ϕ (right), and $\Delta\alpha/\alpha$ (bottom) when considering conformally and disformally coupled matter, along with disformally coupled radiation in the absence of an electromagnetic coupling. In the bottom panel, the solid, dashed, dot–dashed, and dotted lines correspond to $M_r = 24.91,\ 25.45,\ 25.91,\ 26.91$ meV, respectively. The other model parameters are summarised in Table 4.11.

4.6.3.2 Conformal & disformal couplings

We now consider matter to be conformally and disformally coupled, together with disformally coupled radiation. Thence, an exponential matter conformal coupling, along with constant disformal matter and radiation couplings are considered, as summarised in Table 4.11. The range of values for the constant disformal couplings

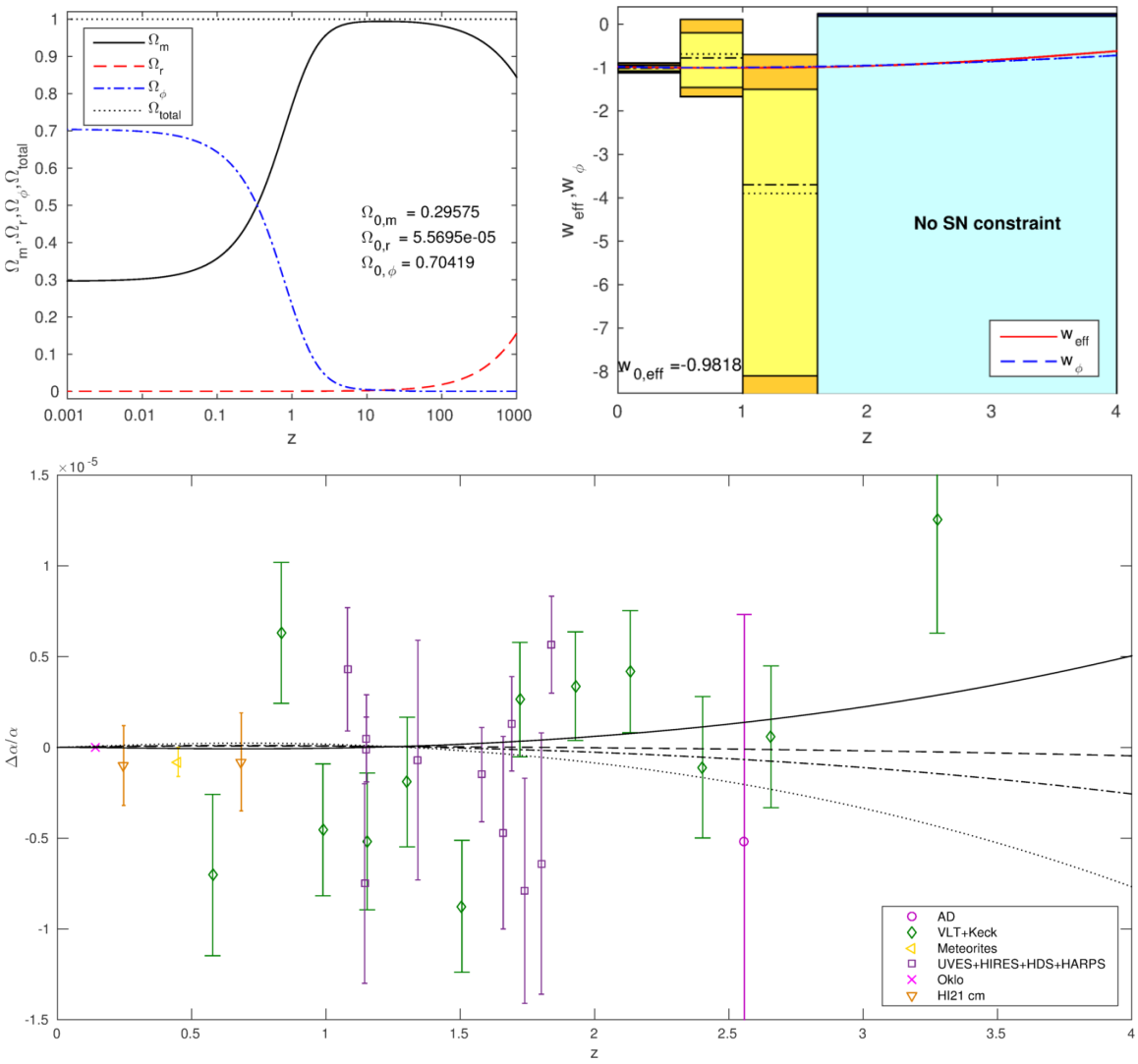

Figure 4.14: Redshift evolution of Ω_i's (left), w_{eff}, w_ϕ (right), and $\Delta\alpha/\alpha$ (bottom) when considering conformally and disformally coupled matter, along with disformally coupled radiation, in the presence of an electromagnetic coupling. In the bottom panel, the solid, dashed, dot–dashed, and dotted lines correspond to $\zeta = -4.9 \times 10^{-6},\ -1 \times 10^{-6},\ 1 \times 10^{-6},\ 4.9 \times 10^{-6}$, respectively. The other model parameters are summarised in Table 4.11.

are chosen, such that the predicted current temporal variation in the fine–structure coupling lies within the limits of the constraint specified by Eq. (4.110), as these are the model parameters which directly influence the evolution of α. We also restrict the values of the other model parameters, mainly the scalar field potential and the conformal matter coupling parameters, in order to be in agreement with the current cosmological values of Table 4.9. Four different constant radiation energy scales are

used in this model, as illustrated in Fig. 4.13. We demonstrate that one can also get a non–zero value for the variation of α, without the introduction of the conventional electromagnetic coupling. In these models $|\Delta\alpha/\alpha|$ at the CMB era, is predicted to be $\mathcal{O}(10^{-8} - 10^{-7})$, which is well within the current bounds.

4.6.3.3 Disformal & electromagnetic couplings

In this case, we consider matter and radiation to be disformally coupled, along with an electromagnetic coupling. We again choose our model parameters, so that we are in agreement with the limits of section 4.6.2. In Fig. 4.12 we only consider constant matter and radiation couplings, as described in Table 4.11. These disformal mass scales together with the non–zero ζ, determine the evolution of the fine–structure coupling. We consider three different values for these parameters, each giving a different redshift evolution of α, although they all predict the same cosmology as long as the other independent parameters are unchanged. The range of $|\Delta\alpha/\alpha|$, for these models at the CMB redshift is $\mathcal{O}(10^{-8} - 10^{-6})$, which lies within the current CMB constraint. In Fig. 4.12 we also plot the purely disformal case, discussed in section 4.6.3.1, in order to see the effect of the electromagnetic coupling on disformally coupled matter and radiation. We can clearly observe that an electromagnetic coupling enhances the cosmological evolution of $\Delta\alpha/\alpha$.

4.6.3.4 Disformal, conformal & electromagnetic couplings

We now combine the previously discussed cases, where we here consider conformally and disformally coupled matter, along with disformally coupled radiation, in the presence of an electromagnetic coupling. We choose a linear electromagnetic coupling as in Eq. (4.118) and an exponential conformal matter coupling. As in the previous cases, we choose our model parameters so that we are in agreement with the limits of section 4.6.2. In Fig. 4.14 we show different theoretical predictions of the variation of α, when considering four different ζ and M_r parameter values, as summarised in Table 4.11. In general, at least for our chosen parameters, we can conclude that the introduction of an electromagnetic coupling slightly enhances the variation of the fine–structure coupling, albeit still in agreement with current observational data. Indeed, for these models, $|\Delta\alpha/\alpha|$ at the CMB era is $\mathcal{O}(10^{-7} - 10^{-6})$, still within the reported CMB constraint.

4.7 Conclusions

In the opening pages of this chapter, we have briefly discussed the emergence of scalar–tensor theories of gravity, which have played a prominent role in the proposal of a vast number of related theories. We have then focused on a generic model,

in which the minimally coupled scalar field was explicitly coupled to multiple fluid components, and performed a thorough analysis of generalised couplings of a scalar field with a single or two matter fluids. More specifically, we first generalised previous literature results by studying a scalar field conformally and disformally coupled to a perfect fluid with an arbitrary equation of state. We investigated the generic existence conditions and evaluated the stability conditions for the particular cases of dust and radiation.

We verified that depending on the value of the logarithmic slope of the disformal coupling $\lambda_D^i = -2(\alpha_i + \beta_i)$, the fixed points may have a region of parameter space that render it stable. In general, the introduction of disformal couplings allows any given fixed point to have a relevant cosmological role at some given epoch of the history of the Universe. For example, the kinetic fixed point for dust turns out to be stable when the disformal coupling is introduced.

We then extended this analysis to a system consisting of two perfect fluids. Here the analysis is far more complex and despite not being able to present results for generic fluids, we were able to understand in detail the cases of a conformal–disformal dust and conformal–disformal radiation, and two conformal–disformal dust components, which are the most relevant cases for cosmological applications. In the case of a conformal dust and conformal–disformal radiation of section 4.4.2, we illustrated an intriguing example of when the radiation component may become important at late–times. We concluded that disformal couplings on their own are repellors, thus the matter metric singularity is safely avoided.

We also looked at some cosmological consequences arising from the obtained fixed points. The introduction of the disformal fixed points lead to an intermediate phase between the radiation era and equivalence, denoted by ϕRDE, and to the modification of an intermediate phase between the matter era and accelerated era, denoted by ϕMDE, where the latter intermediate phase is also present in purely conformal models.

Finally, we illustrated that a varying electromagnetic fine–structure coupling is a characteristic of disformally related metrics. Thus, this offers an alternative mechanism to the conventional non–minimal electromagnetic coupling, which has repeatedly been adopted as a reference model for this phenomenon. In our analyses, we have included this electromagnetic coupling in some of our models, and we observed that this non–minimal coupling enhances the variational evolution of the fine–structure coupling. From our numerical results, we found that when the present temporal variation of the fine–structure coupling constraint is satisfied, the other geochemical and astrophysical constraints are also fulfilled. We should remark that, the Oklo bound is not always satisfied by the chosen model parameters, although we do find some specific models which predict a variation in the fine–structure coupling that fulfil the Oklo constraint. We have also considered the relatively weak

constraint from the CMB, which is well satisfied in all our models. An interesting relationship between the variation of the fine–structure coupling and the dynamical system analysis, has also been discussed.

Although the possibility of space–time variations of the fundamental constants of Nature could be considered as a peculiar idea, it has remarkably played an important role in the progress of theoretical as well as in observational cosmology. Indeed, there are several currently ongoing and proposed facilities which could tighten the current constraints on a varying fine–structure coupling. For instance, high–resolution ultra–stable spectrographs are expected to increase the accuracy of the currently reported spectroscopic measurements, including PEPSI at the Large Binocular Telescope [545, 546], ESPRESSO at the VLT [547], and ELT–HIRES at the European Extremely Large Telescope [548, 549]. Moreover, the Atacama Large Millimeter/submillimeter Array [550, 551] is also expected to increase the sensitivity to detect radio continuum sources, and laboratory measurements with molecular and nuclear clocks are also expected to increase their sensitivity to as high as 10^{-21} yr^{-1} [552]. Other observational constraints coming from compact objects, such as white–dwarfs [553, 554], are equally being explored.

If there isn't any quasi–static Universe after all,
then get rid of the cosmological term.

Albert Einstein

5

On the imprints of generalised interacting dark energy

Certainly, the theoretical understanding of the late–time accelerated expansion of the Universe still remains one of the most important open challenges in modern cosmology. In the previous chapters we have observed that, assuming the validity of General Relativity at the largest observed scales, this recent cosmic epoch can not be explained by standard baryonic matter, but we require a cosmic fluid with a generous negative value of pressure to energy density ratio to dominate the energy budget of the Universe. Consequently, this so–called dark energy constituent of the Universe will be able to drive this accelerated cosmic expansion, in accordance with cosmological observations.

We have already seen that, the simplest candidate of dark energy is in the form of a non–dynamical positive cosmological constant, that lies at the heart of the concordance ΛCDM model, which peculiarly started to dominate the energy budget of the Universe only recently. However, in chapter 3 we showed that more general dynamical forms of dark energy are allowed by current data, thus one can consider the extensively studied quintessence models [325, 327, 466], which were introduced in chapter 4. In these type of models, the accelerated expansion of the Universe is driven by the dynamics of a quintessence scalar field. At late–times, the evolution of the scalar field is primarily dominated by the potential energy rather than its kinetic energy, thus mimicking the standard cosmological constant.

Moreover, dark energy and dark matter are conventionally assumed to be non–interacting and independent components of the dark sector. However, in light of the exotic nature of the dark sector, there is no fundamental reason to suppress or even forbid this direct coupling (see for example Ref. [555] for a quantum field theory formulation). For instance, from solar system [556] and laboratory

[557, 558] tests, we know that a coupling between the baryonic sector, and dark energy is severely constrained, although this does not follow for the dark matter species. Several consequences have been explored in the literature, including the rotation in the direction of the polarisation of light [465], spectral distortions of the cosmic microwave background radiation [472, 559] (see chapter 2), the emission of Cherenkov and bremsstrahlung radiation from charged particles [527], and the variation of the electromagnetic fine–structure constant [2], where the latter was discussed in the previous chapter. Thus, in order to avoid such rigid constraints, we will be considering a coupled quintessence [468] cosmological model in which the standard model particles are uncoupled from the dark sector interaction. Several couplings of this type have been proposed in the literature (see for example Ref. [560] for a review), and their cosmological consequences have been thoroughly studied [4, 5, 471, 480, 481, 485, 486, 535, 561–578].

In this chapter we will be focusing on a coupled quintessence model, in which cold dark matter is coupled to the dark energy scalar field via a conformal and a disformal interaction [485], which have the same form as those used in chapter 4. We will see that the disformal coupling term [448] brings along intriguing features which distinguishes it from the pure conformal coupling term.

In section 5.1 we introduce our coupled quintessence model, while its perturbation equations are given in section 5.3. In sections 5.2 and 5.4, we address the implications of the coupling between the dark sector elements on the cosmic microwave background temperature power spectrum. We then turn our attention to the growth history, and present distinctive features of the matter growth rate function in section 5.5. The small–scale limit of the perturbation equations is studied in section 5.6, and conclude in section 5.7.

5.1 The model and its background dynamics

We here describe the background evolution of our interacting dark energy model. Similar to the adopted formulation of chapter 4, we consider the Einstein frame description of our scalar–tensor theory, specified by the following action:

$$\mathcal{S} = \int \mathrm{d}^4x\sqrt{-g}\left[\frac{M_{\rm Pl}^2}{2}R - \frac{1}{2}g^{\mu\nu}\partial_\mu\phi\,\partial_\nu\phi - V(\phi) + \mathcal{L}_{SM}\right] + \int \mathrm{d}^4x\sqrt{-\tilde{g}}\widetilde{\mathcal{L}}_{DM}\left(\tilde{g}_{\mu\nu},\psi\right), \tag{5.1}$$

where g is the determinant of the minimally coupled metric $g_{\mu\nu}$, and we recall that R is the Ricci scalar, and $M_{\rm Pl}^{-2} = 8\pi G$ such that $M_{\rm Pl} = 2.4\times10^{18}$ GeV is the reduced Planck mass. Dark energy (DE) is described by a quintessence scalar field ϕ, with a potential $V(\phi)$. The uncoupled standard model (SM) particles are described by the Lagrangian $\mathcal{L}_{SM}$, which includes a relativistic sector (r), and a baryon sector (b). Particle quanta of the dark matter (DM) fields ψ, follow the geodesics defined by the metric

$$\tilde{g}_{\mu\nu} = C(\phi)g_{\mu\nu} + D(\phi)\,\partial_\mu\phi\,\partial_\nu\phi\,, \tag{5.2}$$

with $C(\phi)$, $D(\phi)$ being the conformal and disformal coupling functions, respectively. Moreover, the action presented in Eq. (5.1) describes our model in the Einstein frame, which we define to be the frame in which the gravitational sector has the Einstein–Hilbert form, and SM particles are not interacting directly with the quintessence field. Thus, a coupling between DM and DE is induced from the modification of the gravitational field experienced by the DM particles, by the DE scalar field.

For clarity, we will present the field equations computed from the variation of the action (5.1) with respect to the metric $g_{\mu\nu}$. As expected, the Einstein field equations take the usual form

$$R_{\mu\nu} - \frac{1}{2}g_{\mu\nu}R = \kappa^2\left(T^{\phi}_{\mu\nu} + T^{SM}_{\mu\nu} + T^{DM}_{\mu\nu}\right)\,, \tag{5.3}$$

where we recall that $\kappa^2 = M_{\rm Pl}^{-2}$, and that the energy–momentum tensors of the scalar, SM, and DM fields are defined by

$$\begin{aligned} T^{\phi}_{\mu\nu} &= \partial_\mu\phi\partial_\nu\phi - g_{\mu\nu}\left(\frac{1}{2}g^{\rho\sigma}\partial_\rho\phi\partial_\sigma\phi + V(\phi)\right)\,, \\ T^{SM}_{\mu\nu} &= -\frac{2}{\sqrt{-g}}\frac{\delta\left(\sqrt{-g}\mathcal{L}_{SM}\right)}{\delta g^{\mu\nu}}\,,\quad T^{DM}_{\mu\nu} = -\frac{2}{\sqrt{-g}}\frac{\delta\left(\sqrt{-\tilde{g}}\widetilde{\mathcal{L}}_{DM}\right)}{\delta g^{\mu\nu}}\,, \end{aligned} \tag{5.4}$$

respectively. Moreover, the non–conservation of the scalar field energy–momentum

tensor implies the following relation

$$\Box\phi = V_{,\phi} - Q \,, \tag{5.5}$$

where $V_{,\phi} = \mathrm{d}V/\mathrm{d}\phi$, and the coupling function is given by

$$Q = \frac{C_{,\phi}}{2C} T_{DM} + \frac{D_{,\phi}}{2C} T^{\mu\nu}_{DM} \nabla_\mu \phi \nabla_\nu \phi - \nabla_\mu \left[\frac{D}{C} T^{\mu\nu}_{DM} \nabla_\nu \phi \right] \,, \tag{5.6}$$

with T_{DM} being the trace of $T^{\mu\nu}_{DM}$, which, as a consequence of the Bianchi identities (see chapter 1), satisfies a modified conservation equation

$$\nabla^\mu T^{DM}_{\mu\nu} = Q \nabla_\nu \phi \,. \tag{5.7}$$

Since SM particles are not interacting directly with the quintessence field, their energy–momentum tensor obeys the standard conservation equation of

$$\nabla^\mu T^{SM}_{\mu\nu} = 0 \,. \tag{5.8}$$

Similar to the previous chapters, we further consider all species in this model to be described by a perfect fluid energy–momentum tensor

$$T^{\mu\nu}_i = (\rho_i + p_i) \bar{u}^\mu \bar{u}^\nu + p_i g^{\mu\nu} \,, \tag{5.9}$$

where the index i runs over all the constituents making up the dark and visible sectors. Moreover, we denote the zeroth–order four–velocity of the fluid by $\bar{u}^\mu$, and the Einstein frame SM and DM fluid's energy density and pressure by ρ_i and p_i, respectively.

We now consider the background evolution of our model in the spatially flat Friedmann–Lemaître–Robertson–Walker (FLRW) space–time, defined by the line element

$$\mathrm{d}s^2 = g_{\mu\nu} \mathrm{d}x^\mu \mathrm{d}x^\nu = a^2(\tau) \left(-\mathrm{d}\tau^2 + \delta_{ij} \mathrm{d}x^i \mathrm{d}x^j \right) \,, \tag{5.10}$$

where $a(\tau)$ is the cosmological scale factor with conformal time[1] τ. In this setting, the modified Klein–Gordon equation, given by Eq. (5.5), simplifies to

$$\phi'' + 2\mathcal{H}\phi' + a^2 V_{,\phi} = a^2 Q \,, \tag{5.11}$$

[1]We note that, we have adopted the variable τ to denote the conformal time in this chapter, since the variable η, with which we introduced conformal time in chapter 1, will be used in section 5.3 for the definition of the conventional synchronous gauge line–element.

the fluid conservation equations reduce to

$$\rho_r' + 4\mathcal{H}\rho_r = 0\,, \tag{5.12}$$

$$\rho_b' + 3\mathcal{H}\rho_b = 0\,, \tag{5.13}$$

$$\rho_c' + 3\mathcal{H}\rho_c = -Q\phi'\,, \tag{5.14}$$

and the Friedmann equations take their usual form

$$\mathcal{H}^2 = \frac{\kappa^2}{3}a^2\left(\rho_\phi + \rho_b + \rho_r + \rho_c\right)\,, \tag{5.15}$$

$$\mathcal{H}' = -\frac{\kappa^2}{6}a^2\left(\rho_\phi + 3p_\phi + \rho_b + 2\rho_r + \rho_c\right)\,. \tag{5.16}$$

In the above, we denoted coupled DM by a subscript c, a conformal time derivative by a prime, and defined the conformal Hubble parameter by $\mathcal{H} = a'/a$. The scalar field's energy density and pressure have the usual forms of $\rho_\phi = \phi'^2/\left(2a^2\right) + V(\phi)$ and $p_\phi = \rho_\phi - 2V(\phi)$, respectively. The coupling function for a generic coupled perfect fluid with an equation of state w_c, as defined by Eq. (5.6), simplifies to [559]

$$Q = -\frac{a^2C_{,\phi}\left(1-3w_c\right) + D_{,\phi}\phi'^2 - 2D\left(\frac{C_{,\phi}}{C}\phi'^2 + a^2V_{,\phi} + 3\mathcal{H}\left(1+w_c\right)\phi'\right)}{2\left[a^2C + D\left(a^2\rho_c - \phi'^2\right)\right]}\rho_c\,. \tag{5.17}$$

This simplifies considerably in the pure conformal case to

$$Q^{(c)} = -\frac{1}{2}\left(\ln C\right)_{,\phi}\left(1-3w_c\right)\rho_c\,, \tag{5.18}$$

in which the coupling function becomes proportional to the energy density of the coupled matter component.

We will adopt the following functional forms for the couplings and scalar field potential, specified by

$$C(\phi) = e^{2\alpha\kappa\phi}\,, \quad D(\phi) = D_M^4 e^{2\beta\kappa\phi}\,, \quad V(\phi) = V_0^4 e^{-\lambda\kappa\phi}\,, \tag{5.19}$$

where α, D_M, β, V_0, and λ are constants.

We can quantify how the coupled DM dilutes with the expansion by rewriting the conservation equation (5.14) in terms of a coupling induced effective equation of

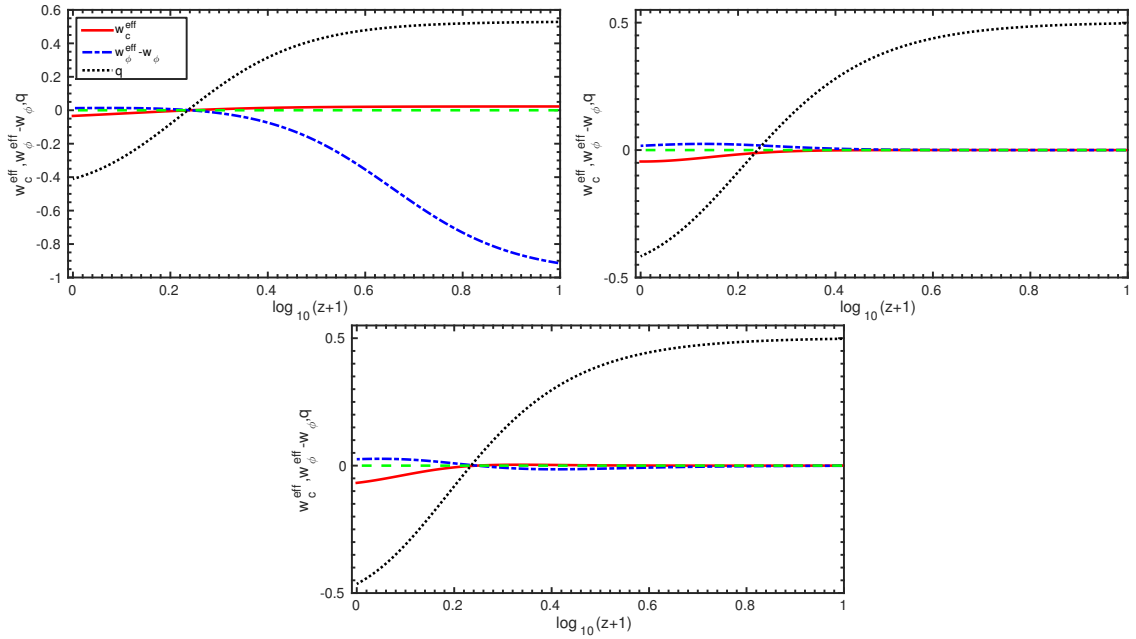

Figure 5.1: These panels show the redshift evolution of $w_c^{\rm eff}$, $w_\phi^{\rm eff} - w_\phi$, and the deceleration parameter q, as defined in section 5.1, while the couplings and scalar field potential are defined in Eq. (5.19). For the conformal case we set $\alpha = 0.2$ (top left), for the disformal case we choose $\beta = 0$, and $D_M = 0.43\,\text{meV}^{-1}$ (top right), and for the mixed case we use $\alpha = 0.2, \beta = 0$, and $D_M = 0.43\,\text{meV}^{-1}$ (bottom). In all cases we set $\lambda = 1.15$, and depict the abscissa by a dashed line.

state for DM

$$\frac{\rho_c'}{\rho_c} + 3\mathcal{H}\left(1 + w_c^{\rm eff}\right) = 0\,, \quad w_c^{\rm eff} = \frac{Q\phi'}{3\mathcal{H}\rho_c}\,. \tag{5.20}$$

Similarly, for the scalar field with a pressure to energy density ratio w_ϕ, we can derive an effective equation of state

$$w_\phi^{\rm eff} = w_\phi - \frac{\rho_c}{\rho_\phi} w_c^{\rm eff}\,. \tag{5.21}$$

Hence, when $w_c^{\rm eff} > 0$, DM dilutes faster than in the standard case of a^{-3}, and furthermore $w_\phi^{\rm eff} < w_\phi$, enhancing the accelerated expansion of the Universe. Conversely, the opposite mechanism takes place when $w_c^{\rm eff} < 0$, leading to an energy flow from DE to DM. We illustrate the evolution of these effective equations of state together with the deceleration parameter $q(z) = -\mathcal{H}'/\mathcal{H}^2$ (see Eq. (1.28)), for three distinct cases in the panels of Fig. 5.1. As expected, the models under consideration give $q(z) < 0$ at late–times, leading to a speeding up of the expansion of the Universe, whereas the models give $q(z) > 0$ at an earlier epoch, meaning that the expansion was slowed down in the past. As depicted in Fig. 5.1, the transition redshift is

model dependent, although the differences from one model to another are small and depend on the choice of parameters for each respective model. The conformal coupling strength parameter was exaggerated (since cosmological observations forbid such large values [4, 574, 576], as we will see in the next chapter) in order to point out that when one introduces a disformal coupling, the energy transfer attributed to the conformal coupling is significantly suppressed. One might think that this makes the model more consistent with cosmological observations, although at the perturbation level, such a model would be in tension with current observations due to an anomalous enhancement in the growth of matter perturbations. We will discuss the evolution of the perturbations in the sections that follow, together with their effects on cosmological observations, while in chapter 6 we will confront this model with cosmological data sets.

5.2 An estimation of the separation of CMB peaks

We here estimate the spacing between the peaks in the cosmic microwave background (CMB) temperature power spectrum using only the background evolution of our interacting DE model. Similar to section 4.6.1, it is convenient to define an effective non–interacting DE perfect fluid with energy density $\rho_{\rm DE,eff}$, and an effective equation of state $w_{\rm DE}^{\rm eff}$ [539], which satisfies the standard conservation equation

$$\rho'_{\rm DE,eff} + 3\mathcal{H}\left(1 + w_{\rm DE}^{\rm eff}\right)\rho_{\rm DE,eff} = 0\,. \tag{5.22}$$

Moreover, in the Friedmann equation (5.15), we shall consider a non–interacting DM component

$$\mathcal{H}^2 = \frac{\kappa^2}{3}a^2\left(\rho_{\rm DE,eff} + \rho_b + \rho_r + \rho_{c,0}a^{-3}\right)\,, \tag{5.23}$$

where $\rho_{c,0}$ is the DM energy density today. By comparing Eq. (5.23) with Eq. (5.15), one can easily observe that the evolution of the interacting DE and DM energy densities is absorbed in $\rho_{\rm DE,eff}$, which is given by

$$\rho_{\rm DE,eff} = \rho_\phi + \rho_c - \rho_{c,0}a^{-3}\,. \tag{5.24}$$

By taking the conformal time derivative of Eq. (5.24), substituting Eq. (5.11) and Eq. (5.14), and comparing the resultant equation with Eq. (5.22), one arrives to an expression for the effective equation of state for this effective DE fluid [539]

$$w_{\rm DE}^{\rm eff} = \frac{p_\phi}{\rho_{\rm DE,eff}}\,. \tag{5.25}$$

In order to estimate the spacing between the CMB peaks at different angular mo-

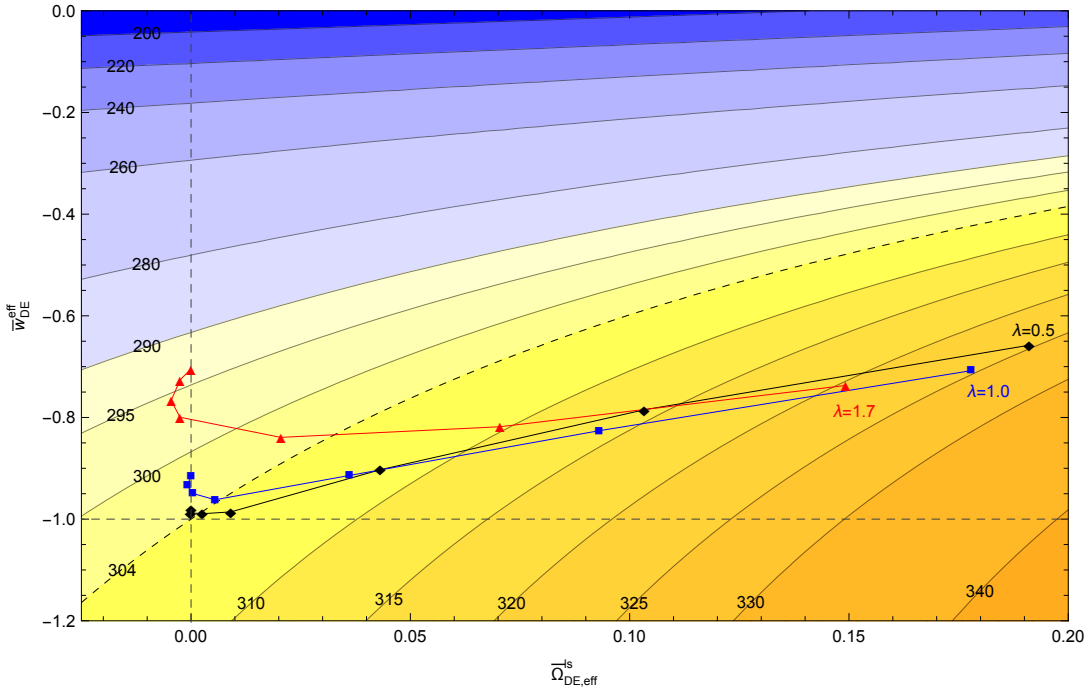

Figure 5.2: This is a contour plot of the peak separation $\Delta\ell$, illustrating conformal models with $\lambda = 0.5\,(\diamond)$, $1.0\,(\square)$, $1.7\,(\triangle)$ as a function of $\overline{\Omega}^{ls}_{\rm DE,eff}$ and $\overline{w}^{\rm eff}_{\rm DE}$, with $a_{ls}^{-1} = 1099.52$ and $\bar{c}_s = 0.515$. From right to left, the consecutive points for every choice of λ depict conformal models with $\alpha = 0.2,\ 0.15,\ 0.1,\ 0.05,\ 0.03,\ 0.01,\ 0$. The ΛCDM model peak separation is shown by the dashed contour.

menta ℓ, we use the approximation [579, 580]

$$\Delta\ell = \pi\frac{\tau_0 - \tau_{ls}}{s} = \pi\frac{\tau_0 - \tau_{ls}}{\bar{c}_s\tau_{ls}}\ , \tag{5.26}$$

where τ_0 and τ_{ls} are the conformal time today and at last scattering, respectively. The sound horizon at last scattering is denoted by $s = \bar{c}_s\tau_{ls}$, where the τ–averaged sound speed until last scattering is given by

$$\bar{c}_s = \tau_{ls}^{-1}\int_0^{\tau_{ls}} c_s\,{\rm d}\tau\ , \tag{5.27}$$

with the standard sound speed

$$c_s^{-2} = 3 + \frac{9}{4}\frac{\rho_b}{\rho_\gamma}\ , \tag{5.28}$$

where ρ_b/ρ_γ is the baryon to photon energy density ratio. We now estimate analytically τ_0 and τ_{ls}. For the latter, we consider the interval $0 \leq \tau \leq \tau_{ls}$, in which we

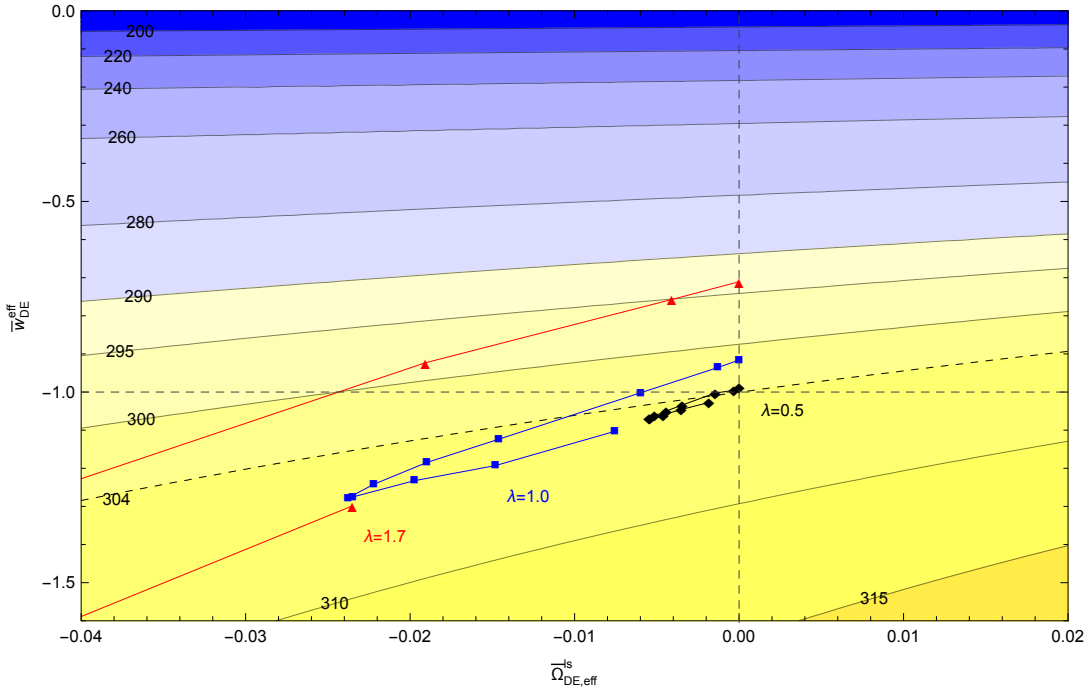

Figure 5.3: This is a contour plot of the peak separation $\Delta\ell$, illustrating disformal models with $\lambda = 0.5\,(\diamond),\ 1.0\,(\square),\ 1.7\,(\triangle)$ and $\beta = 0$ as a function of $\overline{\Omega}^{ls}_{\rm DE,eff}$ and $\overline{w}^{\rm eff}_{\rm DE}$, with $a_{ls}^{-1} = 1099.38$ and $\bar{c}_s = 0.516$. For each choice of λ, the consecutive points starting from the $\overline{\Omega}^{ls}_{\rm DE,eff}$ −axis, depict disformal models with $D_M = 0,\ 0.2,\ 0.3,\ 0.4,\ 0.45,\ 0.5,\ 0.55,\ 0.6,\ 0.7,\ 0.8,\ 1\ \text{meV}^{-1}$. The ΛCDM model peak separation is shown by the dashed contour.

assume that the fraction of the effective DE $\Omega_{\rm DE,eff}(\tau)$, does not change rapidly for a considerable period before decoupling. Thus, we can define an effective average

$$\overline{\Omega}^{ls}_{\rm DE,eff} = \tau_{ls}^{-1} \int_0^{\tau_{ls}} \Omega_{\rm DE,eff}\,(\tau)\,{\rm d}\tau\ , \tag{5.29}$$

with which we can approximate $\Omega_{\rm DE,eff}(\tau)$ during this period. By solving the Friedmann equation (5.23), one arrives to an expression for the conformal time at last scattering, given by

$$\tau_{ls} = 2H_0^{-1} \left(\frac{1-\overline{\Omega}^{ls}_{\rm DE,eff}}{\Omega_{b,0}+\Omega_{c,0}}\right)^{\frac{1}{2}} \left[\left(a_{ls}+\frac{\Omega_{r,0}}{\Omega_{b,0}+\Omega_{c,0}}\right)^{\frac{1}{2}} - \left(\frac{\Omega_{r,0}}{\Omega_{b,0}+\Omega_{c,0}}\right)^{\frac{1}{2}}\right]\ , \tag{5.30}$$

where H_0 is the Hubble constant, a_{ls} is the cosmological scale factor at last scattering, and recall that $\Omega_{b,0}$, $\Omega_{c,0}$, and $\Omega_{r,0}$ are the baryon, DM, and relativistic abundances today. We now estimate the conformal time today by considering the interval $0 \leq$

$\tau \leq \tau_0$. We define an averaged effective equation of state for the effective DE perfect fluid with energy density $\rho_{\rm DE,eff}$, specified by

$$\overline{w}^{\rm eff}_{\rm DE} = \frac{\int_0^{\tau_0} \Omega_{\rm DE,eff}(\tau) w^{\rm eff}_{\rm DE}(\tau) {\rm d}\tau}{\int_0^{\tau_0} \Omega_{\rm DE,eff}(\tau) {\rm d}\tau} \,. \tag{5.31}$$

Thus, for the whole evolution, we estimate the effective equation of state of the effective DE perfect fluid by a constant averaged effective equation of state. From the Friedmann equation (5.23), one arrives to an expression for the conformal time today

$$\tau_0 = 2 H_0^{-1} \mathcal{F} \,, \tag{5.32}$$

where

$$\mathcal{F} = \frac{1}{2} \int_0^1 \left(\Omega_{\phi,0} a^{1-3\overline{w}^{\rm eff}_{\rm DE}} + \Omega_{b,0} a + \Omega_{r,0} + \Omega_{c,0} a \right)^{-\frac{1}{2}} {\rm d}a \,, \tag{5.33}$$

with $\Omega_{\phi,0}$ being the DE fraction today. Hence, the CMB peak separation can be estimated by

$$\Delta\ell = \pi \bar{c}_s^{-1} \left\{ \mathcal{F} \left(\frac{\Omega_{b,0} + \Omega_{c,0}}{1 - \overline{\Omega}^{ls}_{\rm DE,eff}} \right)^{\frac{1}{2}} \left[\left(a_{ls} + \frac{\Omega_{r,0}}{\Omega_{b,0} + \Omega_{c,0}} \right)^{\frac{1}{2}} - \left(\frac{\Omega_{r,0}}{\Omega_{b,0} + \Omega_{c,0}} \right)^{\frac{1}{2}} \right]^{-1} - 1 \right\} . \tag{5.34}$$

We have used the above approach with conformal, disformal, and mixed coupling models, in which we found that this estimation is in very good agreement with the numerical calculations. We compared our estimation with the averaged peak separation over six peaks computed in `CLASS` [120] using the full perturbation equations presented in section 5.3. Indeed, we have checked that when the optimal choice of a_{ls} is chosen for a specific model, the determination of $\Delta\ell$ is $\lesssim 10^{-3}$ percent, and of τ_0 and τ_{ls} is $\lesssim 2-3$ percent. In Figs. 5.2–5.4 we present contour plots of the CMB peak separation as a function of $\overline{\Omega}^{ls}_{\rm DE,eff}$ and $\overline{w}^{\rm eff}_{\rm DE}$ for several parameter choices for the conformal, disformal, and mixed models, respectively. Since every model will have a different value of a_{ls} and $\bar{c}_s$, we have chosen the optimal values of a_{ls} ($\sim 1100^{-1}$) and $\bar{c}_s$ (~ 0.52) which give the minimal departure from the exact numerical results. The other cosmological parameters have been set to the best fit values reported in Ref. [65]. In each contour plot, we show the ΛCDM peak spacing by a dashed contour.

One can easily notice that the CMB spacing is a robust probe for conformal models, since a larger conformal coupling parameter produces a more pronounced deviation from the ΛCDM model which currently fits the data very well, as we clearly illustrated in chapter 2. Thus, the conformal coupling parameter is easily constrained from the temperature power spectrum of the CMB (see for example Refs. [4, 573, 574, 576]), and we will clearly show this in the next chapter. Indeed, the alteration of

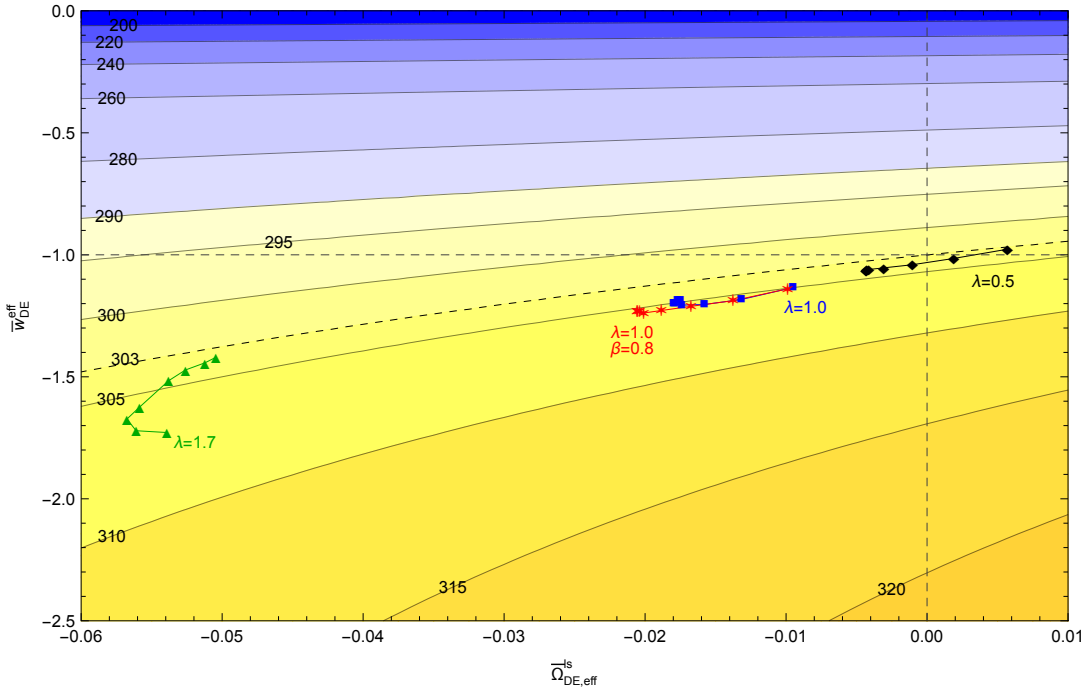

Figure 5.4: This is a contour plot of the peak separation $\Delta\ell$, illustrating mixed models with $\beta = 0$ and $\lambda = 0.5\,(\diamond)$, $1.0\,(\square)$, $1.7\,(\triangle)$ together with models characterised by $\beta = 0.8$ and $\lambda = 1.0\,(*)$ as a function of $\overline{\Omega}^{ls}_{\rm DE,eff}$ and $\overline{w}^{\rm eff}_{\rm DE}$, with $a_{ls}^{-1} = 1096.04$ and $\bar{c}_s = 0.515$. From left to right (in a counter–clockwise direction for the points denoted by a $\triangle$), the consecutive points for every choice of λ and β depict mixed models with $\alpha = 0,\ 0.01,\ 0.03,\ 0.05,\ 0.1,\ 0.15,\ 0.2,\ 0.25$. For all models, we set $D_M V_0 = 1$. The ΛCDM model peak separation is shown by the dashed contour.

the amplitude and the shift of the CMB acoustic peaks to larger multipole moments could be significant as one increases the conformal coupling strength parameter. On the other hand, both the disformal as well as the mixed models are very hard to disentangle from the ΛCDM model as the CMB peak separation of these models does not deviate significantly from that predicted in the concordance model. Thus, we expect that the parameter space of disformal and mixed models will not be constrained very well from the temperature power spectrum of the CMB alone, and will be confirmed in chapter 6.

Another important difference between a purely conformal model and the other interacting models with a disformal coupling, is that in a conformal model the contribution of the effective DE at last scattering $\overline{\Omega}^{ls}_{\rm DE,eff}$, can be much larger than that in the other models. In conformal models, this non–negligible contribution is coming from the fact that DE starts to contribute even at the time of recombination, thus altering the proportions of DM, baryons, and radiation at decoupling. On the other hand, when a disformal coupling is present, DM, baryons, and radiation follow

standard quintessence dynamics for the majority of the cosmic history, and only at very late–times the coupling switches on and modifies the dynamics. These different evolutions of the conformal and the disformal couplings are also behind the fact that conformal models are characterised by a positive $\overline{\Omega}^{ls}_{\rm DE,eff}$, whereas a disformal coupling tends to be associated with a negative $\overline{\Omega}^{ls}_{\rm DE,eff}$. Furthermore, one can assert that conformal models occupy the first quadrant of the $\overline{\Omega}^{ls}_{\rm DE,eff}$–$\overline{w}^{\rm eff}_{\rm DE}$ plane with respect to the origin located at the ΛCDM model, whereas disformal and mixed models are situated in the third quadrant of the same plane, with a slight overlap between conformal and disformal models in the second quadrant.

5.3 Evolution of perturbations

We here present the equations governing the evolution of perturbations in our interacting DE model, in which we consider the perturbation equations for a generic interacting perfect fluid. The study of the growth of small perturbations about an FLRW metric, specified by the line element in Eq. (5.10), is an asset in the understanding of the real Universe [115, 581–583]. We will first discuss the relevant equations in the synchronous gauge, and we later derive the equations that govern the evolution of perturbations in the conformal Newtonian gauge. Although we used the synchronous gauge equations to evolve the perturbed dynamics of our interacting DE model, we have checked that the obtained results in both gauges agree with one another. We implemented these equations in the cosmological Boltzmann code `CLASS`, from which we obtained exact numerical solutions for the background and perturbed evolution of our interacting DE model.

5.3.1 Synchronous gauge

The line element in the synchronous gauge is given by

$$\mathrm{d}s^2 = a^2(\tau)\left[-\mathrm{d}\tau^2 + (\delta_{ij} + h_{ij})\,\mathrm{d}x^i\mathrm{d}x^j\right] \,, \tag{5.35}$$

with metric perturbation h_{ij}. We adopt the convention of Ref. [115] and use the standard two metric perturbation fields h and η, expressed in Fourier space k (see Ref. [115] for further details). In order to compute the first–order perturbed Einstein field equations $\delta G^{\mu}{}_{\nu} = 8\pi G \sum \delta T^{\mu}{}_{\nu}$, where the summation is over all the fluid components and $\delta G^{\mu}{}_{\nu}$ is the perturbed Einstein tensor, we need the first–order perturbation of the zeroth–order energy–momentum tensor specified in Eq. (5.9), leading to

$$\delta T^{\mu}{}_{\nu} = (\delta\rho + \delta p)\,\bar{u}^{\mu}\bar{u}_{\nu} + \delta p\delta^{\mu}{}_{\nu} + (\rho + p)\,(\delta u^{\mu}\bar{u}_{\nu} + \bar{u}^{\mu}\delta u_{\nu}) + p\Pi^{\mu}{}_{\nu} \,, \tag{5.36}$$

where $\bar{u}^\mu$ is the zeroth–order four–velocity of the fluid, with δu^μ being its first–order perturbation. Moreover, $\Pi_{\mu\nu}$ is the traceless anisotropic stress tensor which characterises the difference between the perturbed fluid and a perfect fluid. We note that, the perturbations of the energy density $\delta\rho$, and pressure δp, are of the same order as the metric perturbations. The perturbed Einstein field equations reduce to the following set of coupled differential equations

$$k^2\eta - \frac{1}{2}\mathcal{H}h' = -4\pi G a^2 \sum \delta\rho \,, \tag{5.37}$$

$$k^2\eta' = 4\pi G a^2 \sum \rho(1+w)\theta \,, \tag{5.38}$$

$$h'' + 2\mathcal{H}h' - 2k^2\eta = -24\pi G a^2 \sum \delta p \,, \tag{5.39}$$

$$h'' + 6\eta'' + 2\mathcal{H}\left(h' + 6\eta'\right) - 2k^2\eta = -24\pi G a^2 \sum \rho(1+w)\sigma \,, \tag{5.40}$$

where the sum is over the DM, radiation, and DE fluids, as explicitly illustrated in Eq. (5.3). The re–defined anisotropic stress perturbation σ, is related to the scalar part of the anisotropic stress tensor Π, as defined in Eq. (5.36), by the relation $\sigma = 2w\Pi/3(1+w)$. Moreover, the divergence of the fluid velocity is denoted by θ.

The perturbed continuity and Euler equations of the uncoupled baryonic and radiation (consisting of photons and massless neutrinos) sectors, are governed by the standard first–order perturbation equations $\delta T^{\mu}{}_{\nu;\mu} = 0$, which simplify to the following set of coupled differential equations

$$\delta_i' + 3\mathcal{H}\left(\frac{\delta p_i}{\delta\rho_i} - w_i\right)\delta_i = -\left(1+w_i\right)\left(\theta_i + \frac{h'}{2}\right) \,, \tag{5.41}$$

$$\theta_i' + \left[\mathcal{H}\left(1-3w_i\right) + \frac{w_i'}{1+w_i}\right]\theta_i = \frac{\delta p_i}{\delta\rho_i}\frac{k^2\delta_i}{1+w_i} - k^2\sigma_i \,, \tag{5.42}$$

where $i = \{b,\ r\}$, and the density contrast is denoted by $\delta = \delta\rho/\rho$. We recall that for the radiation sector $w_r = \delta p_r/\delta\rho_r = 1/3$, and for baryons $w_b = \delta p_b/\delta\rho_b \ll 1$ with $\sigma_b = 0$. The only non–negligible contribution to the shear stress comes from the radiation sector [115], which we include in our numerical solutions.

For the coupled fluid, the conservation equation is modified according to Eq. (5.7), leading to the following perturbed continuity and Euler equations

$$\delta_c' + 3\mathcal{H}\left(\frac{\delta p_c}{\delta\rho_c} - w_c\right)\delta_c = -\left(1+w_c\right)\left(\theta_c + \frac{h'}{2}\right) + \frac{Q}{\rho_c}\phi'\delta_c - \frac{Q}{\rho_c}\delta\phi' - \frac{\phi'}{\rho_c}\delta Q\ , \tag{5.43}$$

$$\theta_c' + \left[\mathcal{H}\left(1-3w_c\right) + \frac{w_c'}{1+w_c}\right]\theta_c = \frac{\delta p_c}{\delta\rho_c}\frac{k^2\delta_c}{1+w_c} + \frac{Q}{\rho_c}\phi'\theta_c - \frac{Q}{\rho_c(1+w_c)}k^2\delta\phi\ , \tag{5.44}$$

which are valid for a coupled shear–free fluid with equation of state w_c. The perturbation of the coupled DE scalar field is denoted by $\delta\phi$, and its evolution is governed by the following perturbed Klein–Gordon equation

$$\delta\phi'' + 2\mathcal{H}\delta\phi' + \left(a^2V_{,\phi\phi} + k^2\right)\delta\phi + \frac{h'}{2}\phi' = a^2\delta Q\ . \tag{5.45}$$

The corresponding perturbation of the coupling function Q is given by

$$\delta Q = -\frac{\rho_c}{a^2C + D\left(a^2\rho_c - \phi'^2\right)}\left(\mathfrak{B}_1\delta_c + \mathfrak{B}_2h' + \mathfrak{B}_3\delta\phi' + \mathfrak{B}_4\delta\phi\right)\ , \tag{5.46}$$

where

$$\begin{aligned}\mathfrak{B}_1 =& \frac{1}{2}a^2C_{,\phi}\left(1 - 3\frac{\delta p_c}{\delta\rho_c}\right) - 3\mathcal{H}D\left(1 + \frac{\delta p_c}{\delta\rho_c}\right)\phi' - a^2D\left(V_{,\phi} - Q\right)\\ &- D\phi'^2\left(\frac{C_{,\phi}}{C} - \frac{D_{,\phi}}{2D}\right)\ ,\end{aligned} \tag{5.47}$$

$$\mathfrak{B}_2 = -\frac{1}{2}D\phi'\left(1+w_c\right)\ , \tag{5.48}$$

$$\mathfrak{B}_3 = -3\mathcal{H}D\left(1+w_c\right) - 2D\phi'\left(\frac{Q}{\rho_c} + \frac{C_{,\phi}}{C} - \frac{D_{,\phi}}{2D}\right)\ , \tag{5.49}$$

$$\begin{aligned}\mathfrak{B}_4 =& \frac{1}{2}a^2C_{,\phi\phi}\left(1-3w_c\right) - \left(1+w_c\right)k^2D - a^2DV_{,\phi\phi} - a^2D_{,\phi}V_{,\phi} - 3\mathcal{H}D_{,\phi}\left(1+w_c\right)\phi'\\ &- D\phi'^2\left(\frac{C_{,\phi\phi}}{C} - \frac{C_{,\phi}^2}{C^2} + \frac{C_{,\phi}D_{,\phi}}{CD} - \frac{1}{2}\frac{D_{,\phi\phi}}{D}\right) + \frac{Q}{\rho_c}\left(a^2C_{,\phi} + a^2D_{,\phi}\rho_c - D_{,\phi}\phi'^2\right)\ .\end{aligned} \tag{5.50}$$

For the pure disformal scenario, such that $C(\phi) = 1$, the perturbation of Q simplifies

to the following equation

$$\begin{aligned}\delta Q^{(d)} = &\left[\left(a^2 - D\phi'^2\right)\frac{Q}{\zeta} - \frac{3\mathcal{H}D\rho_c}{\zeta}\left(w_c - \frac{\delta p_c}{\delta\rho_c}\right)\phi'\right]\delta_c + \frac{D\phi'\rho_c}{\zeta}\left(1+w_c\right)\frac{h'}{2} \\ &- \frac{\rho_c}{\zeta^2}\delta\phi'\Bigg\{a^2 D_{,\phi}\phi'\left(1+D\rho_c\right) - D^2\left[2a^2V_{,\phi}\phi' + 3\mathcal{H}\left(1+w_c\right)\left(a^2\rho_c + \phi'^2\right)\right] \\ &\qquad - 3a^2\mathcal{H}D\left(1+w_c\right)\Bigg\} \\ &+ \delta\phi\Bigg\{k^2\frac{D\rho_c}{\zeta}\left(1+w_c\right) + \frac{\rho_c}{2\zeta}\left(2a^2DV_{,\phi\phi} - D_{,\phi\phi}\phi'^2\right) \\ &\qquad + \frac{\rho_c}{2\zeta^2}\left[2a^2D_{,\phi}\left(a^2V_{,\phi} + 3\mathcal{H}\phi'\left(1+w_c\right)\right) + D_{,\phi}^2\phi'^2\left(a^2\rho_c - \phi'^2\right)\right]\Bigg\}\,,\end{aligned} \tag{5.51}$$

where we defined $\zeta = a^2 + D\left(a^2\rho_c - \phi'^2\right)$. In the absence of a disformal coupling the above perturbation equations simplify considerably. Indeed, in the pure conformal case (see also Ref. [563]), the perturbed continuity and Euler equations for a generic coupled fluid reduce to

$$\begin{aligned}&\delta_c' + 3\left(\frac{\delta p_c}{\delta\rho_c} - w_c\right)\left(\mathcal{H} + \frac{1}{2}\left(\ln C\right)_{,\phi}\phi'\right)\delta_c \\ &\quad = -\left(1+w_c\right)\left(\theta_c + \frac{h'}{2}\right) + \frac{1}{2}\left(1-3w_c\right)\left[\left(\ln C\right)_{,\phi}\delta\phi' + \left(\ln C\right)_{,\phi\phi}\phi'\delta\phi\right]\,,\end{aligned} \tag{5.52}$$

$$\begin{aligned}&\theta_c' + \left[\mathcal{H}\left(1-3w_c\right) + \frac{w_c'}{1+w_c} + \frac{1}{2}\left(\ln C\right)_{,\phi}\left(1-3w_c\right)\phi'\right]\theta_c \\ &\quad = k^2\left[\frac{\delta p_c}{\delta\rho_c}\frac{\delta_c}{1+w_c} + \frac{1}{2}\left(\ln C\right)_{,\phi}\left(\frac{1-3w_c}{1+w_c}\right)\delta\phi\right]\,,\end{aligned} \tag{5.53}$$

respectively, and the perturbed Klein–Gordon equation simplifies to the following equation

$$\delta\phi'' + 2\mathcal{H}\delta\phi' + \left[k^2 + a^2 V_{,\phi\phi} + \frac{1}{2}a^2\rho_c\left(1-3w_c\right)\left(\ln C\right)_{,\phi\phi}\right]\delta\phi$$
$$= -\frac{1}{2}h'\phi' - \frac{1}{2}a^2\rho_c\left(\ln C\right)_{,\phi}\left(1 - 3\frac{\delta p_c}{\delta\rho_c}\right)\delta_c \,. \tag{5.54}$$

From Eq. (5.54) we observe that, the conformal coupling modifies the DE mass $\left(m_\phi^2 = V_{,\phi\phi}\right)$ term, by an effective mass term proportional to the second field derivative of the logarithm of the conformal coupling. We should further mention that the above perturbation equations can be derived from the Newtonian gauge perturbation equations, presented in section 5.3.2, by making use of a standard gauge transformation [115, 583]. One can easily obtain the synchronous gauge perturbed coupling $\delta Q^{\rm syn}$, by applying a gauge transformation to the corresponding perturbed coupling expression in the conformal Newtonian gauge $\delta Q^{\rm con}$, where these gauge–dependent perturbed coupling functions are related by $\delta Q^{\rm syn} = \delta Q^{\rm con} - Q' k^{-2}\left(h'/2 + 3\eta'\right)$, with Q being the background coupling function specified in Eq. (5.17). To simplify notation, we drop the latter δQ superscripts in our equations.

5.3.2 Newtonian gauge

In the conformal Newtonian gauge [583], the perturbations are characterised by the conventional scalar potentials Ψ and Φ, which appear in the line element as

$$\mathrm{d}s^2 = a^2(\tau)\left[-\left(1+2\Psi\right)\mathrm{d}\tau^2 + \left(1-2\Phi\right)\delta_{ij}\mathrm{d}x^i\mathrm{d}x^j\right] \,, \tag{5.55}$$

leading to the Newtonian gauge perturbed Einstein field equations

$$k^2\Phi + 3\mathcal{H}\left(\Phi' + \mathcal{H}\Psi\right) = -4\pi G a^2 \sum \delta\rho \,, \tag{5.56}$$

$$k^2\left(\Phi' + \mathcal{H}\Psi\right) = 4\pi G a^2 \sum \rho(1+w)\theta \,, \tag{5.57}$$

$$\Phi'' + \mathcal{H}\left(\Psi' + 2\Phi'\right) + \Psi\left(\mathcal{H}^2 + 2\mathcal{H}'\right) + \frac{k^2}{3}\left(\Phi - \Psi\right) = 4\pi G a^2 \sum \delta p \,, \tag{5.58}$$

$$k^2\left(\Phi - \Psi\right) = 12\pi G a^2 \sum \rho(1+w)\sigma \,, \tag{5.59}$$

where we made use of the same re–definition of the anisotropic stress, as introduced in the preceding synchronous gauge calculation. The uncoupled baryonic and radiation

sectors satisfy the standard perturbed conservation equations, given by

$$\delta_i' + 3\mathcal{H}\left(\frac{\delta p_i}{\delta\rho_i} - w_i\right)\delta_i = -\left(1+w_i\right)\left(\theta_i - 3\Phi'\right) \ , \tag{5.60}$$

$$\theta_i' + \left[\mathcal{H}\left(1-3w_i\right) + \frac{w_i'}{1+w_i}\right]\theta_i = k^2\left[\Psi + \frac{\delta p_i}{\delta\rho_i}\frac{\delta_i}{1+w_i}\right] - k^2\sigma_i \ , \tag{5.61}$$

where $i = \{b,\, r\}$, while the perturbed evolution of a generic shear–free coupled fluid is governed by the modified perturbed continuity and Euler equations

$$\delta_c' + 3\mathcal{H}\left(\frac{\delta p_c}{\delta\rho_c} - w_c\right)\delta_c = -\left(1+w_c\right)\left(\theta_c - 3\Phi'\right) + \frac{Q}{\rho_c}\phi'\delta_c - \frac{Q}{\rho_c}\delta\phi' - \frac{\phi'}{\rho_c}\delta Q \ , \tag{5.62}$$

$$\theta_c' + \left[\mathcal{H}\left(1-3w_c\right) + \frac{w_c'}{1+w_c}\right]\theta_c = k^2\left[\Psi + \frac{\delta p_c}{\delta\rho_c}\frac{\delta_c}{1+w_c}\right] + \frac{Q}{\rho_c}\phi'\theta_c - \frac{Q}{\rho_c\left(1+w_c\right)}k^2\delta\phi \ , \tag{5.63}$$

respectively. Moreover, the evolution of the perturbed scalar field is dictated by the perturbed Klein–Gordon equation

$$\delta\phi'' + 2\mathcal{H}\delta\phi' + \left(k^2 + a^2V_{,\phi\phi}\right)\delta\phi = \left(\Psi' + 3\Phi'\right)\phi' - 2a^2V_{,\phi}\Psi + a^2\delta Q + 2a^2Q\Psi \ . \tag{5.64}$$

The Newtonian gauge perturbation of the coupling function Q, defined in Eq. (5.17), is given by [559]

$$\delta Q = -\frac{\rho_c}{a^2C + D\left(a^2\rho_c - \phi'^2\right)}\left(\widetilde{\mathfrak{B}}_1\delta_c + \widetilde{\mathfrak{B}}_2\Phi' + \widetilde{\mathfrak{B}}_3\Psi + \widetilde{\mathfrak{B}}_4\delta\phi' + \widetilde{\mathfrak{B}}_5\delta\phi\right) \ , \tag{5.65}$$

where

$$\begin{aligned}\widetilde{\mathfrak{B}}_1 =& \frac{1}{2}a^2C_{,\phi}\left(1 - 3\frac{\delta p_c}{\delta\rho_c}\right) - 3\mathcal{H}D\left(1 + \frac{\delta p_c}{\delta\rho_c}\right)\phi' - a^2D\left(V_{,\phi} - Q\right) \\ & - D\phi'^2\left(\frac{C_{,\phi}}{C} - \frac{D_{,\phi}}{2D}\right) \ ,\end{aligned} \tag{5.66}$$

$$\widetilde{\mathfrak{B}}_2 = 3D\phi'\left(1+w_c\right) \ , \tag{5.67}$$

$$\widetilde{\mathfrak{B}}_3 = 6\mathcal{H}D\phi'\left(1+w_c\right) + 2D\phi'^2\left(\frac{Q}{\rho_c} + \frac{C_{,\phi}}{C} - \frac{D_{,\phi}}{2D}\right) \ , \tag{5.68}$$

$$\widetilde{\mathfrak{B}}_4 = -3\mathcal{H}D\left(1+w_c\right) - 2D\phi'\left(\frac{Q}{\rho_c} + \frac{C_{,\phi}}{C} - \frac{D_{,\phi}}{2D}\right) , \tag{5.69}$$

$$\begin{aligned}\widetilde{\mathfrak{B}}_5 =& \frac{1}{2}a^2 C_{,\phi\phi}\left(1-3w_c\right) - \left(1+w_c\right)k^2 D - a^2 D V_{,\phi\phi} - a^2 D_{,\phi} V_{,\phi} - 3\mathcal{H}D_{,\phi}\left(1+w_c\right)\phi' \\ & - D\phi'^2\left(\frac{C_{,\phi\phi}}{C} - \frac{C_{,\phi}^2}{C^2} + \frac{C_{,\phi}D_{,\phi}}{CD} - \frac{1}{2}\frac{D_{,\phi\phi}}{D}\right) + \frac{Q}{\rho_c}\left(a^2 C_{,\phi} + a^2 D_{,\phi}\rho_c - D_{,\phi}\phi'^2\right) .\end{aligned} \tag{5.70}$$

In the pure disformal scenario, the above perturbation equation for the coupling function simplifies as follows

$$\begin{aligned}\delta Q^{(d)} =& \left[\left(a^2 - D\phi'^2\right)\frac{Q}{\zeta} - \frac{3\mathcal{H}D\rho_c}{\zeta}\left(w_c - \frac{\delta p_c}{\delta\rho_c}\right)\phi'\right]\delta_c - 3\frac{D\phi'\rho_c}{\zeta}\left(1+w_c\right)\Phi' \\ & - \frac{a^2\phi'\rho_c}{\zeta^2}\Big\{ - D_{,\phi}\phi'\left(1+D\rho_c\right) + 2D^2\left[V_{,\phi}\phi' + 3\mathcal{H}\left(1+w_c\right)\rho_c\right] \\ & \qquad + 6\mathcal{H}D\left(1+w_c\right)\Big\}\Psi \\ & - \frac{\rho_c}{\zeta^2}\delta\phi'\Big\{a^2 D_{,\phi}\phi'\left(1+D\rho_c\right) - D^2\left[2a^2 V_{,\phi}\phi' + 3\mathcal{H}\left(1+w_c\right)\left(a^2\rho_c + \phi'^2\right)\right] \\ & \qquad - 3a^2\mathcal{H}D\left(1+w_c\right)\Big\} \\ & + \delta\phi\left\{k^2\frac{D\rho_c}{\zeta}\left(1+w_c\right) + \frac{\rho_c}{2\zeta}\left(2a^2 D V_{,\phi\phi} - D_{,\phi\phi}\phi'^2\right)\right. \\ & \qquad \left. + \frac{\rho_c}{2\zeta^2}\left[2a^2 D_{,\phi}\left(a^2 V_{,\phi} + 3\mathcal{H}\phi'\left(1+w_c\right)\right) + D_{,\phi}^2\phi'^2\left(a^2\rho_c - \phi'^2\right)\right]\right\} ,\end{aligned} \tag{5.71}$$

where $\zeta = a^2 + D\left(a^2\rho_c - \phi'^2\right)$, as defined in section 5.3.1. We remark that, this expression for δQ, agrees with the equation given in Ref. [535] for the specific case of a disformally coupled pressureless fluid. Analogous to the synchronous gauge calculation, the above equations simplify significantly in the pure conformally coupled case. Indeed, in the absence of a disformal coupling, the perturbed conservation

equations for the coupled fluid reduce to

$$\begin{aligned}
&\delta_c' + 3\left(\frac{\delta p_c}{\delta\rho_c} - w_c\right)\left(\mathcal{H} + \frac{1}{2}\left(\ln C\right)_{,\phi}\phi'\right)\delta_c \\
&\quad = -\left(1+w_c\right)\left(\theta_c - 3\Phi'\right) + \frac{1}{2}\left(1-3w_c\right)\left[\left(\ln C\right)_{,\phi}\delta\phi' + \left(\ln C\right)_{,\phi\phi}\phi'\delta\phi\right] ,
\end{aligned} \tag{5.72}$$

$$\begin{aligned}
&\theta_c' + \left[\mathcal{H}\left(1-3w_c\right) + \frac{w_c'}{1+w_c} + \frac{1}{2}\left(\ln C\right)_{,\phi}\left(1-3w_c\right)\phi'\right]\theta_c \\
&\quad = k^2\left[\Psi + \frac{\delta p_c}{\delta\rho_c}\frac{\delta_c}{1+w_c} + \frac{1}{2}\left(\ln C\right)_{,\phi}\left(\frac{1-3w_c}{1+w_c}\right)\delta\phi\right] ,
\end{aligned} \tag{5.73}$$

while the perturbed Klein–Gordon equation simplifies as follows

$$\begin{aligned}
&\delta\phi'' + 2\mathcal{H}\delta\phi' + \left[k^2 + a^2 V_{,\phi\phi} + \frac{1}{2}a^2\rho_c\left(1-3w_c\right)\left(\ln C\right)_{,\phi\phi}\right]\delta\phi \\
&\quad = \left(\Psi' + 3\Phi'\right)\phi' - \frac{1}{2}a^2\rho_c\left(\ln C\right)_{,\phi}\left(1 - 3\frac{\delta p_c}{\delta\rho_c}\right)\delta_c \\
&\qquad - a^2\left[2V_{,\phi} + \left(\ln C\right)_{,\phi}\left(1-3w_c\right)\rho_c\right]\Psi .
\end{aligned} \tag{5.74}$$

5.4 The ISW effect & interacting dark energy

We here consider the imprint of interacting DE models, each of which is characterised by a specific choice of coupling functions, on the integrated Sachs–Wolfe (ISW) effect [584] in the CMB temperature power spectrum, which boosts the power at low multipoles. The ISW effect gives a non–zero contribution to the CMB fluctuations whenever the large–scale gravitational potential is time evolving. Thus, this secondary source of CMB anisotropy will not contribute during the matter dominated era, although it will be present after CMB decoupling, and at the very recent times when the expansion of the Universe starts to be dominated by DE. In order to distinguish our interacting DE scenarios from the concordance model, we consider the height of the first three acoustic peaks of the CMB temperature power spectrum relative to the power at $\ell = 10$, by the quantity

$$H_i = \left(\frac{\Delta T_{\ell_i}}{\Delta T_{10}}\right)^2 , \tag{5.75}$$

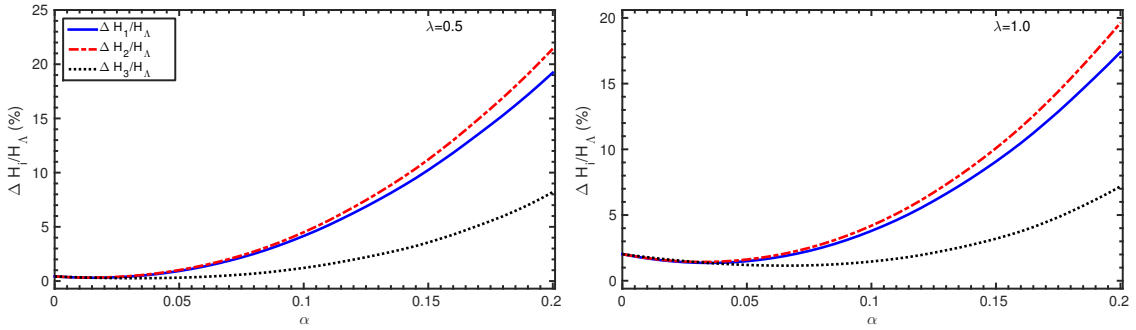

Figure 5.5: These panels show the relative difference of H_1, H_2, and H_3 to the ΛCDM model for conformally coupled models with coupling and potential functions as defined in Eq. (5.19). The slope of the potential has been set to $\lambda = 0.5$ (left) and to $\lambda = 1.0$ (right).

with $i = \{1, 2, 3\}$, and $(\Delta T_{\ell_i})^2 = \ell_i\,(\ell_i + 1)\,C_{\ell_i}/2\pi$, where C_{ℓ_i} is the power spectrum of the multipole moments of the temperature field at peak position ℓ_i [585]. We compare a number of interacting DE models with the ΛCDM model by computing the relative difference of H_i to the ΛCDM model, such that the compared models have identical Hubble constant, spectral index (see chapter 2), baryon density, and DM fraction. We denote this difference by $\Delta H_i/H_\Lambda$, in which we first determine the parameters H_i in the interacting DE model from the CMB spectra, and compare them with those of the ΛCDM model, where we numerically compute all the power spectra with the `CLASS` code.

We illustrate two conformal models in the panels of Fig. 5.5, and a disformal together with a mixed case in Fig. 5.6. In order to clearly discern these interacting DE models from the concordance model, we require that the relative difference of H_i, needs to be comparable with the dominant uncertainty ($\sim 30\%$) [586] arising from cosmic variance at $\ell = 10$.

Thus, an immediate observation from the examples presented in Figs. 5.5–5.6 is that, both a conformal and a disformal coupling in the dark sector of the Universe are hardly distinguishable from the ΛCDM model, particularly when a disformal coupling is present. For a pure conformal coupling, the relative difference from the ΛCDM model increases significantly up to around twenty percent as the coupling strength is enhanced, whereas for disformal and mixed couplings the discrepancy with the Λ case stays at the order of a few percent, even when the disformal coupling strength is increased considerably. Moreover, a conformal coupling together with a disformal coupling tend to decrease the relative difference of H_i, when compared with the pure disformal coupling model, as illustrated in Fig. 5.6. Finally, in conformally coupled models, we can see that H_2 is the best estimator, whereas H_1 gives the largest discrepancy from the ΛCDM model in the disformally and mixed coupled models, analogous to what has been reported for standard quintessence in Ref. [587].

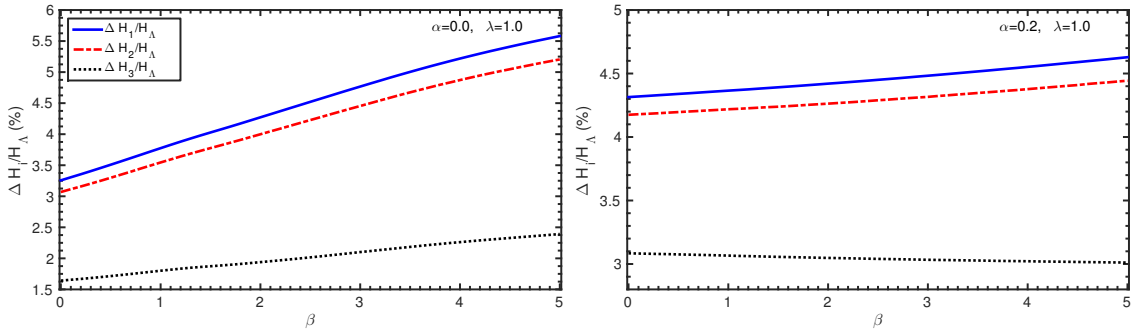

Figure 5.6: In the above panels we show the relative difference of H_1, H_2, and H_3 to the ΛCDM model for disformally coupled models (left) and mixed coupled models (right) with coupling and potential functions as defined in Eq. (5.19). For the disformal model (left) we set $\alpha = 0.0$ and $\lambda = 1.0$, while for the mixed model (right) we use $\alpha = 0.2$ and $\lambda = 1.0$. In both cases we use the relation $D_M V_0 = 1$.

As already mentioned, these best estimators of the ISW effect which give rise to the largest discrepancy between an interacting DE model and the concordance model, are still not able to produce a simple detectable signature due to the cosmic variance uncertainty. One can overcome this difficulty by cross–correlating matter templates constructed from galaxy catalogues with the CMB temperature power spectrum [588–591]. This additional probe of the interaction between the dark sector elements could potentially provide further constraints on our model parameters, although this is beyond the scope of our discussion.

5.5 Imprints on the growth history

We now discuss another intriguing characteristic of our interacting DE models, which is embodied in their growth history. We consider the matter growth rate function, defined by

$$f_m = \frac{\mathrm{d}\ln\delta_m}{\mathrm{d}\ln a} = \frac{\delta_m'}{\mathcal{H}\delta_m}\,, \tag{5.76}$$

where we further defined the matter density contrast by

$$\delta_m = \frac{\rho_b\delta_b + \rho_c\delta_c}{\rho_b + \rho_c}\,, \tag{5.77}$$

with δ_b, δ_c being the baryon and coupled DM density contrasts, respectively. In order to distinguish between the interacting DE models, we consider a useful combination of the product of the matter growth rate function f_m, with the root–mean–square mass fluctuation amplitude in spheres of radius $8\,h^{-1}$Mpc, $\sigma_8(z)$ [592]. In Fig. 5.7 we plot the expansion history against the growth history, more specifically H/H_0 against $f_m\,\sigma_8$, where $H = a^{-1}\mathcal{H}$. We further recall that, the reduced Hubble constant

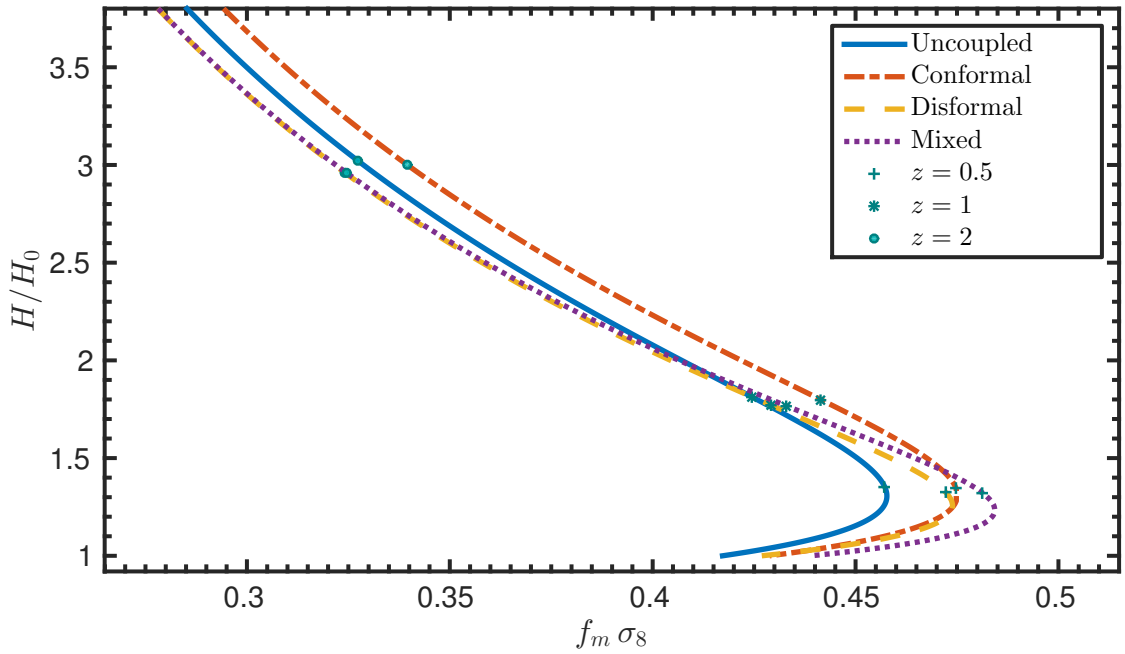

Figure 5.7: This figure shows the expansion history H/H_0, against the matter growth history $f_m\sigma_8$, at wave number $k = 0.1\,h\,\mathrm{Mpc}^{-1}$. For the conformal model we set $\alpha = 0.05$, for the disformal model we choose $D_M = 0.43\,\mathrm{meV}^{-1}$ and $\beta = 0$, and we use the same parameters in the mixed model. We set $\lambda = 1$ in all the models. We depict three specific locations of the redshift along each curve by a $+$, $*$, $\circ$, corresponding to $z = 0.5,\ 1,\ 2$, respectively.

parameter[2] h, is defined via $H_0 = 100\,h\,\mathrm{km\,s^{-1}\,Mpc^{-1}}$. The redshift in Fig. 5.7 runs along the curves, such that it monotonically decreases from top to bottom. Thus, by locating the same redshift on each curve, one can determine if the expansion rate differs from one model to another. In this figure we locate three different redshifts on each curve, and one can easily observe that at any given redshift, these models give a different value of H/H_0, although the difference is rather small.

An important feature in Fig. 5.7 is the turnaround location, which is easily distinguishable for each different model depicted in this figure. This turning point in each curve comes from the fact that as the cosmic evolution enters the accelerating epoch, the growth rate is suppressed with respect to its value in the matter dominated era. Although the expansion history of these models might not be a suitable discriminator, the growth history at late–times turns out to be more informative. For a given value of H/H_0, one can determine if the growth rate is enhanced or suppressed, with respect to a specific model. Indeed, one can observe that conformally coupled models tend to give an enhanced growth rate, with respect to the uncoupled case at

[2]We remark that, although we make use of the same variable, this should not be confused with that of section 5.3.

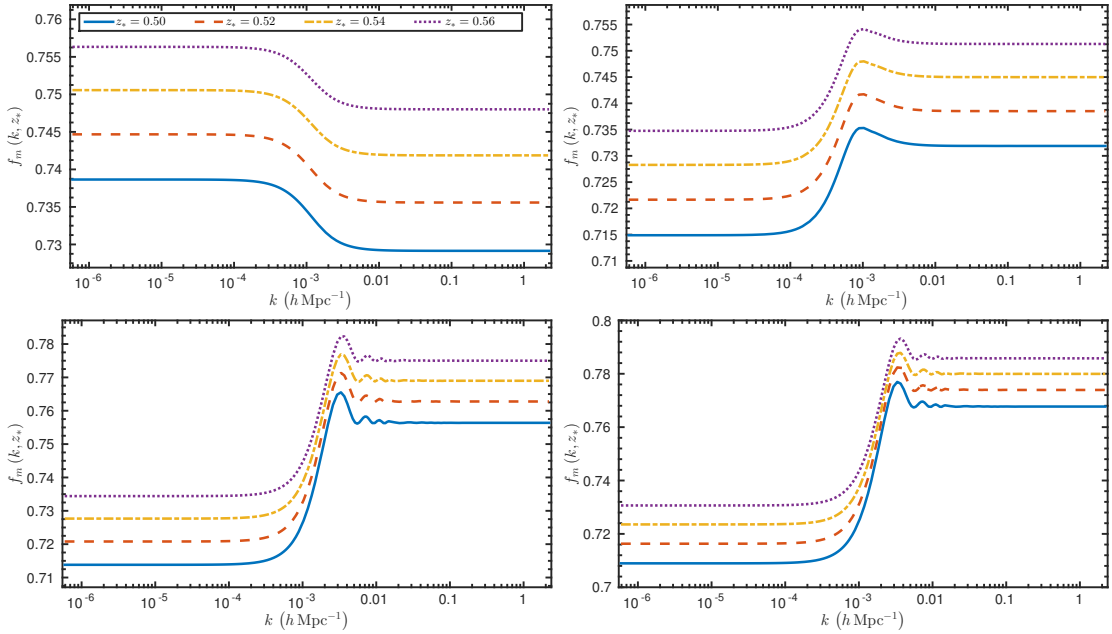

Figure 5.8: These panels show the matter growth rate function $f_m\,(k,\ z_*)$ as a function of the wave number k in h Mpc^{-1}, at the redshifts $z_* = 0.50,\ 0.52,\ 0.54,\ 0.56$. The uncoupled case is shown in the top left panel, the top right panel is the conformal case, the lower left panel is the disformal case, and the lower right panel corresponds to the mixed case. The model parameters are the same as in Fig. 5.7.

all redshifts. On the other hand, models with a disformal coupling tend to suppress the growth of structure when the coupling is still not active, and when the late–time coupling starts to modify the cosmic evolution, the growth rate is enhanced, and overtakes the growth rates of the uncoupled and the conformal models (see also Ref. [485]). One should also remark that a mixed model tends to be characterised by the largest growth rate, since both couplings are contributing for this enhanced growth. This is an interesting feature of the disformal coupling, which distinguishes it from the rest.

We now consider the evolution of $f_m(k, z)$, as a function of the wave number k, covering both the large–scales as well as the small–scales, at several particular redshifts. We present the plots of this wave number evolution in Fig. 5.8, in which we illustrate four different scenarios, including standard quintessence along with the coupled models. As expected, the growth rate in the standard quintessence model, can be regarded as being (nearly) k–independent for the whole range of values being considered in this plot. On the other hand, coupled models are characterised by an enhancement in the growth rate function on the small–scales when compared to the large–scales. In the conformal model, this is a well–known characteristic (see for example Refs. [590, 593]) which is easily observed from the increase in power in the matter power spectrum on small–scales. In this scenario, the increase in the growth

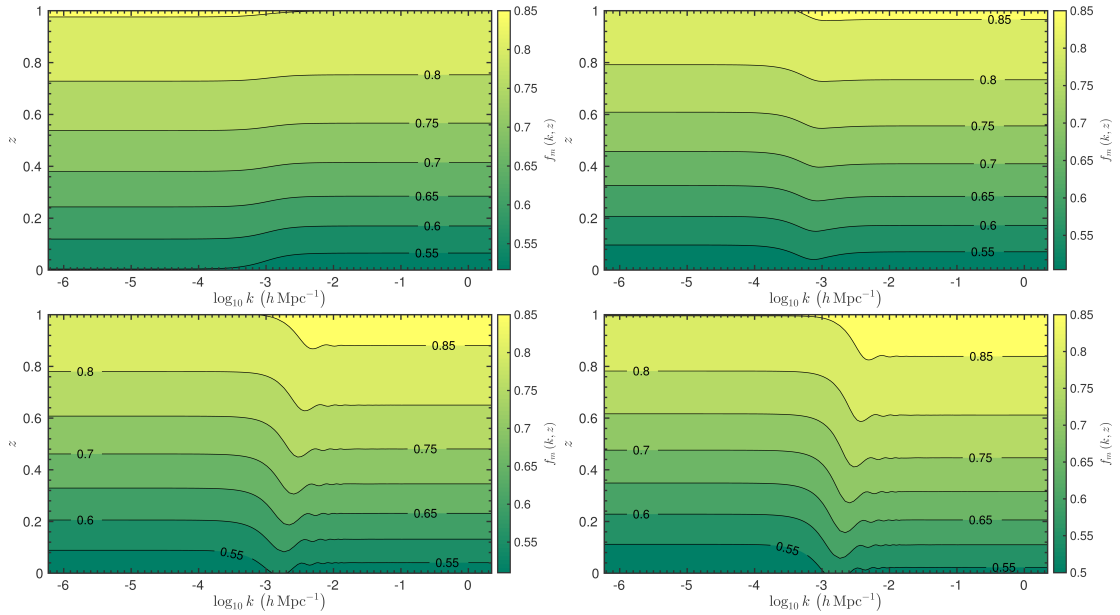

Figure 5.9: The above panels show the contour lines of the matter growth rate function $f_m\,(k,\ z)$ as a function of the wave number $\log_{10} k$ in h Mpc^{-1} and redshift z. The uncoupled case is shown in the top left panel, the top right panel depicts the conformal case, the lower left panel is the disformal case, and the lower right panel corresponds to the mixed case. The model parameters are the same as in Fig. 5.7.

rate on small–scales is a result of the fact that, due to the coupling there is an increase in the DM fraction in the past when compared with that in the uncoupled scenario, leading to an earlier matter radiation equality. Consequently, the wavelengths of the perturbations that enter during the radiation dominated era are shorter, and therefore the turnaround of the matter power spectrum moves to smaller scales, and the small–scale amplitude of the matter power spectrum is boosted. Another feature in the matter power spectrum is the change in location and amplitude of the baryon acoustic oscillations peaks imprinted on the matter power spectrum itself.

In the considered interacting DE models which incorporate a disformal coupling, the increase in the matter growth rate function on small–scales is mainly due to the additional attractive force between the DM particles, as a result of their non–minimal coupling to the scalar field. In section 5.6, we will find that on these scales, the attractive force between the coupled DM particles is enhanced, leading to an enhancement in the growth rate function. This also holds for the conformally coupled models, although disformal couplings tend to be associated with a relatively larger fifth–force. As a consequence of this enhancement in the growth of structure on small–scales, the $\sigma_8(z=0)$ (see Eq. (1.56)) value is also expected to increase in these models. Indeed, in chapter 6 we will clearly illustrate that large–scale structure data sets impose the tightest constraints on the disformal coupling parameters.

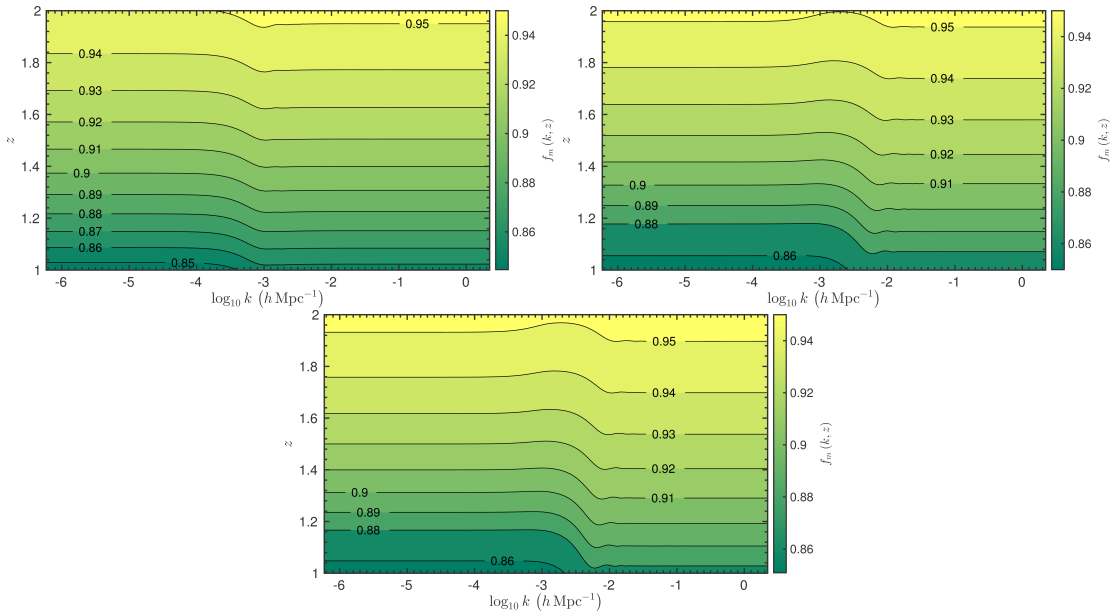

Figure 5.10: The panels of this figure show the contour lines of the matter growth rate function $f_m\,(k,\,z)$ as a function of the wave number $\log_{10} k$ in $h\,\mathrm{Mpc}^{-1}$ and redshift z. The top left panel depicts the conformal case, the top right panel corresponds to the disformal case, and the lower panel is the mixed case. The model parameters are the same as in Fig. 5.7.

Furthermore, in the presence of a disformal coupling, the matter growth rate function is found to be characterised by distinctive intermediate–scales and time–dependent damped oscillations, which we reported for the first time in Ref. [3], attributed to the dynamics of the coupling function itself. These peculiar features only occur when one considers the disformal coupling, since these are not observed in standard quintessence or in conformally coupled models. The oscillations in the matter growth rate function are present when the disformal coupling starts to play an important role in the cosmic evolution, and thus we expect these oscillations to be negligible at relatively higher redshifts. Indeed, this is what happens, as clearly depicted in Figs. 5.9–5.10, in which the oscillatory features are clearly visible at $z < 1$, losing their significance even at $z \simeq 1.5$. Also, from these contour plots, one can see that a disformal coupling induces a slight scale–dependence on the growth rate function. This is expected due to the k–dependence of the perturbed coupling function δQ given in Eq. (5.65). Such time–dependent and scale–dependent characteristics in the matter growth rate function are expected to be probed by upcoming cosmological surveys, including emission–line–galaxy surveys along with intensity mapping observations [594], which will measure the scale–dependence of the matter power spectrum at several cosmic times [595].

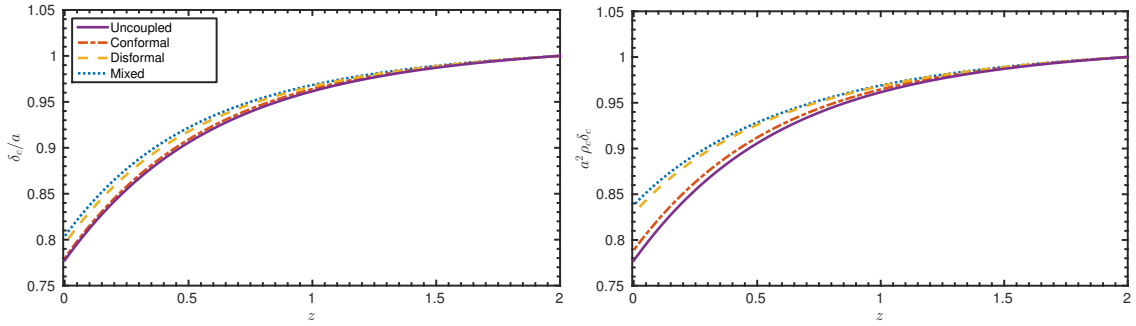

Figure 5.11: These panels show the redshift evolution of the normalised DM growth rate δ_c/a (left), and the normalised combination of $a^2\rho_c\delta_c$ (right) appearing in the Poisson equation, at wave number $k = 0.1\,h\,\mathrm{Mpc}^{-1}$. All model parameters are the same as those adopted in Fig. 5.7.

5.6 The small–scale limit of perturbations

We now discuss the Newtonian limit of the generic perturbation equations presented in section 5.3 for the specific case of a coupled barotropic pressureless fluid. For this analysis, we neglect the anisotropic stress contribution in the field equations, leading to $\Psi = \Phi$. In the small–scale limit $\hat{\lambda} = \mathcal{H}/k \ll 1$, the evolution equations of the gravitational potential Φ, and its conformal time derivative Φ', reduce to the following

$$\Phi \simeq -\frac{\hat{\lambda}^2}{2}\left[\frac{\kappa^2}{\mathcal{H}^2}\left(3\mathcal{H}\phi'\delta\phi + \phi'\delta\phi' + a^2V_{,\phi}\delta\phi\right) + 3\sum_{i=b,r,c}\Omega_i\delta_i\right] , \tag{5.78}$$

$$\Phi' \simeq \frac{1}{2}\left(\kappa^2\phi'\delta\phi - 2\mathcal{H}\Phi\right) . \tag{5.79}$$

Moreover, in this small–scale limit, the evolution of the perturbed scalar field is now governed by the equation

$$\delta\phi'' + 2\mathcal{H}\delta\phi' + \hat{\lambda}^{-2}\mathcal{H}^2\delta\phi \simeq a^2\delta Q , \tag{5.80}$$

in which we have neglected terms proportional to Φ $\left(\sim \hat{\lambda}^2\right)$. Furthermore, we assumed that the term proportional to ϕ'^2, is much less than $\hat{\lambda}^{-2}$, and that the potential is flat enough so that the $V_{,\phi\phi}$ term is negligible with respect to $\hat{\lambda}^{-2}$. The homogeneous solution of Eq. (5.80) averages out to a zero contribution to the perturbed scalar field solution in the very small–scale limit, leaving only the inhomogeneous solution, which, on averaging over the oscillations and neglecting the contributions from $\delta\phi''$ and $\delta\phi'$ (this can be further checked a posteriori), is approximately given

by

$$\delta\phi \simeq \hat{\lambda}^2 a^2 \mathcal{H}^{-2} \delta Q \,. \tag{5.81}$$

In this limit, the perturbation of the coupling function, defined in Eq. (5.65), simplifies significantly to [485, 535]

$$\delta Q \simeq Q \delta_c \,. \tag{5.82}$$

Since $\delta\phi$ is of the order of $\hat{\lambda}^2$, Eq. (5.78) reduces to the conventional Poisson equation

$$\Phi \simeq -\frac{3}{2}\hat{\lambda}^2 \sum_{i=b,r,c} \Omega_i \delta_i \,. \tag{5.83}$$

From the term $a^2\rho_c\delta_c$, appearing on the right hand side of Eq. (5.83), one can determine if this quantity changes drastically in these interacting DE models, which would then lead to a time–evolving gravitational potential. From Fig. 5.11, we observe that although the growth rates at late–times can differ from one another (especially when large couplings are considered), the combination of $a^2\rho_c\delta_c$ does not change appreciably, thus leaving a small imprint of the ISW effect on the CMB temperature power spectrum, in accordance with the results obtained in section 5.4. This is an unusual behaviour of these models, since normally cosmological models with different growth history give rise to a distinguishable ISW effect [596].

Furthermore, the evolution of the coupled pressureless fluid density contrast is now governed by the differential equation

$$\delta_c'' + \mathcal{H}_{\rm eff}\, \delta_c' - \frac{3}{2}\mathcal{H}^2 \frac{G_{\rm eff}}{G}\, \Omega_c \delta_c = \frac{3}{2}\mathcal{H}^2 \left(\Omega_b \delta_b + \Omega_r \delta_r\right) \,. \tag{5.84}$$

Hence, the coupled fluid perturbations experience effectively different values of $\mathcal{H}$ and G, due to the interaction, namely [485]

$$\frac{\mathcal{H}_{\rm eff}}{\mathcal{H}} = 1 - \frac{1}{\mathcal{H}}\frac{Q}{\rho_c}\phi' \,, \qquad \frac{G_{\rm eff}}{G} = 1 + \frac{2}{\kappa^2}\frac{Q^2}{\rho_c^2} \,. \tag{5.85}$$

Thus, the introduction of a coupling between the DE scalar field and DM, induces a modification in the damping term together with an amplification of Newton's gravitational constant in Eq. (5.84). Moreover, the added contribution in the effective gravitational constant is independent of the sign of the coupling function.

Since baryons satisfy the standard uncoupled equation for the evolution of the baryon density contrast, we expect that there will be a bias between baryons and coupled DM. We study this in the DM dominated scenario, $|\Omega_c\delta_c| \gg |\Omega_b\delta_b| \gg |\Omega_r\delta_r|$, and define a constant bias parameter b, by $\delta_b = b\,\delta_c$. We can easily determine the bias by writing Eq. (5.84) and a similar one for baryons (in which we also neglect the

term proportional to its sound speed) in terms of the coupled DM growth parameter $f_c = \mathrm{d}\ln\delta_c/\mathrm{d}N$, where $N = \ln a$. Indeed, we find that the growth rate equations of baryons and coupled DM reduce to

$$\frac{\mathrm{d}f_c}{\mathrm{d}N} + f_c^2 + \frac{1}{2}\left(1 - 3w_{\mathrm{eff}}\right) f_c - \frac{3}{2}\frac{\Omega_c}{b} = 0 \,, \tag{5.86}$$

$$\frac{\mathrm{d}f_c}{\mathrm{d}N} + f_c^2 + \frac{1}{2}\left(1 - 3w_{\mathrm{eff}} - 2\frac{Q}{\rho_c}\frac{\mathrm{d}\phi}{\mathrm{d}N}\right) f_c - \frac{3}{2}\frac{G_{\mathrm{eff}}}{G}\Omega_c = 0 \,, \tag{5.87}$$

respectively. We further adopted a total effective equation of state, which follows from the already defined effective equation of state in Eq. (4.43), that characterises the expansion rate as

$$\frac{1}{\mathcal{H}}\frac{\mathrm{d}\mathcal{H}}{\mathrm{d}N} = -\frac{1}{2}\left(1 + 3w_{\mathrm{eff}}\right) \,. \tag{5.88}$$

From Eq. (5.86) and Eq. (5.87), one arrives to a simplified expression for the bias

$$b = \frac{3\Omega_c}{2\frac{Q}{\rho_c}\frac{\mathrm{d}\phi}{\mathrm{d}N} f_c + 3\frac{G_{\mathrm{eff}}}{G}\Omega_c} \,. \tag{5.89}$$

Indeed, as a result of unequal couplings of these pressureless species, a time–dependent bias develops between them.

5.6.1 Analytical solutions in interacting dark energy models

We will now briefly discuss some analytical solutions of Eq. (5.84) at four particular coupled fixed points in the DM dominated era. The effective equation of state defined in Eq. (5.88) is constant at these fixed points, thus the scale factor evolves as $a \sim \tau^{2/(1+3w_{\mathrm{eff}})}$. In order to relate this analysis with that of chapter 4, for this section only, we shall consider the following coupling and scalar field potential functions

$$C(\phi) = e^{2\alpha\kappa\phi} \,, \quad D(\phi) = D_M^4 e^{2(\alpha+\beta)\kappa\phi} \,, \quad V(\phi) = V_0^4 e^{-\lambda\kappa\phi} \,, \tag{5.90}$$

where we recall that α, D_M, β, V_0, and λ are constants. At any fixed point, one can conveniently write Eq. (5.84) as follows

$$\frac{\mathrm{d}^2\delta_c}{\mathrm{d}N^2} + \xi_1\frac{\mathrm{d}\delta_c}{\mathrm{d}N} + \xi_2\delta_c = 0 \,, \tag{5.91}$$

where ξ_1 and ξ_2 are both constants which depend on the phase–space coordinates of that particular fixed point. Thus, the solution of the coupled DM density contrast

is

$$\delta_c = c_+ a^{m_+} + c_- a^{m_-} \ , \quad m_\pm = \frac{1}{2}\left(-\xi_1 \pm \sqrt{\xi_1^2 - 4\xi_2}\right) \ , \tag{5.92}$$

where $c_\pm$ are integration constants. Moreover, from Eq. (5.83) we find that at these fixed points $\Phi \sim a^{-1-3w_{\rm eff}+m_\pm}$.

Disformal fixed points

We will now consider two disformal fixed points $(3)_{(d)}$ and $(4)_{(d)}$, of section 4.3. For the fixed point $(3)_{(d)}$, which exists when $\beta \geq \sqrt{3/2}$, we find that this leads to a non–standard growth index

$$\begin{aligned} m_\pm = \frac{1}{2}\Bigg\{ & -5 + 3\beta\left(2\beta - \sqrt{4\beta^2 - 6}\right) \\ & \pm \sqrt{1 - 2\beta\left\{\sqrt{4\beta^2-6} + \beta\left[1 - 2\beta\left(2\beta - \sqrt{4\beta^2-6}\right)\right]\right\}} \Bigg\} \ . \end{aligned} \tag{5.93}$$

Similarly, the disformal fixed point $(4)_{(d)}$, which exists for $\beta \leq -\sqrt{3/2}$, is characterised by the growth index

$$\begin{aligned} m_\pm = \frac{1}{2}\Bigg\{ & -5 + 3\beta\left(2\beta + \sqrt{4\beta^2 - 6}\right) \\ & \pm \sqrt{1 + 2\beta\left\{\sqrt{4\beta^2-6} + \beta\left[-1 + 2\beta\left(2\beta + \sqrt{4\beta^2-6}\right)\right]\right\}} \Bigg\} \ . \end{aligned} \tag{5.94}$$

In Fig. 5.12 we illustrate the growth index as a function of the coupling parameter β, for both disformal fixed points. At these fixed points, a non–standard growth index is only obtained for a restricted range of the parameter β. Moreover, we find that for the values of β that we are considering, Φ is a constant to a very good approximation.

Conformal fixed points

We will now cover the conformal scaling fixed point $(8)_{(d)}$, and another transient fixed point which appears in the DM dominated era giving rise to a scalar field matter dominated regime (ϕMDE) $(6)_{(d)}$, which were derived in section 4.3. The

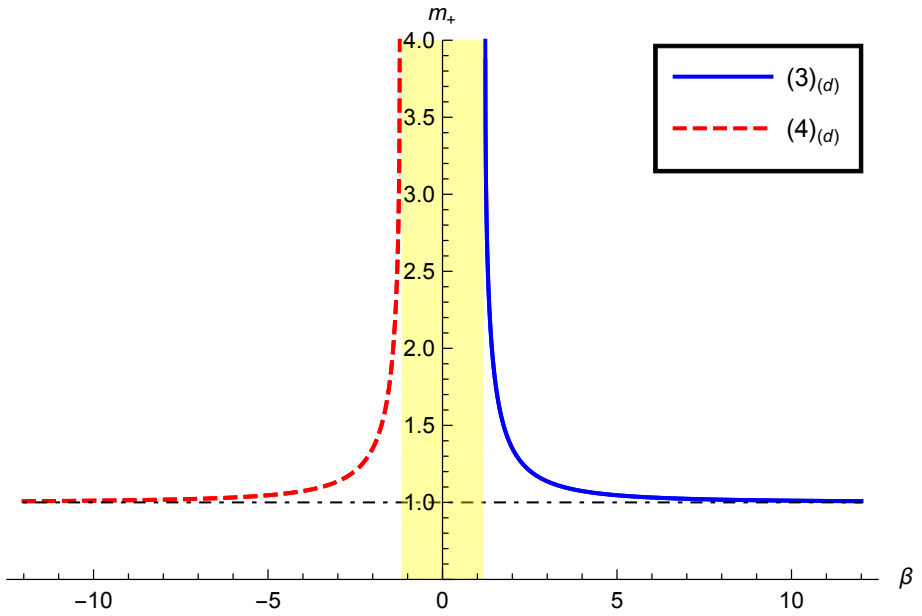

Figure 5.12: We illustrate the growth index m_+, as a function of the coupling parameter β, for the disformal fixed points $(3)_{(d)}$ and $(4)_{(d)}$. The shaded yellow region depicts the range of values of $-\sqrt{3/2} < \beta < \sqrt{3/2}$, at which both fixed points are not defined.

latter fixed point is characterised by

$$m_+ = 1 + 2\alpha^2 \,, \quad m_- = -\frac{3}{2} + \alpha^2 \,, \tag{5.95}$$

leading to an enhanced growth rate of coupled DM when compared with the uncoupled scenario. Moreover, Φ is a constant at the ϕMDE growing mode solution. On the other hand, for the conformal scaling fixed point we have

$$m_\pm = \frac{1}{4}\left[-1 + 9w_{\rm eff} \pm \sqrt{\left(1 - 9w_{\rm eff}\right)^2 + 24\left(1 - \Omega_\phi\right)\left(1 + \frac{6w_{\rm eff}^2}{\Omega_\phi + w_{\rm eff}}\right)}\right] \,, \tag{5.96}$$

where we used $\Omega_\phi = 1 - \Omega_c$. Its growing mode solution gives rise to an enhanced growth of the DM perturbations, and to an anomalous ISW effect in the CMB power spectrum [597]. In Fig. 5.13 we illustrate the growth index m_+, as a function of α and λ, where we have also used the relations

$$\Omega_\phi = \frac{3 + \alpha(\alpha + \lambda)}{(\alpha + \lambda)^2} \,, \quad w_{\rm eff} = -\frac{\alpha}{\alpha + \lambda} \,. \tag{5.97}$$

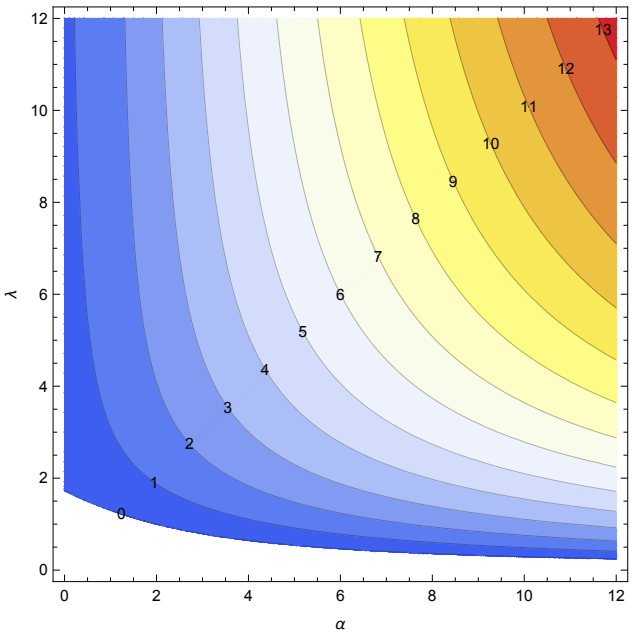

Figure 5.13: A contour plot of the growth index m_+, for the conformal scaling fixed point as a function of the conformal coupling parameter α, and the slope of the exponential potential λ.

5.7 Conclusions

In this chapter we have considered a coupled quintessence model, where the well–established late–time accelerated cosmic expansion is powered by a quintessence scalar field, which is explicitly coupled to DM. In our generic formulation we considered the dark sector constituents to be coupled via a conformal and a disformal coupling, whereas the baryonic and radiation sectors followed their standard cosmic evolution. We showed that the interaction between DE and DM can be viewed as an energy exchange mechanism between the two dark sector elements. Moreover, from the background evolution of the considered coupled scenarios, we observed that a disformal coupling instigates late–time modifications in the cosmological evolution, unlike the pure conformally coupled case.

In order to study the implications of the dark sector coupling on the CMB temperature power spectrum, we have considered the multipole separation of the location of the peaks in the CMB temperature power spectrum together with the ISW effect. For the former, we presented an analytical approach, from which we determined that the deviations of the conformally coupled model from the ΛCDM model are much larger than those in the mixed and the disformally coupled models. Indeed, we found that one is unable to distinguish between the concordance model and the coupled models that are characterised by a disformal coupling, by taking into ac-

count the deviation of the CMB peak separation from the ΛCDM model. Moreover, we found that the discrepancy that arises from the ISW effect between the coupled quintessence models and the ΛCDM model, is also inadequate to decipher the models from one another due to the uncertainty attributed to cosmic variance.

We then turned our attention to the cosmological imprints on the growth of structure, where we clearly distinguished between the interacting DE models themselves, along with the uncoupled model, by simply plotting the expansion history against the growth history. We found that the coupling between DE and DM leads to an enhanced growth with respect to the uncoupled quintessence model, particularly in coupled models which incorporate a non–vanishing disformal coupling. Furthermore, we discussed the matter growth rate function as a function of the wave number, which extends from the small–scales to the large–scales, as well as a function of the redshift. We established that the matter growth rate function is enhanced on small–scales with respect to large–scales, in all interacting DE models. This observed enhancement was further studied via the small–scale approximation of the perturbation equations, which we generically presented in two different gauges, in which we also discussed analytical solutions to the coupled DM density contrast at four specific fixed points.

Interestingly enough, disformal couplings were characterised by distinctive intermediate–scales and time–dependent damped oscillations in the matter growth rate function. This enabled us to further distinguish the coupled models which contain a non–vanishing disformal coupling, from the rest. We will further explore this generic interacting DE model formulation in the next chapter, in which we will determine its viability from the point of view of current cosmological data sets. From the theoretical perspective, one still needs to properly embed these kind of models in a more fundamental theory of Nature.

The search will continue. Not until the empirical resources are exhausted, need we pass on to the dreamy realms of speculation.

Edwin Powell Hubble

6

Status of dark sector interactions

The rapid progression of precision cosmology has undoubtedly led to a wide spectrum of cosmological probes that are able to survey different cosmic epochs. Consequently, this lavish information about the Universe repeatedly challenged our theoretical understanding of the cosmos. As we have clearly illustrated in chapter 2, the simplest cosmological framework of the concordance ΛCDM model is found to be in an excellent agreement with the currently reported cosmological observations, and its parameters have now been determined to an impressive accuracy. Given that this model has survived this bountiful amount of high precision data, robust constraints on new physics beyond the ΛCDM model are always getting tighter [576, 598–603]. Nevertheless, there have been indications in the data that are not well described by the ΛCDM model, as we illustrated in chapter 3.

A rational step towards a more comprehensive view of our Universe is to confront alternative cosmological models with the several cosmological data sets. Here we focus on the coupled quintessence model that we introduced in chapter 5, in which dark matter and dark energy interact with one another via the conformal and disformal couplings, whereas the standard model particles follow their standard cosmological evolution. As we discussed in the previous chapter, since the dark sector of the Universe, which is believed to be composed of dark matter and dark energy, has only been indirectly observed with cosmological observations, interactions between dark matter particles beyond the gravitational force and mediated by dark energy cannot be excluded a priori [456, 465, 468, 562, 604–606]. Moreover, we further illustrated that the additional fifth–force within the dark sector of the Universe modifies the background evolution, as well as the evolution of cosmological perturbations. Indeed, in this chapter we will demonstrate that current cosmological data sets are sensitive to this dark sector interaction.

Coupled dark energy models with a conformal coupling function have been ex-

haustively explored, and tight constraints have been placed on the model parameters [570, 573, 574, 576, 590, 593, 607–609]. On the other hand, we first confronted conformally–disformally coupled dark energy models in Ref. [5], in which we only used their background cosmic evolution, and we placed tighter constraints on the models in Ref. [4] by further adopting the evolution of cosmological perturbations. We should also note that, similar cosmological models which make use of a disformal coupling have been discussed in Refs. [1, 2, 471, 472, 480, 527, 535, 558, 575, 610, 611].

In section 6.1 we briefly introduce our interacting dark energy model, and in section 6.2 we summarise the observational data sets together with the method that will be employed to infer the cosmological parameter constraints. We then present the derived constraints in section 6.3, and draw our final remarks in section 6.4.

6.1 Interacting dark energy model

In this section we briefly review the basic equations of the generic coupled dark energy (DE) model, which we explored in chapter 5. We recall that, the Einstein frame action of this model reads

$$\begin{aligned}\mathcal{S} = &\int \mathrm{d}^4x\sqrt{-g}\left[\frac{M_{\rm Pl}^2}{2}R - \frac{1}{2}g^{\mu\nu}\partial_\mu\phi\,\partial_\nu\phi - V(\phi) + \mathcal{L}_{SM}\right] \\ &+ \int \mathrm{d}^4x\sqrt{-\tilde{g}}\widetilde{\mathcal{L}}_{DM}\left(\tilde{g}_{\mu\nu},\psi\right)\ ,\end{aligned} \tag{6.1}$$

in which the gravitational sector has the standard Einstein–Hilbert form, and recall that $M_{\rm Pl}^{-2} = 8\pi G$ where $M_{\rm Pl} = 2.4\times10^{18}$ GeV is the reduced Planck mass. DE is described by a canonical quintessence scalar field ϕ, with a potential $V(\phi)$. The uncoupled standard model (SM) particles are described by the Lagrangian $\mathcal{L}_{SM}$, which includes a relativistic sector (r), and a baryon sector (b). Particle quanta of the dark matter (DM) fields ψ, follow the geodesics defined by the metric

$$\tilde{g}_{\mu\nu} = C(\phi)g_{\mu\nu} + D(\phi)\,\partial_\mu\phi\,\partial_\nu\phi\ , \tag{6.2}$$

with $C(\phi)$, $D(\phi)$ being the conformal and disformal coupling functions, respectively.

We here adopt the spatially flat Friedmann–Lemaître–Robertson–Walker (FLRW) space–time, in which the scalar field evolves according to a modified Klein–Gordon equation

$$\phi'' + 2\mathcal{H}\phi' + a^2V_{,\phi} = a^2Q\ , \tag{6.3}$$

where $V_{,\phi} = \mathrm{d}V/\mathrm{d}\phi$, a prime denotes a conformal time derivative, and define the conformal Hubble parameter by $\mathcal{H} = a'/a$, with a being the cosmic scale factor.

The DM energy density ρ_c, does not follow the standard redshift evolution of a^{-3}, but is found to satisfy an energy exchange equation

$$\rho_c' + 3\mathcal{H}\rho_c = -Q\phi' \,, \tag{6.4}$$

whereas the radiation and baryonic energy densities satisfy the standard energy conservation equations

$$\rho_r' + 4\mathcal{H}\rho_r = 0 \,, \qquad \rho_b' + 3\mathcal{H}\rho_b = 0 \,, \tag{6.5}$$

respectively. In the FLRW space–time, the generic coupling function of Eq. (5.17) simplifies to

$$Q = \frac{2D\left(\frac{C_{,\phi}}{C}\phi'^2 + a^2V_{,\phi} + 3\mathcal{H}\phi'\right) - a^2C_{,\phi} - D_{,\phi}\phi'^2}{2\left[a^2C + D\left(a^2\rho_c - \phi'^2\right)\right]}\rho_c \,. \tag{6.6}$$

We recall that the Friedmann equations take their usual form, and in order to avoid unnecessary repetitions we refer to chapter 5 for further details.

To be concrete, throughout this chapter we choose an exponential functional form for the couplings and scalar field potential, namely

$$C(\phi) = e^{2\alpha\kappa\phi}, \; D(\phi) = D_M^4 e^{2\beta\kappa\phi}, \; V(\phi) = V_0^4 e^{-\lambda\kappa\phi}, \tag{6.7}$$

where α, D_M, β, V_0, and λ are constants, and recall that $\kappa^2 = M_{\rm Pl}^{-2}$. This explicit interaction between DM and DE modifies both the background dynamics, as well as the evolution of perturbations [3, 476, 485, 537, 563, 564, 597]. For instance, these dark sector couplings modify the cosmological distances, such as the distance to the last–scattering surface, thus have a direct impact on the cosmic microwave background (CMB) temperature power spectrum. In addition, this interaction within the dark sector shifts the epoch of matter–radiation equality, which in turn affects the theoretical matter power spectrum.

In the following sections, we will consider three main specific cases of this generic interacting DE model, which we shall refer to as the conformal, disformal, and mixed models. For the sake of clarity, each of these cases is dealt with separately. Henceforth, in the conformal model we only consider the conformal coupling, for the disformal model we set the conformal coupling to unity and study only the disformal coupling, whereas in the mixed model we simultaneously consider the conformal and disformal couplings.

6.2 Cosmological data sets & procedure

In this section, we discuss the data sets that will be used in our analyses. We will be confronting our coupled DE models with probes that survey the late–time Universe, along with early–time cosmic probes:

1. Cosmic microwave background

In all data set combinations we make use of the low multipole ($2 \leq \ell \leq 29$) publicly available *Planck* 2015 data, which also includes the power spectra of the CMB temperature and polarisation fluctuations [292], as well as the lensing power spectrum [91]. For the high multipole ($l \geq 30$) range, we assess the impact of the polarisation data by making use of the TT and TTTEEE likelihoods, which we denote by TT and TTEE, respectively. Occasionally we further use the *Planck* lensing likelihood in the multipole range $40 \leq \ell \leq 400$, and we refer to this data set as lensing.

2. Background data

In addition, we make use of two background data set combinations which will enable us to break parameter degeneracies from CMB measurements. These combinations consist of baryon acoustic oscillations (BAO) measurements, a supernovae Type Ia (SNIa) sample, a cosmic chronometers data set, and local measurements of the Hubble constant:

A. Baryon acoustic oscillations

BAO features in the clustering of galaxies have repeatedly been used by large–scale surveys as a standard ruler to measure the distance–redshift relation, where these acoustic oscillations in the photon–baryon plasma arise from the tight coupling of baryons and photons in the radiation dominated era. We consider BAO data from the SDSS Main Galaxy Sample at $z_{\rm eff} = 0.15$ [93], the six degree Field Galaxy Survey at $z_{\rm eff} = 0.106$ [92], and the Baryon Oscillation Spectroscopic Survey LOWZ and CMASS samples at $z_{\rm eff} = 0.32$ and $z_{\rm eff} = 0.57$ [612], respectively.

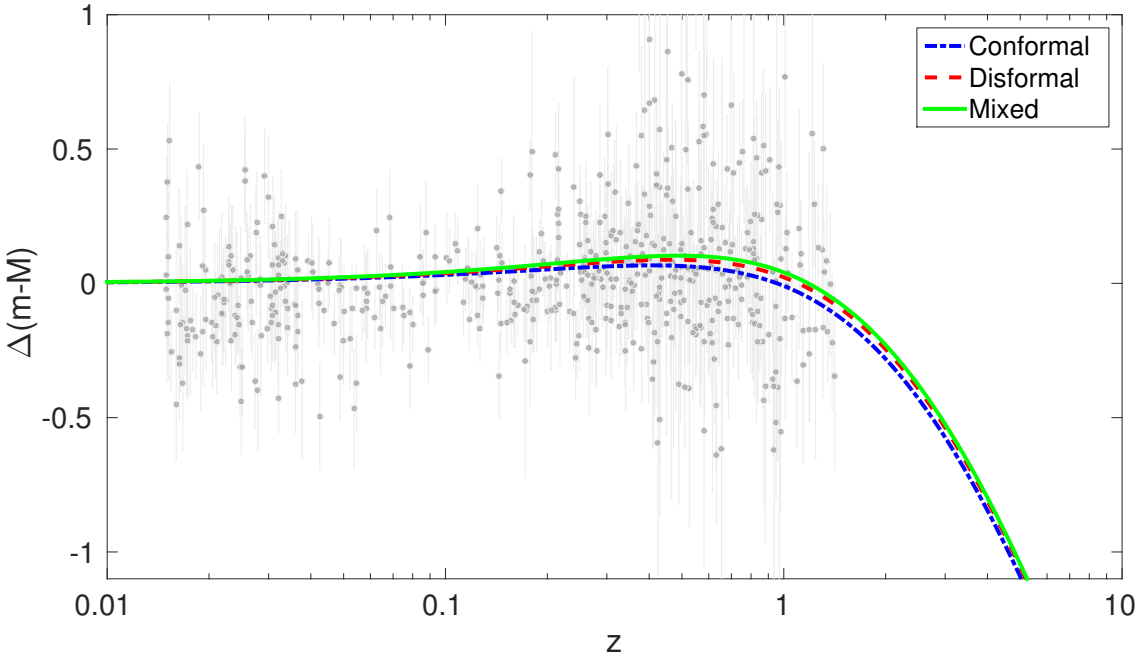

Figure 6.1: In this figure we compare the distance modulus of three interacting DE scenarios with a SNIa data set (gray error bars) [538]. We illustrate a conformal case (dot–dashed) with $\alpha = 0.02$, a constant disformal case (dashed) with $D_M = 0.4\,\mathrm{meV}^{-1}$, and a mixed case (solid) with $\alpha = 0.18$, $D_M = 0.4\,\mathrm{meV}^{-1}$, and $\beta = 0$. In all cases we set $\lambda = 1.1$.

B. Supernovae

Apart from providing the first observational evidence for the accelerating expansion of the Universe [87, 88], SNIa data sets have also been widely used for cosmological model parameter fitting. In Fig. 6.1 we illustrate the residual Hubble diagram from an empty Milne Universe, for three kinds of models when compared to the SNIa data set of Ref. [538], where we define the distance modulus by [613]

$$\Delta(m-M) = (m-M)_{\mathrm{model}} - (m-M)_{\mathrm{Milne}}\,, \tag{6.8}$$

where

$$m - M = 5\log_{10}\left[\frac{D_L(z)}{10\,\mathrm{pc}}\right]\,, \tag{6.9}$$

with m being the apparent magnitude, M is the absolute magnitude of the object, and $D_L(z)$ is the luminosity distance (see

section 1.2.3). In our analyses, we make use of the SDSS–II/ SNLS3 Joint Light–curve Analysis data compilation [95] of SNIa measurements.

C. Cosmic chronometers

We use the compiled measurements [296–301] of the Hubble parameter $H(z) = a^{-1}\mathcal{H}(z)$, which are derived from the cosmic chronometers approach, and span the redshift range $0 < z < 2$. This data is inferred from the differential age technique [614], which is based on measurements of the age difference between two passively–evolving galaxies that formed at the same time, but are separated by a small redshift interval.

D. Local Hubble constant

In order to assess the impact of the local measurements of the Hubble constant on our coupling parameter constraints, we adopt the measurements as reported by Adam Riess and his collaborators (hereafter denoted by $H_0^{\rm R}$) [78], and by George Efstathiou (hereafter denoted by $H_0^{\rm E}$) [96]. The choice of these measurements is motivated by the recent claims of some tension [346, 371, 375] within the concordance cosmological model between the CMB inferred constraint on H_0, and the local measurement $H_0^{\rm R}$, whereas the measurement $H_0^{\rm E}$ is still found to be in very good agreement with early–Universe probes. We refer to chapter 3 for a broader discussion on this matter.

In the following, we denote the background data set combinations BAO + SNIa + $H(z)$ + $H_0^{\rm E}$ and BAO + SNIa + $H(z)$ + $H_0^{\rm R}$, by BSHE and BSHR, respectively.

3. Cluster abundance

We use cluster abundance measurements [362, 363, 365–370] as a probe of the large–scale structure. This data set consists of eight measurements [615] in the form of $\sigma_8(\Omega_m/\tilde{\alpha})^{\tilde{\beta}}$, where the parameters $\tilde{\alpha}$ and $\tilde{\beta}$ are determined from each reported measurement, and we recall that $\sigma_8 = \sigma_8(z = 0)$ denotes the linear theory rms fluctuation in total matter in $8\,h^{-1}\,$Mpc

spheres, and Ω_m denotes the current total fractional abundance of matter with respect to the critical density (see section 1.2.3). We split this data set into two measurements [362, 363] which were found to be in tension with the concordance model (hereafter denoted by Cluster Abundance (CA)), and another subset containing the remaining six measurements [365–370] (hereafter denoted by Alternative Cluster Abundance (ACA)). Although in the analyses that follow we do not report the cosmological parameter constraints obtained from a joint analysis of the CA and ACA data sets, we have checked that in our coupled DE models, the derived constraints from a joint analysis are in an excellent agreement with the results from the CA data set analysis. This is because the two measurements of the CA data set have the smallest error–bars, and thus they dominate in a joint analysis. Moreover, we should mention that these cluster abundance measurements should be taken with a pinch of salt, due to their dependence on the concordance model under which these measurements were inferred. However, our goal is to check if the individual data sets can be brought in good agreement with each other with the inclusion of the DE interactions.

Similar to the analyses of chapter 2, we employ a Bayesian approach to infer the parameter posterior distributions together with their confidence limits. This is implemented by the Markov chain Monte Carlo (MCMC) technique via a customised version of `Monte Python` [291] which is interfaced with a modified version of the cosmological Boltzmann code `CLASS` [120]. Apart from the implementation of our specific coupled DE models' equations, we also included a shooting algorithm in `CLASS` in order to find the scalar field potential energy scale V_0. The equations governing the evolution of perturbations [3] in our specific coupled DE models were implemented in both the Newtonian and synchronous gauge, and verified that we get identical results in the two gauges (see section 5.3). For all the models considered in sections 6.3.1–6.3.3, we also made use of the MCMC analysis package `GetDist` [90], and verified that the results are in an excellent agreement with those obtained from `Monte Python`.

We consider flat priors for the generic cosmological parameters that are allowed to vary in our MCMC analyses. The full range of each flat prior is listed in Table 6.1. The general baseline set of parameters consists of $\Theta = \{\Omega_b h^2,\, \Omega_c h^2,\, 100\,\theta_s,\, \tau_{\rm reio},\, \ln(10^{10} A_s),\, n_s,\, \lambda,\, \alpha,\, D_M,\, \beta\}$. Here, h is defined in terms of the Hubble constant via $H_0 = 100\,h\,{\rm km\,s^{-1}Mpc^{-1}}$, $\Omega_b h^2$ represents the effective fractional abundance of uncoupled baryons, $\Omega_c h^2$ denotes the pressureless coupled cold dark matter effective

Parameter	Prior
$\Omega_b h^2$	[0.005, 0.100]
$\Omega_c h^2$	[0.01, 0.99]
$100\ \theta_s$	[0.5, 10.0]
$\tau_{\rm reio}$	[0.04, 0.80]
$\ln(10^{10} A_s)$	[2.7, 4.0]
n_s	[0.5, 1.5]
λ	[0.0, 1.7]
α	[0.00, 0.48]
$D_M/\,\mathrm{meV}^{-1}$ . . .	[0.0, 1.1]
β	[0, 3]

Table 6.1: External generic flat priors on the cosmological parameters, including the coupling dependent parameters assumed in these analyses.

energy density, $100\,\theta_s$ is the angular scale of the sound horizon at last scattering defined by the ratio of the sound horizon at decoupling to the angular diameter distance to the last scattering surface (see section 1.2.3), $\tau_{\rm reio}$ is the reionization optical depth parameter (see section 1.2.3), $\ln(10^{10} A_s)$ is the log power of the scalar amplitude of the primordial power spectrum together with its scalar spectral index n_s, λ is the slope of the scalar field exponential potential, α is the conformal coupling parameter, and D_M is the energy scale of the disformal coupling together with the disformal exponent β. The chosen parameter space for the exponential functions of Eq. (6.7) guarantees that we avoid the possibility of an instability attributed to ghost and gradient conditions, thus the models are physically viable [1, 485] since the metric transformation is well–defined [447], and refer to chapter 4 for further details on this matter. In addition, due to the smallness of the coupling strength relative to the gravitational strength, we are outside the adiabatic instability regime [616]. We remark that the specific prior for D_M emerges from the fact that within this range of values, the disformal coupling has a maximal effect on the cosmic evolution. The pivot scale in our analyses was set to $k_0 = 0.05\,\mathrm{Mpc}^{-1}$, and we assume purely adiabatic scalar perturbations at very early times without the running of the scalar

spectral index. Moreover, we fix the neutrino effective number to its standard value of $N_{\rm eff} = 3.046$ [106, 107], as well as the photon temperature today to $T_0 = 2.7255\,{\rm K}$ [105]. As mentioned earlier, we assume spatial flatness.

In the top block of Tables 6.2–6.8, we present the constraints on the parameters with flat priors that are varied in the MCMC analyses of the respective coupled DE model. In our analyses, we also consider marginalised constraints on various derived parameters which we present in the lower block of Tables 6.2–6.8. The derived parameters include the present–day value of the Hubble parameter H_0 in ${\rm km\,s^{-1}Mpc^{-1}}$, Ω_m, σ_8, the reionization redshift $z_{\rm reio}$, and the dimensionless age of the Universe $H_0 t_0$, with t_0 being the current age of the Universe.

6.3 Results

In this section we discuss the inferred cosmological parameter constraints following the procedure described in section 6.2. We first consider a coupled DE model with an exponential conformal coupling only, which we discuss in section 6.3.1, and then we present the obtained constraints in the constant as well as in the exponential disformally coupled DE models in section 6.3.2. Finally, in section 6.3.3 we discuss the derived constraints for the mixed coupled model which simultaneously makes use of both the exponential conformal and constant disformal couplings between the dark sector constituents. In the mixed model, we further consider a particular case in which we fix the constant disformal coupling parameter D_M, in order to assess the impact on the conformal coupling parameter constraint.

In Fig. 6.2 we illustrate the obtained cosmological parameter constraints on the usual six varied parameters of the concordance model (see chapter 2) from the MCMC likelihood analyses in the conformal, disformal, and mixed coupled DE models with all data set combinations considered throughout these analyses. For the disformal model we only show the inferred constraints from the constant disformally coupled model, since the 1σ limits do not change appreciably in the exponential disformally coupled case presented in Table 6.6. Similarly, for the mixed coupled model we do not show the constraints from the mixed model with fixed D_M, considered in the last column of Table 6.8.

A common feature of our coupled DE models is that when the cluster abundance data sets are included, $\tau_{\rm reio}$ and A_s are shifted to lower values in comparison with their inferred mean values from the other data set combinations. This shift is predominantly observed when using the CA data set rather than the ACA measurements. The reason behind this is that the measurements contained in the CA data set prefer lower values of σ_8 in all coupled DE models with respect to the other data sets, including those in the ACA data set. Moreover, the major impacts of this shift in the range of σ_8 are found to be on $\tau_{\rm reio}$ and A_s, which follow from the

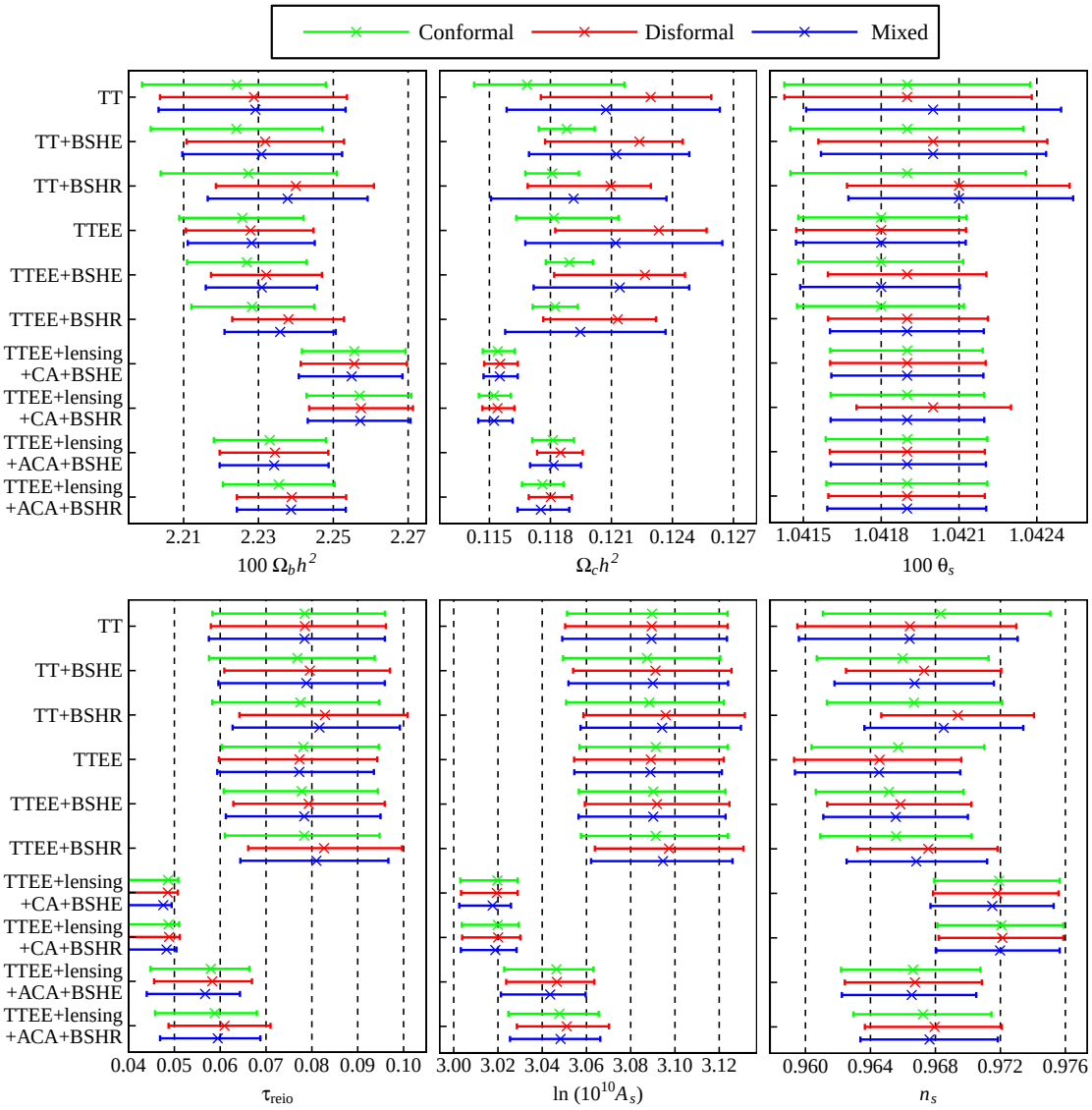

Figure 6.2: Cosmological parameter constraints in three coupled DE models with all data set combinations. The coloured intervals correspond to the marginalised 1σ two–tail limits of each parameter.

degeneracies between $\tau_{\rm reio}$ and σ_8, and between A_s and σ_8. As a consequence of these degeneracies, a discrepancy between the 1σ limits of $\tau_{\rm reio}$ and A_s arises between the data set combinations which make use of the CA measurements with the other data set combinations which do not include the cluster abundance measurements. This is clearly shown in Fig. 6.2. Nonetheless, the inferred values of $\tau_{\rm reio}$ from all data set combinations, including those combinations which use the cluster abundance data sets, are still in agreement with constraints from other reionization probes [620–622]. Clearly, improved accuracy on the reionization optical depth parameter will

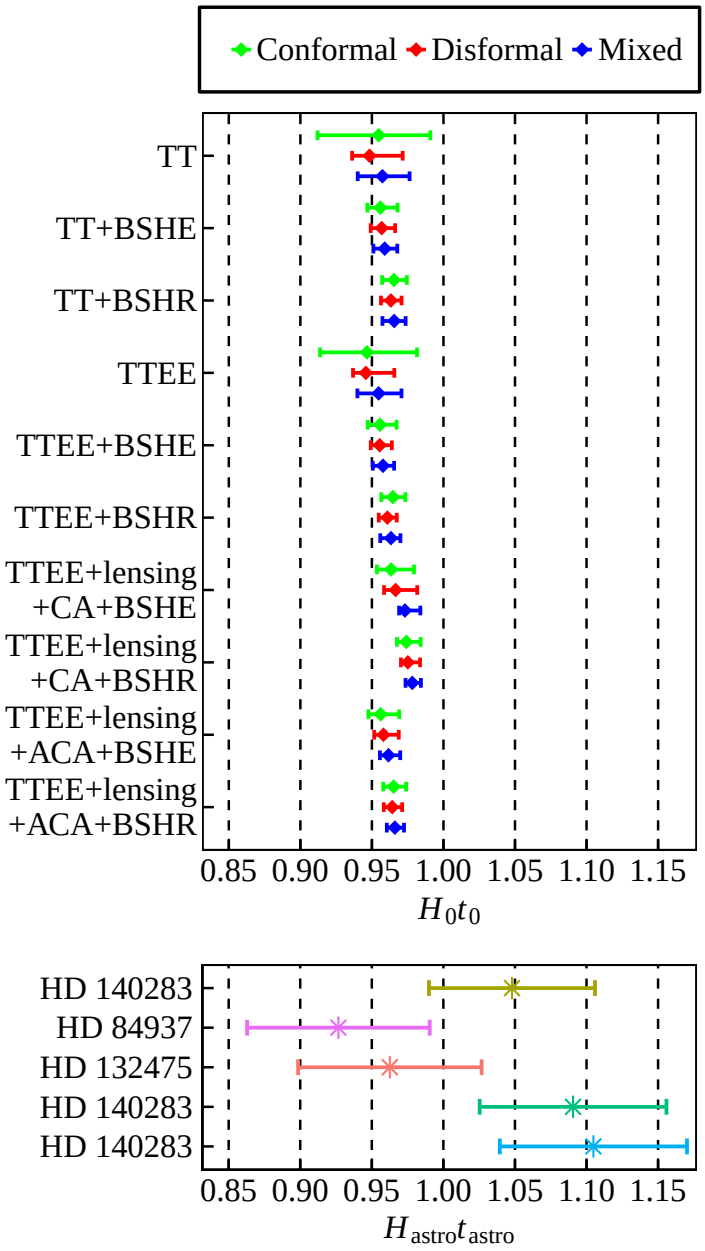

Figure 6.3: In the upper panel we compare the marginalised constraints on the dimensionless age of the Universe in the conformal, disformal, and mixed coupled DE models using all data set combinations considered in these analyses. The lower panel depicts the constraints on $H_{\rm astro} t_{\rm astro}$ from astrophysical objects [617–619] with their names specified on the vertical axis. In the upper panel the coloured intervals correspond to the inferred 1σ two–tail limits on the dimensionless age of the Universe, whereas in the lower panel these intervals show the estimated 1σ constraints.

be useful to break the degeneracies with other cosmological parameters [623, 624]. Furthermore, we should also mention that there is a partial inverse correlation between σ_8 and n_s. Thus, the 1σ limits on n_s shift to slightly larger values for the data set combinations which include the CA measurements with respect to the other data sets.

In the upper panel of Fig. 6.3, we show the inferred constraints on the dimensionless age of the Universe in the models presented in Fig. 6.2, and in the lower panel we show the 1σ intervals from astrophysical objects. For the calculation of

Parameter	TT	TT + BSHE	TT + BSHR	TTEE	TTEE + BSHE	TTEE + BSHR
$100\ \Omega_b h^2$	$2.2242^{+0.0238}_{-0.0253}$	$2.2241^{+0.0230}_{-0.0229}$	$2.2273^{+0.0236}_{-0.0234}$	$2.2257^{+0.0164}_{-0.0169}$	$2.2269^{+0.0160}_{-0.0160}$	$2.2283^{+0.0166}_{-0.0162}$
$\Omega_c h^2$	$0.11685^{+0.00479}_{-0.00260}$	$0.11880^{+0.00138}_{-0.00137}$	$0.11808^{+0.00132}_{-0.00131}$	$0.11817^{+0.00318}_{-0.00185}$	$0.11893^{+0.00116}_{-0.00116}$	$0.11823^{+0.00112}_{-0.00110}$
$100\ \theta_s$	$1.04193^{+0.00047}_{-0.00047}$	$1.04190^{+0.00045}_{-0.00045}$	$1.04193^{+0.00046}_{-0.00045}$	$1.04178^{+0.00033}_{-0.00032}$	$1.04179^{+0.00032}_{-0.00032}$	$1.04180^{+0.00032}_{-0.00032}$
$\tau_{\rm reio}$	$0.078411^{+0.017508}_{-0.020092}$	$0.076849^{+0.016848}_{-0.019297}$	$0.077484^{+0.017183}_{-0.019231}$	$0.078153^{+0.016437}_{-0.017801}$	$0.077784^{+0.016594}_{-0.017016}$	$0.078322^{+0.016436}_{-0.017309}$
$\ln(10^{10} A_s)$	$3.0896^{+0.0342}_{-0.0384}$	$3.0874^{+0.0331}_{-0.0380}$	$3.0884^{+0.0337}_{-0.0376}$	$3.0913^{+0.0326}_{-0.0345}$	$3.0902^{+0.0326}_{-0.0337}$	$3.0913^{+0.0327}_{-0.0338}$
n_s	$0.96832^{+0.00675}_{-0.00725}$	$0.96598^{+0.00529}_{-0.00529}$	$0.96668^{+0.00543}_{-0.00536}$	$0.96571^{+0.00530}_{-0.00533}$	$0.96514^{+0.00459}_{-0.00451}$	$0.96558^{+0.00464}_{-0.00466}$
λ	$< 1.2170(1.6013)$	$< 0.6686(1.0133)$	$< 0.4528(0.8046)$	$< 1.1718(1.5981)$	$< 0.6228(0.9927)$	$< 0.4481(0.7957)$
α	$< 0.0582(0.1037)$	$< 0.0360(0.0543)$	$0.032032^{+0.019815}_{-0.017833}$	$< 0.0496(0.0881)$	$< 0.0394(0.0519)$	$0.032964^{+0.019626}_{-0.014047}$
H_0	$68.373^{+2.815}_{-3.991}$	$68.031^{+0.917}_{-0.805}$	$68.848^{+0.764}_{-0.786}$	$67.553^{+2.746}_{-2.948}$	$68.006^{+0.887}_{-0.783}$	$68.786^{+0.740}_{-0.778}$
Ω_m	$0.30053^{+0.04075}_{-0.03252}$	$0.30491^{+0.00910}_{-0.00985}$	$0.29624^{+0.00843}_{-0.00867}$	$0.30976^{+0.03072}_{-0.03054}$	$0.30546^{+0.00884}_{-0.00934}$	$0.29711^{+0.00843}_{-0.00831}$
σ_8	$0.84733^{+0.03043}_{-0.04386}$	$0.84332^{+0.01870}_{-0.02018}$	$0.85064^{+0.01867}_{-0.02201}$	$0.84285^{+0.02808}_{-0.03587}$	$0.84441^{+0.01706}_{-0.01774}$	$0.85223^{+0.01713}_{-0.01872}$
$z_{\rm reio}$	$9.8999^{+1.6689}_{-1.6576}$	$9.8048^{+1.6436}_{-1.6258}$	$9.8424^{+1.6665}_{-1.6003}$	$9.9114^{+1.5890}_{-1.4639}$	$9.8945^{+1.5883}_{-1.4342}$	$9.9287^{+1.5790}_{-1.4473}$
$H_0 t_0$	$0.95482^{+0.03601}_{-0.04285}$	$0.95592^{+0.01194}_{-0.00908}$	$0.96538^{+0.00905}_{-0.00826}$	$0.94652^{+0.03500}_{-0.03274}$	$0.95571^{+0.01153}_{-0.00862}$	$0.96467^{+0.00869}_{-0.00810}$

Table 6.2: For each model parameter we report the mean values and 1σ errors in the conformally coupled DE scenario. The Hubble constant is given in units of $\mathrm{km\ s^{-1}\ Mpc^{-1}}$. When necessary, for the model parameters λ and α, we also write in brackets the 2σ upper limits. For the data set combinations which include the $H_0^{\rm R}$ local value of the Hubble constant, we quote the mean values of the conformal coupling parameter α, along with their respective 1σ errors, in order to highlight its impact on our results.

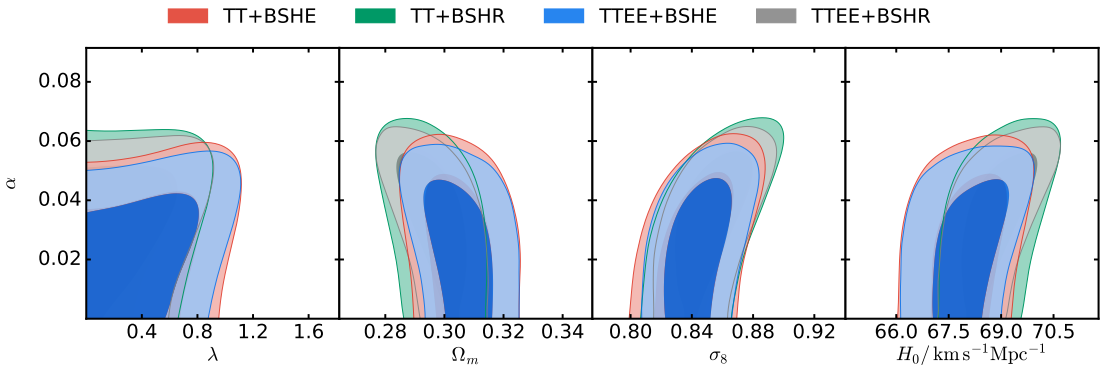

Figure 6.4: Marginalised two–dimensional likelihood constraints for conformally coupled DE with different data set combinations. We show the degeneracy of the conformal coupling parameter α with λ, Ω_m, σ_8, and H_0.

the dimensionless age of the Universe $H_{\rm astro} t_{\rm astro}$, we use the estimation of the astrophysical age of the Universe based on some of the best known oldest stars [617–619],

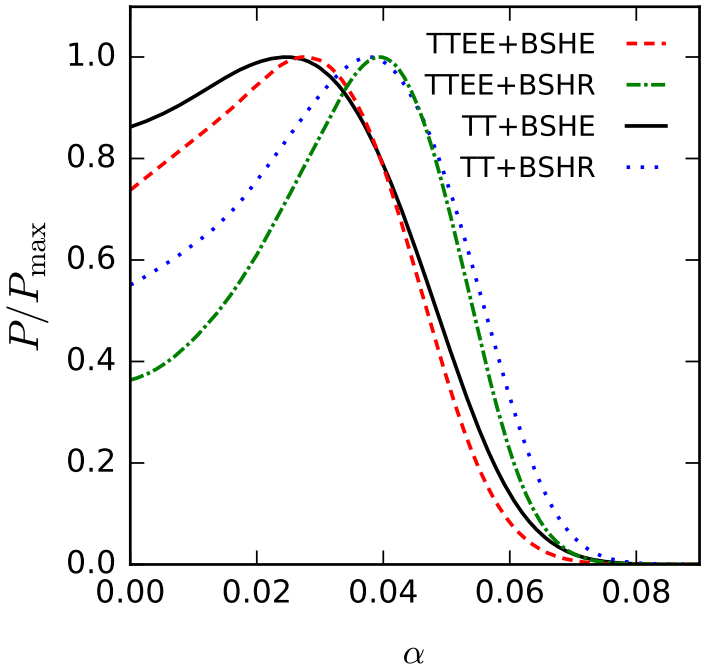

Figure 6.5: Marginalised one–dimensional posterior distributions for the conformal coupling parameter α, with the different data set combinations indicated in the figure. The respective parameter constraints are tabulated in Table 6.2.

and assume the value of the astrophysical Hubble constant to coincide with $H_0^{\rm R}$. We should emphasise that the $H_{\rm astro}t_{\rm astro}$ constraints in Fig. 6.3 are solely used for comparative purposes and not in our cosmological parameter constraints analyses. The comparison of the constraints presented in the upper and lower panels of Fig. 6.3 can be interpreted as a convergence between the theory of General Relativity which governs the cosmological evolution of the Universe, and the laws of Quantum Mechanics which determine the nuclear reactions taking place in stars. Following our MCMC analyses, the present time coincidence of $H_0t_0 = 1$, which has been recently dubbed as the synchronicity problem [625], is not completely fulfilled in our coupled DE models as H_0t_0 is not found to be exactly unity. Nonetheless, it still remains to be seen if this makes the synchronicity problem even worse [626–628].

6.3.1 Conformal model constraints

In this section we discuss the inferred constraints in the exponential conformally coupled model, with the coupling parameter α as defined in Eq. (6.7). In this model we neglect the disformal coupling by fixing D_M to zero. In Tables 6.2 and 6.3 we tabulate the parameter constraints from several data set combinations. The marginalised two–dimensional likelihood constraints and the one–dimensional posterior distributions for the coupling parameter α of Table 6.2 are shown in Fig. 6.4 and Fig. 6.5, respectively. Similarly, the marginalised two–dimensional likelihood constraints and the one–dimensional posterior distributions for the coupling parameter α of Table

Parameter	TTEE + lensing + CA + BSHE	TTEE + lensing + CA + BSHR	TTEE + lensing + ACA + BSHE	TTEE + lensing + ACA + BSHR
$100\ \Omega_b h^2$	$2.2556^{+0.0137}_{-0.0140}$	$2.2570^{+0.0138}_{-0.0141}$	$2.2330^{+0.0150}_{-0.0149}$	$2.2354^{+0.0150}_{-0.0149}$
$\Omega_c h^2$	$0.11541^{+0.00083}_{-0.00074}$	$0.11523^{+0.00082}_{-0.00075}$	$0.11812^{+0.00104}_{-0.00102}$	$0.11761^{+0.00104}_{-0.00101}$
$100\ \theta_s$	$1.04194^{+0.00029}_{-0.00030}$	$1.04195^{+0.00030}_{-0.00029}$	$1.04187^{+0.00031}_{-0.00031}$	$1.04190^{+0.00031}_{-0.00031}$
$\tau_{\rm reio}$	$0.048632^{+0.002228}_{-0.008632}$	$0.048728^{+0.002309}_{-0.008727}$	$0.057948^{+0.008405}_{-0.013138}$	$0.058798^{+0.009195}_{-0.013012}$
$\ln(10^{10} A_s)$ ...	$3.0197^{+0.0092}_{-0.0167}$	$3.0199^{+0.0095}_{-0.0162}$	$3.0464^{+0.0168}_{-0.0236}$	$3.0478^{+0.0177}_{-0.0231}$
n_s	$0.97192^{+0.00373}_{-0.00399}$	$0.97206^{+0.00381}_{-0.00394}$	$0.96662^{+0.00415}_{-0.00443}$	$0.96723^{+0.00421}_{-0.00428}$
λ	$0.61752^{+0.37467}_{-0.24731}$	$< 0.5106(0.8274)$	$< 0.8175(1.0290)$	$< 0.4550(0.7961)$
α	$< 0.0153(0.0301)$	$< 0.0174(0.0325)$	$< 0.0247(0.0423)$	$< 0.0331(0.0467)$
H_0	$68.623^{+1.197}_{-0.816}$	$69.460^{+0.773}_{-0.561}$	$67.998^{+0.982}_{-0.743}$	$68.744^{+0.694}_{-0.682}$
Ω_m	$0.29316^{+0.00756}_{-0.01043}$	$0.28570^{+0.00581}_{-0.00720}$	$0.30392^{+0.00810}_{-0.00962}$	$0.29629^{+0.00763}_{-0.00754}$
σ_8	$0.79003^{+0.01131}_{-0.00893}$	$0.79698^{+0.00805}_{-0.00706}$	$0.81687^{+0.01071}_{-0.01027}$	$0.82300^{+0.00952}_{-0.01058}$
$z_{\rm reio}$	$6.9761^{+0.2440}_{-0.9653}$	$6.9806^{+0.2498}_{-0.9663}$	$7.9986^{+0.9093}_{-1.2186}$	$8.0700^{+0.9729}_{-1.2031}$
$H_0 t_0$	$0.96341^{+0.01600}_{-0.00991}$	$0.97410^{+0.00995}_{-0.00659}$	$0.95609^{+0.01302}_{-0.00855}$	$0.96517^{+0.00872}_{-0.00726}$

Table 6.3: For each model parameter we report the mean values and 1σ errors in the conformally coupled DE scenario. The Hubble constant is given in units of $\mathrm{km\ s^{-1}\ Mpc^{-1}}$. When necessary, for the model parameters λ and α, we also write in brackets the 2σ upper limits. For the first data set combination we highlight the significant peak in the marginalised posterior distribution of λ, by quoting its mean value and 1σ errors (see text for further details).

6.3 are shown in Fig. 6.6 and Fig. 6.7, respectively. As clearly illustrated in Fig. 6.2, marginally tighter constraints on the cosmological parameters are obtained with the TTEE CMB likelihood in comparison with the TT likelihood. Consequently, the 95% confidence level (CL) upper bound on the conformal coupling parameter decreases from $\alpha < 0.1037$ with the TT likelihood, to $\alpha < 0.0881$ when using the TTEE likelihood.

Since the CMB anisotropies mainly probe the high–redshift Universe, we further add some information about the low–redshift Universe from the background data sets BSHE and BSHR, which will also help to break the degeneracy between the

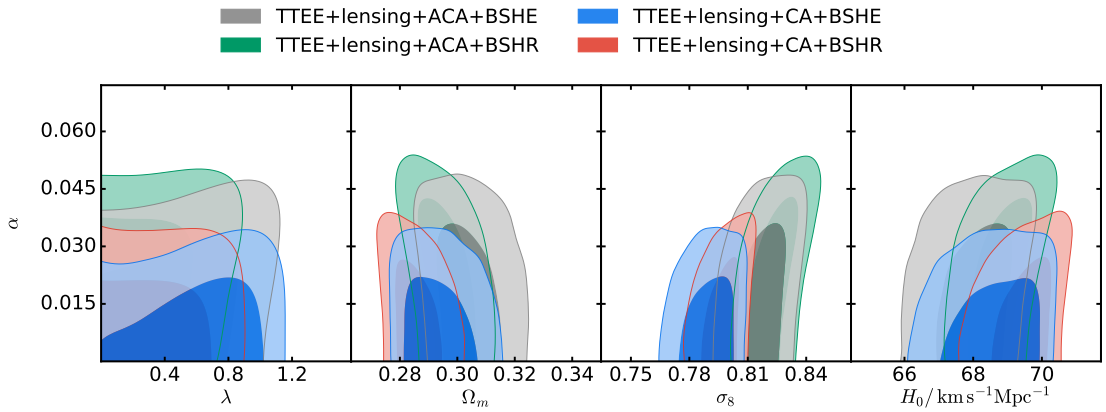

Figure 6.6: Marginalised two–dimensional likelihood constraints on the parameters α, λ, Ω_m, σ_8, and H_0 in the conformal model. The respective parameter constraints are tabulated in Table 6.3.

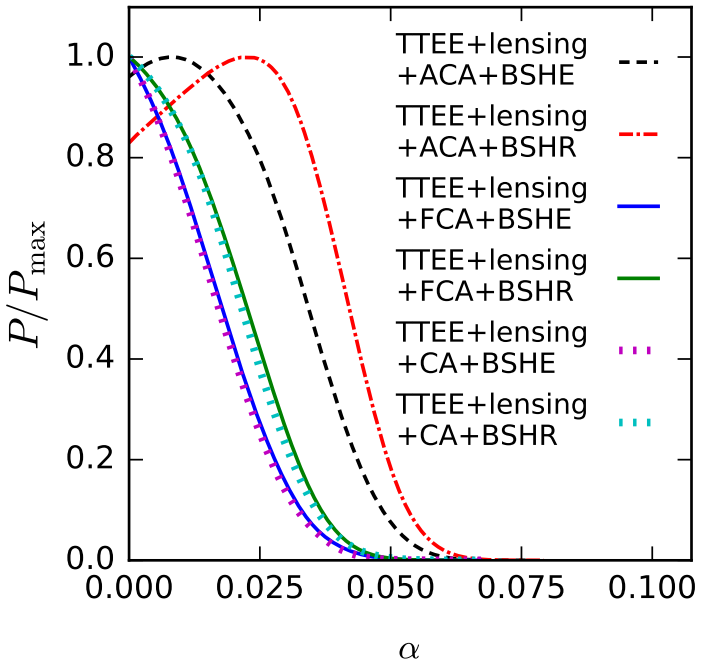

Figure 6.7: Marginalised one–dimensional posterior distributions for the conformal coupling parameter α, with the different data set combinations considered in Table 6.3, together with two other combinations making use of both the ACA and CA measurements (denoted by FCA).

parameters. From Table 6.2 and Fig. 6.2, it follows that the background data sets improve the constraints on the cosmological parameters, particularly on the current matter abundance fraction Ω_m. From the second panel of Fig. 6.4, it is evident that there is a partial inverse correlation between Ω_m and α, thus a lower upper bound on α results into a slightly higher mean value of Ω_m. This clearly follows from the transfer of energy between DM and DE which is governed by the conservation equations (6.3) and (6.4).

Moreover, the coupling parameter α is found to be marginally correlated with the Hubble constant, as depicted in the fourth panel of Fig. 6.4. Indeed, higher upper

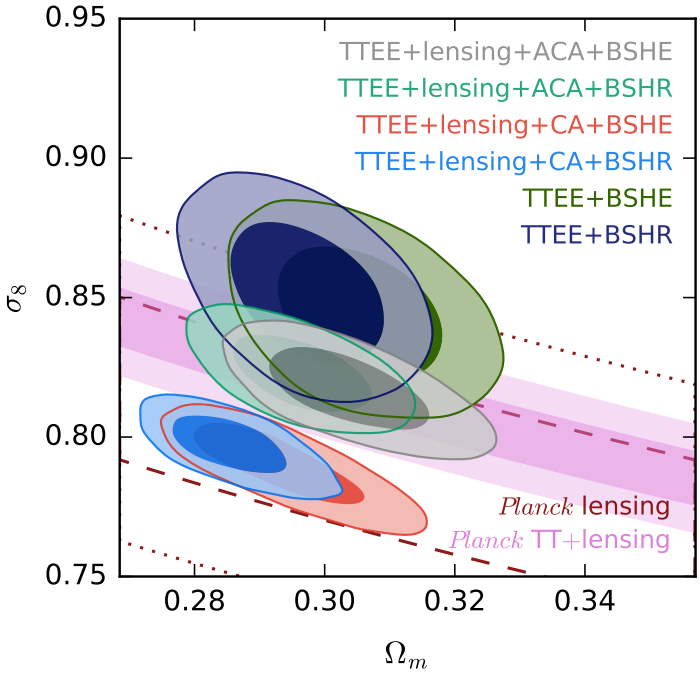

Figure 6.8: Marginalised constraints on parameters of the conformal model using the data sets indicated in the figure. The shaded band depicts the *Planck* TT + lensing constraint, whereas the region enclosed by the dashed (1σ) and dotted (2σ) lines shows the constraint from *Planck* lensing alone [91].

bounds on α are inferred when using the $H_0^{\rm R}$ local value of the Hubble constant in comparison with the analyses making use of $H_0^{\rm E}$. In fact, for the TT + BSHR and TTEE + BSHR combinations, we highlight the observed peaks in the marginalised one–dimensional posterior distributions of α, as depicted in Fig. 6.5, by reporting the non–zero peak locations instead of quoting the upper limits as we did in the other data set combinations. The peak in the marginalised posterior distribution with TT + BSHR is found to be at $\alpha = 0.032032^{+0.019815}_{-0.017833}$, whereas with TTEE + BSHR the peak is at $\alpha = 0.032964^{+0.019626}_{-0.014047}$. Thus, a higher value of H_0 together with the CMB polarisation likelihood enhance the preference of a non–zero α, although in the two mentioned cases the conformal coupling parameter is still found to be consistent with zero at $\sim 2\sigma$. This complements the discussion of this model with an inverse power–law potential in Ref. [576]. Similar indications of a non–null coupling, although with a different coupling function, have also been reported in Ref. [629]. Also, phantom dark energy was found to be preferred when relatively high external local values of H_0 are adopted [388, 630]. The TT/ TTEE + BSHE data set combinations do not give rise to a significant peak in the marginalised posterior distribution of α, although a tighter constraint on the conformal coupling parameter is obtained with the TTEE likelihood in comparison with the constraint from the TT likelihood combination.

The inferred upper bound constraints on the slope of the exponential scalar field potential λ, are significantly improved when we include the background data sets BSHE and BSHR along with the CMB likelihoods. This is mainly due to the fact that the derived constraints on Ω_m are tighter with the background data sets, leading

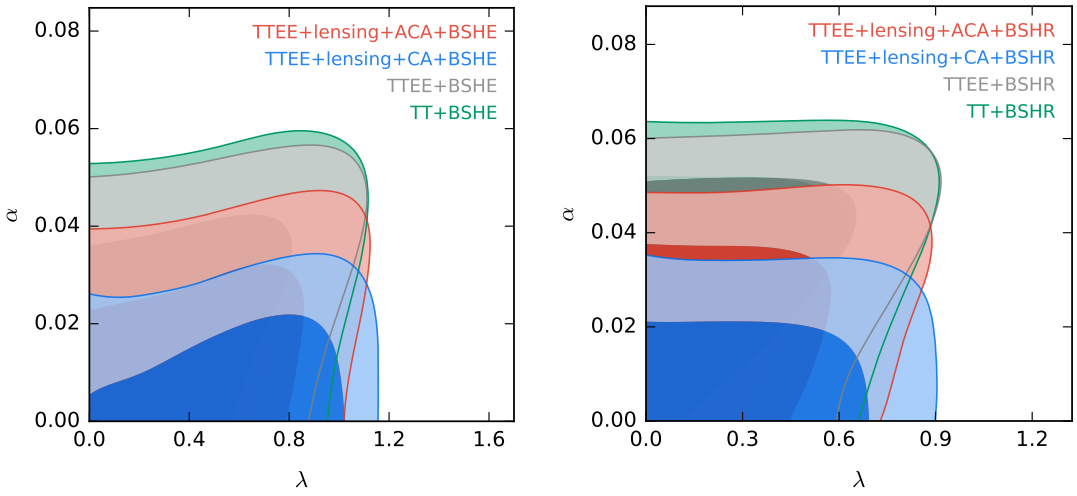

Figure 6.9: A comparison of the marginalised two–dimensional constraints on the conformal coupling parameter α, and the slope of the exponential potential λ, using the local values of the Hubble constant $H_0^{\rm E}$ (left) and $H_0^{\rm R}$ (right).

to a considerable improvement in the upper bounds of λ, which is correlated with Ω_m. The background data sets lower the 95% CL upper bounds on λ, from $\lambda < 1.5981$ with TTEE, to $\lambda < 0.9927$ with TTEE + BSHE, and particularly to $\lambda < 0.7957$ with TTEE + BSHR, all consistent with Refs. [570, 590, 609]. We show the correlation between α and λ in the first panel of Fig. 6.4.

As discussed in chapter 5, conformally coupled DE models are characterised by higher values of σ_8 in comparison with the concordance and uncoupled quintessence models [3, 481, 572] as a result of an enhancement in the growth of perturbations. The correlation between the coupling parameter α and σ_8 is shown in the third panel of Fig. 6.4. In order to probe the growth of perturbations, we now consider the cluster abundance data sets, as well as the CMB gravitational lensing likelihood. In Table 6.3 we further include the lensing, CA, and ACA data sets in our analyses, and we find that the conformal coupling parameter upper bounds are lowered in comparison with the inferred upper bounds from the data sets considered in Table 6.2. The two–dimensional marginalised constraints on α with the parameters λ, Ω_m, σ_8, and H_0 are shown in Fig. 6.6. From the marginalised posterior distributions of the conformal coupling parameter, shown in Fig. 6.7, we find that the observed peaks in Fig. 6.5 are now insignificant when we include the cluster abundance and lensing data sets. In Fig. 6.7, we also show the marginalised posterior distributions of α, inferred from the analyses which include the Full Cluster Abundance (FCA) data set consisting of the CA and ACA measurements altogether. As already mentioned in section 6.2, the derived constraints on α from the FCA data set coincide with the obtained constraints from the CA data set, henceforth we do not report the parameter constraints from the MCMC analyses which make use of the FCA data

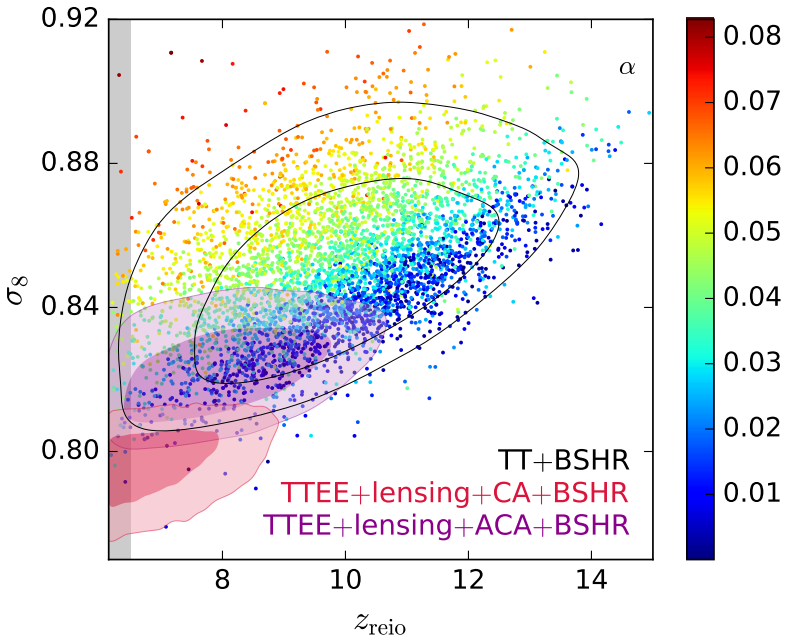

Figure 6.10: Marginalised two–dimensional constraints on the redshift of reionization $z_{\rm reio}$ and σ_8, together with samples from the TT + BSHR data sets colour coded with the value of the conformal coupling parameter α. The gray band denotes the excluded region by observations of the spectra of high redshift quasars [631].

set.

The tightest 95% CL upper bounds on α are derived from the CA data set combinations, since the measurements in this cluster abundance data set favour relatively low values of σ_8. In fact, these CA measurements are in tension with the inferred concordance model σ_8 constraints [65, 363, 615]. In Fig. 6.8, we show the two–dimensional marginalised constraints on σ_8 and Ω_m from two data set combinations which do not include the cluster abundance and lensing data sets, together with the data set combinations which probe the growth of perturbations. For comparative purposes only, we also include the concordance model constraints inferred from the CMB lensing only likelihood (depicted by dashed and dotted lines), and from the CMB TT + lensing likelihoods (depicted by the shaded bands) [91]. From this figure, it is evident that the conformally coupled DE model gives rise to a larger σ_8 in comparison with the concordance model, although when including the ACA and lensing data sets, the inferred contours overlap the *Planck* TT + lensing shaded bands. On the other hand, the CA data set combination pushes the inferred Ω_m–σ_8 contours downwards, deviating from the *Planck* TT + lensing constraint.

From the TTEE + lensing + CA + BSHE data set combination we obtain a 95% CL upper bound of $\alpha < 0.0301$, whereas the upper bound from the TTEE + lensing + CA + BSHR data set combination is of $\alpha < 0.0325$. When we use the ACA data set instead of the CA measurements, we obtain a 95% CL upper bound of $\alpha < 0.0423$ with TTEE + lensing + ACA+ BSHE data sets, and an upper bound of $\alpha < 0.0467$ with TTEE + lensing + ACA + BSHR data sets. Moreover, when using the $H_0^{\rm E}$ local value of the Hubble constant together with the cluster abundance data sets, a larger

Parameter	TT	TT + BSHE	TT + BSHR	TTEE	TTEE + BSHE	TTEE + BSHR
$100\ \Omega_b h^2$	$2.2288^{+0.0248}_{-0.0251}$	$2.2318^{+0.0211}_{-0.0210}$	$2.2400^{+0.0209}_{-0.0214}$	$2.2279^{+0.0168}_{-0.0173}$	$2.2321^{+0.0149}_{-0.0148}$	$2.2380^{+0.0149}_{-0.0150}$
$\Omega_c h^2$.....	$0.12293^{+0.00298}_{-0.00540}$	$0.12238^{+0.00213}_{-0.00464}$	$0.12096^{+0.00198}_{-0.00408}$	$0.12333^{+0.00235}_{-0.00509}$	$0.12265^{+0.00197}_{-0.00446}$	$0.12131^{+0.00188}_{-0.00366}$
$100\ \theta_s$	$1.04195^{+0.00048}_{-0.00047}$	$1.04200^{+0.00044}_{-0.00044}$	$1.04209^{+0.00043}_{-0.00043}$	$1.04180^{+0.00033}_{-0.00033}$	$1.04185^{+0.00031}_{-0.00031}$	$1.04191^{+0.00031}_{-0.00030}$
$\tau_{\rm reio}$.....	$0.078477^{+0.017682}_{-0.020519}$	$0.079563^{+0.017484}_{-0.018663}$	$0.082882^{+0.018012}_{-0.018692}$	$0.077320^{+0.016929}_{-0.017617}$	$0.079307^{+0.016578}_{-0.016441}$	$0.082658^{+0.017012}_{-0.016557}$
$\ln(10^{10} A_s)$.....	$3.0895^{+0.0343}_{-0.0391}$	$3.0912^{+0.0344}_{-0.0372}$	$3.0958^{+0.0358}_{-0.0372}$	$3.0891^{+0.0330}_{-0.0347}$	$3.0919^{+0.0327}_{-0.0326}$	$3.0973^{+0.0337}_{-0.0335}$
n_s	$0.96643^{+0.00655}_{-0.00693}$	$0.96730^{+0.00475}_{-0.00480}$	$0.96938^{+0.00469}_{-0.00471}$	$0.96456^{+0.00503}_{-0.00526}$	$0.96585^{+0.00437}_{-0.00451}$	$0.96756^{+0.00427}_{-0.00436}$
λ	–	–	–	–	–	–
D_M / meV^{-1} ...	> 0.4627	> 0.5883	> 0.6540	> 0.4599	> 0.6031	> 0.6810
H_0	$67.306^{+1.821}_{-1.070}$	$67.969^{+0.736}_{-0.676}$	$68.510^{+0.624}_{-0.600}$	$67.084^{+1.569}_{-0.743}$	$67.846^{+0.662}_{-0.539}$	$68.288^{+0.544}_{-0.518}$
Ω_m	$0.32125^{+0.01594}_{-0.02537}$	$0.31336^{+0.00924}_{-0.01428}$	$0.30554^{+0.00859}_{-0.01192}$	$0.32407^{+0.01215}_{-0.02328}$	$0.31507^{+0.00815}_{-0.01382}$	$0.30821^{+0.00781}_{-0.01096}$
σ_8	$0.90433^{+0.02913}_{-0.11800}$	$0.92196^{+0.03372}_{-0.11257}$	$0.92794^{+0.04409}_{-0.12384}$	$0.90220^{+0.02698}_{-0.11265}$	$0.92580^{+0.03830}_{-0.11204}$	$0.93049^{+0.04199}_{-0.11698}$
$z_{\rm reio}$.....	$9.9392^{+1.7144}_{-1.6766}$	$10.0315^{+1.6446}_{-1.5612}$	$10.2874^{+1.6910}_{-1.5378}$	$9.8610^{+1.6225}_{-1.4832}$	$10.0227^{+1.5982}_{-1.3557}$	$10.2924^{+1.5777}_{-1.3897}$
$H_0 t_0$	$0.94836^{+0.02316}_{-0.01219}$	$0.95684^{+0.00937}_{-0.00768}$	$0.96326^{+0.00747}_{-0.00694}$	$0.94578^{+0.01987}_{-0.00898}$	$0.95546^{+0.00850}_{-0.00626}$	$0.96082^{+0.00656}_{-0.00602}$

Table 6.4: For each data set combination we report the mean values and 1σ errors in the constant disformally coupled DE scenario, in which we set $\beta = 0$. The Hubble constant is given in units of km s^{-1} Mpc^{-1}. These data sets were not able to constrain the parameter λ.

upper bound on λ is allowed, in comparison with the analyses which use $H_0^{\rm R}$. Indeed, for the first data set combination of Table 6.3 we quote the non–zero peak location in the marginalised posterior distribution of λ, instead of its respective upper limits. We find that there is a marginal inverse correlation between λ and σ_8, and a correlation between H_0 and σ_8, thus explaining these shifts in the upper bounds of λ. This is clearly illustrated in Fig. 6.9. Unfortunately, this relationship between H_0 and σ_8 would not be able to alleviate the tension between the low–redshift and high–redshift probes.

Following the discussion on the optical depth of reionization parameter in section 6.3, in Fig. 6.10 we show the correlation between the redshift of reionization $z_{\rm reio}$, and σ_8 in the conformally coupled model. We should remark that this relationship between the mentioned parameters also follows in the other coupled DE models. Apart from the marginalised contours from distinct data set combinations, we also include a few samples from the TT + BSHR data set combination colour coded with the value of α. The marginalised contours of the TT + BSHR and the TTEE + lensing + ACA + BSHR data set combinations only overlap in a region of compatible σ_8 values with the ACA data set. Consequently, tighter constraints are

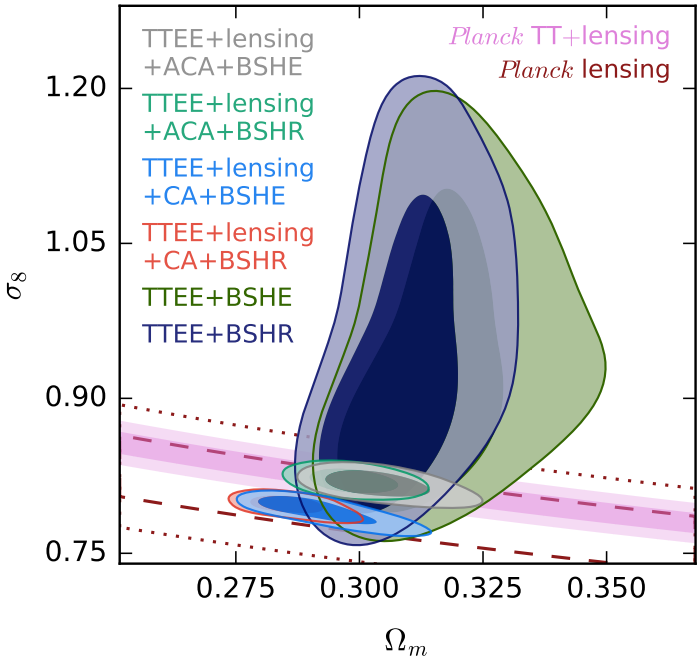

Figure 6.11: Marginalised two–dimensional constraints on parameters of the constant disformal model using the data sets indicated in the figure. The shaded band depicts the *Planck* TT + lensing constraint, whereas the region enclosed by the dashed (1σ) and dotted (2σ) lines shows the constraint from *Planck* lensing alone [91].

placed on the $z_{\rm reio}$–σ_8–α subspace, placing a lower upper bound on α. Moreover, there is a further reduction of the overlapping region between the marginalised contours of the TT + BSHR and the TTEE + lensing + CA + BSHR data set combinations, and the contour from the latter data set combination shifts downwards due to the incompatibility of the CA measurements with high σ_8 values. In Fig. 6.10, we also show an excluded region of $z_{\rm reio}$ inferred by observations of the Gunn–Peterson effect [632] in quasar spectra [631]. As clearly shown in this figure, our constraints are in agreement with the latter observations, although a preference towards lower σ_8 values could eventually shift the marginalised contours into the excluded region.

6.3.2 Disformal model constraints

In this section we present and discuss the MCMC inferred parameter constraints in the constant disformally coupled DE model with the coupling parameter D_M, together with the exponential disformally coupled DE model with the coupling parameter β, as defined in Eq. (6.7). We will start with the former case, in which we set $\beta = 0$ in the disformal coupling function $D(\phi)$, and fix the conformal coupling function to unity. In Tables 6.4 and 6.5 we show the parameter constraints from several data set combinations.

Similar to the conformally coupled scenario discussed in section 6.3.1, marginally tighter constraints on the varied cosmological parameters are obtained with the TTEE CMB likelihood in comparison with the TT likelihood, as clearly seen in Fig. 6.2. In Table 6.4 we present the parameter constraints inferred from the

Parameter	TTEE + lensing + CA + BSHE	TTEE + lensing + CA + BSHR	TTEE + lensing + ACA + BSHE	TTEE + lensing + ACA + BSHR
$100\ \Omega_b h^2$	$2.2556^{+0.0141}_{-0.0143}$	$2.2574^{+0.0139}_{-0.0139}$	$2.2344^{+0.0143}_{-0.0148}$	$2.2389^{+0.0145}_{-0.0147}$
$\Omega_c h^2$	$0.11553^{+0.00087}_{-0.00079}$	$0.11540^{+0.00083}_{-0.00074}$	$0.11850^{+0.00109}_{-0.00116}$	$0.11802^{+0.00103}_{-0.00109}$
$100\ \theta_s$	$1.04194^{+0.00030}_{-0.00030}$	$1.04196^{+0.00030}_{-0.00030}$	$1.04189^{+0.00030}_{-0.00030}$	$1.04194^{+0.00030}_{-0.00030}$
$\tau_{\rm reio}$	$0.048565^{+0.002197}_{-0.008565}$	$0.048860^{+0.002343}_{-0.008860}$	$0.058265^{+0.008664}_{-0.012685}$	$0.060940^{+0.010041}_{-0.012200}$
$\ln(10^{10} A_s)$	$3.0195^{+0.0094}_{-0.0162}$	$3.0201^{+0.0100}_{-0.0163}$	$3.0466^{+0.0170}_{-0.0229}$	$3.0511^{+0.0191}_{-0.0225}$
n_s	$0.97181^{+0.00377}_{-0.00396}$	$0.97212^{+0.00376}_{-0.00392}$	$0.96674^{+0.00412}_{-0.00432}$	$0.96795^{+0.00414}_{-0.00430}$
λ	$< 0.6720(0.9830)$	$< 0.3587(0.7270)$	$< 0.4818(0.8953)$	$< 0.3109(0.6412)$
$D_M/\,\mathrm{meV}^{-1}$ ...	< 0.2500	< 0.3680	< 0.4420	< 0.5730
H_0	$68.817^{+1.162}_{-0.634}$	$69.485^{+0.638}_{-0.438}$	$68.058^{+0.810}_{-0.555}$	$68.552^{+0.559}_{-0.510}$
Ω_m	$0.29175^{+0.00604}_{-0.01032}$	$0.28584^{+0.00489}_{-0.00618}$	$0.30420^{+0.00658}_{-0.00874}$	$0.29885^{+0.00620}_{-0.00662}$
σ_8	$0.79149^{+0.01143}_{-0.00724}$	$0.79668^{+0.00686}_{-0.00607}$	$0.81655^{+0.00948}_{-0.00867}$	$0.82002^{+0.00808}_{-0.00872}$
$z_{\rm reio}$	$6.9709^{+0.2434}_{-0.9637}$	$6.9948^{+0.2564}_{-0.9897}$	$8.0308^{+0.9372}_{-1.1699}$	$8.2758^{+1.0452}_{-1.0987}$
$H_0 t_0$	$0.96655^{+0.01514}_{-0.00806}$	$0.97511^{+0.00853}_{-0.00482}$	$0.95809^{+0.01068}_{-0.00649}$	$0.96419^{+0.00696}_{-0.00588}$

Table 6.5: For each data set combination we report the mean values and 1σ errors in the constant disformally coupled DE scenario, in which we set $\beta = 0$. The Hubble constant is given in units of $\mathrm{km\,s^{-1}\,Mpc^{-1}}$. For the parameter λ, we also write in brackets the 2σ upper limits.

CMB likelihoods, together with the joint combination of the CMB likelihoods with the background data sets. Although the TTEE likelihood seems to improve the parameter constraints, it is still not able to put tight constraints on the scalar field's potential parameter λ, even when this is combined with the background data sets.

A striking difference between the derived cosmological parameter constraints in the conformally coupled DE model and the constant disformally coupled DE model, is the anomalous enhancement in the mean value of σ_8 in the latter coupled DE model. Other interacting DE models that are characterised with relatively high values of σ_8 were discussed in Refs. [629, 633]. Although we are considering the constant disformally coupled DE model, these features are also present in the exponential disformally coupled DE model discussed in the last part of this section. This increase in the mean value of σ_8 in the constant disformally coupled DE model is expected

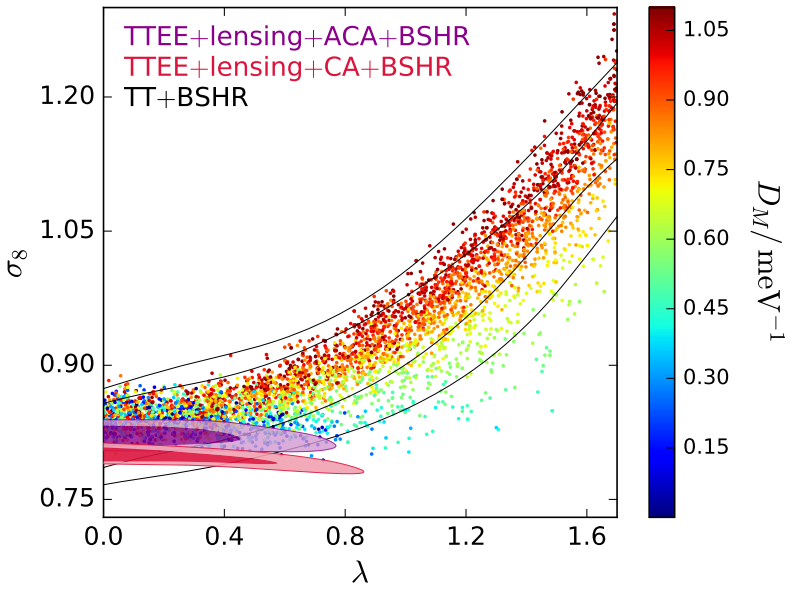

Figure 6.12: Marginalised constraints on parameters of the constant disformal model using the data sets indicated in the figure. The sample points are taken from the TT + BSHR data sets and colour coded with the value of the disformal coupling parameter $D_M/\,\mathrm{meV}^{-1}$.

due to the energy transfer taking place between DM and DE, and particularly as a result of a coupling induced additional force acting between the DM particles [3, 485]. This fifth–force is also present in the conformally coupled DE model, although the strength of this force is found to be the largest in coupled DE models which make use of the disformal coupling. Consequently, this leads to an enhancement in the growth of perturbations in comparison with the uncoupled quintessence and conformally coupled DE models. In chapter 5 we further observed that, when a disformal coupling between DE and DM is present, this induces intermediate–scales time–dependent damped oscillations in the matter growth rate function [3]. In these analyses we are not able to probe these scale–dependent features in the matter growth rate function, although we believe that deriving constraints from the scale–dependence of the matter growth rate function would strengthen our constraints.

The considerably large range of allowed values of σ_8 by the CMB likelihoods and the background data sets is clearly illustrated in Fig. 6.11. The influence of the local value of the Hubble constant is mainly attributed with the constraint on Ω_m, due to the inverse correlation between Ω_m and H_0. Although the marginalised contours of the TTEE + BSHE and TTEE + BSHR data set combinations are still in agreement with the concordance model 1σ and 2σ approximate fit constraints, very weak constraints are inferred from these data set combinations considered in Table 6.4.

In order to shrink these contours, we further add the cluster abundance data sets along with the CMB lensing likelihood. The inferred parameter constraints are tabulated in Table 6.5, in which we are now able to constrain the scalar field's exponent parameter λ, as clearly depicted in Fig. 6.12. As expected, the mea-

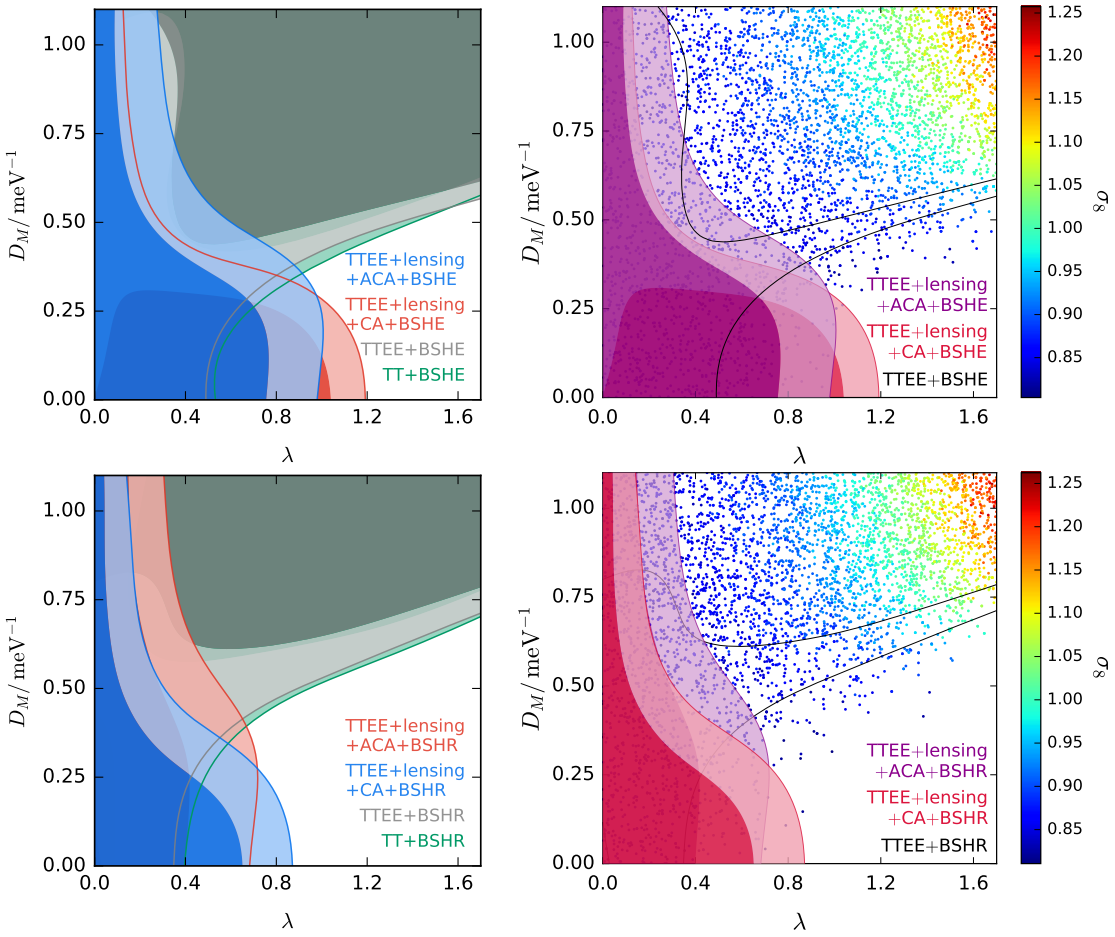

Figure 6.13: Marginalised constraints on the disformal coupling parameter $D_M/\,\mathrm{meV}^{-1}$, and the slope of the scalar field potential λ, in the constant disformally coupled DE model. In the upper two panels we use the H_0^{E} local value of the Hubble constant, and in the lower two panels we use H_0^{R}. The sample points in the top right and lower right panels are colour coded with the value of σ_8, and are taken from the data sets represented by the black solid contour lines of each panel.

surements of the ACA and CA data sets do not allow for such large values of σ_8, and consequently shrink the marginalised contours of Fig. 6.11. Indeed, the marginalised contours of the additional CMB lensing and ACA data sets overlap the *Planck* TT + lensing constraint bands, similar to what happened in the conformally coupled model. Even in this model, the CA data set is still able to lower the mean value of σ_8, in order to be compatible with the relatively low σ_8 measurements of this data set. Moreover, from the coloured samples of the λ–σ_8–D_M subspace of Fig. 6.12, we observe that the inclusion of the cluster abundance data sets and the CMB lensing likelihood exclude the relatively high D_M values which lie along the top section of the λ–σ_8 band inferred from the TT + BSHR data set

Parameter	TTEE + lensing + CA + BSHE	TTEE + lensing + CA + BSHR	TTEE + lensing + ACA + BSHE	TTEE + lensing + ACA + BSHR
$100\ \Omega_b h^2$	$2.2539^{+0.0137}_{-0.0138}$	$2.2568^{+0.0137}_{-0.0135}$	$2.2341^{+0.0144}_{-0.0145}$	$2.2386^{+0.0142}_{-0.0146}$
$\Omega_c h^2$	$0.11572^{+0.00077}_{-0.00075}$	$0.11549^{+0.00080}_{-0.00077}$	$0.11877^{+0.00106}_{-0.00130}$	$0.11816^{+0.00104}_{-0.00113}$
$100\ \theta_s$	$1.04191^{+0.00030}_{-0.00030}$	$1.04195^{+0.00030}_{-0.00029}$	$1.04189^{+0.00029}_{-0.00030}$	$1.04193^{+0.00030}_{-0.00030}$
$\tau_{\rm reio}$	$0.047123^{+0.001780}_{-0.007123}$	$0.048175^{+0.002176}_{-0.008174}$	$0.056890^{+0.007961}_{-0.012251}$	$0.059970^{+0.009571}_{-0.012187}$
$\ln(10^{10} A_s)$...	$3.0169^{+0.0082}_{-0.0141}$	$3.0188^{+0.0091}_{-0.0151}$	$3.0440^{+0.0160}_{-0.0218}$	$3.0492^{+0.0181}_{-0.0224}$
n_s	$0.97118^{+0.00375}_{-0.00389}$	$0.97187^{+0.00371}_{-0.00384}$	$0.96651^{+0.00406}_{-0.00422}$	$0.96773^{+0.00406}_{-0.00423}$
λ	$< 0.1269(0.3360)$	$< 0.1257(0.3090)$	$< 0.2841(0.7847)$	$< 0.2458(0.5702)$
β	< 1.6700	< 1.7100	< 1.5900	< 1.7412
H_0	$69.653^{+0.369}_{-0.375}$	$69.783^{+0.353}_{-0.386}$	$68.356^{+0.599}_{-0.475}$	$68.658^{+0.481}_{-0.481}$
Ω_m	$0.28502^{+0.00439}_{-0.00435}$	$0.28354^{+0.00443}_{-0.00430}$	$0.30209^{+0.00603}_{-0.00778}$	$0.29820^{+0.00610}_{-0.00634}$
σ_8	$0.79966^{+0.00394}_{-0.00505}$	$0.79975^{+0.00416}_{-0.00532}$	$0.82041^{+0.00804}_{-0.00826}$	$0.82179^{+0.00746}_{-0.00861}$
$z_{\rm reio}$	$6.8285^{+0.1997}_{-0.8164}$	$6.9273^{+0.2376}_{-0.9151}$	$7.8974^{+0.8731}_{-1.1287}$	$8.1825^{+0.9975}_{-1.1125}$
$H_0 t_0$	$0.97764^{+0.00406}_{-0.00448}$	$0.97906^{+0.00408}_{-0.00433}$	$0.96203^{+0.00693}_{-0.00595}$	$0.96562^{+0.00564}_{-0.00563}$

Table 6.6: For each data set combination we report the mean values and 1σ errors in the exponential disformally coupled DE scenario, in which we set $D_M V_0 = 1$. The Hubble constant is given in units of $\mathrm{km\,s^{-1}\,Mpc^{-1}}$. For the model parameter λ, we also write in brackets the 2σ upper limits.

combination. Consequently, an upper bound is placed on the disformal coupling parameter D_M, instead of a lower bound as reported in Table 6.4. Tight 95% CL upper bounds are placed on the scalar field's potential exponent parameter of $\lambda < 0.9830$ (TTEE + lensing + CA + BSHE), $\lambda < 0.7270$ (TTEE + lensing + CA + BSHR), $\lambda < 0.8953$ (TTEE + lensing + ACA + BSHE), and of $\lambda < 0.6412$ (TTEE + lensing + ACA + BSHR). Despite of the improved constraints on the parameters, we only obtain 68% CL upper bounds on the constant disformal coupling parameter of $D_M < 0.2500\ \mathrm{meV}^{-1}$ (TTEE + lensing + CA + BSHE), $D_M < 0.3680\ \mathrm{meV}^{-1}$(TTEE + lensing + CA + BSHR), $D_M < 0.4420\ \mathrm{meV}^{-1}$ (TTEE + lensing + ACA + BSHE), and also of $D_M < 0.5730\ \mathrm{meV}^{-1}$ (TTEE + lensing + ACA + BSHR).

In the upper left and lower left panels of Fig. 6.13, we compare the two–

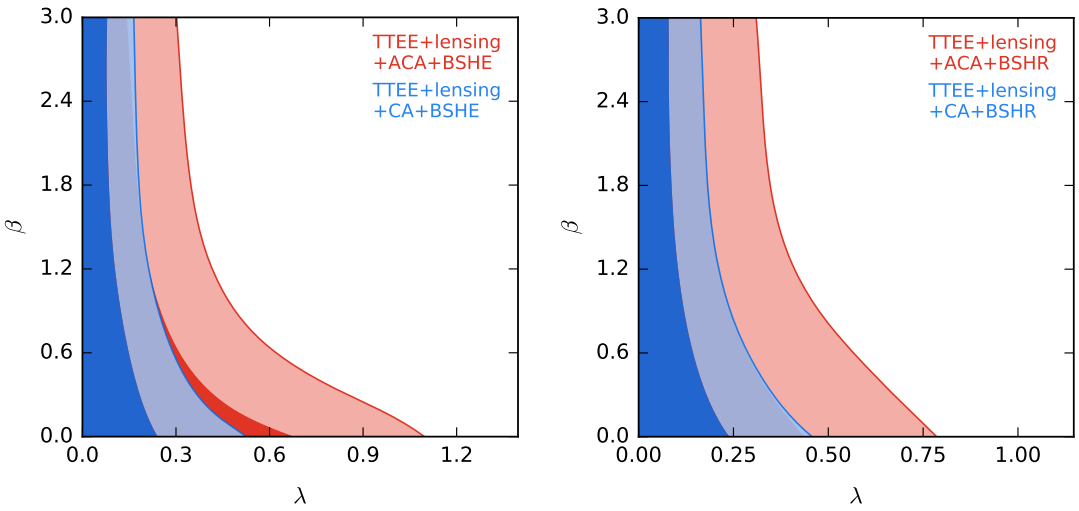

Figure 6.14: Marginalised two–dimensional constraints on the exponential disformal coupling parameter β, and the slope of the exponential potential λ. In the left panel we use the $H_0^{\rm E}$ local value of the Hubble constant, and in the right panel we use $H_0^{\rm R}$. In this model we set $D_M V_0 = 1$.

dimensional marginalised constraints on the constant disformally coupled DE model parameters D_M and λ. We complement these marginalised constraints by their respective λ–D_M–σ_8 subspace, which we show on the right hand side of these panels. Undoubtedly, the allowed large values of D_M and λ by the CMB likelihoods together with the background data sets, will be excluded by the cluster abundance data sets. This is evidently illustrated by the samples located in the vicinity of the top right corner of the panels in Fig. 6.13 depicting the λ–D_M–σ_8 subspace. Thus, the cluster abundance data sets together with the CMB lensing likelihood are able to significantly shrink the allowed range of the parameters D_M and λ. These improved constraints complement the analyses of Ref. [5], in which only the background evolution was considered.

As we indicated in the beginning of this section, we will now consider an exponential disformally coupled model. In this case, we will still set the conformal coupling to unity, but without loss of generality we also fix the constant disformal coupling parameter to $D_M V_0 = 1$. Thus, in this disformally coupled DE model we vary the disformal coupling parameter β in the MCMC analyses. Since the tightest constraints in the constant disformally coupled DE model were obtained when the cluster abundance data sets were considered in the data set combinations, we here only report and discuss the inferred parameter constraints with these data set combinations. These are tabulated in Table 6.6, and in Fig. 6.14 we illustrate the two–dimensional marginalised constraints of β and λ. In the left panel of this figure we use the $H_0^{\rm E}$ local value of the Hubble constant, and in the right panel we instead use $H_0^{\rm R}$, in order to asses their impact on our constraints. Indeed, marginally higher upper bounds for λ are obtained with the $H_0^{\rm E}$ Hubble constant in comparison

Parameter	TT	TT + BSHE	TT + BSHR	TTEE	TTEE + BSHE	TTEE + BSHR
$100\ \Omega_b h^2$	$2.2292^{+0.0241}_{-0.0259}$	$2.2308^{+0.0216}_{-0.0211}$	$2.2378^{+0.0214}_{-0.0214}$	$2.2282^{+0.0168}_{-0.0171}$	$2.2309^{+0.0148}_{-0.0150}$	$2.2358^{+0.0148}_{-0.0149}$
$\Omega_c h^2$	$0.12073^{+0.00560}_{-0.00488}$	$0.12124^{+0.00359}_{-0.00429}$	$0.11914^{+0.00457}_{-0.00406}$	$0.12121^{+0.00524}_{-0.00444}$	$0.12141^{+0.00341}_{-0.00424}$	$0.11947^{+0.00419}_{-0.00370}$
$100\ \theta_s$	$1.04195^{+0.00049}_{-0.00049}$	$1.04197^{+0.00044}_{-0.00043}$	$1.04206^{+0.00044}_{-0.00043}$	$1.04180^{+0.00033}_{-0.00033}$	$1.04183^{+0.00030}_{-0.00031}$	$1.04190^{+0.00030}_{-0.00030}$
$\tau_{\rm reio}$	$0.078386^{+0.017528}_{-0.020861}$	$0.078803^{+0.017096}_{-0.019199}$	$0.081653^{+0.017552}_{-0.018949}$	$0.077251^{+0.016272}_{-0.017890}$	$0.078334^{+0.016638}_{-0.017105}$	$0.080978^{+0.015709}_{-0.016581}$
$\ln(10^{10} A_s)$	$3.0894^{+0.0341}_{-0.0404}$	$3.0900^{+0.0340}_{-0.0381}$	$3.0942^{+0.0356}_{-0.0369}$	$3.0889^{+0.0323}_{-0.0344}$	$3.0902^{+0.0327}_{-0.0338}$	$3.0946^{+0.0314}_{-0.0325}$
n_s	$0.96641^{+0.00665}_{-0.00682}$	$0.96672^{+0.00488}_{-0.00493}$	$0.96851^{+0.00490}_{-0.00488}$	$0.96453^{+0.00500}_{-0.00518}$	$0.96556^{+0.00444}_{-0.00446}$	$0.96682^{+0.00437}_{-0.00429}$
λ	> 0.7928	> 0.7284	$0.88518^{+0.64662}_{-0.41172}$	> 0.7964	> 0.7329	$0.90123^{+0.63771}_{-0.38682}$
α	< 0.3151	< 0.3320	> 0.1747	< 0.3127	< 0.3380	> 0.1801
$D_M\,/\,\mathrm{meV}^{-1}$ ...	> 0.4820	$> 0.5890(0.2578)$	$> 0.5871(0.2271)$	> 0.4970	$> 0.5970(0.2609)$	$> 0.5665(0.2068)$
H_0	$68.040^{+1.539}_{-1.553}$	$68.135^{+0.709}_{-0.654}$	$68.691^{+0.642}_{-0.680}$	$67.811^{+1.389}_{-1.281}$	$68.026^{+0.648}_{-0.573}$	$68.491^{+0.533}_{-0.619}$
Ω_m	$0.30970^{+0.02286}_{-0.02267}$	$0.30937^{+0.01201}_{-0.01351}$	$0.30010^{+0.01379}_{-0.01222}$	$0.31265^{+0.02053}_{-0.01874}$	$0.31072^{+0.01125}_{-0.01324}$	$0.30249^{+0.01337}_{-0.01092}$
σ_8	$0.93857^{+0.05738}_{-0.10765}$	$0.94573^{+0.04282}_{-0.11852}$	$0.94939^{+0.04631}_{-0.11513}$	$0.93770^{+0.04933}_{-0.10742}$	$0.94709^{+0.04707}_{-0.11157}$	$0.94865^{+0.04733}_{-0.10816}$
$z_{\rm reio}$	$9.9238^{+1.6998}_{-1.7209}$	$9.9678^{+1.6604}_{-1.5971}$	$10.1902^{+1.6728}_{-1.5416}$	$9.8484^{+1.5867}_{-1.4909}$	$9.9381^{+1.5636}_{-1.4472}$	$10.1557^{+1.4740}_{-1.3804}$
$H_0 t_0$	$0.95735^{+0.01899}_{-0.01726}$	$0.95894^{+0.00879}_{-0.00790}$	$0.96559^{+0.00795}_{-0.00821}$	$0.95471^{+0.01596}_{-0.01484}$	$0.95775^{+0.00776}_{-0.00711}$	$0.96333^{+0.00660}_{-0.00746}$

Table 6.7: For each data set combination we report the mean values and 1σ errors in the mixed coupled DE model. The Hubble constant is given in units of $\mathrm{km\,s^{-1}\,Mpc^{-1}}$. When necessary, we also write in brackets the 2σ lower limits of the model parameter D_M. For the data set combinations which include the $H_0^{\rm R}$ local value of the Hubble constant, we quote the mean values along with their respective 1σ errors for the parameter λ, in order to highlight the significant peaks in the marginalised posterior distributions.

with the inferred upper bounds from the data set combinations using $H_0^{\rm R}$. In all analyses presented in Table 6.6, we only obtain 68% CL upper bounds on β which are consistent with zero. Similar to the constant disformally coupled DE model analyses, we observe that in this exponential model, the CA data set combinations put tighter constraints on the model parameters in comparison with the ACA data set combinations, especially on the exponent of the scalar field potential λ. Thus, disformally coupled DE models will be further constrained by forthcoming surveys of the large–scale structures in the Universe.

6.3.3 Mixed model constraints

In this section we discuss the derived parameter constraints in the mixed coupled DE model which simultaneously makes use of the conformal and disformal couplings. In

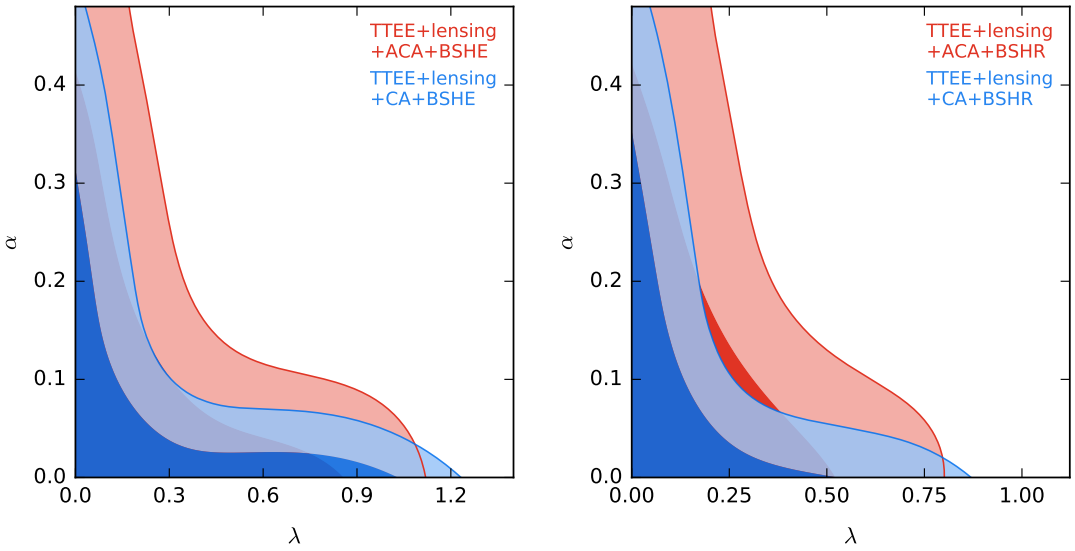

Figure 6.15: Marginalised two–dimensional constraints on the conformal coupling parameter α, and the slope of the exponential potential λ, in the mixed model with the parameter constraints tabulated in Table 6.8. In the left panel we use the local value of the Hubble constant $H_0^{\rm E}$, whereas in the right panel we use $H_0^{\rm R}$.

this model we thus have an extra parameter in our MCMC analyses when compared with the number of parameters in the previous models. We will only consider a constant disformal coupling in this model, since from section 6.3.2 it was evident that the constant disformal model and the exponential disformal model behave in a very similar way. In Tables 6.7 and 6.8 we present the parameter constraints from several data set combinations.

The CMB likelihoods together with the additional information from the background data sets were able to put 95% CL lower bounds on D_M, although only 68% CL constraints were placed on the parameters λ and α. The relatively high value of the Hubble constant $H_0^{\rm R}$ slightly alters the constraints on the parameters λ and α, in comparison with the inferred constraints with $H_0^{\rm E}$. Indeed, a significant peak in the marginalised posterior distribution of λ is derived only in the MCMC analyses with the CMB likelihood and background data set combinations which include $H_0^{\rm R}$. Moreover, a lower bound on α is reported in Table 6.7 with the TT + BSHR and TTEE + BSHR data set combinations, instead of an upper bound which is derived from the other data sets. Furthermore, the TT + BSHE and TTEE + BSHE data set combinations prefer higher values of D_M when compared with the inferred lower bounds from the TT + BSHR and TTEE + BSHR data set combinations. As clearly illustrated in Fig. 6.2, marginally tighter constraints on the cosmological parameters are obtained with the TTEE CMB likelihood in comparison with the

Parameter	TTEE + lensing + CA + BSHE	TTEE + lensing + CA + BSHR	TTEE + lensing + ACA + BSHE	TTEE + lensing + ACA + BSHR	TTEE + lensing + CA + BSHE ($D_M V_0 = 1$)
$100\ \Omega_b h^2$	$2.2549^{+0.0136}_{-0.0141}$	$2.2572^{+0.0134}_{-0.0140}$	$2.2342^{+0.0145}_{-0.0146}$	$2.2387^{+0.0146}_{-0.0145}$	$2.2544^{+0.0138}_{-0.0137}$
$\Omega_c h^2$	$0.11551^{+0.00088}_{-0.00080}$	$0.11523^{+0.00091}_{-0.00078}$	$0.11816^{+0.00134}_{-0.00116}$	$0.11753^{+0.00140}_{-0.00115}$	$0.11563^{+0.00093}_{-0.00088}$
$100\ \theta_s$	$1.04193^{+0.00029}_{-0.00029}$	$1.04195^{+0.00030}_{-0.00029}$	$1.04188^{+0.00030}_{-0.00029}$	$1.04193^{+0.00030}_{-0.00031}$	$1.04192^{+0.00029}_{-0.00030}$
$\tau_{\rm reio}$	$0.047592^{+0.001819}_{-0.007592}$	$0.048296^{+0.002150}_{-0.008295}$	$0.056709^{+0.007606}_{-0.012736}$	$0.059471^{+0.009290}_{-0.012585}$	$0.047212^{+0.001817}_{-0.007211}$
$\ln(10^{10} A_s)$	$3.0176^{+0.0083}_{-0.0151}$	$3.0188^{+0.0096}_{-0.0156}$	$3.0436^{+0.0160}_{-0.0223}$	$3.0483^{+0.0180}_{-0.0228}$	$3.0166^{+0.0083}_{-0.0146}$
n_s	$0.97150^{+0.00378}_{-0.00380}$	$0.97198^{+0.00367}_{-0.00393}$	$0.96654^{+0.00397}_{-0.00430}$	$0.96764^{+0.00420}_{-0.00426}$	$0.97126^{+0.00383}_{-0.00382}$
λ	$< 0.3390(0.9150)$	$< 0.1420(0.5810)$	$< 0.3000(0.8530)$	$< 0.2350(0.5880)$	$< 0.1990(0.5360)$
α	$< 0.0879(0.3323)$	$< 0.1200(0.3541)$	< 0.1450	< 0.1730	$< 0.0522(0.1160)$
$D_M\,/\,\mathrm{meV}^{-1}$ ...	–	> 0.3670	> 0.3590	> 0.4490	/
H_0	$69.317^{+0.861}_{-0.351}$	$69.722^{+0.520}_{-0.403}$	$68.329^{+0.666}_{-0.538}$	$68.697^{+0.515}_{-0.502}$	$69.630^{+0.460}_{-0.407}$
Ω_m	$0.28746^{+0.00443}_{-0.00873}$	$0.28353^{+0.00499}_{-0.00526}$	$0.30105^{+0.00652}_{-0.00841}$	$0.29655^{+0.00650}_{-0.00655}$	$0.28503^{+0.00508}_{-0.00551}$
σ_8	$0.79682^{+0.00980}_{-0.00506}$	$0.79975^{+0.00554}_{-0.00619}$	$0.82170^{+0.00920}_{-0.00973}$	$0.82427^{+0.00837}_{-0.01010}$	$0.79992^{+0.00499}_{-0.00596}$
$z_{\rm reio}$	$6.8724^{+0.2079}_{-0.8750}$	$6.9377^{+0.2395}_{-0.9389}$	$7.8773^{+0.8485}_{-1.1835}$	$8.1323^{+0.9787}_{-1.1564}$	$6.8352^{+0.2075}_{-0.8314}$
$H_0 t_0$	$0.97307^{+0.01082}_{-0.00405}$	$0.97821^{+0.00604}_{-0.00471}$	$0.96159^{+0.00820}_{-0.00600}$	$0.96605^{+0.00639}_{-0.00561}$	$0.97728^{+0.00547}_{-0.00501}$

Table 6.8: For each data set combination we report the mean values and 1σ errors in the mixed coupled DE model. The Hubble constant is given in units of $\mathrm{km\ s^{-1}\ Mpc^{-1}}$. The first data set combination was not able to constrain the parameter D_M. In the last column, we consider the mixed coupled DE model subject to $D_M V_0 = 1$, thus D_M is fixed in this case. When necessary, we also write in brackets the 2σ upper limits of the model parameters λ and α.

TT likelihood, henceforth we will only consider the TTEE CMB likelihood in the data set combinations that include the cluster abundance data sets.

In this mixed coupled DE model, relatively high values of σ_8 are allowed by the CMB likelihoods along with the background data sets. This is expected since in this model the disformal coupling enhances the gravitational attraction between the DM particles leading to an enhancement in the growth of perturbations, in similarity with the pure disformal coupling cases discussed in section 6.3.2. Therefore, in Table 6.8 we consider the data set combinations which are able to probe the growth of perturbations better than the CMB temperature and polarisation likelihoods along

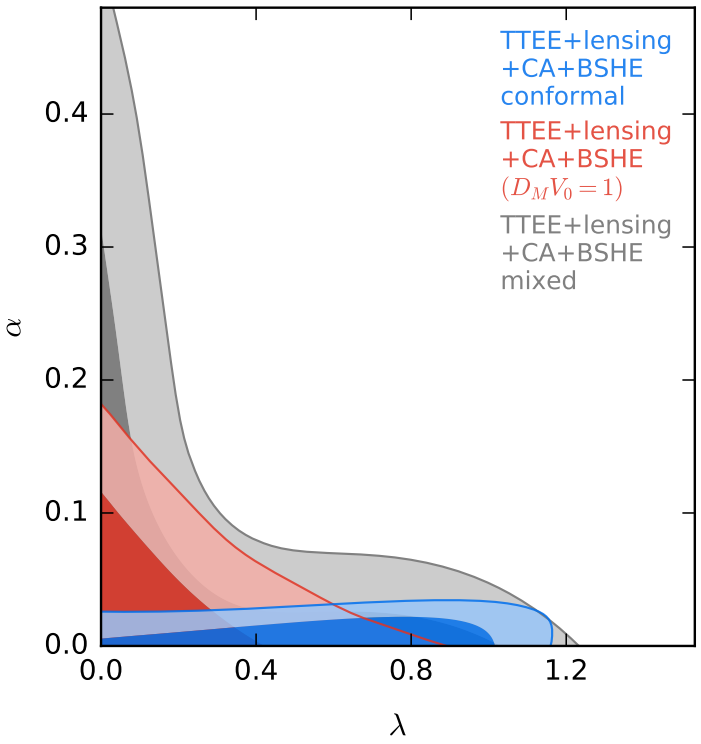

Figure 6.16: A comparison of the marginalised two–dimensional constraints on the conformal coupling parameter α, and the scalar field's potential parameter λ, in mixed models and the conformally coupled model. The mixed model with variable D_M is denoted by mixed, whereas the other mixed model makes use of the relationship $D_M V_0 = 1$. In both mixed models, a constant disformal coupling $(\beta = 0)$ was considered.

with the background data sets. Indeed, significantly tighter constraints are placed on σ_8 with the additional cluster abundance data set combinations together with the CMB lensing likelihood.

Consequently, marginally tighter constraints are derived for the mixed model parameters α and λ. Remarkably, the data set combinations with the BSHR background data set considered in Table 6.8, were able to place upper bounds instead of lower bounds on the conformal coupling parameter α, as reported in Table 6.7. This is expected due to the correlation between σ_8 and α. The CA data set combinations, which prefer low values of σ_8, tightly constrained the conformal coupling parameter to $\alpha < 0.3323$ (TTEE + lensing + CA + BSHE) and $\alpha < 0.3541$ (TTEE + lensing + CA + BSHR) at the 95% confidence level. This is a significant improvement on the inferred constraints of Ref. [5], in which only the background evolution was considered. As expected, the ACA data set combinations allow for slightly larger values of α, since the measurements in this data set allow for marginally larger values of σ_8 which are consistent with the concordance model. The local value of the Hubble constant has a minor influence on the 95% CL upper bounds of α, although the BSHR data set combinations put tighter constraints on λ in comparison with the inferred upper bounds from the BSHE data set combinations. We show the marginalised two–dimensional constraints on α and λ from the first four data set combinations of Table 6.8 in the panels of Fig. 6.15.

Finally, we consider a mixed model having the same number of parameters as the conformal and disformal models considered in section 6.3.1 and section 6.3.2, respectively. We report the MCMC analysis parameter constraints in the last column of Table 6.8, in which we fix the constant disformal coupling parameter according to $D_M V_0 = 1$. As expected, we obtain tighter 95% CL upper bounds on the conformal coupling parameter $\alpha < 0.1160$, as well as on the scalar field's exponent parameter $\lambda < 0.5360$. We collect our marginalised constraints on α and λ in Fig. 6.16, in which we compare the two–dimensional marginalised constraints inferred from the conformal model of section 6.3.1, the mixed model with variable D_M discussed in the first part of this section, along with the last mixed model which satisfies the relationship $D_M V_0 = 1$. From this figure, one can clearly observe that these coupled models are all consistent with a null coupling between DM and DE, although DE models with a disformal coupling still require further investigation.

6.4 Conclusions

We here considered specific interacting DE models in which DE and DM were allowed to interact directly with each other, as thoroughly described in chapter 5. We showed that the cosmological imprints of these direct interactions between the dark sector constituents can be probed by current cosmological observations. For the interactions between DM and DE, we focused on the conformal and disformal couplings which are characterised by different cosmological signatures. We thus considered the conformal, disformal, and mixed models as separate cases of the generic coupled DE model of section 6.1.

We confronted these coupled DE models with several combinations of data sets which are able to probe the early–time as well as the late–time cosmic history of the Universe. Specifically, we considered the *Planck* 2015 temperature, polarisation, and lensing likelihoods, along with BAO measurements, a SNIa sample, Hubble parameter measurements, local values of the Hubble constant, and cluster abundance measurements. The parameter posterior distributions together with their confidence limits were inferred via MCMC analyses.

In all coupled DE models, we found that the additional information from the cluster abundance data set and the CMB gravitational lensing likelihood improves the marginalised constraints on the coupling parameters. In general, we also noticed that the *Planck* 2015 TTEE likelihood provides better marginalised constraints on the cosmological parameters, when compared with the inferred constraints from the CMB temperature likelihood. Also, the CA data set measurements, which prefer relatively low values of σ_8, predominantly shift the marginalised constraints on $\tau_{\rm reio}$ and A_s to lower values, with a proportionately smaller shift of n_s to larger values. Moreover, we constrained the dimensionless age of the Universe in our coupled DE

models, which we found to be close to unity without any significant changes from one model to another.

In the conformal model, the CMB likelihoods are able to constrain the model parameters quite well, since large values of the conformal coupling parameter have a significant impact on the CMB temperature power spectrum, as was illustrated in chapter 5. With the additional information from the background data sets, we improved the constraints on λ, and marginally tighter constraints were placed on α. Furthermore, the relatively high value of the local Hubble constant $H_0^{\rm R}$, gives rise to a significant peak in the marginalised posterior distribution of α, although this is still found to be consistent with zero at around 2σ. This complements the results of Ref. [576], in which a conformally coupled model with an inverse power–law potential was considered. However, with the additional cluster abundance measurements, the 95% CL upper bounds on the coupling parameter are significantly lowered to $\alpha \lesssim 0.03$. In our opinion, these tight limits on the conformal coupling between DM and DE diminishes the attractiveness of this model.

For the disformal model, we first considered a constant disformal coupling and then an exponential disformal coupling. Since a disformal coupling between DM and DE does not modify considerably the CMB temperature power spectrum, it was expected that the CMB likelihoods would not be able to constrain the model very well. Indeed, both the constant and exponential disformally coupled models were better constrained with the additional cluster abundance measurements which directly probe the characterised anomalous growth of perturbations, thus confirming our discussion of chapter 5. By being able to derive tight constraints on σ_8 from the information provided by the cluster abundance measurements, we were then able to place, for the first time, upper bounds on the disformal coupling parameters $D_M \lesssim 0.3\,\mathrm{meV}^{-1}$ and $\beta \lesssim 1.6$. Although the inferred constraints on the disformal model parameters are not as tight as those in the conformally coupled DE model, the disformal coupling is also consistent with a null coupling between the dark sector constituents.

Finally, we considered the mixed conformally–disformally coupled DE model. Similar to the previous models, the tightest constraints were obtained from the MCMC analyses which included the cluster abundance measurements. In this mixed model, significantly larger values of the conformal coupling parameter are allowed ($\alpha \lesssim 0.33$), in comparison with the derived upper bounds in the conformally coupled DE model. Since the disformal coupling parameter is not well constrained in the mixed model, we considered a mixed model which satisfies the relationship $D_M V_0 = 1$. In this case, we obtained the tightest marginalised constraint on the conformal coupling parameter of $\alpha \lesssim 0.12$, which is still considerably larger than the 95% CL upper bounds derived in the conformally coupled model. Although our analyses suggest that Nature is in harmony with a null coupling within the dark sector,

we expect that forthcoming data sets would clearly point out whether dark sector interactions are a characteristic of our Universe.

7 Conclusions

In this thesis we gave a relatively brief account of the extensive subject of cosmology, in which we were mostly interested in the characteristics of the puzzling dark sector of the Universe, along with its cosmological signatures. As we have repeatedly seen, this scientific field of fundamental research has recently been undergoing through rapid developments attributed to the progress of observational cosmology. Consequently, the confrontation of the vast number of cosmological models with observational data became a reality, particularly after the dawn of the precision cosmology era. In our chapters we frequently highlighted how our theoretical framework was recurrently challenged by astronomical and cosmological observations, however theoretical cosmology has consistently been able to come up with a plausible mechanism by which one can give a physical interpretation of the reported observation. Inevitably, our theoretical understanding of the evolution of the Universe has been constantly progressing over the years.

We illustrated that the concordance model of cosmology, which embraces the exquisite gravitational theory of General Relativity, is in an excellent agreement with state–of–the–art cosmological observations. Despite the theoretical simplicity of the model, the concordance model of cosmology suffers from the acute cosmological constant problem along with the coincidence problem. We have seen that the enormous discrepancy between the expected magnitude of the cosmological constant from cosmological observations, and its respective predicted value from elementary particle physics, clearly implies that we still need to work out some of our theoretical foundations of Nature. Furthermore, the currently reported mild tensions from a number of cosmological observations are still unresolved within the concordance model of cosmology, and could potentially turn into realistic disagreements with upcoming cosmological surveys. Thus, it is imperative to explore other cosmological models and study their characteristics which set them apart from the concordance

model of cosmology.

In chapter 4 we have scrutinised a specific scalar–tensor theory, in which the minimally coupled scalar field was assumed to be directly coupled to multiple fluid components through the conformal and disformal coupling functions. We performed a dynamical systems analysis, by which we were able to analytically establish the existence requirements and further evaluated the stability conditions for the particular cases of dust and radiation. We demonstrated that the introduction of disformal couplings in addition to the commonly studied conformal couplings broadens the stability region of a given fixed point, thus allowing this fixed point to play a role in the cosmic history of the Universe. In this chapter we further showed that a varying fine–structure constant arises as a consequence of disformally coupling matter and radiation to the scalar field. Thence, this depicts the dissimilar phenomenology of the conformal and disformal couplings to conventional matter.

In the previous two chapters we have concentrated on a coupled quintessence model, such that baryonic matter was considered to be decoupled from the dark sector interaction of dark matter with a minimally coupled dark energy scalar field. The characteristics attributed to the disformally coupled dark matter were clearly illustrated by its background and perturbation cosmic evolution, particularly through the distinctive intermediate–scales and time–dependent damped oscillations in the matter growth rate function. Moreover, conformal couplings within the dark sector of the Universe were found to be tightly constrained by current cosmological data sets, whereas the scenario of disformally coupled dark matter to dark energy is still relatively feebly constrained. Hence, it is imperative to confront these type of interacting dark matter–dark energy models with forthcoming cosmological data sets. Evidently, a better understanding of the non–linear cosmic evolution of perturbations would be able to shed some light on the still hidden features of these coupled quintessence models. Other distinctive signatures of dark sector interactions might be indirectly detected through observations of the tidal tails of a disrupting satellite galaxy [634], along with the 21 cm hydrogen absorption signal [635]. Certainly, modified theories of gravity have a bright future, and hopefully this exploration might also elucidate the physics beyond the standard model.

A

Compilation of eigenvalues & supplementary set of fixed points

In sections A.1–A.2.3 of this appendix we collect the eigenvalues of the dynamical systems analysis considered in chapter 4. Moreover, we present the fixed points for a conformally coupled perfect fluid with equation of state parameter γ_1, and conformally–disformally coupled perfect fluid with equation of state parameter γ_2, in section A.3. We then describe an extended approach for more general coupling and scalar field potential functions in section A.4.

A.1 Eigenvalues–Single fluid case: Arbitrary equation of state

We present the generic single fluid case eigenvalues for fixed points (1)–(8) of section 4.3, from which one can easily obtain the eigenvalues for a perfect fluid with a specified equation of state parameter γ. We do not list the eigenvalues for dust and radiation here, since both cases are a particular case of these generalised eigenvalues:

(1)
$$e_1 = -2\left(3+\sqrt{6}\beta\right),\ e_2 = 3(2-\gamma) - \sqrt{6}\alpha(4-3\gamma),\ e_3 = 3+\sqrt{3/2}\lambda$$

(2)
$$e_1 = -2\left(3-\sqrt{6}\beta\right),\ e_2 = 3(2-\gamma) + \sqrt{6}\alpha(4-3\gamma),\ e_3 = 3-\sqrt{3/2}\lambda$$

(3)

$$
\begin{aligned}
e_1 =& \frac{3\left(2\beta^2-3\right)}{2\left(\beta\left(2\beta+u_2\right)-3\right)^4}\Big\{u_1\left[3-2\beta\left(u_2+2\beta\right)\right]-\left(2\beta^2-3\right)\\
&\times\Big[9+18\gamma+2\beta\left[2\alpha\left(8\beta^2-9\right)\left(3\gamma-4\right)+\beta\left(21-48\gamma+8\beta^2(4\gamma-3)\right)\right]\\
&+u_2\left[2\alpha\left(8\beta^2-3\right)\left(3\gamma-4\right)+\beta\left(3-24\gamma+8\beta^2(4\gamma-3)\right)\right]\Big]\Big\},\\
e_2 =& \frac{3\left(2\beta^2-3\right)}{2\left(\beta\left(2\beta+u_2\right)-3\right)^4}\Big\{u_1\left[-3+2\beta\left(u_2+2\beta\right)\right]-\left(2\beta^2-3\right)\\
&\times\Big[9+18\gamma+2\beta\left[2\alpha\left(8\beta^2-9\right)\left(3\gamma-4\right)+\beta\left(21-48\gamma+8\beta^2(4\gamma-3)\right)\right]\\
&+u_2\left[2\alpha\left(8\beta^2-3\right)\left(3\gamma-4\right)+\beta\left(3-24\gamma+8\beta^2(4\gamma-3)\right)\right]\Big]\Big\},\\
e_3 =& -\frac{1}{2}\left(u_2-2\beta\right)\left(2\beta-\lambda\right),
\end{aligned}
$$

where u_1 and u_2 are defined as follows

$$
\begin{aligned}
u_1^2 =& \frac{\left(3-2\beta^2\right)^4}{\left(-3+\beta\left(u_2+2\beta\right)\right)^4}\Big\{81-4482\beta^2+23688\beta^4-32640\beta^6+12800\beta^8\\
&+8\alpha^2\left[-27+4\beta^2\left(9-8\beta^2\right)^2\right]\left(4-3\gamma\right)^2-4\left[81-2862\beta^2+11808\beta^4-14208\beta^6+5120\beta^8\right]\gamma\\
&+4\left[81+64\beta^2\left(3-4\beta^2\right)^2\left(-3+2\beta^2\right)\right]\gamma^2\\
&+2u_2\left[-9+18\gamma+4\alpha\beta\left(8\beta^2-9\right)\left(3\gamma-4\right)+2\beta^2\left(51-48\gamma+8\beta^2(4\gamma-5)\right)\right]\\
&\times\left[2\alpha\left(8\beta^2-3\right)\left(3\gamma-4\right)+\beta\left(21-24\gamma+8\beta^2(4\gamma-5)\right)\right]\\
&+16\alpha\beta(3\gamma-4)\left[27(5-7\gamma)+2\beta^2\left(96\beta^2(8-7\gamma)+64\beta^4(4\gamma-5)+9(56\gamma-55)\right)\right]\Big\},
\end{aligned}
$$

$$
u_2^2 = -6+4\beta^2
$$

(4)

$$
\begin{aligned}
e_1 =& \frac{3\left(2\beta^2-3\right)}{2\left(\beta\left(u_2-2\beta\right)+3\right)^4}\Big\{u_3\left[3+2\beta\left(u_2-2\beta\right)\right]-\left(2\beta^2-3\right)\\
&\times\Big[9+18\gamma+2\beta\left[2\alpha\left(8\beta^2-9\right)\left(3\gamma-4\right)+\beta\left(21-48\gamma+8\beta^2(4\gamma-3)\right)\right]\\
&+u_2\left[-2\alpha\left(8\beta^2-3\right)\left(3\gamma-4\right)+\beta\left(-3+24\gamma+8\beta^2(3-4\gamma)\right)\right]\Big]\Big\}\,,\\
e_2 =& \frac{3\left(2\beta^2-3\right)}{2\left(\beta\left(u_2-2\beta\right)+3\right)^4}\Big\{u_3\left[-3-2\beta\left(u_2-2\beta\right)\right]-\left(2\beta^2-3\right)\\
&\times\Big[9+18\gamma+2\beta\left[2\alpha\left(8\beta^2-9\right)\left(3\gamma-4\right)+\beta\left(21-48\gamma+8\beta^2(4\gamma-3)\right)\right]\\
&+u_2\left[-2\alpha\left(8\beta^2-3\right)\left(3\gamma-4\right)+\beta\left(-3+24\gamma+8\beta^2(3-4\gamma)\right)\right]\Big]\Big\}\,,\\
e_3 =& \frac{1}{2}\left(u_2+2\beta\right)\left(2\beta-\lambda\right)\,,
\end{aligned}
$$

where

$$
\begin{aligned}
u_3^2 =& \frac{\left(3-2\beta^2\right)^4}{\left(3+\beta\left(u_2-2\beta\right)\right)^4}\Big\{81-4482\beta^2+23688\beta^4-32640\beta^6+12800\beta^8\\
&+8\alpha^2\left[-27+4\beta^2\left(9-8\beta^2\right)^2\right]\left(4-3\gamma\right)^2-4\left[81-2862\beta^2+11808\beta^4-14208\beta^6+5120\beta^8\right]\gamma\\
&+4\left[81+64\beta^2\left(3-4\beta^2\right)^2\left(-3+2\beta^2\right)\right]\gamma^2\\
&-2u_2\left[-9+18\gamma+4\alpha\beta\left(8\beta^2-9\right)\left(3\gamma-4\right)+2\beta^2\left(51-48\gamma+8\beta^2(4\gamma-5)\right)\right]\\
&\times\left[2\alpha\left(8\beta^2-3\right)\left(3\gamma-4\right)+\beta\left(21-24\gamma+8\beta^2(4\gamma-5)\right)\right]\\
&+16\alpha\beta(3\gamma-4)\left[27(5-7\gamma)+2\beta^2\left(96\beta^2(8-7\gamma)+64\beta^4(4\gamma-5)+9(56\gamma-55)\right)\right]\Big\}
\end{aligned}
$$

(5)

$$e_1 = -3\,(u_4+u_5)\left\{2(\gamma-1)\gamma\left(8(2\alpha+\beta)^2-24\alpha(2\alpha+\beta)\gamma+3\left(6\alpha^2-1\right)\gamma^2\right)^2(-2\beta+\alpha(3\gamma-4))^5\right.$$
$$\times\left[4\alpha^4(4-3\gamma)^4-24\alpha^3\beta(3\gamma-4)^3+3\gamma^2\left(8\beta^2+3(\gamma-4)\gamma\right)-12\alpha^2(4-3\gamma)^2\left(\gamma^2-4\beta^2\right)\right.$$
$$\left.\left.+4\alpha\beta(3\gamma-4)\left(3\gamma^2-8\beta^2\right)\right]\right\}^{-1},$$

$$e_2 = 3\,(u_4-u_5)\left\{2(\gamma-1)\gamma\left(8(2\alpha+\beta)^2-24\alpha(2\alpha+\beta)\gamma+3\left(6\alpha^2-1\right)\gamma^2\right)^2(-2\beta+\alpha(3\gamma-4))^5\right.$$
$$\times\left[4\alpha^4(4-3\gamma)^4-24\alpha^3\beta(3\gamma-4)^3+3\gamma^2\left(8\beta^2+3(\gamma-4)\gamma\right)-12\alpha^2(4-3\gamma)^2\left(\gamma^2-4\beta^2\right)\right.$$
$$\left.\left.+4\alpha\beta(3\gamma-4)\left(3\gamma^2-8\beta^2\right)\right]\right\}^{-1},$$

$$e_3 = \frac{3\gamma(\lambda-2\beta)}{\alpha(6\gamma-8)-4\beta}\,,$$

where u_4 and u_5 are as follows

$$
\begin{aligned}
u_4^2 = &-(2\beta+\alpha(4-3\gamma))^8(\gamma-1)^2\gamma^2\left(8(2\alpha+\beta)^2-24\alpha(2\alpha+\beta)\gamma+3\left(6\alpha^2-1\right)\gamma^2\right)^4\\
&\times\Big[4\alpha^4(4-3\gamma)^4-24\alpha^3\beta(3\gamma-4)^3+3\gamma^2\left(8\beta^2+3(\gamma-4)\gamma\right)-12\alpha^2(4-3\gamma)^2\left(\gamma^2-4\beta^2\right)\\
&+4\alpha\beta(3\gamma-4)\left(3\gamma^2-8\beta^2\right)\Big]\Big\{4\alpha^6(4-3\gamma)^6(4\gamma-1)+8\alpha^5\beta(\gamma-5)(3\gamma-4)^5(4\gamma-1)\\
&+3(\gamma-2)\gamma^2\left[18\gamma^4+8\beta^4(15\gamma-14)-3\beta^2\gamma(8+\gamma(17\gamma-6))\right]\\
&-4\alpha^4(4-3\gamma)^4\left[3\gamma^2(2\gamma-5)+\beta^2(40+\gamma(65\gamma-176))\right]\\
&-\alpha^2(4-3\gamma)^2\left[9\gamma^3\left(4\gamma^2+\gamma-4\right)-12\beta^2\gamma^2(102+\gamma(41\gamma-102))+16\beta^4(20+\gamma(67\gamma-96))\right]\\
&+4\alpha^3\beta(3\gamma-4)^3\left[-3\gamma^2\left(8\gamma^2-26\gamma+37\right)+2\beta^2(40+\gamma(99\gamma-184))\right]\\
&+2\alpha\beta(3\gamma-4)\big[-6\beta^2\gamma^2(124+5\gamma(-32+13\gamma))+16\beta^4(4+\gamma(17\gamma-20))\\
&+9\gamma^3(-8+\gamma(6+\gamma(4\gamma-5)))\big]\Big\},
\end{aligned}
$$

$$
\begin{aligned}
u_5 = &(2\beta+\alpha(4-3\gamma))^4(\gamma-1)\gamma\left[8(2\alpha+\beta)^2-24\alpha(2\alpha+\beta)\gamma+3(6\alpha^2-1)\gamma^2\right]^2\\
&\times\Big\{4\alpha^4\beta(4-3\gamma)^4(\gamma-8)+4\alpha^5(3\gamma-4)^5+3\beta(\gamma-2)\gamma^2\left(8\beta^2+3(\gamma-4)\gamma\right)\\
&-12\alpha^3(3\gamma-4)^3\left(2\beta^2(\gamma-4)+\gamma^2\right)+\alpha(3\gamma-4)\left[-32\beta^4(\gamma-2)+12\beta^2\gamma^3+9(\gamma-4)\gamma^3\right]\\
&+4\alpha^2\beta(4-3\gamma)^2\left(-3(\gamma-3)\gamma^2+4\beta^2(3\gamma-8)\right)\Big\}
\end{aligned}
$$

(6)
$$
e_1=\frac{3(\gamma-2)^2-2\alpha^2(4-3\gamma)^2}{2(\gamma-2)},\ e_2=\frac{2\alpha(3\gamma-4)(\alpha(3\gamma-4)-2\beta)}{\gamma-2}-3\gamma,
$$

$$e_3 = \frac{-2\alpha^2(4-3\gamma)^2 + 2\alpha(3\gamma-4)\lambda + 3(\gamma-2)\gamma}{2(\gamma-2)}$$

(7)

$$e_1 = \lambda(2\beta-\lambda),\ e_2 = \frac{1}{2}\left(\lambda^2-6\right),\ e_3 = \lambda(4\alpha+\lambda) - 3\gamma(1+\alpha\lambda)$$

(8)

$$e_1 = \frac{3\gamma(2\beta-\lambda)}{\alpha(4-3\gamma)+\lambda}\ ,$$

$$e_2 = -\frac{-3(\alpha(6\gamma-8)+(\gamma-2)\lambda)\left[\alpha(4-3\gamma)+\lambda\right]^4 - \sqrt{3}u_6}{4(\alpha(4-3\gamma)+\lambda)^5}\ ,$$

$$e_3 = -\frac{\sqrt{3}u_6 - 3\left[\alpha(4-3\gamma)+\lambda\right]^4(\alpha(6\gamma-8)+(\gamma-2)\lambda)}{4(\alpha(4-3\gamma)+\lambda)^5}\ ,$$

where

$$u_6^2 = (\alpha(4-3\gamma)+\lambda)^8\Big[16\alpha^3(3\gamma-4)^3\lambda + 4\alpha^2(4-3\gamma)^2\left(12\gamma-8\lambda^2+3\right)$$

$$-4\alpha(3\gamma-4)\lambda\left(6\gamma^2-3\gamma-4\lambda^2+6\right) - 3(\gamma-2)\left(24\gamma^2-9\gamma\lambda^2+2\lambda^2\right)\Big]$$

A.2 Eigenvalues–Two fluid cases

A.2.1 Conformal–disformal dust & conformal–disformal radiation

(*a*)

$$e_1 = -\frac{\alpha_1^5 + \sqrt{\alpha_1^8\left(2-3\alpha_1^2\right)}}{2\alpha_1^5},\ e_2 = -\frac{1}{2} + \frac{\sqrt{\alpha_1^8\left(2-3\alpha_1^2\right)}}{2\alpha_1^5},\ e_3 = -4 - \frac{2\beta_1}{\alpha_1},$$

$$e_4 = -4 - \frac{2\beta_2}{\alpha_1},\ e_5 = 2 + \frac{\lambda}{2\alpha_1}$$

(b)

$$e_1 = -4 + \frac{4\beta_2}{\beta_1},\ e_2 = 2 - \frac{\lambda}{\beta_1},$$

$$e_3 = \frac{-12 + u_9^{2/3} + 16\alpha_1^2 + 20\alpha_1\beta_1 + 13\beta_1^2 + u_9^{1/3}(4\alpha_1 + \beta_1)}{3u_9^{1/3}\beta_1},$$

$$e_4 = \frac{i\left(i+\sqrt{3}\right)u_9^{2/3} + 2u_9^{1/3}(4\alpha_1+\beta_1) + \left(-1-i\sqrt{3}\right)\left(-12+16\alpha_1^2+20\alpha_1\beta_1+13\beta_1^2\right)}{6u_9^{1/3}\beta_1},$$

$$e_5 = \frac{\left(-1-i\sqrt{3}\right)u_9^{2/3} + 2u_9^{1/3}(4\alpha_1+\beta_1) + i\left(i+\sqrt{3}\right)\left(-12+16\alpha_1^2+20\alpha_1\beta_1+13\beta_1^2\right)}{6u_9^{1/3}\beta_1},$$

where

$$u_7^2 = -\left(1 + 4\alpha_1^2 + 5\alpha_1\beta_1 + \beta_1^2\right)^2\left(-16 + 9\beta_1^2\right),$$

$$u_8 = 18 + 8\alpha_1^2 + 10\alpha_1\beta_1 - 7\beta_1^2,$$

$$u_9 = 6\sqrt{3}u_7 + 8u_8\alpha_1 + 5u_8\beta_1$$

A.2.2 Conformal dust & conformal–disformal radiation

(1)

$$e_1 = 2,\ e_2 = \frac{1}{2}\left(3 - \sqrt{6}\alpha_1\right),\ e_3 = -2\left(3 + \sqrt{6}\beta\right),\ e_4 = 3 + \sqrt{\frac{3}{2}}\lambda$$

$(6)_{(r)}$

$$e_1 = -4,\ e_2 = 2,\ e_3 = -1,\ e_4 = \frac{1}{2}$$

(2)

$$e_1 = 2,\ e_2 = \frac{1}{2}\left(3 + \sqrt{6}\alpha_1\right),\ e_3 = -2\left(3 - \sqrt{6}\beta\right),\ e_4 = 3 - \sqrt{\frac{3}{2}}\lambda$$

(a)

$$e_1 = -\frac{\alpha_1^5 + \sqrt{\alpha_1^8\left(2 - 3\alpha_1^2\right)}}{2\alpha_1^5},\ e_2 = -\frac{1}{2} + \frac{\sqrt{\alpha_1^8\left(2-3\alpha_1^2\right)}}{2\alpha_1^5},\ e_3 = -4 - \frac{2\beta}{\alpha_1},\ e_4 = 2 + \frac{\lambda}{2\alpha_1}$$

$(6)_{(d)}$

$$e_1 = -\frac{3}{2} + \alpha_1^2,\ e_2 = -1 + 2\alpha_1^2,\ e_3 = -3 - 2\alpha_1(\alpha_1 + 2\beta),\ e_4 = \frac{3}{2} + \alpha_1(\alpha_1 + \lambda)$$

$(5)_{(r)}$

$$e_1 = \frac{1}{2} + \frac{\alpha_1}{\beta},$$

$$e_2 = -\frac{27\beta^{11} - 72\beta^9 + 60\beta^7 - 16\beta^5 + \sqrt{\beta^8\left(2 - 3\beta^2\right)^4\left(81\beta^6 - 312\beta^4 + 368\beta^2 - 128\right)}}{2\beta^5\left(2 - 3\beta^2\right)^2\left(3\beta^2 - 4\right)},$$

$$e_3 = \frac{-27\beta^{11} + 72\beta^9 - 60\beta^7 + 16\beta^5 + \sqrt{\beta^8\left(2 - 3\beta^2\right)^4\left(81\beta^6 - 312\beta^4 + 368\beta^2 - 128\right)}}{2\beta^5\left(2 - 3\beta^2\right)^2\left(3\beta^2 - 4\right)},$$

$$e_4 = 2 - \frac{\lambda}{\beta}$$

$(3)_{(r)}$

$$e_1 = -\frac{3}{2} - \frac{1}{2}(\alpha_1 + 2\beta)\left(-2\beta + u_2\right),$$

$$e_2 = -\frac{14\beta^2 + 7\beta u_2 - 33 + \sqrt{225 - 66\beta^2 + 8\beta^4 - 30\beta u_2 + 4\beta^3 u_2}}{8\beta^2 + 4\beta u_2 - 6},$$

$$e_3 = \frac{-14\beta^2 - 7\beta u_2 + 33 + \sqrt{225 - 66\beta^2 + 8\beta^4 - 30\beta u_2 + 4\beta^3 u_2}}{8\beta^2 + 4\beta u_2 - 6},$$

$$e_4 = -\frac{1}{2}(-2\beta + u_2)(2\beta - \lambda)$$

$(4)_{(r)}$

$$e_1 = -\frac{3}{2} + \frac{1}{2}(\alpha_1 + 2\beta)\,(2\beta + u_2)\,,$$

$$e_2 = -\frac{-14\beta^2 + 7\beta u_2 + 33 + \sqrt{225 - 66\beta^2 + 8\beta^4 + 30\beta u_2 - 4\beta^3 u_2}}{-8\beta^2 + 4\beta u_2 + 6},$$

$$e_3 = \frac{14\beta^2 - 7\beta u_2 - 33 + \sqrt{225 - 66\beta^2 + 8\beta^4 + 30\beta u_2 - 4\beta^3 u_2}}{-8\beta^2 + 4\beta u_2 + 6},$$

$$e_4 = \frac{1}{2}(2\beta + u_2)(2\beta - \lambda)$$

$(8)_{(r)}$

$$e_1 = -4 + \frac{8\beta}{\lambda},\ e_2 = \frac{1}{2} + \frac{2\alpha_1}{\lambda},\ e_3 = -\frac{\lambda^5 + \sqrt{\lambda^8\,(64 - 15\lambda^2)}}{2\lambda^5},\ e_4 = -\frac{1}{2} + \frac{\sqrt{\lambda^8\,(64 - 15\lambda^2)}}{2\lambda^5}$$

(7)

$$e_1 = (2\beta - \lambda)\lambda,\ e_2 = \frac{1}{2}\left(\lambda^2 - 6\right),\ e_3 = \lambda^2 - 4,\ e_4 = \frac{1}{2}(-3 + \lambda(\alpha_1 + \lambda))$$

$(8)_{(d)}$

$$e_1 = \frac{6\beta - 3\lambda}{\alpha_1 + \lambda},\ e_2 = -\frac{4\alpha_1 + \lambda}{\alpha_1 + \lambda},$$

$$e_3 = -\frac{6\alpha_1^2 + 9\alpha_1\lambda + 3\lambda^2 + \sqrt{3}\sqrt{-(\alpha_1 + \lambda)^2\left(-72 + 16\alpha_1^3\lambda + 21\lambda^2 + 4\alpha_1\lambda\,(4\lambda^2 - 9) + 4\alpha_1^2\,(8\lambda^2 - 15)\right)}}{4(\alpha_1 + \lambda)^2},$$

$$e_4 = \frac{-6\alpha_1^2 - 9\alpha_1\lambda - 3\lambda^2 + \sqrt{3}\sqrt{-(\alpha_1 + \lambda)^2\left(-72 + 16\alpha_1^3\lambda + 21\lambda^2 + 4\alpha_1\lambda\,(4\lambda^2 - 9) + 4\alpha_1^2\,(8\lambda^2 - 15)\right)}}{4(\alpha_1 + \lambda)^2}$$

A.2.3 Two conformal–disformal dust components

(1)

$$e_1 = \frac{1}{2}\left(3 - \sqrt{6}\alpha_1\right),\ e_2 = 3 - \sqrt{6}\alpha_2,\ e_3 = -2\left(3 + \sqrt{6}\beta_1\right),\ e_4 = -2\left(3 + \sqrt{6}\beta_2\right),$$

$$e_5 = 3 + \sqrt{\frac{3}{2}}\lambda$$

(c)

$$e_1 = -3,\ e_2 = -3,\ e_3 = \frac{3}{2},\ e_4 = \frac{1}{4}\left(-3 + \frac{\sqrt{3}}{\alpha_2}\sqrt{\frac{\alpha_2}{\alpha_2 - \alpha_1}}\sqrt{-\alpha_2(\alpha_1 - \alpha_2)(3 + 16\alpha_1\alpha_2)}\right),$$

$$e_5 = -\frac{1}{4}\left(3 + \frac{\sqrt{3}}{\alpha_2}\sqrt{\frac{\alpha_2}{\alpha_2 - \alpha_1}}\sqrt{-\alpha_2(\alpha_1 - \alpha_2)(3 + 16\alpha_1\alpha_2)}\right)$$

(2)

$$e_1 = \frac{1}{2}\left(3 + \sqrt{6}\alpha_1\right),\ e_2 = 3 + \sqrt{6}\alpha_2,\ e_3 = -2\left(3 - \sqrt{6}\beta_1\right),\ e_4 = -2\left(3 - \sqrt{6}\beta_2\right),$$

$$e_5 = 3 - \sqrt{\frac{3}{2}}\lambda$$

$(6)^1_{(d)}$

$$e_1 = -\frac{3}{2} + \alpha_1^2,\ e_2 = 2\alpha_1(\alpha_1 - \alpha_2),\ e_3 = -3 - 2\alpha_1(\alpha_1 + 2\beta_1),\ e_4 = -3 - 2\alpha_1(\alpha_1 + 2\beta_2),$$

$$e_5 = \frac{3}{2} + \alpha_1(\alpha_1 + \lambda)$$

$(6)^2_{(d)}$

$$e_1 = \alpha_2(\alpha_2 - \alpha_1),\ e_2 = -\frac{3}{2} + \alpha_2^2,\ e_3 = -3 - 2\alpha_2(\alpha_2 + 2\beta_1),\ e_4 = -3 - 2\alpha_2(\alpha_2 + 2\beta_2),$$

$$e_5 = \frac{3}{2} + \alpha_2(\alpha_2 + \lambda)$$

$(3)^1_{(d)}$

$$e_1 = \frac{3\left(2\beta_1^2-3\right)\left(2\alpha_2\beta_1+\sqrt{2}\alpha_2 u_{10}+3\right)}{\left(2\beta_1^2+\sqrt{2}\beta_1 u_{10}-3\right)^2},$$

$$e_2 = \frac{3\left(2\beta_1^2-3\right)\left((2\alpha_1-\beta_1)\left(2\beta_1+\sqrt{2}u_{10}\right)+9\right)-3u_{11}}{2\left(2\beta_1^2+\sqrt{2}\beta_1 u_{10}-3\right)^2},$$

$$e_3 = \frac{3\left(\left(2\beta_1^2-3\right)\left((2\alpha_1-\beta_1)\left(2\beta_1+\sqrt{2}u_{10}\right)+9\right)+u_{11}\right)}{2\left(2\beta_1^2+\sqrt{2}\beta_1 u_{10}-3\right)^2},$$

$$e_4 = 2\left(\beta_1-\beta_2\right)\left(\sqrt{2}u_{10}-2\beta_1\right), \quad e_5 = -\frac{1}{2}\left(2\beta_1-\lambda\right)\left(\sqrt{2}u_{10}-2\beta_1\right),$$

where

$$u_{10}^2 = -3+2\beta_1^2,$$

$$u_{11}^2 = \frac{1}{\left(2\beta_1^2+\sqrt{2}\beta_1 u_{10}-3\right)^2}\left(2\beta_1^2-3\right)^3\Big(16\alpha_1\left(16\beta_1^4-12\beta_1^2-9\right)\beta_1+8\alpha_1^2\left(32\beta_1^4-48\beta_1^2+9\right)+64\beta_1^6$$

$$-54\beta_1^2+4\sqrt{2}u_{10}\left(4\beta_1\left(2\alpha_1+\beta_1\right)+3\right)\left(\alpha_1\left(4\beta_1^2-3\right)+2\beta_1^3\right)-27\Big)$$

$(4)^1_{(d)}$

$$e_1 = \left(\alpha_2+2\beta_1\right)\left(2\beta_1+\sqrt{2}u_{10}\right)-3,\ e_2 = -\frac{3\left(\left(2\beta_1^2-3\right)\left((\beta_1-2\alpha_1)\left(-\left(\sqrt{2}u_{10}-2\beta_1\right)\right)-9\right)+u_{12}\right)}{2\left(-2\beta_1^2+\sqrt{2}\beta_1 u_{10}+3\right)^2},$$

$$e_3 = \frac{3u_{12}-3\left(2\beta_1^2-3\right)\left((\beta_1-2\alpha_1)\left(-\left(\sqrt{2}u_{10}-2\beta_1\right)\right)-9\right)}{2\left(-2\beta_1^2+\sqrt{2}\beta_1 u_{10}+3\right)^2},\ e_4 = -2\left(\beta_1-\beta_2\right)\left(2\beta_1+\sqrt{2}u_{10}\right),$$

$$e_5 = \frac{1}{2}\left(2\beta_1-\lambda\right)\left(2\beta_1+\sqrt{2}u_{10}\right),$$

where

$$u_{12}^2 = -\frac{1}{\left(-2\beta_1^2+\sqrt{2}\beta_1 u_{10}+3\right)^2}\left(2\beta_1^2-3\right)^3\Big(16\alpha_1\left(-16\beta_1^4+12\beta_1^2+9\right)\beta_1-8\alpha_1^2\left(32\beta_1^4-48\beta_1^2+9\right)$$

$$-64\beta_1^6+54\beta_1^2+4\sqrt{2}u_{10}\left(4\beta_1\left(2\alpha_1+\beta_1\right)+3\right)\left(\alpha_1\left(4\beta_1^2-3\right)+2\beta_1^3\right)+27\Big)$$

$(3)^2_{(d)}$

$$e_1 = 2\left(\beta_2 - \beta_1\right)\left(u_{13} - 2\beta_2\right),\ e_2 = -\frac{1}{2}\left(\alpha_1 + 2\beta_2\right)\left(u_{13} - 2\beta_2\right) - \frac{3}{2},$$

$$e_3 = \frac{3\left(2\beta_2^2 - 3\right)\left(4\alpha_2\beta_2 - 2\beta_2^2 + u_{13}\left(2\alpha_2 - \beta_2\right) + 9\right) - 3u_{14}}{2\left(2\beta_2^2 + \beta_2 u_{13} - 3\right)^2},$$

$$e_4 = \frac{3\left(\left(2\beta_2^2 - 3\right)\left(4\alpha_2\beta_2 - 2\beta_2^2 + u_{13}\left(2\alpha_2 - \beta_2\right) + 9\right) + u_{14}\right)}{2\left(2\beta_2^2 + \beta_2 u_{13} - 3\right)^2},$$

$$e_5 = -\frac{1}{2}\left(2\beta_2 - \lambda\right)\left(u_{13} - 2\beta_2\right)\ ,$$

where

$$u_{13}^2 = -6 + 4\beta_2^2\ ,$$

$$u_{14}^2 = \frac{\left(2\beta_2^2 - 3\right)^3}{\left(2\beta_2^2 + \beta_2 u_{13} - 3\right)^2}\left(16\alpha_2\left(16\beta_2^4 - 12\beta_2^2 - 9\right)\beta_2 + 8\alpha_2^2\left(32\beta_2^4 - 48\beta_2^2 + 9\right)\right.$$

$$\left. + 64\beta_2^6 - 54\beta_2^2 + 4u_{13}\left(4\beta_2\left(2\alpha_2 + \beta_2\right) + 3\right)\left(\alpha_2\left(4\beta_2^2 - 3\right) + 2\beta_2^3\right) - 27\right)$$

$(4)^2_{(d)}$

$$e_1 = 2\left(\beta_1 - \beta_2\right)\left(2\beta_2 + u_{13}\right),\ e_2 = \frac{1}{2}\left(\left(\alpha_1 + 2\beta_2\right)\left(2\beta_2 + u_{13}\right) - 3\right),$$

$$e_3 = \frac{3\left(2\beta_2^2 - 3\right)\left(4\alpha_2\beta_2 - 2\beta_2^2 + u_{13}\left(\beta_2 - 2\alpha_2\right) + 9\right) - 3u_{15}}{2\left(-2\beta_2^2 + \beta_2 u_{13} + 3\right)^2},$$

$$e_4 = \frac{3\left(\left(2\beta_2^2 - 3\right)\left(4\alpha_2\beta_2 - 2\beta_2^2 + u_{13}\left(\beta_2 - 2\alpha_2\right) + 9\right) + u_{15}\right)}{2\left(-2\beta_2^2 + \beta_2 u_{13} + 3\right)^2},$$

$$e_5 = \frac{1}{2}\left(2\beta_2 - \lambda\right)\left(2\beta_2 + u_{13}\right)\ ,$$

where

$$u_{15}^2 = \frac{\left(2\beta_2^2-3\right)^3}{\left(-2\beta_2^2+\beta_2 u_{13}+3\right)^2}\Big(16\alpha_2\left(16\beta_2^4-12\beta_2^2-9\right)\beta_2+8\alpha_2^2\left(32\beta_2^4-48\beta_2^2+9\right)$$

$$+64\beta_2^6-54\beta_2^2-4u_{13}\left(4\beta_2\left(2\alpha_2+\beta_2\right)+3\right)\left(\alpha_2\left(4\beta_2^2-3\right)+2\beta_2^3\right)-27\Big)$$

(7)

$$e_1 = (2\beta_1-\lambda)\lambda,\ e_2 = (2\beta_2-\lambda)\lambda,\ e_3 = \frac{1}{2}\left(\lambda^2-6\right),\ e_4 = \frac{1}{2}\left(\lambda(\alpha_1+\lambda)-3\right),$$

$$e_5 = \lambda(\alpha_2+\lambda)-3$$

$(8)^1_{(d)}$

$$e_1 = -\frac{3(\alpha_1-\alpha_2)}{\alpha_1+\lambda},\ e_2 = \frac{3(2\beta_1-\lambda)}{\alpha_1+\lambda},\ e_3 = \frac{3(2\beta_2-\lambda)}{\alpha_1+\lambda},$$

$$e_4 = -\frac{3(\alpha_1+\lambda)^3(2\alpha_1+\lambda)+\sqrt{3}\sqrt{-(\alpha_1+\lambda)^6\left(-72+16\alpha_1^3\lambda+21\lambda^2+4\alpha_1\lambda(4\lambda^2-9)+4\alpha_1^2(8\lambda^2-15)\right)}}{4(\alpha_1+\lambda)^4},$$

$$e_5 = \frac{-3(\alpha_1+\lambda)^3(2\alpha_1+\lambda)+\sqrt{3}\sqrt{-(\alpha_1+\lambda)^6\left(-72+16\alpha_1^3\lambda+21\lambda^2+4\alpha_1\lambda(4\lambda^2-9)+4\alpha_1^2(8\lambda^2-15)\right)}}{4(\alpha_1+\lambda)^4}$$

$(8)^2_{(d)}$

$$e_1 = \frac{3(\alpha_1-\alpha_2)}{2(\alpha_2+\lambda)},\ e_2 = \frac{3(2\beta_1-\lambda)}{\alpha_2+\lambda},\ e_3 = \frac{3(2\beta_2-\lambda)}{\alpha_2+\lambda},$$

$$e_4 = -\frac{3(\alpha_2+\lambda)^3(2\alpha_2+\lambda)+\sqrt{3}\sqrt{-(\alpha_2+\lambda)^6\left(-72+16\alpha_2^3\lambda+21\lambda^2+4\alpha_2\lambda(4\lambda^2-9)+4\alpha_2^2(8\lambda^2-15)\right)}}{4(\alpha_2+\lambda)^4},$$

$$e_5 = \frac{-3(\alpha_2+\lambda)^3(2\alpha_2+\lambda)+\sqrt{3}\sqrt{-(\alpha_2+\lambda)^6\left(-72+16\alpha_2^3\lambda+21\lambda^2+4\alpha_2\lambda(4\lambda^2-9)+4\alpha_2^2(8\lambda^2-15)\right)}}{4(\alpha_2+\lambda)^4}$$

A.3 Supplementary two fluid fixed points

x	y	z_1	σ_2
-1	0	0	0
1	0	0	0
$\frac{\sqrt{2}\beta-\sqrt{2\beta^2-3}}{\sqrt{3}}$	0	0	$\frac{1}{18}\left(2\beta\left(2\beta+\sqrt{4\beta^2-6}\right)-3\right)$
$\frac{\sqrt{2}\beta+\sqrt{2\beta^2-3}}{\sqrt{3}}$	0	0	$\frac{1}{18}\left(2\beta\left(2\beta-\sqrt{4\beta^2-6}\right)-3\right)$
$\frac{\sqrt{\frac{3}{2}}\gamma_1}{2\beta+\alpha_1(4-3\gamma_1)}$	0	$\sqrt{\frac{-8(2\alpha_1+\beta)^2+8(2\alpha_1+\beta)(3\alpha_1+\beta)\gamma_1-3\left(1+6\alpha_1^2+4\alpha_1\beta\right)\gamma_1^2}{2(2\beta+\alpha_1(4-3\gamma_1))^2(\gamma_1-1)}}$	$\frac{(2\beta+\alpha_1(4-3\gamma_1))^2}{9\gamma_1^2}$
$\frac{\sqrt{\frac{2}{3}}\alpha_1(4-3\gamma_1)}{\gamma_1-2}$	0	$\sqrt{\frac{3(\gamma_1-2)^2-2\alpha_1^2(4-3\gamma_1)^2}{3(\gamma_1-2)^2}}$	0
$\frac{\sqrt{6}(\gamma_2-\gamma_1)}{\alpha_1(6\gamma_1-8)+\alpha_2(8-6\gamma_2)}$	0	$\sqrt{\frac{2\alpha_2^2(4-3\gamma_2)^2+3(\gamma_1-\gamma_2)(\gamma_2-2)-2\alpha_1\alpha_2(3\gamma_1-4)(3\gamma_2-4)}{2(\alpha_1(3\gamma_1-4)+\alpha_2(4-3\gamma_2))^2}}$	0
$\frac{\sqrt{\frac{3}{2}}\gamma_2}{2\beta+\alpha_2(4-3\gamma_2)}$	0	0	$\frac{(2\beta+\alpha_2(4-3\gamma_2))^2\left(4\alpha_2\beta(4-3\gamma_2)+2\alpha_2^2(4-3\gamma_2)^2-3(\gamma_2-2)\gamma_2\right)}{9(\gamma_2-1)\gamma_2\left(8(2\alpha_2+\beta)^2-24\alpha_2(2\alpha_2+\beta)\gamma_2+3(6\alpha_2^2-1)\gamma_2^2\right)}$
$\frac{\sqrt{\frac{2}{3}}\alpha_2(4-3\gamma_2)}{\gamma_2-2}$	0	0	0
$\frac{\sqrt{\frac{3}{2}}\gamma_1}{\alpha_1(4-3\gamma_1)+\lambda}$	$\sqrt{\frac{2\alpha_1^2(4-3\gamma_1)^2-3(\gamma_1-2)\gamma_1+\alpha_1(8-6\gamma_1)\lambda}{2(\alpha_1(4-3\gamma_1)+\lambda)^2}}$	$\sqrt{\frac{\lambda(4\alpha_1+\lambda)-3\gamma_1(1+\alpha_1\lambda)}{(\alpha_1(4-3\gamma_1)+\lambda)^2}}$	0
$\frac{\lambda}{\sqrt{6}}$	$\sqrt{1-\frac{\lambda^2}{6}}$	0	0
$\frac{\sqrt{\frac{3}{2}}\gamma_2}{(4-3\gamma_2)\alpha_2+\lambda}$	$\sqrt{\frac{2\alpha_2^2(4-3\gamma_2)^2-3(\gamma_2-2)\gamma_2+\alpha_2(8-6\gamma_2)\lambda}{2(\alpha_2(4-3\gamma_2)+\lambda)^2}}$	0	0

Table A.1: The fixed points of the system (4.28)–(4.37) for a conformally coupled fluid with equation of state parameter γ_1, in the presence of a conformally–disformally coupled fluid with equation of state parameter γ_2, as described in section 4.4.2.

x	y	σ_1	σ_2	z_1	z_2
0	$\sqrt{\frac{2\lambda_C^1}{2\lambda_C^1-\lambda_V}}$	$\forall\sigma_1$	$\forall\sigma_2$	$\sqrt{\frac{\lambda_V}{\lambda_V-2\lambda_C^1}}$	0

Table A.2: A non–trivial fixed point of the system (A.1)–(A.5) when $x = 0$, and the scalar field freezes.

A.4 Beyond the exponential form of the couplings and potential

In chapter 4 the functions $V(\phi)$, $C_i(\phi)$, and $D_i(\phi)$ were of exponential form, for which λ_V, λ_C^i, and λ_D^i are constant. While these are well motivated cases, there are other types of models, in which the field sits in the minimum of an effective potential defined by $3H^2\lambda_V y^2 + \kappa(Q_1 + Q_2) = 0$, at finite values of $\phi = \phi_*$. Alternatively the functions can be, for example, of power–law form, in which case λ_V, λ_C^i, and λ_D^i are varying. In these situations, it is useful to introduce another equation related to x, which closes the system. The full system now reads

$$x' = -\left(3 + \frac{H'}{H}\right) x + \sqrt{\frac{3}{2}}\left(\lambda_V y^2 + \frac{\kappa Q_1}{3H^2} + \frac{\kappa Q_2}{3H^2}\right) , \tag{A.1}$$

$$y' = -\sqrt{\frac{3}{2}}\left(\lambda_V x + \sqrt{\frac{2}{3}}\frac{H'}{H}\right) y , \tag{A.2}$$

$$z_i' = -\frac{3}{2}\left(1 + w_i + \frac{2}{3}\frac{H'}{H} + \frac{1}{3}\sqrt{\frac{2}{3}}\frac{\kappa Q_i}{H^2}\frac{x}{z_i^2}\right) z_i , \tag{A.3}$$

$$\sigma_i' = \left(\sqrt{6}(\lambda_C^i - \lambda_D^i)x + 2\frac{H'}{H}\right) \sigma_i , \tag{A.4}$$

$$\phi' = \frac{\sqrt{6}}{\kappa}\, x . \tag{A.5}$$

It then becomes possible to classify all the asymptotic behaviours of the cosmological model in relation to the functional features of the potential and disformal parameters. In particular, we find a non–trivial fixed point given in Table A.2. Although this requires that $w_1 = -1$, this fixed point is distinct from a bare cosmological constant due to the non–vanishing couplings.

B

Disformal transformations

We here derive some variable transformations between the Einstein frame and the tilde frames discussed in section 4.6. We refer to Refs. [470, 472, 485, 535–537] for further details. To keep the discussion simple and generic, we write the Jordan frame metric of Eq. (4.58), and radiation frame metric of Eq. (4.59), as a single tilde metric, namely

$$\tilde{g}_{\mu\nu} = C g_{\mu\nu} + D\phi_{,\mu}\phi_{,\nu} \,, \tag{B.1}$$

and then apply the variable transformations to each frame. From Eq. (B.1), it follows that the inverse metric is given by

$$\tilde{g}^{\mu\nu} = \frac{1}{C}\left(g^{\mu\nu} - \bar{\gamma}^2 \partial^\mu\phi\partial^\nu\phi\right) , \tag{B.2}$$

where

$$\bar{\gamma}^2 = \frac{D}{C + D g^{\mu\nu}\phi_{,\mu}\phi_{,\nu}} \,. \tag{B.3}$$

Furthermore, the determinants are related via

$$\sqrt{\frac{-\tilde{g}}{-g}} = C^2\sqrt{1 + \frac{D}{C}\phi_{,\mu}\phi^{,\mu}} \,. \tag{B.4}$$

We now derive a relationship between the energy–momentum tensors in the Einstein frame and in the tilde frame, specified by the metric of Eq. (B.1). Using the definition of the energy–momentum tensor and the chain rule, we obtain the following

$$T^{\mu\nu} = \frac{2}{\sqrt{-g}} \frac{\delta\left(\sqrt{-\tilde{g}}\widetilde{\mathcal{L}}\right)}{\delta g_{\mu\nu}} = \sqrt{\frac{-\tilde{g}}{-g}} \frac{\delta \tilde{g}_{\alpha\beta}}{\delta g_{\mu\nu}} \left(\frac{2}{\sqrt{-\tilde{g}}} \frac{\delta\left(\sqrt{-\tilde{g}}\widetilde{\mathcal{L}}\right)}{\delta \tilde{g}_{\alpha\beta}} \right) = \sqrt{\frac{-\tilde{g}}{-g}} \frac{\delta \tilde{g}_{\alpha\beta}}{\delta g_{\mu\nu}} \widetilde{T}^{\alpha\beta}. \tag{B.5}$$

Hence, together with Eqs. (B.1)–(B.4), the contravariant and mixed energy–momentum tensor relations between the Einstein frame and tilde frame, are as follows

$$T^{\mu\nu} = C^3 \sqrt{1 + \frac{D}{C}\phi_{,\mu}\phi^{,\mu}}\, \widetilde{T}^{\mu\nu} \,, \tag{B.6}$$

$$T^{\mu}{}_{\nu} = C^2 \sqrt{1 + \frac{D}{C}\phi_{,\mu}\phi^{,\mu}} \left[\delta^{\rho}{}_{\nu} - \frac{D\phi_{,\nu}\phi^{,\rho}}{C + D\phi_{,\mu}\phi^{,\mu}} \right] \widetilde{T}^{\mu}{}_{\rho} \,. \tag{B.7}$$

On specifying a perfect fluid energy–momentum tensor in both frames, such that

$$T^{\mu\nu} = (\rho + p)u^{\mu}u^{\nu} + pg^{\mu\nu} \,, \tag{B.8}$$

$$\widetilde{T}^{\mu\nu} = (\tilde{\rho} + \tilde{p})\tilde{u}^{\mu}\tilde{u}^{\nu} + \tilde{p}\tilde{g}^{\mu\nu} \,, \tag{B.9}$$

we get the following mappings for the energy density, pressure, and the equation of state parameter, respectively

$$\tilde{\rho} = \frac{\rho}{C^2} \sqrt{1 + \frac{D}{C}\phi_{,\mu}\phi^{,\mu}} \,, \tag{B.10}$$

$$\tilde{p} = \frac{p}{C^2 \sqrt{1 + \frac{D}{C}\phi_{,\mu}\phi^{,\mu}}} \,, \tag{B.11}$$

$$\widetilde{w} \equiv \frac{\tilde{p}}{\tilde{\rho}} = \frac{w}{1 + \frac{D}{C}\phi_{,\mu}\phi^{,\mu}} \,, \tag{B.12}$$

when considering a spatially flat FLRW Einstein frame metric and a time–dependent scalar field. Using this tilde metric of Eq. (B.1), we also derive a relationship between the four–velocity in the Einstein frame u^{μ}, and that in the tilde frame $\tilde{u}^{\mu}$, given by the following equation

$$\tilde{u}^{\mu} = \frac{u^{\mu}}{\sqrt{C}\sqrt{1 + \frac{D}{C}\phi_{,\mu}\phi^{,\mu}}} \,. \tag{B.13}$$

References

[1] C. van de Bruck, J. Mifsud, J. P. Mimoso, and N. J. Nunes, *Generalized dark energy interactions with multiple fluids*, *JCAP* **1611** (2016) 031, [arXiv:1605.03834].

[2] C. van de Bruck, J. Mifsud, and N. J. Nunes, *The variation of the fine–structure constant from disformal couplings*, *JCAP* **1512** (2015) 018, [arXiv:1510.00200].

[3] J. Mifsud and C. van de Bruck, *Probing the imprints of generalized interacting dark energy on the growth of perturbations*, *JCAP* **1711** (2017) 001, [arXiv:1707.07667].

[4] C. van de Bruck and J. Mifsud, *Searching for dark matter – dark energy interactions: Going beyond the conformal case*, *Phys. Rev.* **D97** (2018) 023506, [arXiv:1709.04882].

[5] C. van de Bruck, J. Mifsud, and J. Morrice, *Testing coupled dark energy models with their cosmological background evolution*, *Phys. Rev.* **D95** (2017) 043513, [arXiv:1609.09855].

[6] A. Kox, M. Klein, and R. Schulmann, *The collected papers of Albert Einstein*, vol. 6. Princeton University Press, 1996.

[7] U. J. Le Verrier, *Theorie DU mouvement de Mercure*, *Annales de l'Observatoire de Paris* **5** (1859) 1.

[8] R. S. Park, W. M. Folkner, A. S. Konopliv, J. G. Williams, D. E. Smith, and M. T. Zuber, *Precession of Mercury's perihelion from ranging to the MESSENGER spacecraft*, *Astron. J.* **153** (2017) 121.

[9] S. S. Shapiro, J. L. Davis, D. E. Lebach, and J. S. Gregory, *Measurement of the solar gravitational deflection of radio waves using geodetic very–long–baseline interferometry data, 1979–1999*, *Phys. Rev. Lett.* **92** (2004) 121101.

[10] F. W. Dyson, A. S. Eddington, and C. Davidson, *A determination of the deflection of light by the Sun's gravitational field, from observations made at the total eclipse of May 29, 1919*, *Phil. Trans. Roy. Soc. Lond.* **A220** (1920) 291–333.

[11] **Virgo, LIGO Scientific** Collaboration, B. P. Abbott et al., *Observation of gravitational waves from a binary black hole merger*, *Phys. Rev. Lett.* **116** (2016) 061102, [arXiv:1602.03837].

[12] **Virgo, LIGO Scientific** Collaboration, B. P. Abbott et al., *GW151226: Observation of gravitational waves from a 22–solar–mass binary black hole coalescence*, *Phys. Rev. Lett.* **116** (2016) 241103, [arXiv:1606.04855].

[13] **VIRGO, LIGO Scientific** Collaboration, B. P. Abbott et al., *GW170104: Observation of a 50–solar–mass binary black hole coalescence at redshift 0.2*, *Phys. Rev. Lett.* **118** (2017) 221101, [arXiv:1706.01812].

[14] **Virgo, LIGO Scientific** Collaboration, B. P. Abbott et al., *GW170608: Observation of a 19–solar–mass binary black hole coalescence*, *Astrophys. J.* **851** (2017) L35, [arXiv:1711.05578].

[15] **Virgo, LIGO Scientific** Collaboration, B. P. Abbott et al., *GW170814: A three–detector observation of gravitational waves from a binary black hole coalescence*, *Phys. Rev. Lett.* **119** (2017) 141101, [arXiv:1709.09660].

[16] **Virgo, LIGO Scientific** Collaboration, B. P. Abbott et al., *GW170817: Observation of gravitational waves from a binary neutron star inspiral*, *Phys. Rev. Lett.* **119** (2017) 161101, [arXiv:1710.05832].

[17] A. Goldstein et al., *An ordinary short gamma–ray burst with extraordinary implications: Fermi–GBM detection of GRB 170817A*, *Astrophys. J.* **848** (2017) L14, [arXiv:1710.05446].

[18] **Virgo, Fermi–GBM, INTEGRAL, LIGO Scientific** Collaboration, B. P. Abbott et al., *Gravitational waves and gamma–rays from a binary neutron star merger: GW170817 and GRB 170817A*, *Astrophys. J.* **848** (2017) L13, [arXiv:1710.05834].

[19] G. Nordström, *Zur Theorie der Gravitation vom Standpunkt des Relativitätsprinzips*, *Annalen der Physik* **347** (1913) 533–554.

[20] P. Touboul et al., *MICROSCOPE mission: First results of a space test of the equivalence principle*, *Phys. Rev. Lett.* **119** (2017) 231101, [arXiv:1712.01176].

[21] A. A. Michelson and E. W. Morley, *On the relative motion of the Earth and of the luminiferous Ether*, *Sidereal Messenger* **6** (1887) 306–310.

[22] V. W. Hughes, H. G. Robinson, and V. Beltran-Lopez, *Upper limit for the anisotropy of inertial mass from nuclear resonance experiments*, *Phys. Rev. Lett.* **4** (1960) 342–344.

[23] R. W. P. Drever, *A search for anisotropy of inertial mass using a free precession technique*, *Phil. Mag.* **6** (1961) 683–687.

[24] S. K. Lamoreaux, J. P. Jacobs, B. R. Heckel, F. J. Raab, and E. N. Fortson, *New limits on spatial anisotropy from optically pumped He–201 and Hg–199*, *Phys. Rev. Lett.* **57** (1986) 3125–3128.

[25] R. F. C. Vessot et al., *Test of relativistic gravitation with a space–borne hydrogen maser*, *Phys. Rev. Lett.* **45** (1980) 2081–2084.

[26] A. Einstein, *Kosmologische Betrachtungen zur allgemeinen Relativitätstheorie*, *Sitzungsberichte der Königlich Preußischen Akademie der Wissenschaften* (1917) 142–152.

[27] W. de Sitter, *Einstein's theory of gravitation and its astronomical consequences. Third paper*, *Mon. Not. Roy. Astron. Soc.* **78** (1917) 3–28.

[28] A. Friedmann, *Über die Krümmung des Raumes*, *Zeitschrift für Physik* **10** (1922) 377–386.

[29] A. Einstein, *Bemerkung zu der Arbeit von A. Friedmann "Über die Krümmung des Raumes"*, *Zeitschrift für Physik* **11** (1922) 326.

[30] H. Nussbaumer, *Einstein's conversion from his static to an expanding Universe*, *Eur. Phys. J.* **H39** (2014) 37–62, [arXiv:1311.2763].

[31] A. G. Lemaître, *Un Univers homogène de masse constante et de rayon croissant rendant compte de la vitesse radiale des nébuleuses extra–galactiques*, *Annales de la Société Scientifique de Bruxelles* **47** (1927) 49–59.

[32] G. Stromberg, *Analysis of radial velocities of globular clusters and non–galactic nebulae*, *Astrophys. J.* **61** (1925).

[33] E. P. Hubble, *Extragalactic nebulae*, *Astrophys. J.* **64** (1926) 321–369.

[34] E. P. Hubble, *A relation between distance and radial velocity among extra–galactic nebulae*, *Proceedings of the National Academy of Sciences* **15** (1929) 168–173.

[35] A. S. Eddington, *On the instability of Einstein's spherical world*, *Mon. Not. Roy. Astron. Soc.* **90** (1930) 668–678.

[36] A. Einstein, *Zum kosmologischen Problem der allgemeinen Relativitätstheorie*, *Sitzungsberichte der Königlich Preußischen Akademie der Wissenschaften* (1931) 235–237.

[37] A. Einstein and W. de Sitter, *On the relation between the expansion and the mean density of the Universe*, *Proc. Nat. Acad. Sci.* **18** (1932) 213–214.

[38] A. G. Lemaître, *Contributions to a British association discussion on the evolution of the Universe*, *Nature* **128** (1931) 704–706.

[39] G. Gamow, *Nuclear transformations and the origin of the chemical elements*, *Ohio J. Sci.* **35** (1935) 406–413.

[40] G. Gamow, *Expanding Universe and the origin of elements*, *Phys. Rev.* **70** (1946) 572–573.

[41] G. Gamow, *Concerning the origin of chemical elements*, *Journal of the Washington Academy of Sciences* **32** (1942) 353–355.

[42] G. Gamow, *The origin of elements and the separation of galaxies*, *Phys. Rev.* **74** (1948) 505–506.

[43] G. Gamow, *The evolution of the Universe*, *Nature* **162** (1948) 680.

[44] R. A. Alpher, R. C. Herman, and G. A. Gamow, *Thermonuclear reactions in the expanding Universe*, *Phys. Rev.* **74** (1948) 1198–1199.

[45] R. A. Alpher and R. C. Herman, *On the relative abundance of the elements*, *Phys. Rev.* **74** (1948) 1737–1742.

[46] R. A. Alpher and R. C. Herman, *Theory of the origin and relative abundance distribution of the elements*, *Rev. Mod. Phys.* **22** (1950) 153–212.

[47] R. A. Alpher, H. Bethe, and G. Gamow, *The origin of chemical elements*, *Phys. Rev.* **73** (1948) 803–804.

[48] R. A. Alpher and R. C. Herman, *Neutron–capture theory of element formation in an expanding Universe*, *Phys. Rev.* **84** (1951) 60–68.

[49] R. A. Alpher and R. C. Herman, *Big Bang cosmology and the cosmic black–body radiation*, *Proceedings of the American Philosophical Society* **119** (1975) 325–348.

[50] R. A. Alpher, J. W. Follin, and R. C. Herman, *Physical conditions in the initial stages of the expanding Universe*, *Phys. Rev.* **92** (1953) 1347–1361.

[51] R. A. Alpher and R. C. Herman, *Evolution of the Universe*, *Nature* **162** (1948) 774.

[52] R. A. Alpher and R. C. Herman, *Remarks on the evolution of the expanding Universe*, *Phys. Rev.* **75** (1949) 1089–1095.

[53] A. A. Penzias and R. W. Wilson, *A measurement of excess antenna temperature at 4080* Mc/s, *Astrophys. J.* **142** (1965) 419–421.

[54] A. A. Penzias, *Measurement of cosmic microwave background radiation*, *IEEE Transactions on Microwave Theory and Techniques* **16** (1968) 608–611.

[55] R. H. Dicke, P. J. E. Peebles, P. G. Roll, and D. T. Wilkinson, *Cosmic black body radiation*, *Astrophys. J.* **142** (1965) 414–419.

[56] H. Bondi and T. Gold, *The steady–state theory of the expanding Universe*, *Mon. Not. Roy. Astron. Soc.* **108** (1948) 252.

[57] F. Hoyle, *A new model for the expanding Universe*, *Mon. Not. Roy. Astron. Soc.* **108** (1948) 372.

[58] J. C. Mather et al., *Measurement of the cosmic microwave background spectrum by the COBE FIRAS instrument*, *Astrophys. J.* **420** (1994) 439–444.

[59] D. J. Fixsen, E. S. Cheng, J. M. Gales, J. C. Mather, R. A. Shafer, and E. L. Wright, *The cosmic microwave background spectrum from the full COBE FIRAS data set*, *Astrophys. J.* **473** (1996) 576, [astro-ph/9605054].

[60] P. Molaro, S. A. Levshakov, M. Dessauges-Zavadsky, and S. D'Odorico, *The cosmic microwave background radiation temperature at $z = 3.025$ toward QSO 0347–3819*, *Astron. Astrophys.* **381** (2002) L64, [astro-ph/0111589].

[61] P. Noterdaeme, P. Petitjean, R. Srianand, C. Ledoux, and S. Lopez, *The evolution of the cosmic microwave background temperature: Measurements of $T_{\rm CMB}$ at high redshift from carbon monoxide excitation*, *Astron. Astrophys.* **526** (2011) L7, [arXiv:1012.3164].

[62] R. Srianand, P. Petitjean, and C. Ledoux, *The microwave background temperature at the redshift of 2.33771*, *Nature* **408** (2000) 931, [astro-ph/0012222].

[63] A. P. Serebrov et al., *Neutron lifetime measurements with the big gravitational trap for ultracold neutrons*, *Phys. Rev.* **C97** (2018) 055503, [arXiv:1712.05663].

[64] **SLD Electroweak Group, DELPHI, ALEPH, SLD, SLD Heavy Flavour Group, OPAL, LEP Electroweak Working Group, L3** Collaboration, S. Schael et al., *Precision electroweak measurements on the Z resonance*, *Phys. Rept.* **427** (2006) 257–454, [hep-ex/0509008].

[65] **Planck** Collaboration, P. A. R. Ade et al., *Planck 2015 results. XIII. Cosmological parameters*, *Astron. Astrophys.* **594** (2016) A13, [arXiv:1502.01589].

[66] C. Marinoni, J. Bel, and A. Buzzi, *The scale of cosmic isotropy*, *JCAP* **1210** (2012) 036, [arXiv:1205.3309].

[67] C. Blake and J. Wall, *A velocity dipole in the distribution of radio galaxies*, *Nature* **416** (2002) 150–152, [astro-ph/0203385].

[68] G. A. Marques, C. P. Novaes, A. Bernui, and I. S. Ferreira, *Isotropy analyses of the Planck convergence map*, *Mon. Not. Roy. Astron. Soc.* **473** (2018) 165–172, [arXiv:1708.09793].

[69] D. W. Hogg, D. J. Eisenstein, M. R. Blanton, N. A. Bahcall, J. Brinkmann, J. E. Gunn, and D. P. Schneider, *Cosmic homogeneity demonstrated with luminous red galaxies*, *Astrophys. J.* **624** (2005) 54–58, [astro-ph/0411197].

[70] B. Pandey and S. Sarkar, *Testing homogeneity in the Sloan Digital Sky Survey data release twelve with Shannon entropy*, *Mon. Not. Roy. Astron. Soc.* **454** (2015) 2647–2656, [arXiv:1507.03124].

[71] A. G. Lemaître, *The expanding Universe*, *Gen. Rel. Grav.* **29** (1997) 641–680. [Annales Soc. Sci. Bruxelles **A53** (1933) 51].

[72] R. C. Tolman, *Effect of inhomogeneity on cosmological models*, *Proc. Nat. Acad. Sci.* **20** (1934) 169–176. [Gen. Rel. Grav. **29** (1997) 935].

[73] H. Bondi, *Spherically symmetrical models in General Relativity*, *Mon. Not. Roy. Astron. Soc.* **107** (1947) 410–425.

[74] S. Nadathur and S. Sarkar, *Reconciling the local void with the CMB*, *Phys. Rev.* **D83** (2011) 063506, [arXiv:1012.3460].

[75] R. R. Caldwell and A. Stebbins, *A test of the Copernican principle*, *Phys. Rev. Lett.* **100** (2008) 191302, [arXiv:0711.3459].

[76] H. P. Robertson, *On the foundations of relativistic cosmology*, *Proceedings of the National Academy of Sciences* **15** (1929) 822–829.

[77] A. G. Walker, *On Milne's theory of world–structure*, *Proc. London Math. Soc.* **s2–42** (1936) 90–127.

[78] A. G. Riess et al., *A 2.4% determination of the local value of the Hubble constant*, *Astrophys. J.* **826** (2016) 56, [arXiv:1604.01424].

[79] A. G. Riess et al., *Milky Way Cepheid standards for measuring cosmic distances and application to Gaia DR2: Implications for the Hubble constant*, arXiv:1804.10655.

[80] H. P. Robertson, *The theoretical aspects of the nebular redshift*, *Publications of the Astronomical Society of the Pacific* **67** (1955) 82.

[81] M. L. Humason, N. U. Mayall, and A. R. Sandage, *Redshifts and magnitudes of extragalactic nebulae*, *Astron. J.* **61** (1956) 97–162.

[82] A. R. Sandage, *The ability of the 200–inch telescope to discriminate between selected world models*, *Astrophys. J.* **133** (1961) 355.

[83] A. R. Sandage, *Cosmology: A search for two numbers*, *Physics Today* **23** (1970) 34–41.

[84] A. Friedmann, *Über die Möglichkeit einer Welt mit konstanter negativer Krümmung des Raumes*, *Zeitschrift für Physik* **21** (1924) 326–332.

[85] M. M. Phillips, *The absolute magnitudes of Type IA supernovae*, *Astrophys. J.* **413** (1993) L105–L108.

[86] S. Chandrasekhar, *The maximum mass of ideal white dwarfs*, *Astrophys. J.* **74** (1931) 81.

[87] **Supernova Search Team** Collaboration, A. G. Riess et al., *Observational evidence from supernovae for an accelerating Universe and a cosmological constant*, *Astron. J.* **116** (1998) 1009–1038, [astro-ph/9805201].

[88] **Supernova Cosmology Project** Collaboration, S. Perlmutter et al., *Measurements of Ω and Λ from 42 high–redshift supernovae*, *Astrophys. J.* **517** (1999) 565–586, [astro-ph/9812133].

[89] **Planck** Collaboration, "Planck Legacy Archive." http://pla.esac.esa.int/pla/#home, 2018. [Online; accessed 22–06–2018].

[90] A. Lewis and S. Bridle, *Cosmological parameters from CMB and other data: A Monte Carlo approach*, *Phys. Rev.* **D66** (2002) 103511, [astro-ph/0205436].

[91] **Planck** Collaboration, P. A. R. Ade et al., *Planck 2015 results. XV. Gravitational lensing*, *Astron. Astrophys.* **594** (2016) A15, [arXiv:1502.01591].

[92] F. Beutler, C. Blake, M. Colless, D. H. Jones, L. Staveley-Smith, L. Campbell, Q. Parker, W. Saunders, and F. Watson, *The 6dF galaxy survey: Baryon acoustic oscillations and the local Hubble constant*, *Mon. Not. Roy. Astron. Soc.* **416** (2011) 3017–3032, [arXiv:1106.3366].

[93] A. J. Ross, L. Samushia, C. Howlett, W. J. Percival, A. Burden, and M. Manera, *The clustering of the SDSS DR7 main galaxy sample – I. A 4 percent distance measure at $z = 0.15$*, *Mon. Not. Roy. Astron. Soc.* **449** (2015) 835–847, [arXiv:1409.3242].

[94] **BOSS** Collaboration, L. Anderson et al., *The clustering of galaxies in the SDSS–III Baryon Oscillation Spectroscopic Survey: Baryon acoustic oscillations in the data releases 10 and 11 galaxy samples*, *Mon. Not. Roy. Astron. Soc.* **441** (2014) 24–62, [arXiv:1312.4877].

[95] **SDSS** Collaboration, M. Betoule et al., *Improved cosmological constraints from a joint analysis of the SDSS–II and SNLS supernova samples*, *Astron. Astrophys.* **568** (2014) A22, [arXiv:1401.4064].

[96] G. Efstathiou, *H_0 revisited*, *Mon. Not. Roy. Astron. Soc.* **440** (2014) 1138–1152, [arXiv:1311.3461].

[97] **Planck** Collaboration, P. A. R. Ade et al., *Planck 2013 results. I. Overview of products and scientific results*, *Astron. Astrophys.* **571** (2014) A1, [arXiv:1303.5062].

[98] **Planck** Collaboration, R. Adam et al., *Planck 2015 results. I. Overview of products and scientific results*, *Astron. Astrophys.* **594** (2016) A1, [arXiv:1502.01582].

[99] **Planck** Collaboration, P. A. R. Ade et al., *Planck 2013 results. XVI. Cosmological parameters*, *Astron. Astrophys.* **571** (2014) A16, [arXiv:1303.5076].

[100] M. Fukugita and P. J. E. Peebles, *The cosmic energy inventory*, *Astrophys. J.* **616** (2004) 643–668, [astro-ph/0406095].

[101] R. Cooke, M. Pettini, R. A. Jorgenson, M. T. Murphy, and C. C. Steidel, *Precision measures of the primordial abundance of deuterium*, *Astrophys. J.* **781** (2014) 31, [arXiv:1308.3240].

[102] R. J. Cooke, M. Pettini, K. M. Nollett, and R. Jorgenson, *The primordial deuterium abundance of the most metal–poor damped Lyman–α system*, *Astrophys. J.* **830** (2016) 148, [arXiv:1607.03900].

[103] R. J. Cooke, M. Pettini, and C. C. Steidel, *One percent determination of the primordial deuterium abundance*, *Astrophys. J.* **855** (2018) 102, [arXiv:1710.11129].

[104] E. O. Zavarygin, J. K. Webb, V. Dumont, and S. Riemer-Sørensen, *The primordial deuterium abundance at $z_{\rm abs} = 2.504$ from a high signal–to–noise spectrum of Q1009+2956*, *Mon. Not. Roy. Astron. Soc.* **477** (2018) 5536–5553, [arXiv:1706.09512].

[105] D. J. Fixsen, *The temperature of the cosmic microwave background*, *Astrophys. J.* **707** (2009) 916–920, [arXiv:0911.1955].

[106] G. Mangano, G. Miele, S. Pastor, and M. Peloso, *A Precision calculation of the effective number of cosmological neutrinos*, *Phys. Lett.* **B534** (2002) 8–16, [astro-ph/0111408].

[107] G. Mangano, G. Miele, S. Pastor, T. Pinto, O. Pisanti, and P. D. Serpico, *Relic neutrino decoupling including flavor oscillations*, *Nucl. Phys.* **B729** (2005) 221–234, [hep-ph/0506164].

[108] G. Steigman, D. N. Schramm, and J. E. Gunn, *Cosmological limits to the number of massive leptons*, *Phys. Lett.* **B66** (1977) 202–204.

[109] S. Sarkar, *Big Bang nucleosynthesis and physics beyond the standard model*, *Rept. Prog. Phys.* **59** (1996) 1493–1610, [hep-ph/9602260].

[110] O. Pisanti, A. Cirillo, S. Esposito, F. Iocco, G. Mangano, G. Miele, and P. D. Serpico, *PArthENoPE: Public algorithm evaluating the nucleosynthesis of primordial elements*, *Comput. Phys. Commun.* **178** (2008) 956–971, [arXiv:0705.0290].

[111] E. Lifshitz, *Republication of: On the gravitational stability of the expanding Universe*, *J. Phys.(USSR)* **10** (1946) 116.

[112] P. J. E. Peebles and J. T. Yu, *Primeval adiabatic perturbation in an expanding Universe*, *Astrophys. J.* **162** (1970) 815.

[113] J. R. Bond and G. Efstathiou, *Cosmic background radiation anisotropies in Universes dominated by nonbaryonic dark matter*, *Astrophys. J.* **285** (1984) L45–L48.

[114] J. R. Bond and G. Efstathiou, *The statistics of cosmic background radiation fluctuations*, *Mon. Not. Roy. Astron. Soc.* **226** (1987) 655–687.

[115] C.-P. Ma and E. Bertschinger, *Cosmological perturbation theory in the synchronous and conformal Newtonian gauges*, *Astrophys. J.* **455** (1995) 7–25, [astro-ph/9506072].

[116] N. Vittorio and J. Silk, *Fine–scale anisotropy of the cosmic microwave background in a Universe dominated by cold dark matter*, *Astrophys. J.* **285** (1984) L39–L43.

[117] N. Sugiyama, *Cosmic background anistropies in CDM cosmology*, *Astrophys. J. Suppl.* **100** (1995) 281, [astro-ph/9412025].

[118] U. Seljak and M. Zaldarriaga, *A line of sight integration approach to cosmic microwave background anisotropies*, *Astrophys. J.* **469** (1996) 437–444, [astro-ph/9603033].

[119] M. Doran, *CMBEASY: An object oriented code for the cosmic microwave background*, *JCAP* **0510** (2005) 011, [astro-ph/0302138].

[120] D. Blas, J. Lesgourgues, and T. Tram, *The Cosmic Linear Anisotropy Solving System (CLASS) II: Approximation schemes*, *JCAP* **1107** (2011) 034, [arXiv:1104.2933].

[121] G. F. Smoot, M. V. Gorenstein, and R. A. Muller, *Detection of anisotropy in the cosmic black body radiation*, *Phys. Rev. Lett.* **39** (1977) 898.

[122] G. F. Smoot et al., *Structure in the COBE differential microwave radiometer first–year maps*, *Astrophys. J.* **396** (1992) L1–L5.

[123] **WMAP** Collaboration, C. L. Bennett et al., *First year Wilkinson Microwave Anisotropy Probe (WMAP) observations: Preliminary maps and basic results*, *Astrophys. J. Suppl.* **148** (2003) 1–27, [astro-ph/0302207].

[124] **WMAP** Collaboration, D. N. Spergel et al., *First–year Wilkinson Microwave Anisotropy Probe (WMAP) observations: Determination of cosmological parameters*, *Astrophys. J. Suppl.* **148** (2003) 175–194, [astro-ph/0302209].

[125] **Planck** Collaboration, J. Tauber, M. Bersanelli, J. M. Lamarre, G. Efstathiou, C. Lawrence, F. Bouchet, E. Martinez-Gonzalez, S. Matarrese, D. Scott, M. White, et al., *The scientific programme of Planck*, astro-ph/0604069.

[126] A. Lewis, *Cosmological parameters from WMAP 5–year temperature maps*, *Phys. Rev.* **D78** (2008) 023002, [arXiv:0804.3865].

[127] C. Blake and K. Glazebrook, *Probing dark energy using baryonic oscillations in the galaxy power spectrum as a cosmological ruler*, *Astrophys. J.* **594** (2003) 665–673, [astro-ph/0301632].

[128] J. A. Holtzman, *Microwave background anisotropies and large–scale structure in Universes with cold dark matter, baryons, radiation, and massive and massless neutrinos*, *Astrophys. J.* **71** (1989) 1–24.

[129] D. J. Eisenstein, W. Hu, and M. Tegmark, *Cosmic complementarity: H_0 and Ω_m from combining CMB experiments and redshift surveys*, *Astrophys. J.* **504** (1998) L57–L61, [astro-ph/9805239].

[130] D. J. Eisenstein, W. Hu, and M. Tegmark, *Cosmic complementarity: Joint parameter estimation from CMB experiments and redshift surveys*, *Astrophys. J.* **518** (1999) 2–23, [astro-ph/9807130].

[131] G. F. R. Ellis, *Relativistic cosmology*, *Gen. Rel. Grav.* **41** (2009) 581–660.

[132] R. A. Alpher, *A neutron–capture theory of the formation and relative abundance of the elements*, *Phys. Rev.* **74** (1948) 1577–1589.

[133] F. Hoyle, *The Nature of the Universe*. Harper, New York, 1950.

[134] R. Weymann, *The energy spectrum of radiation in the expanding Universe*, *Astrophys. J.* **145** (1966) 560.

[135] Y. B. Zel'dovich and R. A. Sunyaev, *The interaction of matter and radiation in a hot–model Universe*, *Astrophys. Space Sci.* **4** (1969) 301–316.

[136] R. A. Sunyaev and Y. B. Zel'dovich, *The interaction of matter and radiation in the hot–model of the Universe*, *Astrophys. Space Sci.* **7** (1970) 20–30.

[137] R. A. Daly, *Spectral distortions of the microwave background radiation resulting from the damping of pressure waves*, *Astrophys. J.* **371** (1991) 14–28.

[138] J. D. Barrow and P. Coles, *Primordial density fluctuations and the microwave background spectrum*, *Mon. Not. Roy. Astron. Soc.* **248** (1991) 52–57.

[139] R. Khatri and R. A. Sunyaev, *Beyond y and μ: The shape of the CMB spectral distortions in the intermediate epoch,* $1.5 \times 10^4 < z < 2 \times 10^5$, *JCAP* **1209** (2012) 016, [arXiv:1207.6654].

[140] H. P. Nordberg and G. F. Smoot, *The cosmic microwave background spectrum: An analysis of observations*, astro-ph/9805123.

[141] W. Hu and J. Silk, *Thermalization constraints and spectral distortions for massive unstable relic particles*, *Phys. Rev. Lett.* **70** (1993) 2661–2664.

[142] X.-L. Chen and M. Kamionkowski, *Particle decays during the cosmic dark ages*, *Phys. Rev.* **D70** (2004) 043502, [astro-ph/0310473].

[143] N. Padmanabhan and D. P. Finkbeiner, *Detecting dark matter annihilation with CMB polarization: Signatures and experimental prospects*, *Phys. Rev.* **D72** (2005) 023508, [astro-ph/0503486].

[144] J. Chluba, *Could the cosmological recombination spectrum help us understand annihilating dark matter?*, *Mon. Not. Roy. Astron. Soc.* **402** (2010) 1195, [arXiv:0910.3663].

[145] J. Silk, *Cosmic black body radiation and galaxy formation*, *Astrophys. J.* **151** (1968) 459–471.

[146] M. Seiffert et al., *Interpretation of the ARCADE 2 absolute sky brightness measurement*, *Astrophys. J.* **734** (2011) 6.

[147] M. Gervasi, M. Zannoni, A. Tartari, G. Boella, and G. Sironi, *TRIS II: Search for CMB spectral distortions at 0.60, 0.82 and 2.5 GHz*, *Astrophys. J.* **688** (2008) 24, [arXiv:0807.4750].

[148] A. Kogut et al., *The Primordial Inflation Explorer (PIXIE): A nulling polarimeter for cosmic microwave background observations*, *JCAP* **1107** (2011) 025, [arXiv:1105.2044].

[149] J. Chluba and R. A. Sunyaev, *The evolution of CMB spectral distortions in the early Universe*, *Mon. Not. Roy. Astron. Soc.* **419** (2012) 1294–1314, [arXiv:1109.6552].

[150] R. Khatri and R. A. Sunyaev, *Creation of the CMB spectrum: Precise analytic solutions for the blackbody photosphere*, *JCAP* **1206** (2012) 038, [arXiv:1203.2601].

[151] J. Chluba, R. Khatri, and R. A. Sunyaev, *CMB at 2×2 order: The dissipation of primordial acoustic waves and the observable part of the associated energy release*, *Mon. Not. Roy. Astron. Soc.* **425** (2012) 1129–1169, [arXiv:1202.0057].

[152] R. Khatri, R. A. Sunyaev, and J. Chluba, *Mixing of blackbodies: Entropy production and dissipation of sound waves in the early Universe*, *Astron. Astrophys.* **543** (2012) A136, [arXiv:1205.2871].

[153] R. Khatri and R. A. Sunyaev, *Forecasts for CMB μ and i–type spectral distortion constraints on the primordial power spectrum on scales $8 \lesssim k \lesssim 10^4\,\mathrm{Mpc}^{-1}$ with the future Pixie–like experiments*, *JCAP* **1306** (2013) 026, [arXiv:1303.7212].

[154] A. Kosowsky and M. S. Turner, *CBR anisotropy and the running of the scalar spectral index*, *Phys. Rev.* **D52** (1995) R1739–R1743, [astro-ph/9504071].

[155] P. J. E. Peebles and J. T. Yu, *Primeval adiabatic perturbation in an expanding Universe*, *Astrophys. J.* **162** (1970) 815–836.

[156] N. Kaiser, *Small–angle anisotropy of the microwave background radiation in the adiabatic theory*, *Mon. Not. Roy. Astron. Soc.* **202** (1983) 1169–1180.

[157] M. Zaldarriaga and D. D. Harari, *Analytic approach to the polarization of the cosmic microwave background in flat and open Universes*, *Phys. Rev.* **D52** (1995) 3276–3287, [astro-ph/9504085].

[158] P. J. E. Peebles, *Recombination of the primeval plasma*, *Astrophys. J.* **153** (1968) 1.

[159] Y. B. Zel'dovich, V. G. Kurt, and R. A. Sunyaev, *Recombination of hydrogen in the hot–model of the Universe*, *Soviet Journal of Experimental and Theoretical Physics* **28** (1969) 146.

[160] J. Chluba, *Which spectral distortions does ΛCDM actually predict?*, *Mon. Not. Roy. Astron. Soc.* **460** (2016) 227–239, [arXiv:1603.02496].

[161] R. C. Tolman, *On the theoretical requirements for a periodic behaviour of the Universe*, *Phys. Rev.* **38** (1931) 1758–1771.

[162] J. Chluba and D. Jeong, *Teasing bits of information out of the CMB energy spectrum*, *Mon. Not. Roy. Astron. Soc.* **438** (2014) 2065–2082, [arXiv:1306.5751].

[163] L. Danese and G. de Zotti, *Double Compton process and the spectrum of the microwave background*, *Astron. Astrophys.* **107** (1982) 39–42.

[164] C. Burigana, L. Danese, and G. de Zotti, *Formation and evolution of early distortions of the microwave background spectrum – a numerical study*, *Astron. Astrophys.* **246** (1991) 49–58.

[165] W. Hu and J. Silk, *Thermalization and spectral distortions of the cosmic background radiation*, *Phys. Rev.* **D48** (1993) 485–502.

[166] W. Hu, D. Scott, and J. Silk, *Power spectrum constraints from spectral distortions in the cosmic microwave background*, *Astrophys. J.* **430** (1994) L5–L8, [astro-ph/9402045].

[167] Y. B. Zel'dovich and E. V. Levich, *Stationary state of electrons in a non–equilibrium radiation field*, *Soviet Journal of Experimental and Theoretical Physics Letters* **11** (1970) 35–38.

[168] E. V. Levich and R. A. Sunyaev, *Heating of gas near quasars, Seyfert–Galaxy nuclei, and pulsars by low–frequency radiation*, *Soviet Ast.* **15** (1971) 363.

[169] N. Itoh, T. Sakamoto, S. Kusano, S. Nozawa, and Y. Kohyama, *Relativistic thermal bremsstrahlung gaunt factor for the intracluster plasma. II. Analytic fitting formulae*, *Astrophys. J. Suppl.* **128** (2000) 125–138, [astro-ph/9906342].

[170] E. Pajer and M. Zaldarriaga, *A new window on primordial non–Gaussianity*, *Phys. Rev. Lett.* **109** (2012) 021302, [arXiv:1201.5375].

[171] R. Emami, E. Dimastrogiovanni, J. Chluba, and M. Kamionkowski, *Probing the scale dependence of non–Gaussianity with spectral distortions of the cosmic microwave background*, *Phys. Rev.* **D91** (2015) 123531, [arXiv:1504.00675].

[172] J. Chluba, A. L. Erickcek, and I. Ben-Dayan, *Probing the inflaton: Small–scale power spectrum constraints from measurements of the CMB energy spectrum*, *Astrophys. J.* **758** (2012) 76, [arXiv:1203.2681].

[173] F. Zwicky, *Die Rotverschiebung von extragalaktischen Nebeln*, *Helvetica Physica Acta* **6** (1933) 110–127.

[174] F. Zwicky, *On the masses of nebulae and of clusters of nebulae*, *Astrophys. J.* **86** (1937) 217.

[175] S. Smith, *The mass of the Virgo cluster*, *Astrophys. J.* **83** (1936) 23.

[176] B. Lindblad, *On the state of motion in the galactic system*, *Mon. Not. Roy. Astron. Soc.* **87** (1927) 553–564.

[177] H. W. Babcock, *The rotation of the Andromeda nebula*, *Lick Observatory Bulletin* **19** (1939) 41–51.

[178] N. U. Mayall and L. H. Aller, *The rotation of the spiral nebula Messier 33*, *Astrophys. J.* **95** (1942) 5.

[179] J. H. Oort, *Observational evidence confirming Lindblad's hypothesis of a rotation of the galactic system*, *Bull. Astron. Inst. the Netherlands* **3** (1927) 275–282.

[180] K. C. Freeman, *On the disks of spiral and S0 galaxies*, *Astrophys. J.* **160** (1970) 811.

[181] J. P. Ostriker, P. J. E. Peebles, and A. Yahil, *The size and mass of galaxies, and the mass of the Universe*, *Astrophys. J.* **193** (1974) L1–L4.

[182] J. Einasto, A. Kaasik, and E. Saar, *Dynamic evidence on massive coronas of galaxies*, *Nature* **250** (1974) 309.

[183] S. M. Faber and J. S. Gallagher, *Masses and mass–to–light ratios of galaxies*, *Annual review of astronomy and astrophysics* **17** (1979) 135–187.

[184] **2dFGRS** Collaboration, W. J. Percival et al., *The 2dF galaxy redshift survey: The power spectrum and the matter content of the Universe*, *Mon. Not. Roy. Astron. Soc.* **327** (2001) 1297, [astro-ph/0105252].

[185] J. A. Tyson, G. P. Kochanski, and I. P. Dell'Antonio, *Detailed mass map of CL0024+1654 from strong lensing*, *Astrophys. J.* **498** (1998) L107, [astro-ph/9801193].

[186] S. Cole, S. Hatton, D. H. Weinberg, and C. S. Frenk, *Mock 2dF and SDSS galaxy redshift surveys*, *Mon. Not. Roy. Astron. Soc.* **300** (1998) 945–966, [astro-ph/9801250].

[187] M. Battaglieri et al., *US cosmic visions: New ideas in dark matter 2017: Community report*, arXiv:1707.04591.

[188] G. Bertone, D. Hooper, and J. Silk, *Particle dark matter: Evidence, candidates and constraints*, *Phys. Rept.* **405** (2005) 279–390, [hep-ph/0404175].

[189] P. J. E. Peebles, *Large–scale background temperature and mass fluctuations due to scale–invariant primeval perturbations*, *Astrophys. J.* **263** (1982) L1–L5.

[190] G. Steigman and M. S. Turner, *Cosmological constraints on the properties of weakly interacting massive particles*, *Nucl. Phys.* **B253** (1985) 375–386.

[191] G. Jungman, M. Kamionkowski, and K. Griest, *Supersymmetric dark matter*, *Phys. Rept.* **267** (1996) 195–373.

[192] B. W. Lee and S. Weinberg, *Cosmological lower bound on heavy–neutrino masses*, *Phys. Rev. Lett.* **39** (1977) 165–168.

[193] **XENON100** Collaboration, E. Aprile et al., *Dark matter results from 225 live days of XENON100 data*, *Phys. Rev. Lett.* **109** (2012) 181301.

[194] **XENON** Collaboration, E. Aprile et al., *Search for WIMP inelastic scattering off Xenon nuclei with XENON100*, *Phys. Rev.* **D96** (2017) 022008, [arXiv:1705.05830].

[195] **CDMS** Collaboration, R. Agnese et al., *Silicon detector dark matter results from the final exposure of CDMS II*, *Phys. Rev. Lett.* **111** (2013) 251301, [arXiv:1304.4279].

[196] S. J. Witte and G. B. Gelmini, *Updated constraints on the dark matter interpretation of CDMS–II–Si Data*, *JCAP* **1705** (2017) 026, [arXiv:1703.06892].

[197] **SuperCDMS** Collaboration, R. Agnese et al., *Results from the Super Cryogenic Dark Matter Search experiment at Soudan*, *Phys. Rev. Lett.* **120** (2018) 061802, [arXiv:1708.08869].

[198] **LUX** Collaboration, D. S. Akerib et al., *Results from a search for dark matter in the complete LUX exposure*, *Phys. Rev. Lett.* **118** (2017) 021303, [arXiv:1608.07648].

[199] **CDEX** Collaboration, L. T. Yang et al., *Limits on light WIMPs with a 1* kg*–scale germanium detector at 160 eVee physics threshold at the China Jinping underground laboratory*, *Chin. Phys.* **C42** (2018) 023002, [arXiv:1710.06650].

[200] **LZ** Collaboration, D. S. Akerib et al., *LUX–ZEPLIN (LZ) conceptual design report*, arXiv:1509.02910.

[201] **DARWIN** Collaboration, J. Aalbers et al., *DARWIN: Towards the ultimate dark matter detector*, *JCAP* **1611** (2016) 017, [arXiv:1606.07001].

[202] **XENON** Collaboration, E. Aprile et al., *Physics reach of the XENON1T dark matter experiment*, *JCAP* **1604** (2016) 027, [arXiv:1512.07501].

[203] R. D. Peccei and H. R. Quinn, CP *conservation in the presence of pseudoparticles*, *Phys. Rev. Lett.* **38** (1977) 1440–1443.

[204] R. D. Peccei and H. R. Quinn, *Constraints imposed by* CP *conservation in the presence of pseudoparticles*, *Phys. Rev.* **D16** (1977) 1791–1797.

[205] S. Weinberg, *A new light boson?*, *Phys. Rev. Lett.* **40** (1978) 223–226.

[206] P. W. Graham, I. G. Irastorza, S. K. Lamoreaux, A. Lindner, and K. A. van Bibber, *Experimental searches for the axion and axion–like particles*, *Ann. Rev. Nucl. Part. Sci.* **65** (2015) 485–514, [arXiv:1602.00039].

[207] C. Abel et al., *Search for axionlike dark matter through nuclear spin precession in electric and magnetic fields*, *Phys. Rev.* **X7** (2017) 041034, [arXiv:1708.06367].

[208] J. Lesgourgues and S. Pastor, *Neutrino mass from cosmology*, *Adv. High Energy Phys.* **2012** (2012) 608515, [arXiv:1212.6154].

[209] J. R. Bond and A. S. Szalay, *The collisionless damping of density fluctuations in an expanding Universe*, *Astrophys. J.* **274** (1983) 443–468.

[210] M. Davis, G. Efstathiou, C. S. Frenk, and S. D. M. White, *The evolution of large–scale structure in a Universe dominated by cold dark matter*, *Astrophys. J.* **292** (1985) 371–394.

[211] J. R. Bond and G. Efstathiou, *Cosmic background radiation anisotropies in Universes dominated by nonbaryonic dark matter*, *Astrophys. J.* **285** (1984) L45–L48.

[212] J. R. Bond, L. Kofman, and D. Pogosyan, *How filaments are woven into the cosmic web*, *Nature* **380** (1996) 603–606, [astro-ph/9512141].

[213] J. P. Ostriker and P. J. Steinhardt, *New light on dark matter*, *Science* **300** (2003) 1909–1913, [astro-ph/0306402].

[214] E. Gawiser and J. Silk, *Extracting primordial density fluctuations*, *Science* **280** (1998) 1405, [astro-ph/9806197].

[215] S. Colombi, S. Dodelson, and L. M. Widrow, *Large–scale structure tests of warm dark matter*, *Astrophys. J.* **458** (1996) 1.

[216] R. Cen, *Decaying cold dark matter model and small–scale power*, *Astrophys. J.* **546** (2001) L77–L80, [astro-ph/0005206].

[217] J. Goodman, *Repulsive dark matter*, *New Astron.* **5** (2000) 103, [astro-ph/0003018].

[218] K. M. Belotsky, A. D. Dmitriev, E. A. Esipova, V. A. Gani, A. V. Grobov, M. Yu. Khlopov, A. A. Kirillov, S. G. Rubin, and I. V. Svadkovsky, *Signatures of primordial black hole dark matter*, *Mod. Phys. Lett.* **A29** (2014) 1440005, [arXiv:1410.0203].

[219] G. F. Chapline, *Cosmological effects of primordial black holes*, *Nature* **253** (1975) 251.

[220] Y. B. Zel'dovich and I. D. Novikov, *The hypothesis of cores retarded during expansion and the hot cosmological model*, *Soviet Ast.* **10** (1967) 602.

[221] B. J. Carr and S. W. Hawking, *Black holes in the early Universe*, *Mon. Not. Roy. Astron. Soc.* **168** (1974) 399–416.

[222] S. W. Hawking, *Black hole explosions?*, *Nature* **248** (1974) 30–31.

[223] S. W. Hawking, *Gravitationally collapsed objects of very low mass*, *Mon. Not. Roy. Astron. Soc.* **152** (1971) 75.

[224] J. Weber, *Detection and generation of gravitational waves*, *Phys. Rev.* **117** (1960) 306–313.

[225] J. H. Taylor and J. M. Weisberg, *A new test of General Relativity – Gravitational radiation and the binary pulsar PSR 1913+16*, *Astrophys. J.* **253** (1982) 908–920.

[226] R. A. Hulse and J. H. Taylor, *Discovery of a pulsar in a binary system*, *Astrophys. J.* **195** (1975) L51–L53.

[227] K. Belczynski, T. Bulik, C. L. Fryer, A. Ruiter, F. Valsecchi, J. S. Vink, and J. R. Hurley, *On the maximum mass of stellar black holes*, *Astrophys. J.* **714** (2010) 1217–1226, [arXiv:0904.2784].

[228] A. H. Prestwich, R. Kilgard, P. A. Crowther, S. Carpano, A. M. T. Pollock, A. Zezas, S. H. Saar, T. P. Roberts, and M. J. Ward, *The orbital period of the Wolf–Rayet binary IC 10 X–1: Dynamic evidence that the compact object is a black hole*, *Astrophys. J.* **669** (2007) L21–L24, [arXiv:0709.2892].

[229] J. M. Silverman and A. V. Filippenko, *On IC 10 X–1, the most massive known stellar–mass black hole*, *Astrophys. J.* **678** (2008) L17–L20, [arXiv:0802.2716].

[230] **Virgo, LIGO Scientific** Collaboration, B. P. Abbott et al., *Astrophysical implications of the binary black–hole merger GW150914*, *Astrophys. J.* **818** (2016) L22, [arXiv:1602.03846].

[231] S. Bird, I. Cholis, J. B. Muñoz, Y. Ali-Haïmoud, M. Kamionkowski, E. D. Kovetz, A. Raccanelli, and A. G. Riess, *Did LIGO detect dark matter?*, *Phys. Rev. Lett.* **116** (2016) 201301, [arXiv:1603.00464].

[232] B. J. Carr, J. H. Gilbert, and J. E. Lidsey, *Black hole relics and inflation: Limits on blue perturbation spectra*, *Phys. Rev.* **D50** (1994) 4853–4867, [astro-ph/9405027].

[233] Y. Sendouda, S. Nagataki, and K. Sato, *Mass spectrum of primordial black holes from inflationary perturbation in the Randall–Sundrum braneworld: A limit on blue spectra*, *JCAP* **0606** (2006) 003, [astro-ph/0603509].

[234] B. J. Carr, *The primordial black hole mass spectrum*, *Astrophys. J.* **201** (1975) 1–19.

[235] A. G. Polnarev and I. Musco, *Curvature profiles as initial conditions for primordial black hole formation*, *Class. Quant. Grav.* **24** (2007) 1405–1432, [gr-qc/0605122].

[236] I. Musco, J. C. Miller, and L. Rezzolla, *Computations of primordial black hole formation*, *Class. Quant. Grav.* **22** (2005) 1405–1424, [gr-qc/0412063].

[237] T. Harada and B. J. Carr, *Upper limits on the size of a primordial black hole*, *Phys. Rev.* **D71** (2005) 104009, [astro-ph/0412134].

[238] M. Kopp, S. Hofmann, and J. Weller, *Separate Universes do not constrain primordial black hole formation*, *Phys. Rev.* **D83** (2011) 124025, [arXiv:1012.4369].

[239] D. Blais, T. Bringmann, C. Kiefer, and D. Polarski, *Accurate results for primordial black holes from spectra with a distinguished scale*, *Phys. Rev.* **D67** (2003) 024024, [astro-ph/0206262].

[240] T. Bringmann, C. Kiefer, and D. Polarski, *Primordial black holes from inflationary models with and without broken scale invariance*, *Phys. Rev.* **D65** (2002) 024008, [astro-ph/0109404].

[241] A. S. Josan, A. M. Green, and K. A. Malik, *Generalised constraints on the curvature perturbation from primordial black holes*, *Phys. Rev.* **D79** (2009) 103520, [arXiv:0903.3184].

[242] M. Drees and E. Erfani, *Running spectral index and formation of primordial black holes in single field inflation models*, *JCAP* **1201** (2012) 035, [arXiv:1110.6052].

[243] M. Drees and E. Erfani, *Running–mass inflation model and primordial black holes*, *JCAP* **1104** (2011) 005, [arXiv:1102.2340].

[244] W. H. Press and P. Schechter, *Formation of galaxies and clusters of galaxies by selfsimilar gravitational condensation*, *Astrophys. J.* **187** (1974) 425–438.

[245] A. M. Green, A. R. Liddle, K. A. Malik, and M. Sasaki, *A new calculation of the mass fraction of primordial black holes*, *Phys. Rev.* **D70** (2004) 041502, [astro-ph/0403181].

[246] B. J. Carr, K. Kohri, Y. Sendouda, and J. Yokoyama, *New cosmological constraints on primordial black holes*, *Phys. Rev.* **D81** (2010) 104019, [arXiv:0912.5297].

[247] A. Barnacka, J. F. Glicenstein, and R. Moderski, *New constraints on primordial black holes abundance from femtolensing of gamma–ray bursts*, *Phys. Rev.* **D86** (2012) 043001, [arXiv:1204.2056].

[248] P. W. Graham, S. Rajendran, and J. Varela, *Dark matter triggers of supernovae*, *Phys. Rev.* **D92** (2015) 063007, [arXiv:1505.04444].

[249] F. Capela, M. Pshirkov, and P. Tinyakov, *Constraints on primordial black holes as dark matter candidates from capture by neutron stars*, *Phys. Rev.* **D87** (2013) 123524, [arXiv:1301.4984].

[250] H. Niikura, M. Takada, N. Yasuda, R. H. Lupton, T. Sumi, S. More, A. More, M. Oguri, and M. Chiba, *Microlensing constraints on primordial black holes with the Subaru/HSC Andromeda observation*, arXiv:1701.02151.

[251] K. Griest, A. M. Cieplak, and M. J. Lehner, *Experimental limits on primordial black hole dark matter from the first 2 yr of Kepler data*, *Astrophys. J.* **786** (2014) 158, [arXiv:1307.5798].

[252] **EROS–2** Collaboration, P. Tisserand et al., *Limits on the MACHO content of the galactic halo from the EROS–2 survey of the Magellanic Clouds*, *Astron. Astrophys.* **469** (2007) 387–404, [astro-ph/0607207].

[253] M. Oguri, J. M. Diego, N. Kaiser, P. L. Kelly, and T. Broadhurst, *Understanding caustic crossings in giant arcs: Characteristic scales, event rates, and constraints on compact dark matter*, *Phys. Rev.* **D97** (2018) 023518, [arXiv:1710.00148].

[254] **Macho** Collaboration, R. A. Allsman et al., *MACHO project limits on black hole dark matter in the 1–30 solar mass range*, *Astrophys. J.* **550** (2001) L169, [astro-ph/0011506].

[255] D. P. Quinn, M. I. Wilkinson, M. J. Irwin, J. Marshall, A. Koch, and V. Belokurov, *On the reported death of the MACHO era*, *Mon. Not. Roy. Astron. Soc.* **396** (2009) 11, [arXiv:0903.1644].

[256] M. A. Monroy-Rodríguez and C. Allen, *The end of the MACHO–era revisited: new limits on MACHO masses from halo wide binaries*, *Astrophys. J.* **790** (2014) 159, [arXiv:1406.5169].

[257] S. M. Koushiappas and A. Loeb, *Dynamics of dwarf galaxies disfavor stellar–mass black holes as dark matter*, *Phys. Rev. Lett.* **119** (2017) 041102, [arXiv:1704.01668].

[258] Y. Ali-Haïmoud and M. Kamionkowski, *Cosmic microwave background limits on accreting primordial black holes*, *Phys. Rev.* **D95** (2017) 043534, [arXiv:1612.05644].

[259] T. D. Brandt, *Constraints on MACHO dark matter from compact stellar systems in ultra–faint dwarf galaxies*, *Astrophys. J.* **824** (2016) L31, [arXiv:1605.03665].

[260] Y. Inoue and A. Kusenko, *New X–ray bound on density of primordial black holes*, *JCAP* **1710** (2017) 034, [arXiv:1705.00791].

[261] P. N. Wilkinson, D. R. Henstock, I. W. A. Browne, A. G. Polatidis, P. Augusto, A. C. S. Readhead, T. J. Pearson, W. Xu, G. B. Taylor, and R. C. Vermeulen, *Limits on the cosmological abundance of supermassive compact objects from a search for multiple imaging in compact radio sources*, *Phys. Rev. Lett.* **86** (2001) 584–587, [astro-ph/0101328].

[262] B. Carr, F. Kuhnel, and M. Sandstad, *Primordial black holes as dark matter*, *Phys. Rev.* **D94** (2016) 083504, [arXiv:1607.06077].

[263] M. Khlopov, *Cosmological probes for supersymmetry*, *Symmetry* **7** (2015) 815–842, [arXiv:1505.08077].

[264] R. Lehoucq, M. Casse, J. M. Casandjian, and I. Grenier, *New constraints on the primordial black hole number density from galactic gamma–ray astronomy*, *Astron. Astrophys.* **502** (2009) 37, [arXiv:0906.1648].

[265] B. J. Carr, K. Kohri, Y. Sendouda, and J. Yokoyama, *Constraints on primordial black holes from the galactic gamma–ray background*, *Phys. Rev.* **D94** (2016) 044029, [arXiv:1604.05349].

[266] K. J. Mack and D. H. Wesley, *Primordial black holes in the dark ages: Observational prospects for future 21cm surveys*, arXiv:0805.1531.

[267] J. H. MacGibbon, B. J. Carr, and D. N. Page, *Do evaporating black holes form photospheres?*, *Phys. Rev.* **D78** (2008) 064043, [arXiv:0709.2380].

[268] S. W. Hawking, *Particle creation by black holes*, *Commun. Math. Phys.* **43** (1975) 199–220.

[269] W. Hu and N. Sugiyama, *Thermal history constraints on the isocurvature baryon model*, *Astrophys. J.* **436** (1994) 456–466, [astro-ph/9403031].

[270] B. J. Carr and J. E. Lidsey, *Primordial black holes and generalized constraints on chaotic inflation*, *Phys. Rev.* **D48** (1993) 543–553.

[271] H. Kim and C. H. Lee, *Constraints on the spectral index from primordial black holes*, *Phys. Rev.* **D54** (1996) 6001–6007.

[272] A. M. Green and A. R. Liddle, *Constraints on the density perturbation spectrum from primordial black holes*, *Phys. Rev.* **D56** (1997) 6166–6174.

[273] S. M. Leach, I. J. Grivell, and A. R. Liddle, *Black hole constraints on the running mass inflation model*, *Phys. Rev.* **D62** (2000) 043516, [astro-ph/0004296].

[274] M. Ricotti, J. P. Ostriker, and K. J. Mack, *Effect of primordial black holes on the cosmic microwave background and cosmological parameter estimates*, *Astrophys. J.* **680** (2008) 829, [arXiv:0709.0524].

[275] J. B. Dent, D. A. Easson, and H. Tashiro, *Cosmological constraints from CMB distortion*, *Phys. Rev.* **D86** (2012) 023514, [arXiv:1202.6066].

[276] B. A. Powell, *Scalar runnings and a test of slow–roll from CMB distortions*, arXiv:1209.2024.

[277] J. Chluba, *Distinguishing different scenarios of early energy release with spectral distortions of the cosmic microwave background*, *Mon. Not. Roy. Astron. Soc.* **436** (2013) 2232–2243, [arXiv:1304.6121].

[278] J. Chluba and D. Grin, *CMB spectral distortions from small–scale isocurvature fluctuations*, *Mon. Not. Roy. Astron. Soc.* **434** (2013) 1619–1635, [arXiv:1304.4596].

[279] S. Clesse, B. Garbrecht, and Y. Zhu, *Testing inflation and curvaton scenarios with CMB distortions*, *JCAP* **1410** (2014) 046, [arXiv:1402.2257].

[280] E. Erfani, *Modulated inflation models and primordial black holes*, *Phys. Rev.* **D89** (2014) 083511.

[281] G. Cabass, E. di Valentino, A. Melchiorri, E. Pajer, and J. Silk, *Constraints on the running of the running of the scalar tilt from CMB anisotropies and spectral distortions*, *Phys. Rev.* **D94** (2016) 023523, [arXiv:1605.00209].

[282] G. Cabass, A. Melchiorri, and E. Pajer, *μ distortions or running: A guaranteed discovery from CMB spectrometry*, *Phys. Rev.* **D93** (2016) 083515, [arXiv:1602.05578].

[283] J. B. Muñoz, E. D. Kovetz, A. Raccanelli, M. Kamionkowski, and J. Silk, *Towards a measurement of the spectral runnings*, *JCAP* **1705** (2017) 032, [arXiv:1611.05883].

[284] Y. Akrami, F. Kuhnel, and M. Sandstad, *Uncertainties in primordial black hole constraints on the primordial power spectrum*, *Phys. Dark Univ.* **19** (2018) 124–128, [arXiv:1611.10069].

[285] B. Carr, T. Tenkanen, and V. Vaskonen, *Primordial black holes from inflaton and spectator field perturbations in a matter–dominated era*, *Phys. Rev.* **D96** (2017) 063507, [arXiv:1706.03746].

[286] J. P. P. Vieira, C. T. Byrnes, and A. Lewis, *Can power spectrum observations rule out slow–roll inflation?*, *JCAP* **1801** (2018) 019, [arXiv:1710.08408].

[287] T. Nakama, B. Carr, and J. Silk, *Limits on primordial black holes from μ distortions in cosmic microwave background*, *Phys. Rev.* **D97** (2018) 043525, [arXiv:1710.06945].

[288] P. S. Cole and C. T. Byrnes, *Extreme scenarios: The tightest possible constraints on the power spectrum due to primordial black holes*, *JCAP* **1802** (2018) 019, [arXiv:1706.10288].

[289] J. Luis Bernal, N. Bellomo, A. Raccanelli, and L. Verde, *Cosmological implications of primordial black holes*, *JCAP* **1710** (2017) 052, [arXiv:1709.07465].

[290] Y. Ali-Haïmoud and C. M. Hirata, *HyRec: A fast and highly accurate primordial hydrogen and helium recombination code*, *Phys. Rev.* **D83** (2011) 043513, [arXiv:1011.3758].

[291] B. Audren, J. Lesgourgues, K. Benabed, and S. Prunet, *Conservative constraints on early cosmology: An illustration of the* `Monte Python` *cosmological parameter inference code*, *JCAP* **1302** (2013) 001, [arXiv:1210.7183].

[292] **Planck** Collaboration, N. Aghanim et al., *Planck 2015 results. XI. CMB power spectra, likelihoods, and robustness of parameters*, *Astron. Astrophys.* **594** (2016) A11, [arXiv:1507.02704].

[293] M. Ata et al., *The clustering of the SDSS–IV extended Baryon Oscillation Spectroscopic Survey DR14 quasar sample: First measurement of baryon acoustic oscillations between redshift 0.8 and 2.2*, *Mon. Not. Roy. Astron. Soc.* **473** (2018) 4773–4794, [arXiv:1705.06373].

[294] J. E. Bautista et al., *Measurement of baryon acoustic oscillation correlations at $z = 2.3$ with SDSS DR12 Lyα–Forests*, *Astron. Astrophys.* **603** (2017) A12, [arXiv:1702.00176].

[295] **BOSS** Collaboration, S. Alam et al., *The clustering of galaxies in the completed SDSS–III Baryon Oscillation Spectroscopic Survey: Cosmological analysis of the DR12 galaxy sample*, *Mon. Not. Roy. Astron. Soc.* **470** (2017) 2617–2652, [arXiv:1607.03155].

[296] J. Simon, L. Verde, and R. Jimenez, *Constraints on the redshift dependence of the dark energy potential*, *Phys. Rev.* **D71** (2005) 123001, [astro-ph/0412269].

[297] D. Stern, R. Jimenez, L. Verde, M. Kamionkowski, and S. A. Stanford, *Cosmic chronometers: Constraining the equation of state of dark energy. I: $H(z)$ measurements*, *JCAP* **1002** (2010) 008, [arXiv:0907.3149].

[298] C. Zhang, H. Zhang, S. Yuan, T.-J. Zhang, and Y.-C. Sun, *Four new observational $H(z)$ data from luminous red galaxies in the Sloan Digital Sky Survey data release seven*, *Res. Astron. Astrophys.* **14** (2014) 1221–1233, [arXiv:1207.4541].

[299] M. Moresco et al., *Improved constraints on the expansion rate of the Universe up to $z \sim 1.1$ from the spectroscopic evolution of cosmic chronometers*, *JCAP* **1208** (2012) 006, [arXiv:1201.3609].

[300] M. Moresco, *Raising the bar: New constraints on the Hubble parameter with cosmic chronometers at $z \sim 2$*, *Mon. Not. Roy. Astron. Soc.* **450** (2015) L16–L20, [arXiv:1503.01116].

[301] M. Moresco, L. Pozzetti, A. Cimatti, R. Jimenez, C. Maraston, L. Verde, D. Thomas, A. Citro, R. Tojeiro, and D. Wilkinson, *A 6% measurement of the Hubble parameter at $z \sim 0.45$: Direct evidence of the epoch of cosmic re–acceleration*, *JCAP* **1605** (2016) 014, [arXiv:1601.01701].

[302] G. Aslanyan, L. C. Price, J. Adams, T. Bringmann, H. A. Clark, R. Easther, G. F. Lewis, and P. Scott, *Ultracompact minihalos as probes of inflationary cosmology*, *Phys. Rev. Lett.* **117** (2016) 141102, [arXiv:1512.04597].

[303] **PRISM** Collaboration, P. Andre et al., *PRISM (Polarized Radiation Imaging and Spectroscopy Mission): A white paper on the ultimate polarimetric spectro–imaging of the microwave and far–infrared sky*, arXiv:1306.2259.

[304] R. Khatri, R. A. Sunyaev, and J. Chluba, *Does Bose–Einstein condensation of CMB photons cancel μ distortions created by dissipation of sound waves in the early Universe?*, *Astron. Astrophys.* **540** (2012) A124, [arXiv:1110.0475].

[305] B. Carr, M. Raidal, T. Tenkanen, V. Vaskonen, and H. Veermäe, *Primordial black hole constraints for extended mass functions*, *Phys. Rev.* **D96** (2017) 023514, [arXiv:1705.05567].

[306] E. B. Gliner, *Algebraic properties of the energy–momentum tensor and vacuum–like states of matter*, *Soviet Journal of Experimental and Theoretical Physics* **22** (1966) 378.

[307] R. Brout, F. Englert, and E. Gunzig, *The creation of the Universe as a quantum phenomenon*, *Annals Phys.* **115** (1978) 78.

[308] A. A. Starobinsky, *Spectrum of relic gravitational radiation and the early state of the Universe*, *JETP Lett.* **30** (1979) 682–685.

[309] A. H. Guth, *The inflationary Universe: A possible solution to the horizon and flatness problems*, *Phys. Rev.* **D23** (1981) 347–356.

[310] A. D. Linde, *A new inflationary Universe scenario: A possible solution of the horizon, flatness, homogeneity, isotropy and primordial monopole problems*, *Phys. Lett.* **108B** (1982) 389–393.

[311] V. F. Mukhanov and G. V. Chibisov, *Quantum fluctuations and a nonsingular Universe*, *JETP Lett.* **33** (1981) 532–535.

[312] L. M. Krauss and M. S. Turner, *The cosmological constant is back*, *Gen. Rel. Grav.* **27** (1995) 1137–1144, [astro-ph/9504003].

[313] J. P. Ostriker and P. J. Steinhardt, *The observational case for a low density Universe with a nonzero cosmological constant*, *Nature* **377** (1995) 600–602.

[314] L. Verde et al., *The 2dF galaxy redshift survey: The bias of galaxies and the density of the Universe*, *Mon. Not. Roy. Astron. Soc.* **335** (2002) 432, [astro-ph/0112161].

[315] J. Mehra and H. Rechenberg, *Planck's half–quanta: A history of the concept of zero–point energy*, *Foundations of Physics* **29** (1999) 91–132.

[316] M. J. Sparnaay, *Attractive forces between flat plates*, *Nature* **180** (1957) 334.

[317] H. B. G. Casimir, *On the attraction between two perfectly conducting plates*, *Indag. Math.* **10** (1948) 261–263.

[318] Y. B. Zel'dovich, *Cosmological constant and elementary particles*, *JETP Lett.* **6** (1967) 316.

[319] Y. B. Zel'dovich, *The cosmological constant and the theory of elementary particles*, *Sov. Phys. Usp.* **11** (1968) 381.

[320] S. Weinberg, *The cosmological constant problem*, *Rev. Mod. Phys.* **61** (1989) 1–23.

[321] B. Zumino, *Supersymmetry and the vacuum*, *Nucl. Phys.* **B89** (1975) 535.

[322] B. Carter, *Confrontation of cosmological theories with observational data*. International Astronomical Union Symposia. Springer Netherlands, 1974. Edited by M.S. Longair.

[323] S. Weinberg, *Anthropic bound on the cosmological constant*, *Phys. Rev. Lett.* **59** (1987) 2607.

[324] M. S. Turner and M. J. White, *CDM models with a smooth component*, *Phys. Rev.* **D56** (1997) R4439, [astro-ph/9701138].

[325] C. Wetterich, *Cosmology and the fate of dilatation symmetry*, *Nucl. Phys.* **B302** (1988) 668.

[326] B. Ratra and P. J. E. Peebles, *Cosmological consequences of a rolling homogeneous scalar field*, *Phys. Rev.* **D37** (1988) 3406.

[327] P. J. E. Peebles and B. Ratra, *Cosmology with a time variable cosmological constant*, *Astrophys. J.* **325** (1988) L17.

[328] R. R. Caldwell, R. Dave, and P. J. Steinhardt, *Cosmological imprint of an energy component with general equation of state*, *Phys. Rev. Lett.* **80** (1998) 1582–1585, [astro-ph/9708069].

[329] I. Zlatev, L.-M. Wang, and P. J. Steinhardt, *Quintessence, cosmic coincidence, and the cosmological constant*, *Phys. Rev. Lett.* **82** (1999) 896–899, [astro-ph/9807002].

[330] T. Chiba, T. Okabe, and M. Yamaguchi, *Kinetically driven quintessence*, *Phys. Rev.* **D62** (2000) 023511, [astro-ph/9912463].

[331] C. Armendariz-Picon, V. F. Mukhanov, and P. J. Steinhardt, *Essentials of k–essence*, *Phys. Rev.* **D63** (2001) 103510, [astro-ph/0006373].

[332] C. Armendariz-Picon, V. F. Mukhanov, and P. J. Steinhardt, *A dynamical solution to the problem of a small cosmological constant and late–time cosmic acceleration*, *Phys. Rev. Lett.* **85** (2000) 4438–4441, [astro-ph/0004134].

[333] B. A. Bassett, P. S. Corasaniti, and M. Kunz, *The essence of quintessence and the cost of compression*, *Astrophys. J.* **617** (2004) L1–L4, [astro-ph/0407364].

[334] D. Huterer and M. S. Turner, *Probing the dark energy: Methods and strategies*, *Phys. Rev.* **D64** (2001) 123527, [astro-ph/0012510].

[335] J. Weller and A. Albrecht, *Future supernovae observations as a probe of dark energy*, *Phys. Rev.* **D65** (2002) 103512, [astro-ph/0106079].

[336] M. Chevallier and D. Polarski, *Accelerating Universes with scaling dark matter*, *Int. J. Mod. Phys.* **D10** (2001) 213–224, [gr-qc/0009008].

[337] A. Melchiorri, L. Mersini-Houghton, C. J. Odman, and M. Trodden, *The state of the dark energy equation of state*, *Phys. Rev.* **D68** (2003) 043509, [astro-ph/0211522].

[338] S. M. Carroll, M. Hoffman, and M. Trodden, *Can the dark energy equation of state parameter w be less than -1?*, *Phys. Rev.* **D68** (2003) 023509, [astro-ph/0301273].

[339] E. V. Linder, *Probing gravitation, dark energy, and acceleration*, *Phys. Rev.* **D70** (2004) 023511, [astro-ph/0402503].

[340] H. K. Jassal, J. S. Bagla, and T. Padmanabhan, *WMAP constraints on low redshift evolution of dark energy*, *Mon. Not. Roy. Astron. Soc.* **356** (2005) L11–L16, [astro-ph/0404378].

[341] E. Calabrese, A. Slosar, A. Melchiorri, G. F. Smoot, and O. Zahn, *Cosmic microwave weak lensing data as a test for the dark Universe*, *Phys. Rev.* **D77** (2008) 123531, [arXiv:0803.2309].

[342] **BOSS** Collaboration, T. Delubac et al., *Baryon acoustic oscillations in the Lyα forest of BOSS DR11 quasars*, *Astron. Astrophys.* **574** (2015) A59, [arXiv:1404.1801].

[343] E. Aubourg et al., *Cosmological implications of baryon acoustic oscillation measurements*, *Phys. Rev.* **D92** (2015) 123516, [arXiv:1411.1074].

[344] H. Hildebrandt et al., *KiDS–450: Cosmological parameter constraints from tomographic weak gravitational lensing*, *Mon. Not. Roy. Astron. Soc.* **465** (2017) 1454, [arXiv:1606.05338].

[345] M. Raveri, *Are cosmological data sets consistent with each other within the Λ cold dark matter model?*, *Phys. Rev.* **D93** (2016) 043522, [arXiv:1510.00688].

[346] J. L. Bernal, L. Verde, and A. G. Riess, *The trouble with H_0*, *JCAP* **1610** (2016) 019, [arXiv:1607.05617].

[347] **DES** Collaboration, T. M. C. Abbott et al., *Dark Energy Survey year 1 results: Cosmological constraints from galaxy clustering and weak lensing*, arXiv:1708.01530.

[348] W. L. Freedman, *Cosmology at a crossroads*, *Nat. Astron.* **1** (2017) 0121, [arXiv:1706.02739].

[349] W. Lin and M. Ishak, *Cosmological discordances: A new measure, marginalization effects, and application to geometry versus growth current data sets*, *Phys. Rev.* **D96** (2017) 023532, [arXiv:1705.05303].

[350] G. Efstathiou and P. Lemos, *Statistical inconsistencies in the KiDS–450 dataset*, *Mon. Not. Roy. Astron. Soc.* **476** (2018) 151–157, [arXiv:1707.00483].

[351] **HST** Collaboration, W. L. Freedman et al., *Final results from the Hubble Space Telescope key project to measure the Hubble constant*, *Astrophys. J.* **553** (2001) 47–72, [astro-ph/0012376].

[352] A. G. Riess et al., *A redetermination of the Hubble constant with the Hubble Space Telescope from a differential distance ladder*, *Astrophys. J.* **699** (2009) 539–563, [arXiv:0905.0695].

[353] A. G. Riess, L. Macri, S. Casertano, H. Lampeitl, H. C. Ferguson, A. V. Filippenko, S. W. Jha, W. Li, and R. Chornock, *A 3% solution: Determination of the Hubble constant with the Hubble Space Telescope and Wide Field Camera 3*, *Astrophys. J.* **730** (2011) 119, [arXiv:1103.2976].

[354] W. L. Freedman, B. F. Madore, V. Scowcroft, C. Burns, A. Monson, S. E. Persson, M. Seibert, and J. Rigby, *Carnegie Hubble Program: A mid–infrared calibration of the Hubble constant*, *Astrophys. J.* **758** (2012) 24, [arXiv:1208.3281].

[355] A. G. Riess et al., *New parallaxes of galactic Cepheids from spatially scanning the Hubble Space Telescope : Implications for the Hubble constant*, *Astrophys. J.* **855** (2018) 136.

[356] **WMAP** Collaboration, D. N. Spergel et al., *Wilkinson Microwave Anisotropy Probe (WMAP) three year results: Implications for cosmology*, *Astrophys. J. Suppl.* **170** (2007) 377, [astro-ph/0603449].

[357] **WMAP** Collaboration, E. Komatsu et al., *Five–year Wilkinson Microwave Anisotropy Probe (WMAP) observations: Cosmological interpretation*, *Astrophys. J. Suppl.* **180** (2009) 330–376, [arXiv:0803.0547].

[358] **WMAP** Collaboration, E. Komatsu et al., *Seven–year Wilkinson Microwave Anisotropy Probe (WMAP) observations: Cosmological interpretation*, *Astrophys. J. Suppl.* **192** (2011) 18, [arXiv:1001.4538].

[359] **WMAP** Collaboration, G. Hinshaw et al., *Nine–year Wilkinson Microwave Anisotropy Probe (WMAP) observations: Cosmological parameter results*, *Astrophys. J. Suppl.* **208** (2013) 19, [arXiv:1212.5226].

[360] **LIGO Scientific, VINROUGE, Las Cumbres Observatory, DES, DLT40, Virgo, 1M2H, Dark Energy Camera GW-E, MASTER** Collaboration, B. P. Abbott et al., *A gravitational–wave standard siren measurement of the Hubble constant*, *Nature* **551** (2017) 85–88, [arXiv:1710.05835].

[361] J. Huchra, "Estimates of the Hubble constant." https://www.cfa.harvard.edu/~dfabricant/huchra, 2010. [Online; accessed 04–07–2018].

[362] A. Vikhlinin et al., *Chandra cluster cosmology project III: Cosmological parameter constraints*, *Astrophys. J.* **692** (2009) 1060–1074, [arXiv:0812.2720].

[363] **Planck** Collaboration, P. A. R. Ade et al., *Planck 2013 results. XX. Cosmology from Sunyaev–Zel'dovich cluster counts*, *Astron. Astrophys.* **571** (2014) A20, [arXiv:1303.5080].

[364] C. Heymans et al., *CFHTLenS tomographic weak lensing cosmological parameter constraints: Mitigating the impact of intrinsic galaxy alignments*, *Mon. Not. Roy. Astron. Soc.* **432** (2013) 2433, [arXiv:1303.1808].

[365] A. Mantz, S. W. Allen, D. Rapetti, and H. Ebeling, *The observed growth of massive galaxy clusters I: Statistical methods and cosmological constraints*, *Mon. Not. Roy. Astron. Soc.* **406** (2010) 1759–1772, [arXiv:0909.3098].

[366] A. Hajian, N. Battaglia, D. N. Spergel, J. Richard Bond, C. Pfrommer, and J. L. Sievers, *Measuring the thermal Sunyaev–Zel'dovich effect through the cross–correlation of Planck and WMAP maps with ROSAT galaxy cluster catalogs*, *JCAP* **1311** (2013) 064, [arXiv:1309.3282].

[367] B. A. Benson et al., *Cosmological constraints from Sunyaev–Zel'dovich–selected clusters with X–ray observations in the first 178 square degrees of the South Pole Telescope survey*, *Astrophys. J.* **763** (2013) 147, [arXiv:1112.5435].

[368] J. P. Henry, A. E. Evrard, H. Hoekstra, A. Babul, and A. Mahdavi, *The X–ray cluster normalization of the matter power spectrum*, *Astrophys. J.* **691** (2009) 1307–1321, [arXiv:0809.3832].

[369] **DSDD** Collaboration, E. Rozo et al., *Cosmological constraints from the SDSS maxBCG cluster catalog*, *Astrophys. J.* **708** (2010) 645–660, [arXiv:0902.3702].

[370] J. L. Tinker et al., *Cosmological constraints from galaxy clustering and the mass–to–number ratio of galaxy clusters*, *Astrophys. J.* **745** (2012) 16, [arXiv:1104.1635].

[371] W. Cardona, M. Kunz, and V. Pettorino, *Determining H_0 with Bayesian hyper–parameters*, *JCAP* **1703** (2017) 056, [arXiv:1611.06088].

[372] B. Follin and L. Knox, *Insensitivity of the distance ladder Hubble constant determination to Cepheid calibration modeling choices*, arXiv:1707.01175.

[373] S. Dhawan, S. W. Jha, and B. Leibundgut, *Measuring the Hubble constant with Type Ia supernovae as near–infrared standard candles*, *Astron. Astrophys.* **609** (2018) A72, [arXiv:1707.00715].

[374] S. M. Feeney, D. J. Mortlock, and N. Dalmasso, *Clarifying the Hubble constant tension with a Bayesian hierarchical model of the local distance ladder*, *Mon. Not. Roy. Astron. Soc.* **476** (2018) 3861–3882, [arXiv:1707.00007].

[375] H.-Y. Wu and D. Huterer, *Sample variance in the local measurements of the Hubble constant*, *Mon. Not. Roy. Astron. Soc.* **471** (2017) 4946–4955, [arXiv:1706.09723].

[376] F. Köhlinger et al., *KiDS–450: The tomographic weak lensing power spectrum and constraints on cosmological parameters*, *Mon. Not. Roy. Astron. Soc.* **471** (2017) 4412–4435, [arXiv:1706.02892].

[377] E. van Uitert et al., *KiDS + GAMA: Cosmology constraints from a joint analysis of cosmic shear, galaxy–galaxy lensing and angular clustering*, arXiv:1706.05004.

[378] S. Joudaki et al., *CFHTLenS revisited: assessing concordance with Planck including astrophysical systematics*, *Mon. Not. Roy. Astron. Soc.* **465** (2017) 2033–2052, [arXiv:1601.05786].

[379] **SPT** Collaboration, G. Simard et al., *Constraints on cosmological parameters from the angular power spectrum of a combined 2500 deg^2 SPT–SZ and Planck gravitational lensing map*, *Astrophys. J.* **860** (2018) 137, [arXiv:1712.07541].

[380] R. A. Battye, T. Charnock, and A. Moss, *Tension between the power spectrum of density perturbations measured on large and small scales*, *Phys. Rev.* **D91** (2015) 103508, [arXiv:1409.2769].

[381] M. Wyman, D. H. Rudd, R. A. Vanderveld, and W. Hu, *Neutrinos help reconcile Planck measurements with the local Universe*, *Phys. Rev. Lett.* **112** (2014) 051302, [arXiv:1307.7715].

[382] R. A. Battye and A. Moss, *Evidence for massive neutrinos from cosmic microwave background and lensing observations*, *Phys. Rev. Lett.* **112** (2014) 051303, [arXiv:1308.5870].

[383] S. Joudaki et al., *KiDS–450: Testing extensions to the standard cosmological model*, *Mon. Not. Roy. Astron. Soc.* **471** (2017) 1259–1279, [arXiv:1610.04606].

[384] A. Rest et al., *Cosmological constraints from measurements of Type Ia supernovae discovered during the first 1.5 yr of the Pan–STARRS1 survey*, *Astrophys. J.* **795** (2014) 44, [arXiv:1310.3828].

[385] D. Scolnic et al., *Systematic uncertainties associated with the cosmological analysis of the first Pan–STARRS1 Type Ia supernova sample*, *Astrophys. J.* **795** (2014) 45, [arXiv:1310.3824].

[386] C. Cheng and Q.-G. Huang, *Dark side of the Universe after Planck data*, *Phys. Rev.* **D89** (2014) 043003, [arXiv:1306.4091].

[387] J.-Q. Xia, H. Li, and X. Zhang, *Dark energy constraints after Planck*, *Phys. Rev.* **D88** (2013) 063501, [arXiv:1308.0188].

[388] D. L. Shafer and D. Huterer, *Chasing the phantom: A closer look at Type Ia supernovae and the dark energy equation of state*, *Phys. Rev.* **D89** (2014) 063510, [arXiv:1312.1688].

[389] E. di Valentino, A. Melchiorri, and J. Silk, *Beyond six parameters: Extending ΛCDM*, *Phys. Rev.* **D92** (2015) 121302, [arXiv:1507.06646].

[390] G.-B. Zhao et al., *Dynamical dark energy in light of the latest observations*, *Nat. Astron.* **1** (2017) 627–632, [arXiv:1701.08165].

[391] H. Weyl, *Gravitation und Elektrizität*, *Sitzungsber. Preuss. Akad. d. Wiss. Teil* **1** (1918) 465–480.

[392] E. Schrödinger, *Über eine bemerkenswerte Eigenschaft der Quantenbahnen eines einzelnen Elektrons*, *Zeitschrift für Physik* **12** (1923) 13–23.

[393] F. London, *Quantum mechanical interpretation of the Weyl theory*, *Zeitschrift für Physik* **42** (1927) 375–389.

[394] H. Weyl, *Elektron und Gravitation I.*, *Zeitschrift für Physik* **56** (1929) 330–352.

[395] H. A. Buchdahl, *Non–linear Lagrangians and cosmological theory*, *Mon. Not. Roy. Astron. Soc.* **150** (1970) 1.

[396] A. A. Starobinsky, *A new type of isotropic cosmological models without singularity*, *Phys. Lett.* **B91** (1980) 99–102.

[397] S. Capozziello, *Curvature quintessence*, *Int. J. Mod. Phys.* **D11** (2002) 483–492, [gr-qc/0201033].

[398] S. Capozziello, V. F. Cardone, S. Carloni, and A. Troisi, *Curvature quintessence matched with observational data*, *Int. J. Mod. Phys.* **D12** (2003) 1969–1982, [astro-ph/0307018].

[399] S. Capozziello, S. Carloni, and A. Troisi, *Quintessence without scalar fields*, *Recent Res. Dev. Astron. Astrophys.* **1** (2003) 625, [astro-ph/0303041].

[400] T. Chiba, $1/R$ *gravity and scalar–tensor gravity*, *Phys. Lett.* **B575** (2003) 1–3, [astro-ph/0307338].

[401] A. D. Dolgov and M. Kawasaki, *Can modified gravity explain accelerated cosmic expansion?*, *Phys. Lett.* **B573** (2003) 1–4, [astro-ph/0307285].

[402] T. P. Sotiriou and V. Faraoni, $f(R)$ *theories of gravity*, *Rev. Mod. Phys.* **82** (2010) 451–497, [arXiv:0805.1726].

[403] A. de Felice and S. Tsujikawa, $f(R)$ *theories*, *Living Rev. Rel.* **13** (2010) 3, [arXiv:1002.4928].

[404] S. Capozziello and M. de Laurentis, *Extended theories of gravity*, *Phys. Rept.* **509** (2011) 167–321, [arXiv:1108.6266].

[405] S. M. Carroll, A. de Felice, V. Duvvuri, D. A. Easson, M. Trodden, and M. S. Turner, *The cosmology of generalized modified gravity models*, *Phys. Rev.* **D71** (2005) 063513, [astro-ph/0410031].

[406] S. Carloni, P. K. S. Dunsby, S. Capozziello, and A. Troisi, *Cosmological dynamics of* R^n *gravity*, *Class. Quant. Grav.* **22** (2005) 4839–4868, [gr-qc/0410046].

[407] S. Capozziello and M. Francaviglia, *Extended theories of gravity and their cosmological and astrophysical applications*, *Gen. Rel. Grav.* **40** (2008) 357–420, [arXiv:0706.1146].

[408] S. Tsujikawa, *Observational signatures of* $f(R)$ *dark energy models that satisfy cosmological and local gravity constraints*, *Phys. Rev.* **D77** (2008) 023507, [arXiv:0709.1391].

[409] A. A. Starobinsky, *Disappearing cosmological constant in* $f(R)$ *gravity*, *JETP Lett.* **86** (2007) 157–163, [arXiv:0706.2041].

[410] R. Bean, D. Bernat, L. Pogosian, A. Silvestri, and M. Trodden, *Dynamics of linear perturbations in* $f(R)$ *gravity*, *Phys. Rev.* **D75** (2007) 064020, [astro-ph/0611321].

[411] A. Abebe, A. de la Cruz-Dombriz, and P. K. S. Dunsby, *Large scale structure constraints for a class of* $f(R)$ *theories of gravity*, *Phys. Rev.* **D88** (2013) 044050, [arXiv:1304.3462].

[412] T. Kaluza, *Zum Unitätsproblem in der Physik*, *Sitzungsber. Preuss. Akad. Wiss.* (1921) 966–972.

[413] O. Klein, *Quantentheorie und fünfdimensionale Relativitätstheorie*, *Zeitschrift für Physik* **37** (1926) 895–906.

[414] O. Klein, *The atomicity of electricity as a Quantum Theory Law*, *Nature* **118** (1926) 516.

[415] P. A. M. Dirac, *The cosmological constants*, *Nature* **139** (1937) 323.

[416] P. A. M. Dirac, *New basis for cosmology*, *Proc. Roy. Soc. Lond.* **A165** (1938) 199–208.

[417] P. Jordan, *Zur projektiven Relativitätstheorie*, *Nachr. Akad. Wiss. Göttingen. Math.–Phys. Kl.* (1945) 39–41.

[418] W. Scherrer, *Zur Theorie der Elementarteilchen*, *Verh. Schweiz. Naturf. Ges.* **121** (1941) 86–87.

[419] O. Veblen and B. Hoffmann, *Projective relativity*, *Phys. Rev.* **36** (1930) 810–822.

[420] P. Jordan, *Relativistische Gravitationstheorie mit variabler Gravitationskonstante*, *Naturwissenschaften* **33** (1946) 250–251.

[421] P. Jordan and C. Müller, *Über die Feldgleichungen der Gravitation bei variabler "Gravitationskonstante"*, *Z. Naturforschg.* **2a** (1947) 1–2.

[422] P. Jordan, *Fünfdimensionale Kosmologie*, *Astron. Nachr.* **276** (1948) 193–208.

[423] A. Lichnerowicz and Y. Thiry, *Problèmes de calcul des variations liés à la dynamique classique et á la théorie unitaire du champ*, *Compt. Rend. Acad. Sci.* **224** (1947) 529–531.

[424] Y. Thiry, *Les équations de la théorie unitaire de Kaluza*, *Compt. Rend. Acad. Sci.* **226** (1948) 216–218.

[425] M. Fierz, *Über die physikalische Deutung der erweiterten Gravitationstheorie P. Jordans*, *Helv. Phys. Acta* **29** (1956) 128–134.

[426] C. H. Brans and R. H. Dicke, *Mach's principle and a relativistic theory of gravitation*, *Phys. Rev.* **124** (1961) 925–935.

[427] C. H. Brans, *Mach's principle and a relativistic theory of gravitation. II*, *Phys. Rev.* **125** (1962) 2194–2201.

[428] R. H. Dicke, *Mach's principle and invariance under transformation of units*, *Phys. Rev.* **125** (1962) 2163–2167.

[429] G. Ludwig and C. Müller, *Ein Modell des Kosmos und der Sternentstehung*, *Annalen der Physik* **437** (1948) 76–84.

[430] G. W. Horndeski, *Second–order scalar–tensor field equations in a four–dimensional space*, *Int. J. Theor. Phys.* **10** (1974) 363–384.

[431] C. Deffayet, X. Gao, D. A. Steer, and G. Zahariade, *From k–essence to generalised Galileons*, *Phys. Rev.* **D84** (2011) 064039, [arXiv:1103.3260].

[432] T. Kobayashi, M. Yamaguchi, and J. Yokoyama, *Generalized G–inflation: Inflation with the most general second–order field equations*, *Prog. Theor. Phys.* **126** (2011) 511–529, [arXiv:1105.5723].

[433] M. Ostrogradsky, *Mémoires sur les équations différentielles, relatives au problème des isopérimètres*, *Mem. Acad. St. Petersbourg* **6** (1850) 385–517.

[434] R. Woodard, *Avoiding dark energy with* $1/R$ *modifications of gravity*, pp. 403–433. Springer Berlin Heidelberg, Berlin, Heidelberg, 2007.

[435] T.-j. Chen, M. Fasiello, E. A. Lim, and A. J. Tolley, *Higher derivative theories with constraints: Exorcising Ostrogradski's ghost*, *JCAP* **1302** (2013) 042, [arXiv:1209.0583].

[436] E. Bellini and I. Sawicki, *Maximal freedom at minimum cost: Linear large–scale structure in general modifications of gravity*, *JCAP* **1407** (2014) 050, [arXiv:1404.3713].

[437] J. M. Ezquiaga and M. Zumalacárregui, *Dark energy after GW170817: Dead ends and the road ahead*, *Phys. Rev. Lett.* **119** (2017) 251304, [arXiv:1710.05901].

[438] T. Baker, E. Bellini, P. G. Ferreira, M. Lagos, J. Noller, and I. Sawicki, *Strong constraints on cosmological gravity from GW170817 and GRB 170817A*, *Phys. Rev. Lett.* **119** (2017) 251301, [arXiv:1710.06394].

[439] J. Sakstein and B. Jain, *Implications of the neutron star merger GW170817 for cosmological scalar–tensor theories*, *Phys. Rev. Lett.* **119** (2017) 251303, [arXiv:1710.05893].

[440] P. Creminelli and F. Vernizzi, *Dark energy after GW170817 and GRB 170817A*, *Phys. Rev. Lett.* **119** (2017) 251302, [arXiv:1710.05877].

[441] R. Kase and S. Tsujikawa, *Dark energy scenario consistent with GW170817 in theories beyond Horndeski gravity*, *Phys. Rev.* **D97** (2018) 103501, [arXiv:1802.02728].

[442] L. Amendola, M. Kunz, I. D. Saltas, and I. Sawicki, *Fate of large–scale structure in modified gravity after GW170817 and GRB170817A*, *Phys. Rev. Lett.* **120** (2018) 131101, [arXiv:1711.04825].

[443] M. Crisostomi and K. Koyama, *Self–accelerating Universe in scalar–tensor theories after GW170817*, *Phys. Rev.* **D97** (2018) 084004, [arXiv:1712.06556].

[444] Y. Gong, E. Papantonopoulos, and Z. Yi, *Constraints on scalar–tensor theory of gravity by the recent observational results on gravitational waves*, arXiv:1711.04102.

[445] C. Deffayet, O. Pujolas, I. Sawicki, and A. Vikman, *Imperfect dark energy from kinetic gravity braiding*, *JCAP* **1010** (2010) 026, [arXiv:1008.0048].

[446] T. Chiba and M. Yamaguchi, *Conformal–frame (in)dependence of cosmological observations in scalar–tensor theory*, *JCAP* **1310** (2013) 040, [arXiv:1308.1142].

[447] D. Bettoni and S. Liberati, *Disformal invariance of second order scalar–tensor theories: Framing the Horndeski action*, *Phys. Rev.* **D88** (2013) 084020, [arXiv:1306.6724].

[448] J. D. Bekenstein, *The relation between physical and gravitational geometry*, *Phys. Rev.* **D48** (1993) 3641–3647, [gr-qc/9211017].

[449] P. J. Steinhardt, L.-M. Wang, and I. Zlatev, *Cosmological tracking solutions*, *Phys. Rev.* **D59** (1999) 123504, [astro-ph/9812313].

[450] E. J. Copeland, A. R. Liddle, and D. Wands, *Exponential potentials and cosmological scaling solutions*, *Phys. Rev.* **D57** (1998) 4686–4690, [gr-qc/9711068].

[451] A. R. Liddle and R. J. Scherrer, *A classification of scalar field potentials with cosmological scaling solutions*, *Phys. Rev.* **D59** (1999) 023509, [astro-ph/9809272].

[452] P. G. Ferreira and M. Joyce, *Cosmology with a primordial scaling field*, *Phys. Rev.* **D58** (1998) 023503, [astro-ph/9711102].

[453] J.-P. Uzan, *Cosmological scaling solutions of nonminimally coupled scalar fields*, *Phys. Rev.* **D59** (1999) 123510, [gr-qc/9903004].

[454] L. Amendola, *Scaling solutions in general nonminimal coupling theories*, *Phys. Rev.* **D60** (1999) 043501, [astro-ph/9904120].

[455] T. Chiba, *Quintessence, the gravitational constant, and gravity*, *Phys. Rev.* **D60** (1999) 083508, [gr-qc/9903094].

[456] D. J. Holden and D. Wands, *Selfsimilar cosmological solutions with a nonminimally coupled scalar field*, *Phys. Rev.* **D61** (2000) 043506, [gr-qc/9908026].

[457] D. Spergel and U.-L. Pen, *Cosmology in a string dominated Universe*, *Astrophys. J.* **491** (1997) L67–L71, [astro-ph/9611198].

[458] J. A. Frieman, C. T. Hill, A. Stebbins, and I. Waga, *Cosmology with ultralight pseudo Nambu–Goldstone bosons*, *Phys. Rev. Lett.* **75** (1995) 2077–2080, [astro-ph/9505060].

[459] P. Binetruy, *Models of dynamical supersymmetry breaking and quintessence*, *Phys. Rev.* **D60** (1999) 063502, [hep-ph/9810553].

[460] A. Masiero, M. Pietroni, and F. Rosati, *SUSY QCD and quintessence*, *Phys. Rev.* **D61** (2000) 023504, [hep-ph/9905346].

[461] P. Brax and J. Martin, *Quintessence and supergravity*, *Phys. Lett.* **B468** (1999) 40–45, [astro-ph/9905040].

[462] P. Brax, J. Martin, and A. Riazuelo, *Quintessence with two energy scales*, *Phys. Rev.* **D64** (2001) 083505, [hep-ph/0104240].

[463] E. J. Copeland, N. J. Nunes, and F. Rosati, *Quintessence models in supergravity*, *Phys. Rev.* **D62** (2000) 123503, [hep-ph/0005222].

[464] R. Kallosh, A. D. Linde, S. Prokushkin, and M. Shmakova, *Supergravity, dark energy and the fate of the Universe*, *Phys. Rev.* **D66** (2002) 123503, [hep-th/0208156].

[465] S. M. Carroll, *Quintessence and the rest of the world*, *Phys. Rev. Lett.* **81** (1998) 3067–3070, [astro-ph/9806099].

[466] R. D. Peccei, J. Sola, and C. Wetterich, *Adjusting the cosmological constant dynamically: Cosmons and a new force weaker than gravity*, *Phys. Lett.* **B195** (1987) 183–190.

[467] J. R. Ellis, S. Kalara, K. A. Olive, and C. Wetterich, *Density dependent couplings and astrophysical bounds on light scalar particles*, *Phys. Lett.* **B228** (1989) 264–272.

[468] C. Wetterich, *The Cosmon model for an asymptotically vanishing time dependent cosmological "constant"*, *Astron. Astrophys.* **301** (1995) 321–328, [hep-th/9408025].

[469] T. Damour and A. M. Polyakov, *The string dilaton and a least coupling principle*, *Nucl. Phys.* **B423** (1994) 532–558, [hep-th/9401069].

[470] M. Zumalacárregui and J. García-Bellido, *Transforming gravity: From derivative couplings to matter to second–order scalar–tensor theories beyond the Horndeski Lagrangian*, *Phys. Rev.* **D89** (2014) 064046, [arXiv:1308.4685].

[471] T. Koivisto, D. Wills, and I. Zavala, *Dark D–brane cosmology*, *JCAP* **1406** (2014) 036, [arXiv:1312.2597].

[472] C. van de Bruck, J. Morrice, and S. Vu, *Constraints on nonconformal couplings from the properties of the cosmic microwave background radiation*, *Phys. Rev. Lett.* **111** (2013) 161302, [arXiv:1303.1773].

[473] S. C. C. Ng, N. J. Nunes, and F. Rosati, *Applications of scalar attractor solutions to cosmology*, *Phys. Rev.* **D64** (2001) 083510, [astro-ph/0107321].

[474] J. D. Barrow and A. A. H. Graham, *General dynamics of varying–α Universes*, *Phys. Rev.* **D88** (2013) 103513, [arXiv:1307.6816].

[475] A. Nunes and J. P. Mimoso, *On the potentials yielding cosmological scaling solutions*, *Phys. Lett.* **B488** (2000) 423–427, [gr-qc/0008003].

[476] L. Amendola, *Coupled quintessence*, *Phys. Rev.* **D62** (2000) 043511, [astro-ph/9908023].

[477] A. Salam and E. Sezgin, *Chiral compactification on Minkowski $\times S^2$ of $N = 2$ Einstein–Maxwell supergravity in six–dimensions*, *Phys. Lett.* **B147** (1984) 47.

[478] H. Nishino and E. Sezgin, *Matter and gauge couplings of $N = 2$ supergravity in six–dimensions*, *Phys. Lett.* **B144** (1984) 187–192.

[479] J. J. Halliwell, *Scalar fields in cosmology with an exponential potential*, *Phys. Lett.* **B185** (1987) 341.

[480] J. Sakstein, *Towards viable cosmological models of disformal theories of gravity*, *Phys. Rev.* **D91** (2015) 024036, [arXiv:1409.7296].

[481] E. J. Copeland, M. Sami, and S. Tsujikawa, *Dynamics of dark energy*, *Int. J. Mod. Phys.* **D15** (2006) 1753–1936, [hep-th/0603057].

[482] L. Amendola, T. Barreiro, and N. J. Nunes, *Multifield coupled quintessence*, *Phys. Rev.* **D90** (2014) 083508, [arXiv:1407.2156].

[483] B. Gumjudpai, T. Naskar, M. Sami, and S. Tsujikawa, *Coupled dark energy: Towards a general description of the dynamics*, *JCAP* **0506** (2005) 007, [hep-th/0502191].

[484] C. Robinson, *Dynamical systems: Stability, symbolic dynamics, and chaos*. Studies in Advanced Mathematics. CRC–Press, 1999.

[485] C. van de Bruck and J. Morrice, *Disformal couplings and the dark sector of the Universe*, *JCAP* **1504** (2015) 036, [arXiv:1501.03073].

[486] A. W. Brookfield, C. van de Bruck, and L. M. H. Hall, *New interactions in the dark sector mediated by dark energy*, *Phys. Rev.* **D77** (2008) 043006, [arXiv:0709.2297].

[487] R. Bean, S. H. Hansen, and A. Melchiorri, *Early Universe constraints on dark energy*, *Phys. Rev.* **D64** (2001) 103508.

[488] R. H. Cyburt, B. D. Fields, K. A. Olive, and E. Skillman, *New BBN limits on physics beyond the standard model from ^4He*, *Astropart. Phys.* **23** (2005) 313–323, [astro-ph/0408033].

[489] M. Baldi, *Multiple dark matter as a self–regulating mechanism for dark sector interactions*, *Annalen Phys.* **524** (2012) 602–617, [arXiv:1204.0514].

[490] A. Chodos and S. L. Detweiler, *Where has the fifth–dimension gone?*, *Phys. Rev.* **D21** (1980) 2167.

[491] Y.-S. Wu and Z. Wang, *The time variation of Newton's gravitational constant in superstring theories*, *Phys. Rev. Lett.* **57** (1986) 1978.

[492] P. Mohr, B. Taylor, and D. Newell, *The 2014 CODATA recommended values of the fundamental physical constants (web version 7.0)*, 2015. This database was developed by J. Baker, M. Douma, and S. Kotochigova. Available: http://physics.nist.gov/constants [Thursday, 27-Aug-2015 10:53:20 EDT]. National Institute of Standards and Technology, Gaithersburg, MD 20899.

[493] C. J. A. P. Martins, *The status of varying constants: A review of the physics, searches, and implications*, arXiv:1709.02923.

[494] J. K. Webb, J. A. King, M. T. Murphy, V. V. Flambaum, R. F. Carswell, and M. B. Bainbridge, *Indications of a spatial variation of the fine–structure constant*, *Phys. Rev. Lett.* **107** (2011) 191101, [arXiv:1008.3907].

[495] A. Songaila and L. L. Cowie, *Constraining the variation of the fine–structure constant with observations of narrow quasar absorption lines*, *Astrophys. J.* **793** (2014) 103, [arXiv:1406.3628].

[496] P. Molaro, D. Reimers, I. I. Agafonova, and S. A. Levshakov, *Bounds on the fine–structure constant variability from FeII absorption lines in QSO spectra*, *Eur. Phys. J. ST* **163** (2008) 173–189, [arXiv:0712.4380].

[497] H. Chand, R. Srianand, P. Petitjean, B. Aracil, R. Quast, and D. Reimers, *On the variation of the fine–structure constant: Very high resolution spectrum of QSO HE 0515–4414*, *Astron. Astrophys.* **451** (2006) 45–56, [astro-ph/0601194].

[498] I. I. Agafonova, P. Molaro, S. A. Levshakov, and J. L. Hou, *First measurement of Mg isotope abundances at high redshifts and accurate estimate of $\Delta\alpha/\alpha$*, *Astron. Astrophys.* **529** (2011) A28, [arXiv:1102.2967].

[499] P. Molaro et al., *The UVES large program for testing fundamental physics: I Bounds on a change in α towards quasar HE 2217–2818*, *Astron. Astrophys.* **555** (2013) A68, [arXiv:1305.1884].

[500] T. M. Evans et al., *The UVES large program for testing fundamental physics – III. Constraints on the fine–structure constant from three telescopes*, *Mon. Not. Roy. Astron. Soc.* **445** (2014) 128–150, [arXiv:1409.1923].

[501] M. T. Murphy, J. K. Webb, V. V. Flambaum, M. J. Drinkwater, F. Combes, and T. Wiklind, *Improved constraints on possible variation of physical constants from HI 21cm and molecular QSO absorption lines*, *Mon. Not. Roy. Astron. Soc.* **327** (2001) 1244, [astro-ph/0101519].

[502] J. A. King, J. K. Webb, M. T. Murphy, V. V. Flambaum, R. F. Carswell, M. B. Bainbridge, M. R. Wilczynska, and F. E. Koch, *Spatial variation in the fine–structure constant – new results from VLT/UVES*, *Mon. Not. Roy. Astron. Soc.* **422** (2012) 3370–3413, [arXiv:1202.4758].

[503] H. Rahmani, R. Srianand, N. Gupta, P. Petitjean, P. Noterdaeme, and D. A. Vásquez, *Constraining the variation of fundamental constants at $z \sim 1.3$ using 21cm absorbers*, *Mon. Not. Roy. Astron. Soc.* **425** (2012) 556–576, [arXiv:1206.2653].

[504] M. T. Murphy, V. V. Flambaum, J. K. Webb, V. V. Dzuba, J. X. Prochaska, and A. M. Wolfe, *Constraining variations in the fine–structure constant, quark masses, and the strong interaction*, *Lect. Notes Phys.* **648** (2004) 131–150, [astro-ph/0310318].

[505] M. T. Murphy, J. K. Webb, V. V. Flambaum, J. X. Prochaska, and A. M. Wolfe, *Further constraints on variation of the fine–structure constant from alkali doublet QSO absorption lines*, *Mon. Not. Roy. Astron. Soc.* **327** (2001) 1237, [astro-ph/0012421].

[506] K. A. Olive, M. Pospelov, Y.-Z. Qian, G. Manhes, E. Vangioni-Flam, A. Coc, and M. Casse, *A re–examination of the Re–187 bound on the variation of fundamental couplings*, *Phys. Rev.* **D69** (2004) 027701, [astro-ph/0309252].

[507] Y. Fujii, A. Iwamoto, T. Fukahori, T. Ohnuki, M. Nakagawa, H. Hidaka, Y. Oura, and P. Moller, *Nuclear data in Oklo and time variability of fundamental coupling constants*, hep-ph/0205206.

[508] E. D. Davis and L. Hamdan, *Reappraisal of the limit on the variation in α implied by the Oklo natural fission reactors*, *Phys. Rev.* **C92** (2015) 014319, [arXiv:1503.06011].

[509] T. Rosenband, D. Hume, P. Schmidt, C. Chou, A. Brusch, L. Lorini, W. Oskay, R. Drullinger, T. Fortier, J. Stalnaker, S. Diddams, W. Swann, N. Newbury, W. Itano, D. Wineland, and B. J., *Frequency ratio of Al^+ and Hg^+ single–ion optical clocks; Metrology at the 17th decimal place*, *Science* **319** (2008) 1808.

[510] F. Iocco, G. Mangano, G. Miele, O. Pisanti, and P. D. Serpico, *Primordial nucleosynthesis: From precision cosmology to fundamental physics*, *Phys. Rept.* **472** (2009) 1–76, [arXiv:0809.0631].

[511] **Planck** Collaboration, P. A. R. Ade et al., *Planck intermediate results – XXIV. Constraints on variations in fundamental constants*, *Astron. Astrophys.* **580** (2015) A22, [arXiv:1406.7482].

[512] A. Hees, O. Minazzoli, and J. Larena, *Breaking of the equivalence principle in the electromagnetic sector and its cosmological signatures*, *Phys. Rev.* **D90** (2014) 124064, [arXiv:1406.6187].

[513] J. D. Bekenstein, *Fine–structure constant: Is it really a constant?*, *Phys. Rev.* **D25** (1982) 1527–1539.

[514] H. B. Sandvik, J. D. Barrow, and J. Magueijo, *A simple cosmology with a varying fine–structure constant*, *Phys. Rev. Lett.* **88** (2002) 031302, [astro-ph/0107512].

[515] J. D. Barrow and S. Z. W. Lip, *A generalized theory of varying α*, *Phys. Rev.* **D85** (2012) 023514, [arXiv:1110.3120].

[516] J. D. Barrow and A. A. H. Graham, *General dynamics of varying–α Universes*, *Phys. Rev.* **D88** (2013) 103513, [arXiv:1307.6816].

[517] O. Minazzoli, *Conservation laws in theories with universal gravity/matter coupling*, *Phys. Rev.* **D88** (2013) 027506, [arXiv:1307.1590].

[518] O. Minazzoli and A. Hees, *Late–time cosmology of a scalar–tensor theory with a universal multiplicative coupling between the scalar field and the matter Lagrangian*, *Phys. Rev.* **D90** (2014) 023017, [arXiv:1404.4266].

[519] I. Etherington, *On the definition of distance in General Relativity*, *Philos. Mag.* **15** (1933) 761.

[520] I. Etherington, *Republication of: LX. On the definition of distance in General Relativity*, *Gen. Relativ. Gravit.* **39** (2007) 1055.

[521] G. Ellis, *On the definition of distance in General Relativity: I. M. H. Etherington (Philosophical Magazine ser. 7, vol. 15, 761 (1933))*, *Gen. Relativ. Gravit.* **39** (2007) 1047.

[522] G. F. R. Ellis, R. Poltis, J.-P. Uzan, and A. Weltman, *Blackness of the cosmic microwave background spectrum as a probe of the distance–duality relation*, *Phys. Rev.* **D87** (2013) 103530, [arXiv:1301.1312].

[523] J. A. S. Lima, *Thermodynamics of decaying vacuum cosmologies*, *Phys. Rev.* **D54** (1996) 2571–2577, [gr-qc/9605055].

[524] J. A. S. Lima, A. I. Silva, and S. M. Viegas, *Is the radiation temperature redshift relation of the standard cosmology in accordance with the data?*, *Mon. Not. Roy. Astron. Soc.* **312** (2000) 747–752.

[525] P. Brax, C. Burrage, and A.-C. Davis, *Shining light on modifications of gravity*, *JCAP* **1210** (2012) 016, [arXiv:1206.1809].

[526] P. Brax, C. Burrage, A.-C. Davis, and G. Gubitosi, *Cosmological tests of the disformal coupling to radiation*, *JCAP* **1311** (2013) 001, [arXiv:1306.4168].

[527] C. van de Bruck, C. Burrage, and J. Morrice, *Vacuum Cherenkov radiation and bremsstrahlung from disformal couplings*, *JCAP* **1608** (2016) 003, [arXiv:1605.03567].

[528] T. Damour, F. Piazza, and G. Veneziano, *Violations of the equivalence principle in a dilaton runaway scenario*, *Phys. Rev.* **D66** (2002) 046007, [hep-th/0205111].

[529] T. Damour, F. Piazza, and G. Veneziano, *Runaway dilaton and equivalence principle violations*, *Phys. Rev. Lett.* **89** (2002) 081601, [gr-qc/0204094].

[530] T. Damour and A. M. Polyakov, *String theory and gravity*, *Gen. Rel. Grav.* **26** (1994) 1171–1176, [gr-qc/9411069].

[531] E. J. Copeland, N. J. Nunes, and M. Pospelov, *Models of quintessence coupled to the electromagnetic field and the cosmological evolution of α*, *Phys. Rev.* **D69** (2004) 023501, [hep-ph/0307299].

[532] K. A. Olive and M. Pospelov, *Evolution of the fine–structure constant driven by dark matter and the cosmological constant*, *Phys. Rev.* **D65** (2002) 085044, [hep-ph/0110377].

[533] N. J. Nunes and J. E. Lidsey, *Reconstructing the dark energy equation of state with varying α*, *Phys. Rev.* **D69** (2004) 123511, [astro-ph/0310882].

[534] J.-P. Uzan, *Varying constants, gravitation, and cosmology*, *Living Rev. Rel.* **14** (2011) 2, [arXiv:1009.5514].

[535] M. Zumalacárregui, T. S. Koivisto, and D. F. Mota, *DBI Galileons in the Einstein frame: Local gravity and cosmology*, *Phys. Rev.* **D87** (2013) 083010, [arXiv:1210.8016].

[536] M. Minamitsuji, *Disformal transformation of cosmological perturbations*, *Phys. Lett.* **B737** (2014) 139–150, [arXiv:1409.1566].

[537] T. S. Koivisto, D. F. Mota, and M. Zumalacárregui, *Screening modifications of gravity through disformally coupled fields*, *Phys. Rev. Lett.* **109** (2012) 241102, [arXiv:1205.3167].

[538] N. Suzuki et al., *The Hubble Space Telescope cluster supernova survey: V. Improving the dark energy constraints above $z > 1$ and building an early–type–hosted supernova sample*, *Astrophys. J.* **746** (2012) 85, [arXiv:1105.3470].

[539] S. Das, P. S. Corasaniti, and J. Khoury, *Super–acceleration as signature of dark sector interaction*, *Phys. Rev.* **D73** (2006) 083509, [astro-ph/0510628].

[540] T. Chiba, *The constancy of the constants of Nature: Updates*, *Prog. Theor. Phys.* **126** (2011) 993–1019, [arXiv:1111.0092].

[541] P. Brax and C. Burrage, *Constraining disformally coupled scalar fields*, *Phys. Rev.* **D90** (2014) 104009, [arXiv:1407.1861].

[542] G. R. Dvali and M. Zaldarriaga, *Changing α with time: Implications for fifth force type experiments and quintessence*, *Phys. Rev. Lett.* **88** (2002) 091303, [hep-ph/0108217].

[543] E. Calabrese, E. Menegoni, C. J. A. P. Martins, A. Melchiorri, and G. Rocha, *Constraining variations in the fine–structure constant in the presence of early dark energy*, *Phys. Rev.* **D84** (2011) 023518, [arXiv:1104.0760].

[544] C. J. A. P. Martins and A. M. M. Pinho, *Fine–structure constant constraints on dark energy*, *Phys. Rev.* **D91** (2015) 103501, [arXiv:1505.02196].

[545] K. G. Strassmeier et al., *PEPSI: The high–resolution échelle spectrograph and polarimeter for the Large Binocular Telescope*, *Astron. Nachr.* **336** (2015) 324–361.

[546] K. G. Strassmeier, I. Ilyin, and M. Steffen, *PEPSI deep spectra. I. The Sun–as–a–star*, *Astron. Astrophys.* **612** (2018) A44, [arXiv:1712.06960].

[547] F. Pepe et al., *ESPRESSO – An Echelle SPectrograph for Rocky Exo–planets Search and Stable Spectroscopic Observations*, *The Messenger (ESO)* **153** (2013) 6.

[548] ESO, "The E–ELT construction proposal." http://www.eso.org/public/products/books/book_0046, 2011. [Online; accessed 12–07–2018].

[549] R. Maiolino et al., *A community science case for E–ELT HIRES*, arXiv:1310.3163.

[550] V. Fish et al., *High–angular–resolution and high–sensitivity science enabled by beamformed ALMA*, arXiv:1309.3519.

[551] R. P. J. Tilanus et al., *Future mmVLBI research with ALMA: A European vision*, arXiv:1406.4650.

[552] C. J. A. P. Martins, *Fundamental cosmology in the E–ELT era: The status and future role of tests of fundamental coupling stability*, *Gen. Rel. Grav.* **47** (2015) 1843, [arXiv:1412.0108].

[553] J. Bagdonaite, E. J. Salumbides, S. P. Preval, M. A. Barstow, J. D. Barrow, M. T. Murphy, and W. Ubachs, *Limits on a gravitational field dependence of the proton–electron mass ratio from H_2 in white dwarf stars*, *Phys. Rev. Lett.* **113** (2014) 123002, [arXiv:1409.1000].

[554] J. C. Berengut, V. V. Flambaum, A. Ong, J. K. Webb, J. D. Barrow, M. A. Barstow, S. P. Preval, and J. B. Holberg, *Limits on the dependence of the fine–structure constant on gravitational potential from white–dwarf spectra*, *Phys. Rev. Lett.* **111** (2013) 010801, [arXiv:1305.1337].

[555] G. D'Amico, T. Hamill, and N. Kaloper, *Quantum field theory of interacting dark matter and dark energy: Dark monodromies*, *Phys. Rev.* **D94** (2016) 103526, [arXiv:1605.00996].

[556] H. Y. Ip, J. Sakstein, and F. Schmidt, *Solar system constraints on disformal gravity theories*, *JCAP* **1510** (2015) 051, [arXiv:1507.00568].

[557] P. Brax, C. Burrage, and C. Englert, *Disformal dark energy at colliders*, *Phys. Rev.* **D92** (2015) 044036, [arXiv:1506.04057].

[558] P. Brax, C. Burrage, C. Englert, and M. Spannowsky, *LHC signatures of scalar dark energy*, *Phys. Rev.* **D94** (2016) 084054, [arXiv:1604.04299].

[559] C. van de Bruck and G. Sculthorpe, *Modified gravity and the radiation dominated epoch*, *Phys. Rev.* **D87** (2013) 044004, [arXiv:1210.2168].

[560] Yu. L. Bolotin, A. Kostenko, O. A. Lemets, and D. A. Yerokhin, *Cosmological evolution with interaction between dark energy and dark matter*, *Int. J. Mod. Phys.* **D24** (2014) 1530007, [arXiv:1310.0085].

[561] W. Zimdahl and D. Pavon, *Interacting quintessence*, *Phys. Lett.* **B521** (2001) 133–138, [astro-ph/0105479].

[562] G. R. Farrar and P. J. E. Peebles, *Interacting dark matter and dark energy*, *Astrophys. J.* **604** (2004) 1–11, [astro-ph/0307316].

[563] L. Amendola, *Linear and non–linear perturbations in dark energy models*, *Phys. Rev.* **D69** (2004) 103524, [astro-ph/0311175].

[564] A. V. Maccio, C. Quercellini, R. Mainini, L. Amendola, and S. A. Bonometto, *N–body simulations for coupled dark energy: Halo mass function and density profiles*, *Phys. Rev.* **D69** (2004) 123516, [astro-ph/0309671].

[565] T. Koivisto, *Growth of perturbations in dark matter coupled with quintessence*, *Phys. Rev.* **D72** (2005) 043516, [astro-ph/0504571].

[566] S. Lee, G.-C. Liu, and K.-W. Ng, *Constraints on the coupled quintessence from cosmic microwave background anisotropy and matter power spectrum*, *Phys. Rev.* **D73** (2006) 083516, [astro-ph/0601333].

[567] Z.-K. Guo, N. Ohta, and S. Tsujikawa, *Probing the coupling between dark components of the Universe*, *Phys. Rev.* **D76** (2007) 023508, [astro-ph/0702015].

[568] R. Mainini and S. Bonometto, *Limits on coupling between dark components*, *JCAP* **0706** (2007) 020, [astro-ph/0703303].

[569] M. Baldi, V. Pettorino, G. Robbers, and V. Springel, *Hydrodynamical N–body simulations of coupled dark energy cosmologies*, *Mon. Not. Roy. Astron. Soc.* **403** (2010) 1684–1702, [arXiv:0812.3901].

[570] R. Bean, E. E. Flanagan, I. Laszlo, and M. Trodden, *Constraining interactions in cosmology's dark sector*, *Phys. Rev.* **D78** (2008) 123514, [arXiv:0808.1105].

[571] E. R. M. Tarrant, C. van de Bruck, E. J. Copeland, and A. M. Green, *Coupled quintessence and the halo mass function*, *Phys. Rev.* **D85** (2012) 023503, [arXiv:1103.0694].

[572] A. Pourtsidou, C. Skordis, and E. J. Copeland, *Models of dark matter coupled to dark energy*, *Phys. Rev.* **D88** (2013) 083505, [arXiv:1307.0458].

[573] V. Pettorino, *Testing modified gravity with Planck: The case of coupled dark energy*, *Phys. Rev.* **D88** (2013) 063519, [arXiv:1305.7457].

[574] J.-Q. Xia, *New limits on coupled dark energy from Planck*, *JCAP* **1311** (2013) 022, [arXiv:1311.2131].

[575] J. Sakstein, *Disformal theories of gravity: From the Solar System to cosmology*, *JCAP* **1412** (2014) 012, [arXiv:1409.1734].

[576] **Planck** Collaboration, P. A. R. Ade et al., *Planck 2015 results. XIV. Dark energy and modified gravity*, *Astron. Astrophys.* **594** (2016) A14, [arXiv:1502.01590].

[577] J. Gleyzes, D. Langlois, M. Mancarella, and F. Vernizzi, *Effective theory of interacting dark energy*, *JCAP* **1508** (2015) 054, [arXiv:1504.05481].

[578] C. Skordis, A. Pourtsidou, and E. J. Copeland, *Parametrized post-Friedmannian framework for interacting dark energy theories*, *Phys. Rev.* **D91** (2015) 083537, [arXiv:1502.07297].

[579] W. Hu and N. Sugiyama, *Anisotropies in the cosmic microwave background: An analytic approach*, *Astrophys. J.* **444** (1995) 489–506, [astro-ph/9407093].

[580] M. Doran, M. J. Lilley, J. Schwindt, and C. Wetterich, *Quintessence and the separation of CMB peaks*, *Astrophys. J.* **559** (2001) 501–506, [astro-ph/0012139].

[581] J. M. Bardeen, *Gauge invariant cosmological perturbations*, *Phys. Rev.* **D22** (1980) 1882–1905.

[582] H. Kodama and M. Sasaki, *Cosmological perturbation theory*, *Prog. Theor. Phys. Suppl.* **78** (1984) 1–166.

[583] V. F. Mukhanov, H. A. Feldman, and R. H. Brandenberger, *Theory of cosmological perturbations. Part 1. Classical perturbations. Part 2. Quantum theory of perturbations. Part 3. Extensions*, *Phys. Rept.* **215** (1992) 203–333.

[584] R. K. Sachs and A. M. Wolfe, *Perturbations of a cosmological model and angular variations of the microwave background*, *Astrophys. J.* **147** (1967) 73–90. [Gen. Rel. Grav. **39** (2007) 1929].

[585] W. Hu, M. Fukugita, M. Zaldarriaga, and M. Tegmark, *CMB observables and their cosmological implications*, *Astrophys. J.* **549** (2001) 669, [astro-ph/0006436].

[586] W. Hu and S. Dodelson, *Cosmic microwave background anisotropies*, *Ann. Rev. Astron. Astrophys.* **40** (2002) 171–216, [astro-ph/0110414].

[587] P. S. Corasaniti, B. A. Bassett, C. Ungarelli, and E. J. Copeland, *Model–independent dark energy differentiation with the ISW effect*, *Phys. Rev. Lett.* **90** (2003) 091303, [astro-ph/0210209].

[588] R. G. Crittenden and N. Turok, *Looking for Λ with the Rees–Sciama effect*, *Phys. Rev. Lett.* **76** (1996) 575, [astro-ph/9510072].

[589] G. Olivares, F. Atrio-Barandela, and D. Pavon, *The Integrated Sachs–Wolfe effect in interacting dark energy models*, *Phys. Rev.* **D77** (2008) 103520, [arXiv:0801.4517].

[590] J.-Q. Xia, *Constraint on coupled dark energy models from observations*, *Phys. Rev.* **D80** (2009) 103514, [arXiv:0911.4820].

[591] B. Wang, E. Abdalla, F. Atrio-Barandela, and D. Pavon, *Dark matter and dark energy interactions: Theoretical challenges, cosmological implications and observational signatures*, *Rept. Prog. Phys.* **79** (2016) 096901, [arXiv:1603.08299].

[592] E. V. Linder, *Cosmic growth and expansion conjoined*, *Astropart. Phys.* **86** (2017) 41–45, [arXiv:1610.05321].

[593] L. Amendola, V. Pettorino, C. Quercellini, and A. Vollmer, *Testing coupled dark energy with next–generation large–scale observations*, *Phys. Rev.* **D85** (2012) 103008, [arXiv:1111.1404].

[594] M. P. van Haarlem et al., *LOFAR: The LOw–Frequency ARray*, *Astron. Astrophys.* **556** (2013) A2, [arXiv:1305.3550].

[595] O. F. Hernández, *Neutrino masses, scale–dependent growth, and redshift–space distortions*, *JCAP* **1706** (2017) 018, [arXiv:1608.08298].

[596] T. Clemson, K. Koyama, G.-B. Zhao, R. Maartens, and J. Valiviita, *Interacting dark energy – constraints and degeneracies*, *Phys. Rev.* **D85** (2012) 043007, [arXiv:1109.6234].

[597] D. Tocchini-Valentini and L. Amendola, *Stationary dark energy with a baryon dominated era: Solving the coincidence problem with a linear coupling*, *Phys. Rev.* **D65** (2002) 063508, [astro-ph/0108143].

[598] **Planck** Collaboration, P. A. R. Ade et al., *Planck 2015 results. XX. Constraints on inflation*, *Astron. Astrophys.* **594** (2016) A20, [arXiv:1502.02114].

[599] G.-B. Zhao, L. Pogosian, A. Silvestri, and J. Zylberberg, *Searching for modified growth patterns with tomographic surveys*, *Phys. Rev.* **D79** (2009) 083513, [arXiv:0809.3791].

[600] M. Raveri, B. Hu, N. Frusciante, and A. Silvestri, *Effective field theory of cosmic acceleration: Constraining dark energy with CMB data*, *Phys. Rev.* **D90** (2014) 043513, [arXiv:1405.1022].

[601] B. Hu and M. Raveri, *Can modified gravity models reconcile the tension between the CMB anisotropy and lensing maps in Planck–like observations?*, *Phys. Rev.* **D91** (2015) 123515, [arXiv:1502.06599].

[602] E. Bellini, A. J. Cuesta, R. Jimenez, and L. Verde, *Constraints on deviations from ΛCDM within Horndeski gravity*, *JCAP* **1602** (2016) 053, [arXiv:1509.07816].

[603] L. Samushia et al., *The clustering of galaxies in the SDSS–III Baryon Oscillation Spectroscopic Survey: Measuring growth rate and geometry with anisotropic clustering*, *Mon. Not. Roy. Astron. Soc.* **439** (2014) 3504–3519, [arXiv:1312.4899].

[604] T. Damour, G. W. Gibbons, and C. Gundlach, *Dark matter, time–varying G, and a dilaton field*, *Phys. Rev. Lett.* **64** (1990) 123–126.

[605] S. S. Gubser and P. J. E. Peebles, *Cosmology with a dynamically screened scalar interaction in the dark sector*, *Phys. Rev.* **D70** (2004) 123511, [hep-th/0407097].

[606] S. M. Carroll, S. Mantry, M. J. Ramsey-Musolf, and C. W. Stubbs, *Dark–matter–induced weak equivalence principle violation*, *Phys. Rev. Lett.* **103** (2009) 011301, [arXiv:0807.4363].

[607] L. Amendola and C. Quercellini, *Tracking and coupled dark energy as seen by WMAP*, *Phys. Rev.* **D68** (2003) 023514, [astro-ph/0303228].

[608] V. Pettorino, L. Amendola, C. Baccigalupi, and C. Quercellini, *Constraints on coupled dark energy using CMB data from WMAP and SPT*, *Phys. Rev.* **D86** (2012) 103507, [arXiv:1207.3293].

[609] V. Miranda, M. Carrillo González, E. Krause, and M. Trodden, *Finding structure in the dark: Coupled dark energy, weak lensing, and the mildly nonlinear regime*, *Phys. Rev.* **D97** (2018) 063511, [arXiv:1707.05694].

[610] M. Zumalacárregui, T. S. Koivisto, D. F. Mota, and P. Ruiz-Lapuente, *Disformal scalar fields and the dark sector of the Universe*, *JCAP* **1005** (2010) 038, [arXiv:1004.2684].

[611] T. S. Koivisto, *Disformal quintessence*, arXiv:0811.1957.

[612] A. J. Cuesta et al., *The clustering of galaxies in the SDSS–III Baryon Oscillation Spectroscopic Survey: Baryon acoustic oscillations in the correlation function of LOWZ and CMASS galaxies in data release 12*, *Mon. Not. Roy. Astron. Soc.* **457** (2016) 1770–1785, [arXiv:1509.06371].

[613] L. Amendola, M. Gasperini, and F. Piazza, *Fitting type Ia supernovae with coupled dark energy*, *JCAP* **0409** (2004) 014, [astro-ph/0407573].

[614] R. Jimenez and A. Loeb, *Constraining cosmological parameters based on relative galaxy ages*, *Astrophys. J.* **573** (2002) 37–42, [astro-ph/0106145].

[615] J. L. Bernal, L. Verde, and A. J. Cuesta, *Parameter splitting in dark energy: Is dark energy the same in the background and in the cosmic structures?*, *JCAP* **1602** (2016) 059, [arXiv:1511.03049].

[616] R. Bean, E. E. Flanagan, and M. Trodden, *Adiabatic instability in coupled dark energy–dark matter models*, *Phys. Rev.* **D78** (2008) 023009, [arXiv:0709.1128].

[617] O. L. Creevey et al., *Benchmark stars for Gaia: Fundamental properties of the population II star HD 140283 from interferometric, spectroscopic, and photometric data*, *Astron. Astrophys.* **575** (2015) A26.

[618] D. A. VandenBerg, H. E. Bond, E. P. Nelan, P. E. Nissen, G. H. Schaefer, and D. Harmer, *Three ancient halo subgiants: Precise parallaxes, compositions, ages, and implications for globular clusters*, *Astrophys. J.* **792** (2014) 110.

[619] H. E. Bond, E. P. Nelan, D. A. VandenBerg, G. H. Schaefer, and D. Harmer, *HD 140283: A star in the solar neighborhood that formed shortly after the Big Bang*, *Astrophys. J.* **765** (2013) L12.

[620] B. E. Robertson, R. S. Ellis, S. R. Furlanetto, and J. S. Dunlop, *Cosmic reionization and early star–forming galaxies: A joint analysis of new constraints from Planck and the Hubble Space Telescope*, *Astrophys. J.* **802** (2015) L19, [arXiv:1502.02024].

[621] G. D. Becker, J. S. Bolton, and A. Lidz, *Reionization and high–redshift galaxies: The view from quasar absorption lines*, *Publ. Astron. Soc. Austral.* **32** (2015) 45, [arXiv:1510.03368].

[622] M. McQuinn, *The evolution of the intergalactic medium*, *Ann. Rev. Astron. Astrophys.* **54** (2016) 313, [arXiv:1512.00086].

[623] **Planck** Collaboration, N. Aghanim et al., *Planck intermediate results. XLVI. Reduction of large–scale systematic effects in HFI polarization maps and estimation of the reionization optical depth*, *Astron. Astrophys.* **596** (2016) A107, [arXiv:1605.02985].

[624] **Planck** Collaboration, R. Adam et al., *Planck intermediate results. XLVII. Planck constraints on reionization history*, *Astron. Astrophys.* **596** (2016) A108, [arXiv:1605.03507].

[625] A. Avelino and R. P. Kirshner, *The dimensionless age of the Universe: A riddle for our time*, *Astrophys. J.* **828** (2016) 35, [arXiv:1607.00002].

[626] F. Melia, *The cosmic horizon*, *Mon. Not. Roy. Astron. Soc.* **382** (2007) 1917–1921, [arXiv:0711.4181].

[627] F. Melia and A. Shevchuk, *The $R_h = ct$ Universe*, *Mon. Not. Roy. Astron. Soc.* **419** (2012) 2579–2586, [arXiv:1109.5189].

[628] P. van Oirschot, J. Kwan, and G. F. Lewis, *Through the looking glass: Why the 'cosmic horizon' is not a horizon*, *Mon. Not. Roy. Astron. Soc.* **404** (2010) 1633–1638, [arXiv:1001.4795].

[629] E. di Valentino, A. Melchiorri, and O. Mena, *Can interacting dark energy solve the H_0 tension?*, *Phys. Rev.* **D96** (2017) 043503, [arXiv:1704.08342].

[630] V. Bonvin et al., *H0LiCOW – V. New COSMOGRAIL time delays of HE 0435–1223: H_0 to 3.8% precision from strong lensing in a flat ΛCDM model*, *Mon. Not. Roy. Astron. Soc.* **465** (2017) 4914–4930, [arXiv:1607.01790].

[631] X.-H. Fan, M. A. Strauss, R. H. Becker, R. L. White, J. E. Gunn, G. R. Knapp, G. T. Richards, D. P. Schneider, J. Brinkmann, and M. Fukugita, *Constraining the evolution of the ionizing background and the epoch of reionization with $z \sim 6$ quasars II: A sample of 19 quasars*, *Astron. J.* **132** (2006) 117–136, [astro-ph/0512082].

[632] J. E. Gunn and B. A. Peterson, *On the density of neutral hydrogen in intergalactic space*, *Astrophys. J.* **142** (1965) 1633.

[633] R. Murgia, S. Gariazzo, and N. Fornengo, *Constraints on the coupling between dark energy and dark matter from CMB data*, *JCAP* **1604** (2016) 014, [arXiv:1602.01765].

[634] M. Kesden and M. Kamionkowski, *Tidal tails test the equivalence principle in the dark sector*, *Phys. Rev.* **D74** (2006) 083007, [astro-ph/0608095].

[635] L.-F. Xiao, R. An, L. Zhang, B. Yue, Y. Xu, and B. Wang, *Can conformal and disformal couplings between dark sectors explain the EDGES 21cm anomaly?*, arXiv:1807.05541.